Silicon-based Systems for Microscopic and Volumetric Terahertz Imaging

Dissertation
Submitted in partial fulfillment of the requirements for the degree of
Doktor der Ingenierwissenschaften

at the
University of Wuppertal, Germany
School of Electrical, Information and Media Engineering

by
Philipp Hillger
from Wuppertal, Germany

April 2020

The PhD thesis can be quoted as follows:

urn:nbn:de:hbz:468-20200420-111817-4
[http://nbn-resolving.de/urn/resolver.pl?urn=urn%3Anbn%3Ade%3Ahbz%3A468-20200420-111817-4]

DOI: 10.25926/346h-5p75
[https://doi.org/10.25926/346h-5p75]

Referent: Prof. Dr. rer. nat. Ullrich Pfeiffer
Korreferent: Prof. Dr. rer. nat. Thomas Riedl

Tag der mündlichen Prüfung: 31. Januar 2020

Acknowledgements

I would like to express my sincere gratitude to my advisor Prof. Ullrich Pfeiffer, who has been an endless source of inspiration, guidance, and knowledge during this journey. With his innovative spirit and dedication, he has nurtured my passion in academic research. From the very beginning of my doctoral project, he put confidence into me and opened any opportunity to me to grow as a professional. He has taught me to be a scientist.

Moreover, I would like to acknowledge my associate advisor Prof. Thomas Riedl for co-examining my doctoral thesis. I appreciate the effort and time he devoted.

I owe my gratitude to the German Research Foundation (Deutsche Forschungsgemeinschaft) for providing economic support and scientific opportunities.

I have been lucky to be surrounded by great colleagues at the IHCT who supported me along the way and made the last years a truly enjoyable time. I am particularly indebted to Dr. Janusz Grzyb for teaching me the power of critical reasoning in engineering. His contributions to both the design and publication of my work have been essential to my professional development in the last years. I would also like to thank Ritesh Jain and Dr. Stefan Malz for countless empowering personal and technical discussions, and for challenging my thinking every day. They have truly been the best officemates I could imagine. Moreover, I would like to thank Thomas Bücher for his valuable help in reviewing this manuscript and for all his support during the writing phase. Special thanks is reserved for Wolfgang Förster. His his support and contributions to the design of the discrete electronics were fundamental to this work.

I would also like to acknowledge Quentin Cassar for all his support and valuable discussions, and I would like to thank Manuel Theisen and Christian Tückmantel for their help with the tissue imaging experiments.

My deep gratitude goes to my parents for their love and unconditional support throughout my education. Finally, I would like to thank my wonderful wife, Verena, for understanding and being at my side all this time. She is the center of my world. Without my family, all this would not have been possible. I dedicate this thesis to them.

Abstract

Owing to the unique characteristics of terahertz (THz) waves and their interaction with matter, THz imaging has significant potential in diverse fields, including life sciences, non-destructive quality control, and security. However, today's THz technology faces major obstacles in providing the cost, compactness, and functional scope that is required to facilitate a wide-reaching use outside the laboratory. Therefore, the general aim of this thesis is to increase the societal impact of THz technology by exploring novel THz imaging modalities with integrated circuits (ICs) based on conventional silicon technolgy.

Previous research in THz ICs mostly focused on building compact integrated source and detector components for far-field imaging systems that exploit the ability of THz waves to penetrate through diverse dielectric materials. One part of this thesis joins this research and demonstrates low-cost volumetric THz imaging based on computed tomography with silicon components for the first time. To this end, a high-power 0.43 THz source in 0.13 µm silicon-germanium heterojunction bipolar transistor (SiGe HBT) technology is developed in this thesis. However, the resolution of THz far-field imaging is limited by diffraction to the millimeter range, whereas some of the most promising THz applications in life sciences, such as intraoperative imaging of cancerous tissue, are in need for a microscopic resolution to resolve material properties on the cellular level.

This thesis presents the realization of microscopic THz imaging with a silicon-based sensor system. The central contribution of this work is the development and analysis of a 128-pixel THz near-field sensor System-on-a-Chip (SoC) operating at 0.55 THz and showing a spatial resolution around 10 µm. The sensor exploits the capacitive near-field interaction between split-ring-resonator probes and imaging objects, giving an imaging contrast based on the dielectric permittivity. To simultaneously enable real-time image acquisition, high sensor sensitivity, and an integration level that is comparable to conventional consumer electronics, the full integration capabilities of a high-speed 0.13 µm SiGe bipolar CMOS (SiGe-BiCMOS) technology are exploited. In particular, the presented SoC employs cointegration of a chip-scale one-dimensional THz sensor front-end, analog signal processing, and digital circuitry for controlling the chip and external communication. The achieved results in terms of imaging speed, system cost, and integration level reach well beyond the state of the art in THz near-field imaging.

The ability to rapidly acquire THz images with micrometer-scale resolution will be of benefit to fundamental research into material properties in the THz range and lays the foundation for the exploration of THz bioimaging applications on the cellular level. In particular, the sensor enables the conduction of large-scale clinical studies on the relevance of microscopic THz imaging to *ex vivo* tumor margin assessment in breast cancer surgeries for the first time.

Zusammenfassung

Aufgrund der spezifischen Eigenschaften von THz-Wellen und deren Wechselwirkung mit Materie bietet die THz-Bildgebung erhebliches Potenzial in diversen Anwendungsbereichen, unter anderem in den Biowissenschaften, der zerstörungsfreien Qualitätskontrolle und in Sicherheitsanwendungen. Die gegenwärtigen THz-Systeme erfüllen jedoch nicht die Voraussetzungen in Bezug auf Kosten, Kompaktheit und Funktionsumfang, um eine weitreichende Verwendung außerhalb von Laborumgebungen zu ermöglichen. Das übergeordnete Ziel dieser Dissertation ist es daher, den gesellschaftlichen Einfluss von THz-Technologie durch die Realisierung neuartiger THz-Bildgebungsmodalitäten mit integrierten Schaltungen (IC) in konventioneller Siliziumtechnologie zu erhöhen.

Die bisherige Forschung in THz-ICs fokussierte sich vorwiegend auf die Entwicklung kompakter Strahlungsquellen und Detektoren für Fernfeld-Bildgebungssysteme, welche die Eigenschaft von THz-Wellen, verschiedene dielektrische Materialien zu durchdringen, ausnutzen. Ein Teil dieser Dissertation fügt sich in diese Forschung ein und demonstriert erstmals die kostengünstige volumetrische THz-Bildgebung unter Verwendung des Prinzips der Computertomographie mit Siliziumkomponenten. Dazu wird im Rahmen dieser Dissertation eine hochkompakte 430 GHz Quelle mit hoher Sendeleistung in einer 0.13 µm SiGe-HBT Technologie entwickelt. Die räumliche Auflösung von solchen Fernfeldbildgebungssystemen wird allerdings durch Beugungseffekte bei Terahertzwellen auf den Millimeterbereich begrenzt. Einige der vielversprechensten THz-Anwendungen in den Biowissenschaften, wie die intraoperative Bildgebung von Krebsgewebe, benötigen jedoch eine Auflösung im Mikrometerbereich, um die Messung von Materialeigenschaften auf zellulärer Ebene zu ermöglichen.

Diese Dissertation präsentiert die Realisierung von THz-Mikroskopie mit einem siliziumbasierten Sensorsystem. Der zentrale Beitrag dieser Arbeit ist die Entwicklung und die Analyse eines 128-pixel THz Nahfeldsensorchips, welcher bei einer Frequenz von 550 GHz arbeitet und eine Auflösung von ca. 10 µm aufweist. Der Sensor nutzt die kapazitive Nahfeldwechselwirkung zwischen Split-Ring-Resonatoren (SRRs) und dem Objekt und ermöglicht somit einen Bildgebungskontrast, der von der dielektrischen Permittivität bestimmt wird. Um gleichzeitig eine Bildgebung in Echtzeit, eine hohe Sensorempfindlichkeit und ein Integrationsniveau zu ermöglichen, das mit herkömmlicher Unterhaltungselektronik vergleichbar ist, werden die vollständigen Integrationsfähigkeiten einer 0.13 µm SiGe-BiCMOS-Technologie genutzt. In dem Chip wird ein eindimensionales THz-Sensor-Frontend, die analoge Signalverarbeitung und eine digitale Schaltung für die Steuerung und die externe Kommunikation kointegriert. Die so erzielten Ergebnisse in Bezug auf Bildgebungsgeschwindigkeit, Systemkosten, und Integrationsniveau gehen weit über den aktuellen Stand der Technik der THz-Nahfeld-Bildgebung hinaus.

Die Fähigkeit, mikroskopische THz-Aufnahmen schnell zu erzeugen, wird der Erforschung von Materialeigenschaften im THz-Frequenzbereich zu Gute kommen und legt die Grundlage für die Untersuchung von Anwendungen in der biologischen THz-Bildgebung auf zellulärer Ebene. Insbesondere können mit dem hier präsentierten Sensor erstmals umfassende Studien zur klinischen Relevanz von THz-Wellen für die intraoperative mikroskopische Tumorranderkennung bei der Brustkrebsbehandlung durchgeführt werden.

Contents

Abstract iii

Zusammenfassung iv

I. Context 1

1. Introduction 3
- 1.1. Central Research Questions and Contributions . . . 6
- 1.2. Thesis Structure . . . 8

2. Terahertz Imaging and Sensing 9
- 2.1. Contrast in Terahertz Imaging . . . 9
  - 2.1.1. Macroscopic Electrodynamics . . . 9
  - 2.1.2. Absorption and Dispersion . . . 11
  - 2.1.3. Reflection and Transmission at Material Boundaries . . . 12
  - 2.1.4. Wave-Matter Interaction Phenomena in the THz Band . . . 14
  - 2.1.5. Application: Breast Cancer Margin Assessment . . . 21
- 2.2. Spatial Resolution in Terahertz Imaging . . . 23
  - 2.2.1. Limitations of Far-Field Imaging . . . 23
  - 2.2.2. Breaking the Diffraction Limit . . . 26
- 2.3. Review of Contemporary THz Technology . . . 27
  - 2.3.1. Review of THz Near-Field Imaging Methods . . . 28
  - 2.3.2. Traditional THz Technology . . . 30
  - 2.3.3. Silicon Technology for THz Systems . . . 31
  - 2.3.4. THz Components in Silicon Technology . . . 32

II. Far-Field Imaging 37

3. Frequency-Doubler-Based 0.43 THz Source for Active Far-Field Imaging 39
- 3.1. Design Considerations . . . 40

3.2. Implementation 42
3.3. Experimental Characterization 44
3.4. Summary and Conclusions 47

4. 3D Terahertz Imaging Based on Computed Tomography 49
4.1. Fundamentals of Computed Tomography 50
4.2. THz Computed Tomography with Silicon-Based Components 53
4.2.1. Experimental Setup 53
4.2.2. Imaging Results 56
4.2.3. Discussion 57
4.3. Summary and Conclusions 57

III. Near-Field Imaging 61

5. THz Near-Field Sensing in Silicon Technology 63
5.1. Resonator-Based Sensing in Planar Technology 64
5.1.1. Perturbation Theory 65
5.1.2. Planar SRRs for Imaging 66
5.2. Incoherent Sensing Concept 67
5.2.1. Concept Description 68
5.2.2. Sensor Illumination 70
5.2.3. Power Detection 73
5.2.4. Figure-of-Merits 75
5.3. Single-Pixel THz Near-Field Sensors 77
5.3.1. Cross-Bridged Double Split-Ring Resonator 77
5.3.2. On Imaging and Practicability 81
5.4. Summary 83

6. Modeling of Cross-Bridged Double Split-Ring Resonators 85
6.1. Modeling of the Sensing Strips 85
6.1.1. Response to Varying Material Properties 87
6.1.2. Response to Spatial Object Displacements 87
6.2. Modeling of the Resonator Topology 90
6.2.1. Analysis of the Object-Induced Frequency Shift 92
6.2.2. Parameter Extraction 92
6.3. Model Validation 93
6.4. Discussion 95
6.4.1. Sensor Response Ambiguity 95
6.4.2. Considerations for Practical Applications 96

7. A THz Near-Field Sensor System-on-a-Chip in SiGe-HBT Technology 99
7.1. A Scalable Front-End for THz Near-Field Sensors . . . 101
7.1.1. A 1D Multi-Pixel Architecture . . . 102
7.1.2. Design of a Shielded Wilkinson Power Splitter Network . . . 102
7.1.3. Impact of Parasitic Cross-Coupling Effects . . . 105
7.2. Design and Implementation of the SoC . . . 108
7.2.1. System-on-a-Chip Architecture . . . 109
7.2.2. Triple-Push Illumination Source . . . 112
7.2.3. Power Detection Circuits . . . 113
7.2.4. Analog Signal Processing . . . 115
7.2.5. Digital Interfacing and ASIC . . . 116
7.2.6. SoC Reference Generation . . . 118
7.3. Sensor Module . . . 119
7.3.1. Packaging . . . 119
7.3.2. Module and Electronic Periphery . . . 120
7.4. Experimental Characterization . . . 121
7.4.1. Oscillator Breakout Measurements . . . 122
7.4.2. Measurement of the Lateral Resolution . . . 124
7.4.3. Analog Read-Out . . . 125
7.4.4. Measurement of the Response Decay-Rate . . . 131
7.4.5. Measurement of Pixel Cross-Coupling . . . 131
7.4.6. Impact of Process Variations . . . 132
7.4.7. Digital Read-Out . . . 132
7.5. Imaging Experiments . . . 134
7.5.1. Imaging of a Human Fingerprint . . . 134
7.5.2. Imaging of a Nickel Grid . . . 137
7.5.3. Imaging of Breast Tissue . . . 139
7.6. Summary and Conclusion . . . 143

IV. Conclusion 147

8. Thesis Summary 149
8.1. Summary and Conclusions . . . 149
8.2. Future Directions . . . 151

Bibliography 153

List of Publications

Journal Publications

1. U. R. Pfeiffer, **P. Hillger**, R. Jain, J. Grzyb, T. Bücher, Q. Cassar, G. MacGrogan, J.-P. Guillet, P. Mounaix, and T. Zimmer, "Advances Towards a Silicon-Based Terahertz Near-Field Imaging Sensor for Ex Vivo Breast Tumor Identification," *IEEE Microwave Magazine*, vol. 20, no. 9, pp. 32-46, Sept. 2019.

2. **P. Hillger**, J. Grzyb, R. Jain, and U. R. Pfeiffer, "Terahertz Imaging and Sensing Applications With Silicon-Based Technologies," *IEEE Trans. THz Sci. Technol.*, vol. 9, no. 1, pp. 1–19, Jan. 2019, (Invited).

3. **P. Hillger**, R. Jain, J. Grzyb, W. Förster, B. Heinemann, G. MacGrogan, P. Mounaix, T. Zimmer, and U. R. Pfeiffer, "A 128-Pixel System-on-a-Chip for Real-Time Super-Resolution Terahertz Near-Field Imaging," *IEEE J. Solid-State Circuits*, vol. 53, no. 12, pp. 3599–3612, Dec. 2018.

4. Q. Cassar, A. Al-Ibadi, L. Mavarani, **P. Hillger**, J. Grzyb, G. MacGrogan, T. Zimmer, U. R. Pfeiffer, J.-P. Guillet, and P. Mounaix, "Pilot study of freshly excised breast tissue response in the 300 – 600 GHz range," *Biomed. Opt. Express*, vol. 9, no. 7, pp. 2930–2942, Jul. 2018.

5. L. Mavarani, **P. Hillger**, T. Bücher, J. Grzyb, U. R. Pfeiffer, Q. Cassar, A. Al-Ibadi, T. Zimmer, J.-P. Guillet, P. Mounaix, and G. MacGrogan, "NearSense – Advances Towards a Silicon-Based Terahertz Near-Field Imaging Sensor for Ex Vivo Breast Tumour Identification," *Frequenz*, vol 72, no. 3-4, pp. 93-99, Mar. 2018.

6. D. A. Funke, **P. Hillger**, J. Oehm, P. Mayr, L. Straczek, N. Pohl, and J. S. McCaskill, "A 200 μm by 100 μm Smart Submersible System With an Average Current Consumption of 1.3nA and a Compatible Voltage Converter," *IEEE Trans. on Circuits and Systems I: Regular Papers*, vol 64, no. 12, pp. 3013-3024, Dec. 2017.

Conference Publications

1. U. R. Pfeiffer, R. Jain, J. Grzyb, S. Malz, **P. Hillger** and P. Rodríguez-Vízquez, "Current Status of Terahertz Integrated Circuits - From Components to Systems," *2018 IEEE BiCMOS and Compound Semiconductor Integrated Circuits and Technology Symposium (BCICTS)*, San Diego, CA, 2018, pp. 1-7.

2. D. Headland, **P. Hillger**, R. Zatta and U. Pfeiffer, "Incoherent, spatially-mapped THz spectral analysis," *2018 43rd International Conference on Infrared, Millimeter, and Terahertz Waves (IRMMW-THz)*, Nagoya, 2018, pp. 1-2.

3. Q. Cassar, A. Al-Ibadi, L. Mavarani, **P. Hillger**, J. Grzyb, G. MacGrogan, U. R. Pfeiffer, T. Zimmer, J. P. Guillet, and P. Mounaix, "Studies on PCA for Breast Tissue Segmentation," *2018 43rd International Conference on Infrared, Millimeter, and Terahertz Waves (IRMMW-THz)*, Nagoya, 2018, pp. 1-2.

4. **P. Hillger**, R. Jain, J. Grzyb, L. Mavarani , B. Heinemann, G. M. Grogan, P. Mounaix, T. Zimmer, and U. Pfeiffer, "A 128-pixel 0.56THz sensing array for real-time near-field imaging in 0.13μm SiGe BiCMOS," *2018 IEEE International Solid - State Circuits Conference - (ISSCC)*, San Francisco, CA, 2018, pp. 418-420.

5. L. Mavarani, **P. Hillger**, J. Grzyb, Q. Cassar, A. Al-Ibadi, T. Zimmer, G. MacGrogan, J. P. Guillet, P. Mounaix, and U. R. Pfeiffer., "A novel approach of aqueous solution analysis using a fully-integrated terahertz near-field sensor," *2017 42nd International Conference on Infrared, Millimeter, and Terahertz Waves (IRMMW-THz)*, Cancun, 2017, pp. 1-2.

6. **P. Hillger**, A. Schlüter, R. Jain, S. Malz, J. Grzyb and U. Pfeiffer, "Low-Cost 0.5 THz computed tomography based on silicon components," *2017 42nd International Conference on Infrared, Millimeter, and Terahertz Waves (IRMMW-THz)*, Cancun, 2017, pp. 1-2.

7. T. Meister, F. Ellinger, J. W. Bartha, M. Berroth, J. Burghartz, M. Claus, L. Frey, A. Gagliardi, M. Grundmann, J. Hesselbarth, H. Klauk, K. Leo, P. Lugli, S. Mannsfeld, Y. Manoli, R. Negra, D. Neumaier, U. Pfeiffer, T. Riedl, S. Scheinert, U. Scherf, A. Thiede, G. Tröster, M. Vossiek, R. Weigel, C. Wenger, G. Alavi, M. Becherer, C. A. Chavarin, M. Darwish, M. Ellinger, C. Fan, M. Fritsch, F. Grotjahn, M. Gunia, K. Haase, **P. Hillger**, K. Ishida, M. Jank, S. Knobelspies, M. Kuhl, G. Lupina, S. M. Naghadeh, N. Münzenrieder, S. Özbek, M. Rasteh, G. A. Salvatore, D. Schrüfer, C. Strobel, M. Theisen, C. Tückmantel, H. von Wenckstern, Z. Wang, and Z. Zhang, "Program FFlexCom — High frequency flexible bendable electronics for wireless

communication systems," *2017 IEEE International Conference on Microwaves, Antennas, Communications and Electronic Systems (COMCAS)*, Tel-Aviv, 2017, pp. 1-6.

8. A. Al-Ibadi, Q. Cassar, T. Zimmer, G. MacGrogan, L. Mavarani, **P. Hillger**, J. Grzyb, U. R. Pfeiffer, J. P. Guillet, and P. Mounaix, "THz spectroscopy and imaging for breast cancer detection in the 300–500 GHz range," *2017 42nd International Conference on Infrared, Millimeter, and Terahertz Waves (IRMMW-THz)*, Cancun, 2017, pp. 1-1.

9. L. Mavarani, **P. Hillger**, J. Grzyb, Q. Cassar, A. Al-Ibadi, T. Zimmer, G. Mac Grogan, J.P. Guillet, P. Mounaix and U.R. Pfeiffer, "A silicon-based terahertz near-field imaging sensor for ex vivo life-science applications", *9th THz Days*, Dunkerque, France, June 2017 .

10. **P. Hillger**, J. Grzyb, S. Malz, B. Heinemann and U. Pfeiffer, "A lens-integrated 430 GHz SiGe HBT source with up to -6.3 dBm radiated power," *2017 IEEE Radio Frequency Integrated Circuits Symposium (RFIC)*, Honolulu, HI, 2017, pp. 160-163.

11. **P. Hillger**, J. Grzyb, and U.R. Pfeiffer, "Super-Resolution Near-Field Imaging Based on Sensors Fully-Integrated in Silicon Technolgy", *German THz Conference 2017*, Bochum, Germany, Mar. 2017.

12. S. Malz, **P. Hillger**, B. Heinemann and U. R. Pfeiffer, "A 275 GHz amplifier in 0.13μ m SiGe," 2016 11th European Microwave Integrated Circuits Conference (EuMIC), London, 2016, pp. 185-188.

13. **P. Hillger**, J. Grzyb and U. Pfeiffer, "A fully-integrated terahertz near-field sensor for super-resolution imaging in SiGe BiCMOS," *2016 41st International Conference on Infrared, Millimeter, and Terahertz waves (IRMMW-THz)*, Copenhagen, 2016, pp. 1-2.

14. **P. Hillger**, J. Grzyb, R. Lachner and U. Pfeiffer, "An antenna-coupled 0.49 THz SiGe HBT source for active illumination in terahertz imaging applications," *2015 10th European Microwave Integrated Circuits Conference (EuMIC)*, Paris, 2015, pp. 180-183.

15. C. Schultz and **P. Hillger**, "Analysis of a class of direct sampling receiver architectures from signal processing and system perspective," *2014 IEEE 11th International Multi-Conference on Systems, Signals and Devices (SSD14)*, Barcelona, 2014, pp. 1-6.

Book Chapters

1. U. Pfeiffer, R. Jain, J. Grzyb, and **P. Hillger** "Millimeter-wave and Terahertz Systems", in *Silicon-Germanium Heterojunction Bipolar Transistors for mm-Wave Systems: Technology, Modeling and Circuit Applications*, N. Rinaldi, M. Schröter, Ed. Gistrup, Denmark: River Publishers, 2018, ch. 6.2, pp. 245–298.

Contributions of Others

This work would clearly not have been possible without the contributions from group members and project partners. Some circuit blocks utilized in this work were designed by group members of the Institute for High-Frequency and Communication Technology (IHCT) at the University of Wuppertal, led by Prof. Dr. rer. nat. Ullrich R. Pfeiffer. The central part of this work, addressing silicon-based near-field imaging and the biological applications for near-field imaging, is the result of a collaboration between the IHCT, the University of Bordeaux, and the Institut Bergonié within the project *Near-Sense: A silicon-based terahertz near-field imaging array for ex vivo life-science applications*, which was funded by the German Research Foundation within the Priority Program SPP 1857 *Electromagnetic Sensors for Life Sciences (ESSENCE)*. All contributions are detailed below. The research not included in the list below has been conducted by myself.

Chapter 2 This chapter gives the motivation and the scientific context for this thesis. Biomedical imaging with THz waves is motivated by highlighting that water is an important contrast agent in applications such as human tissue imaging. In this context, THz time-domain spectroscopy measurements for water are shown in Section 2.1.4. This measurement and the extraction of the Debye-parameters for water were conducted by Quentin Cassar. Quentin Cassar moreover conducted the measurements for the 560 GHz tissue sample images demonstrated in Section 2.1.5. The corresponding histopathology was done by medical scientists of the Institut Bergonié.

Chapter 3 This chapter presents a high-power silicon-integrated radiation source at 430 GHz. The circular-slot antenna was designed by Janusz Grzyb.

Chapter 4 This chapter presents THz computed tomography (CT) with silicon components. The SiGe HBT THz direct detector used in the CT system was designed by Janusz Grzyb. The experimental characterization of this detector was done by Marcel Andree.

Chapter 5 This chapter provides the background for THz near-field sensing in silicon technology. It shows and analyzes single-pixel near-field sensors which present the founda-

tion of my research. These sensors were not designed by myself. The split-ring-resonator described in Section 5.3 was designed by Janusz Grzyb. Moreover, the triple-push oscillator design and the physical implementation of the single-pixel sensors was done by Ullrich Pfeiffer.

Chapter 6 This chapter presents an equivalent model of the previously mentioned split-ring-resonator designed by Janusz Grzyb. This chapter only includes original contributions.

Chapter 7 This chapter presents a System-on-a-Chip for near-field sensing. The design of this chip was a collaborative work. Janusz Grzyb designed the split-ring-resonators, Ritesh Jain designed the switched-capacitor filter and the 3-stage switched-capacitor low-pass filter of the on-chip lock-in amplifier. Ritesh Jain also designed the digital-to-analog converter for the detector biasing. The triple-push oscillators and the application-specific integrated circuit were designed by Ullrich Pfeiffer. Wolfgang Förster designed the printed circuit boards and the electronic periphery. Janusz Grzyb conducted the measurements of the lateral resolution described in Section 7.4.2. The tissue sample imaged in Section 7.5.3 was provided by Quentin Cassar.

Part I.

Context

Chapter 1

Introduction

The observation of the interaction of electromagnetic waves with matter is the most potent means of acquiring information about our surroundings. It is no surprise that vision emerged as the principal orientation and localization sense of humans and other developed species. However, being optimized to the intensity of the sun's radiation perceived on earth, human sight accesses only a small portion of the electromagnetic spectrum, and diverse characteristics of wave-matter interaction are hidden to our eyes. Ever since Maxwell laid the theoretical foundations of electromagnetism, researchers have hence aimed to access waves that are not covered by human vision to enhance the understanding of nature and to explore new technology. For the majority of the electromagnetic spectrum, they were successful, and related inventions have profoundly impacted our daily life. For instance, the exploitation of radio waves and long microwaves for wireless communication and radar is a core pillar of the new information age. These frequency bands are today conveniently accessed with modern low-cost nanoelectronics based on silicon technology. Furthermore, photonic technology for the mid/near-infrared, visible, and ultraviolet frequency bands has steadily matured, leveraging applications in vision, microscopy, spectroscopy, and wire-line communications. On another note, X-ray technology emerged as an indispensable tool in modern medical diagnosis and treatment.

The terahertz (THz) range has lagged behind others in terms of utilization and societal impact because of the inability of electronic and photonic technology to access this band efficiently. The THz range lies between the microwave and the infrared region, as shown in Figure 1.1. While the exact definition of the THz range varies among communities and is a matter of individual preference, this work uses the most common classification in the electronics community and defines frequencies from 0.3 THz to 3 THz as the THz range.

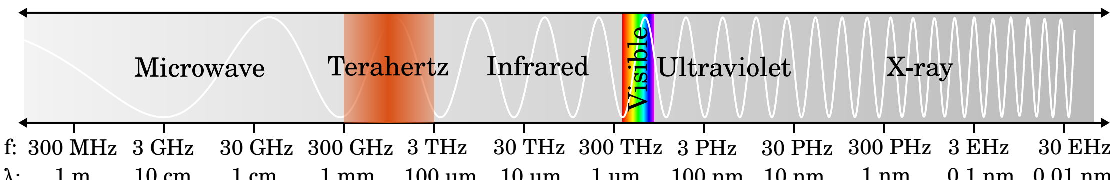

Figure 1.1.: The part of the electromagnetic spectrum spanning from microwaves to X-rays. (f: Frequency, λ: Wavelength).

Just like other electromagnetic waves, THz waves and their interaction with matter are unique from a phenomenological standpoint. On the one hand, THz waves show promise for material characterization. The photon energy levels of THz waves are common to many rotational and vibrational resonances of gas phases, to fundamental excitations of crystalline solids, and to collective vibrational modes of biomolecules and hydrogen-bond networks [1]–[4]. On the other hand, THz waves possess unique properties for imaging. Due to the low photon energy, THz radiation is not harmful, and many optically opaque materials like paper, plastics, and cardboard are transparent to THz radiation. Besides, water molecules strongly absorb, and metals reflect THz waves, providing a distinct contrast in imaging applications.

Despite these intriguing properties, the lack of compact and low-cost technology solutions has limited the utilization of THz waves to a few application niches and fundamental sciences. Highly sophisticated electronic instrumentation has been used for decades in radio astronomy to analyze the thermal emission lines of the interstellar medium [5], [6]. Moreover, electronic THz systems relying on split-block hollow waveguide assemblies combined with III-V circuits or Schottky diodes show promise to be utilized in some low-volume imaging applications, e.g., in mass transit security and loss prevention in industry [7], [8]. The research in material characterization with THz waves is mostly driven from the photonics domain. With the advent of THz time-domain spectroscopy (TDS) 30 years ago [9], [10], researchers gained access to a laboratory tool for broadband THz spectroscopy. A diverse set of potential applications has since then been identified, ranging from the detection of hazardous materials in security applications to biomedical applications such as label-free DNA detection [11] and cancer diagnostics [own1], [own2].

Most of the contemporary research in THz applications addresses far-field imaging and sensing involving free-space traveling waves. Due to diffraction, the resolution of observations in the far-field is limited to the macroscopic scale for imaging with THz waves. The relevant characteristic features of many applications in biomedicine, quality control, and fundamental science, however, range far below the diffraction limit and require devices for microscopic and nanoscopic imaging operating in the near-field. Figure 1.2 compares the characteristic length scales of some potential applications in the THz fre-

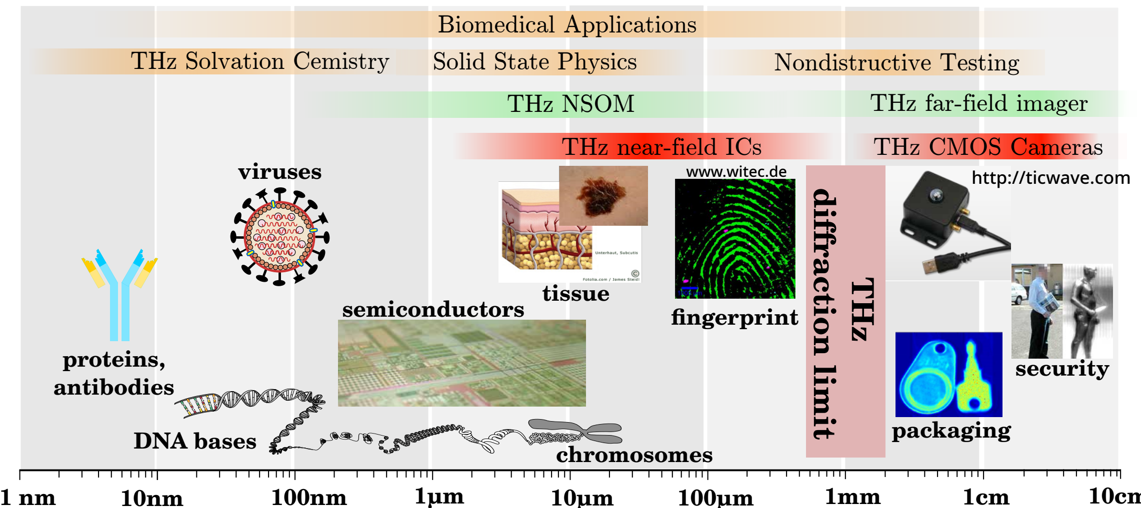

Figure 1.2.: Potential terahertz imaging and sensing applications ordered by characteristic length scales of the relevant features.

quency range. As of yet, THz imaging beyond the diffraction limit is implemented using THz near-field scanning optical microscopy (NSOM) [12]. Although very high spatial resolution down to 20 nm–40 nm can be achieved [13], typical NSOM systems require demanding instrumentation and long measurement times to reach a reasonable system sensitivity. As a result, THz NSOM systems are constrained to the laboratory use and applications in fundamental science such as the visualization of carrier dynamics in semiconductors [14].

The previous remarks underline that the traditionally exploited photonic and electronic platforms for both far-field and near-field THz imaging suffer from severe drawbacks for practical adoption, including high system cost, low achievable integration level, or low reliability. Therefore, the broad aim of this thesis is to leverage THz applications by means of integration and miniaturization of THz systems. This thesis contributes to the disciplines of THz far-field and THz near-field imaging. The herein presented integrated systems and components are based on modern nanoscale silicon process technologies. Silicon technology addresses the shortcomings of present THz technology by concurrently offering economies of scale, small form-factors, and unprecedented integration capability at the highest industry standards. Although silicon devices are pushed to operate in their technological limits in the THz range, latest advancements in high-speed silicon process technology and THz circuit design techniques have led to first demonstrations of highly capable integrated THz systems. Further research in THz integrated circuits (ICs), such as the one presented in this thesis, will thus be central for the exploration of THz applications that require compact THz microsystems for sensing [15]–[17] or far-field imaging components at a reasonable price-performance ratio [own3][18].

The primary aim of this thesis is to put forward a method for microscopic THz material characterization and imaging that is more practically applicable as compared to NSOM. To this end, a miniaturized THz near-field sensor system based on cutting-edge silicon technology is developed. It is hoped that the herein presented findings open doors for further research in yet inaccessible biomedical THz applications with significant relevance. In particular, the presented device should allow to conduct comprehensive studies on the clinical relevance of THz waves to microscopic *ex vivo* tumor margin assessment in breast cancer surgery for the first time [own1], [own2].

1.1. Central Research Questions and Contributions

The research questions that are sought to be answered in this thesis are listed below. The related original contributions of this work are also given.

Central Research Question

How to build silicon-based THz systems for real-time microscopy in the THz frequency band?

To resolve microscopic object features in the THz band, THz sensors relying on the confined interaction of electromagnetic waves with objects in the near-field have to be employed. Previous research presented silicon-integrated single-pixel near-field sensors based on split-ring-resonator (SRR) probes with a microscopic resolution at around 550 GHz [15][19]. This work aims to integrate such sensors into chip-scale multi-pixel sensor systems by exploring the full integration capabilities of silicon technology. Integration efforts targeting high-speed image acquisition are vital to the development of future THz sensor systems for biomedical applications. In this context, the following research sub-questions arise:

- How to understand and model the contrast mechanisms of SRR-based integrated THz near-field sensors?
- How to build a scalable system architecture to enable chip-scale multi-pixel arrays of THz near-field sensors with minimum pixel pitch?
- Can multi-pixel near-field sensor systems be advanced towards System-on-a-Chip (SoC)-level integration, combining THz with low-frequency mixed-signal functionality to concurrently enable imaging with high sensitivity and high speed?

- Can such systems be used as a tool for biomedical applications such as tumor margin assessment in breast cancer surgery?

Original Contributions:

The most significant contribution of this thesis is the development of a chip-scale THz near-field sensor array with 128-pixels, real-time imaging capabilities, and a spatial imaging resolution around 10 µm in 0.13 µm silicon-germanium (SiGe) heterojunction bipolar transistor (HBT) technology [own1], [own4]–[own6]. The presented device employs the cointegration of a scalable one-dimensional THz sensor front-end, including all functions such as illumination, sensing, and detection with mixed-signal processing. Moreover, this work develops and analyzes an equivalent circuit model to advance the understanding in near-field interaction of SRR probes with objects and the formation of the sensor response. Finally, the study presents human tissue imaging experiments to demonstrate the utility of the device. To the best of the author's knowledge, the presented device is the world's first integrated multi-pixel sensor for microscopic THz imaging.

Supplementary Research Question

How to realize advanced THz far-field imaging concepts, such as 3D imaging, with miniaturized silicon-based THz components?

To enhance utilization and acceptance of THz far-field imaging systems, compact source and detector systems offering a reasonable price-performance ratio and increased functionality are required. In particular, advanced far-field imaging concepts such as volumetric imaging with computed tomography (CT) [own3], diffuse scene imaging [20], and compressed imaging [own7] show high potential regarding practical adoption if the required components can be integrated into low-cost silicon technology. However, the limited speed of silicon devices constitutes an ongoing scientific challenge, requiring new design methodologies and integration concepts to make THz imaging systems in silicon applicable. Thus, another part of this thesis serves to advance the discipline of silicon-based THz far-field imaging. The study is limited to the design of incoherent THz sources in silicon technology and their application in CT imaging. In this context, the following research sub-questions arise:

- How to achieve acceptable power levels with silicon-based THz sources for practical imaging applications?
- Can THz CT be realized when only relying on silicon-based components?

Original Contributions:

The design of an integrated incoherent (unlocked) doubler-based THz source in 0.13 µm SiGe HBT technology is explored in the scope of this thesis. The source utilizes optimized extraction of the second harmonic and shows a total radiated power of −6.3 dBm at around 430 GHz [own8]. To the best of the author's knowledge, this is the highest radiated power reported among silicon-based single-radiator sources above 350 GHz. The presented source and a state-of-the-art SiGe HBT power detector are furthermore employed in a low-cost THz CT system [own3], [own7]. With this system, 3D imaging of hidden objects is presented. To the best of the author's knowledge, the THz CT imaging system is the first one to rely only on low-cost silicon components.

1.2. Thesis Structure

This thesis is divided into four major parts, comprising a total of eight chapters. They are organized as follows:

Part I: Context. Part I, including Chapter 1 and Chapter 2, gives the motivation and the scientific context for this thesis. Chapter 2 first provides the theoretical background regarding the contrast mechanisms and spatial resolution in THz imaging. The chapter concludes with a literature review of previous work in the field of THz technology.

Part II: Far-field Imaging. This part addresses the supplementary research question and systems for diffraction-limited far-field THz imaging. Chapter 3 presents the design of the silicon-based 430 GHz source. Chapter 4 briefly introduces the fundamentals of CT and thereafter, demonstrates THz CT with silicon components.

Part III: Near-field Imaging. This part addresses the central research question and systems for THz imaging in the near-field. Chapter 5 provides the necessary background for THz near-field imaging in silicon technology. Chapter 6 presents a lumped equivalent circuit model of the sensor. Chapter 7 presents the design and experimental characterization of the chip-scale THz near-field sensor array.

Part IV: Conclusion. This part summarizes the thesis and gives suggestions for future research.

Chapter 2

Terahertz Imaging and Sensing

This chapter opens with a brief introduction of the theoretical principles that govern imaging and sensing with THz waves. The discussion evolves around the fundamental quantities of imaging systems: contrast and spatial resolution. Imaging contrast originates from the spatial variation of the optical properties of a sample, which are dictated by the dielectric permittivity. Starting from Maxwell's equation, the dielectric permittivity is defined, and the fundamental principles of wave-matter interaction are described. The specifics of the constitution of the dielectric permittivity in the THz range are highlighted. Thereafter, the chapter elaborates on spatial resolution. The diffraction limit in far-field imaging systems and the means to circumvent the diffraction limit with near-field imaging are discussed. It is shown that the spatial resolution of THz far-field imaging systems is not sufficient for applications such as biomedical tissue imaging, which forms the motivation for the design of the integrated near-field THz imaging systems presented Part III of this thesis. The chapter closes with a literature review on contemporary THz technology for imaging and sensing.

2.1. Contrast in Terahertz Imaging

2.1.1. Macroscopic Electrodynamics

The interaction of THz waves with matter is governed by Maxwell's equations. THz imaging is usually concerned with the macroscopic interaction of source-free matter with

time-harmonic fields. In this case, Maxwell's equations are given as:

$$\nabla \times \boldsymbol{E} = -j\omega \boldsymbol{B}, \tag{2.1}$$

$$\nabla \times \boldsymbol{H} = j\omega \boldsymbol{D} + \boldsymbol{j}_f, \tag{2.2}$$

$$\nabla \cdot \boldsymbol{D} = \rho_f, \tag{2.3}$$

$$\nabla \cdot \boldsymbol{B} = 0, \tag{2.4}$$

where $\boldsymbol{E}$ denotes the electric field, $\boldsymbol{B}$ the magnetic flux density, $\boldsymbol{H}$ the magnetic field, $\boldsymbol{D}$ the electric displacement, $\boldsymbol{j}_f$ the free current density, and ρ_f the free charge density. The properties of matter appear in the definitions of $\boldsymbol{D}$ and $\boldsymbol{H}$, which relate to the fundamental fields $\boldsymbol{E}$ and $\boldsymbol{B}$ as follows:

$$\boldsymbol{D} = \epsilon \boldsymbol{E} = \epsilon_0 \boldsymbol{E} + \boldsymbol{P} = \epsilon_r \epsilon_0 \boldsymbol{E}, \tag{2.5}$$

$$\boldsymbol{H} = \frac{1}{\mu} \boldsymbol{B} = \frac{1}{\mu_0} - \boldsymbol{M} = \frac{1}{\mu_0 \mu_r} \boldsymbol{B}, \tag{2.6}$$

where ϵ_0 and μ_0 are free-space permittivity and permeability, ϵ and μ are the permittivity and permeability, ϵ_r and μ_r are the relative permittivity and the relative permeability. $\boldsymbol{P}$ and $\boldsymbol{M}$ denote the polarization and magnetization, respectively. Since magnetic interaction tapers off in the lower GHz frequency range in natural materials ($\mu \to \mu_0$), we are mostly concerned with the electric material properties at THz frequencies. Three phenomena describe these: i.) The current conduction losses caused by the collision of free carriers within the material, ii.) polarization, i.e., the alignment and generation of electric dipoles, and iii.) dielectric losses. The conduction losses relate $\boldsymbol{j}_f$ to $\boldsymbol{E}$ through the conductivity σ as:

$$\boldsymbol{j}_f = \sigma \boldsymbol{E}. \tag{2.7}$$

The dielectric effects are described by the complex-valued relative permittivity ϵ_r:

$$\epsilon_r = \epsilon_r' - j\epsilon_r'', \tag{2.8}$$

where the real part covers phase shift and dispersion, and the imaginary covers the dielectric losses. Combining Equation 2.7 and Equation 2.8 with the Maxwell-Ampère law (Equation 2.2) gives:

$$\nabla \times \boldsymbol{H} = j\omega\epsilon \boldsymbol{E} + \sigma \boldsymbol{E} = (\sigma + \omega\epsilon_0\epsilon_r'')\boldsymbol{E} + j\omega\epsilon_0\epsilon_r'\boldsymbol{E} = j\omega \left[\epsilon_0\epsilon_r' - j\left(\epsilon_0\epsilon_r'' + \frac{\sigma}{\omega}\right)\right] \boldsymbol{E}. \tag{2.9}$$

This equation reveals that the conductive loss and the dielectric loss behave phenomenologically similar. Hence, it is convenient to combine both in a modified imaginary part of

the relative permittivity with $\epsilon_r'' + \frac{\sigma}{\epsilon_0 \omega} \rightarrow \epsilon_r''$. This leads to the definition of an 'effective' relative complex permittivity, which will be denoted with ϵ_r throughout the rest of this thesis. Furthermore, the complex-plane angle of the reaction to an external $\boldsymbol{E}$ field in Equation 2.2 can be defined as the loss tangent:

$$\tan\delta = \frac{\epsilon_r''}{\epsilon_r'} + \frac{\sigma}{\omega\epsilon_0\epsilon_r'}. \tag{2.10}$$

As of yet, no restrictions have been made on the permittivity itself, and in fact, it reflects all the complexity of the underlying physical processes. It can be non-linear, anisotropic, and a function of time and temperature. But most importantly, the permittivity is frequency-dependent[1].

The optical properties of materials are often more conveniently expressed in terms of the complex refractive index $\widetilde{n}$, defined as the square root of the permittivity:

$$\widetilde{n} = \sqrt{\epsilon_r} = n - j\kappa, \tag{2.11}$$

where n is the real refractive index, and κ is the extinction coefficient.

2.1.2. Absorption and Dispersion

The effect of the material properties on electromagnetic waves and related observables can be examined based on the general expression of propagating plane waves:

$$\boldsymbol{E} = \boldsymbol{E}_0 e^{j(\omega t - kx)}, \tag{2.12}$$

where the wavenumber k is connected to the permittivity through the dispersion relation for nonmagnetic materials as:

$$k = \sqrt{\epsilon_r \epsilon_0 \mu_0}\,\omega. \tag{2.13}$$

Since the permittivity is complex, the wavenumber can be split into a real part and an imaginary part with $k = \beta - j\frac{\alpha}{2}$, thereby giving for the electric field of the wave:

$$\boldsymbol{E} = \boldsymbol{E}_0 e^{-\frac{\alpha}{2}x} e^{j(\omega t - \beta x)}. \tag{2.14}$$

Here, α is the attenuation constant describing the absorption of waves in media, and β is the phase constant describing the spatial scale of oscillation. Typical detectors for THz

[1] It is noted that not only the real part describing dispersion, but also the imaginary part describing losses is frequency-dependent ($\epsilon_r(\omega) = \epsilon_r'(\omega) - j\epsilon_r''(\omega)$). They are related to each other through Kramers-Kronig relations [21]. The indication of frequency dependency is herein dropped for simplicity.

waves measure the radiation intensity I, which is proportional to the square of Equation 2.14. The magnitude of the time-averaged Poynting vector gives the radiation intensity and has the form of the Beer–Lambert Law:

$$|< \boldsymbol{S} >| = I = \frac{1}{2}\sqrt{\frac{\epsilon_r \epsilon_0}{\mu_0}} E_0^2 e^{-\alpha x} = I_0 e^{-\alpha x}. \tag{2.15}$$

Hence, an attenuation constant greater than zero leads to an exponential attenuation of the wave intensity in space. To provide a better understanding of the relationship between wave propagation and the material properties, α and β can be expressed in terms of the dielectric permittivity:

$$\alpha = 2\frac{\omega\sqrt{\mu_0\epsilon_0}}{\sqrt{2}}\sqrt{|\epsilon_r' - j\epsilon_r''| - \epsilon_r'} \tag{2.16}$$

$$\beta = \frac{\omega\sqrt{\mu_0\epsilon_0}}{\sqrt{2}}\sqrt{|\epsilon_r' - j\epsilon_r''| + \epsilon_r'}. \tag{2.17}$$

Based on these relationships, a few interesting observations can be made. There are two ways of how a wave can be attenuated ($\alpha > 0$). Either, the material possesses a non-zero imaginary part of the permittivity ($\epsilon_r'' > 0$), i.e., the material is lossy such that the energy of the wave is converted into heat. The relationship between attenuation and losses is nonlinear but monotonic, such that an increase in material losses always leads to an increase in attenuation. This is the typical case for lossy dielectrics or for conductors above the plasma frequency (see Section 2.1.4). Or, the material shows a negative real part of the permittivity. Assuming a lossless material ($\epsilon_r'' = 0$), the absorption coefficient and the phase constant then become $\alpha = 2\omega\sqrt{\mu_0\epsilon_0}\sqrt{|\epsilon_r'|}$ and $\beta = 0$, respectively. This describes an exponentially decaying standing wave, which is commonly termed as an evanescent wave. Notably, a wave incident on such material does not lose energy but is rather completely reflected back. As it will be shown in Section 2.1.4, metals exhibit a large negative real part of the permittivity in the THz range, which is why they are excellent reflectors.

2.1.3. Reflection and Transmission at Material Boundaries

When a wave hits the boundary between two plane media, it is split into a transmitted and a reflected wave whose magnitudes and propagation directions depend on the material properties and the incident angle. Most generally, we consider arbitrarily polarized transverse electromagnetic waves, which can be decomposed into perpendicular (s-polarized) and parallel (p-polarized) components. The polarizations are orthogonal to each other and reference to the plane of incidence. Figure 2.1 depicts the geometrical relations and the direction of the field components. Maxwell's Equations imply that the tangential compo-

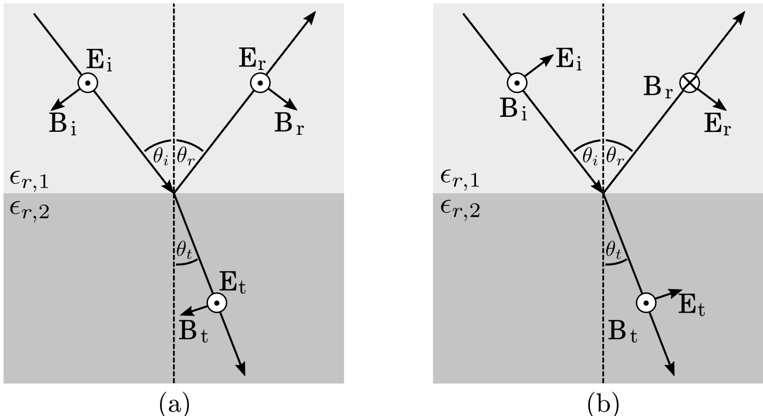

Figure 2.1.: Illustration of the field components of an electromagnetic wave at a planar boundary for s-polarized (a) and p-polarized (b) waves.

nents of the electric and the magnetic field are continuous across the boundary. This can be used to derive the law of refraction, generally known as Snell's law, and the law of reflection. For nonmagnetic materials, they are respectively given as:

$$\sqrt{\epsilon_{r,1}}\sin\theta_i = \sqrt{\epsilon_{r,2}}\sin\theta_t \quad \text{and} \tag{2.18}$$

$$\theta_i = \theta_r. \tag{2.19}$$

The boundary conditions furthermore determine the reflection and transmission coefficients for the amplitudes of the s-polarized and p-polarized wave components:

$$r_s = \frac{\sqrt{\epsilon_{r,1}}\cos\theta_i - \sqrt{\epsilon_{r,2}}\cos\theta_t}{\sqrt{\epsilon_{r,1}}\cos\theta_i + \sqrt{\epsilon_{r,2}}\cos\theta_t} \tag{2.20}$$

$$t_s = \frac{2\sqrt{\epsilon_{r,1}}\cos\theta_i}{\sqrt{\epsilon_{r,1}}\cos\theta_i + \sqrt{\epsilon_{r,2}}\cos\theta_t} \tag{2.21}$$

$$r_p = \frac{\sqrt{\epsilon_{r,2}}\cos\theta_i - \sqrt{\epsilon_{r,1}}\cos\theta_t}{\sqrt{\epsilon_{r,2}}\cos\theta_i + \sqrt{\epsilon_{r,1}}\cos\theta_t} \tag{2.22}$$

$$t_p = \frac{2\sqrt{\epsilon_{r,1}}\cos\theta_i}{\sqrt{\epsilon_{r,2}}\cos\theta_i + \sqrt{\epsilon_{r,1}}\cos\theta_t}. \tag{2.23}$$

The fraction of the intensity of the wave that is reflected at the boundary is termed the reflectance R. Since the intensity is proportional to the square of the amplitude (see Equation 2.15), the reflectance can be written as:

$$R_s = |r_s|^2 \quad \text{and} \quad R_p = |r_p|^2, \tag{2.24}$$

whereas the reflectance needs to be calculated individually for both polarizations. Because power needs to be conserved at the boundary, the fraction of the intensity of the wave

transmitted is given as:

$$T_s = 1 - R_s = \frac{\sqrt{\epsilon_{r,2}}\cos\theta_t}{\sqrt{\epsilon_{r,1}}\cos\theta_i}|t_s|^2 \quad \text{and} \quad T_p = 1 - R_p = \frac{\sqrt{\epsilon_{r,2}}\cos\theta_t}{\sqrt{\epsilon_{r,1}}\cos\theta_i}|t_p|^2. \tag{2.25}$$

Typical dielectrics are considerably polarizable in the THz band ($\epsilon_r > 1$). Therefore, the contrast in THz imaging systems relying on propagating waves does not only originate from the characteristic absorption but also from Fresnel losses, i.e., from power loss due to reflection or refraction at material boundaries.

2.1.4. Wave-Matter Interaction Phenomena in the THz Band

The previous sections discussed how the dielectric permittivity of matter influences wave propagation. This section gives a brief overview on the physical effects defining the dielectric permittivity in the THz range. The interaction of time-harmonic fields with matter is governed by the dynamics of the induced motion of charged particles. There are multiple mechanisms related to the microscopic atomic, molecular, and intermolecular structures that add up to the overall macroscopic dispersion and absorption of matter. All of them depend on the photon energy $E = hf$, and thus the frequency. Several characteristic energies of such mechanisms fall into the THz band ($E = 1.2\,\text{meV}$–$12\,\text{meV}$). In the following, the classical models to describe the effects defining the permittivity at THz frequencies are briefly discussed, including the Lorentz model for resonance excitation of bound charges, the Drude model for conduction of free carriers, and the Debye model for dipolar relaxation processes.

Resonance Effects: The Lorentz Oscillator Model

The interaction of waves with bound charges influences the dielectric function. Bound charges are displaced with respect to their average equilibrium position by an external field due to the Lorentz force. This causes a net dipole moment, which contributes to the polarization. Upon displacement, bound charges experience a restoring force, which gives rise to a harmonic oscillation motion characterized by a resonant frequency ω_0. This oscillator model is called the Lorentz oscillator model. It was initially introduced to describe electrical polarization, i.e., the displacement of the electron shell with respect to its nucleus. The resonance frequency of electrical polarization is typically in the ultra-violet frequency range ($f_0 \approx 10^{15}$ Hz) due to the small mass of the involved particles. However, the Lorentz oscillator model provides a good qualitative description of other effects that are resonant in the THz band, such as low-frequency vibrations in ionic crystals [2] and bending and stretching of hydrogen bonds [22].

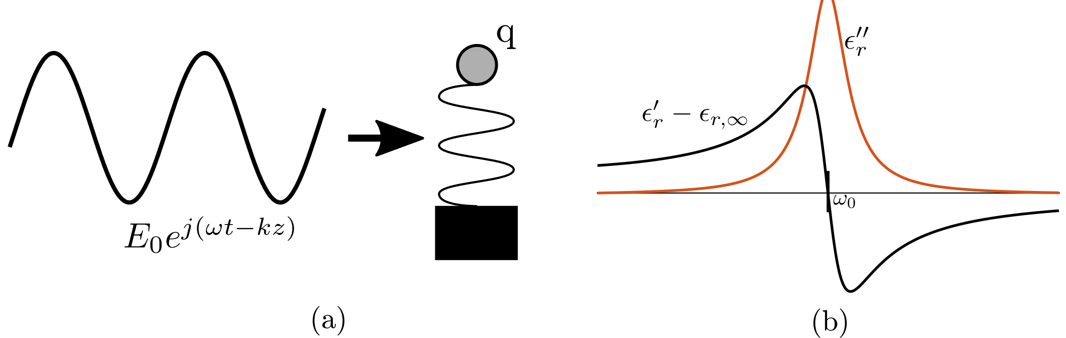

Figure 2.2.: Classical Lorentz model for bound-charge resonance effects. Illustration, after [23] (a), and relative permittivity close to the resonance frequency (b).

Figure 2.2(a) illustrates the Lorentz oscillator model [23], which is analogous to the spring-mass systems of classical mechanics. The equation of motion for the interaction of a bound charge with a monochromatic wave of the form $E(t) = E_0e^{j\omega t}$ is written as:

$$\frac{d^2x}{dt^2} + \gamma\frac{dx}{dt} + \omega_0^2 x = \frac{q}{m^*}E(t), \tag{2.26}$$

where q is the charge, m^* is the effective mass of the particle, and γ is the damping coefficient describing the average rate at which the oscillator loses energy. The motion induces a polarization, which is given by the average displacement x of the bound charges with a carrier density N:

$$P = Nqx = (\epsilon_r - \epsilon_{r,\infty})\epsilon_0 E(t), \tag{2.27}$$

where $\epsilon_{r,\infty}$ is the real relative permittivity in the high-frequency limit. Equation 2.26 and Equation 2.26 can be combined into a polarization equation:

$$\frac{d^2P}{dt^2} + \gamma\frac{dP}{dt} + \omega_0 P = \frac{Nq^2}{m^*}E(t). \tag{2.28}$$

Solving the polarization equation for the complex relative permittivity yields:

$$\epsilon_r = \epsilon_{r,\infty} + \frac{\omega_p^2}{\omega_0^2 - \omega^2 + j\omega\gamma}, \tag{2.29}$$

where the plasma frequency $\omega_p = \frac{Nq^2}{m^*\epsilon_0}$ was introduced. Figure 2.2(b) depicts the real and imaginary part of the relative permittivity close to the resonant frequency ω_0. The imaginary part peaks at the resonance frequency, giving rise to strong absorption, according to Equation 2.14.

Free Carrier Conduction: The Drude Model

Materials possessing a significant amount of free carriers, such as metals or semiconductors, can be modeled with the Drude model. Free electrons are not bound with a restoring force or potential barrier but rather move against a fixed background of positive ions. In other words, the spring in Figure 2.2 is cut, and charges are allowed to move freely. Current conduction thus represents a limiting case of the Lorentz oscillator model with $\omega_0 \to 0$. Therefore, Equation 2.29 simplifies to the Drude permittivity as:

$$\epsilon_r = \epsilon_{r,\infty} - \frac{\omega_p^2}{\omega^2 - j\omega\gamma}, \tag{2.30}$$

where γ denotes the average rate of collisions of the carriers with the lattice. The carriers are assumed to lose their momentum in the scattering process. Figure 2.3 depicts the real and imaginary parts of the relative permittivity for gold in the electromagnetic spectrum from the upper millimeter-wave (mmWave) band to the ultra-violet band [24]. For frequencies below the plasma frequency ($\omega \ll \omega_p$), the Drude model gives a large real and imaginary part for the permittivity. This results in the typical wave-interaction for metals characterized by small penetration depths and strong reflective behavior.

For frequencies above the plasma frequency, conductors resemble the behavior of lossy dielectrics. Incident waves are thus able to propagate, and the conductor becomes mostly transparent. The plasma frequency is proportional to the square root of the carrier density and thus very large for metals (typically in the ultra-violet frequency range). Intrinsic semiconductors, however, show plasma frequencies well below the THz band. For example, the plasma frequency of intrinsic silicon with a carrier density in the order of $1 \times 10^{10}\,\mathrm{cm}^{-3}$ is below 1 GHz. This leads to low-loss wave propagation and has motivated the use of silicon lenses for optical purposes in the THz band.

Relaxation: The Debye Model

The Lorentz model described in Section 2.1.4 is based on the assumption that a restoring force repels the system back into equilibrium. Such behavior is typically related to induced dipoles rather than permanent dipoles. The orientation of permanent dipoles in matter is normally arbitrary. If an electrical field is applied, the dipoles are reoriented slightly in their thermal motion, thereby yielding a net polarization. In contrast to the Lorentz oscillator, there is no resonance behavior when the field is turned off. The reorientation of the dipoles towards equilibrium is rather a relaxation process governed by the interaction of dipoles with their environment in the statistical process of thermal motion. The

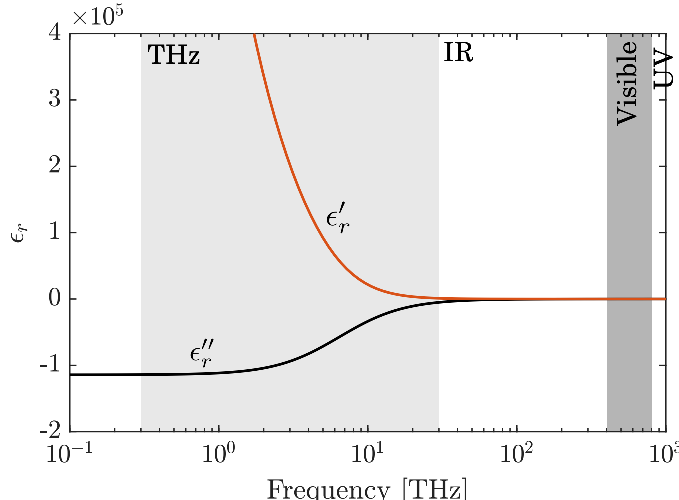

Figure 2.3.: Real and imaginary part of the relative permittivity of gold as a function of frequency. The relative permittivity is calculated based on the Drude model with $\epsilon_{r,\infty} = 1$, $\omega_p/2/\pi = 2.18 \times 10^3$ THz, and $\gamma/2/\pi = 6.45$ THz. After [24].

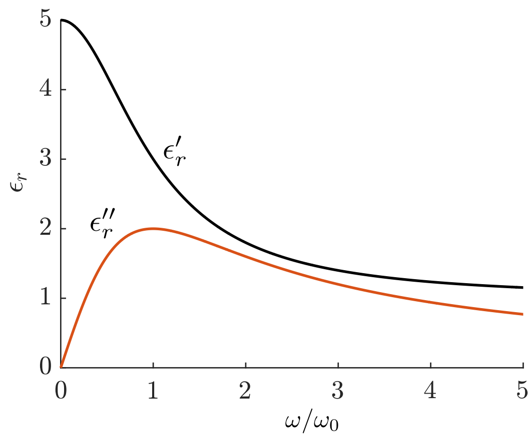

Figure 2.4.: Debye-type frequency dependency of the relative permittivity for a hypothetical material with $\epsilon_s = 5$ and $\epsilon_\infty = 1$, and $\tau = 1/\omega_0$.

related polarization mechanism is called oriental polarization or Debye relaxation and is of cardinal importance for describing the properties of polar liquids in the microwave and THz bands.

In the simplest form, the relative permittivity of this mechanism can be described by the Debye equation:

$$\epsilon_r = \epsilon_{r,\infty} + \frac{\epsilon_s - \epsilon_{r,\infty}}{1 + j\omega\tau}, \tag{2.31}$$

where ϵ_s denotes the static relative permittivity at $\omega = 0$, and τ is the relaxation time. Figure 2.4 shows the real and imaginary parts of the relative permittivity for a hypothetical Debye-type material. At low frequencies ($\omega \ll 1/\tau$), the dipoles follow applied electric fields with a phase lag, which is described by the real part of the permittivity.

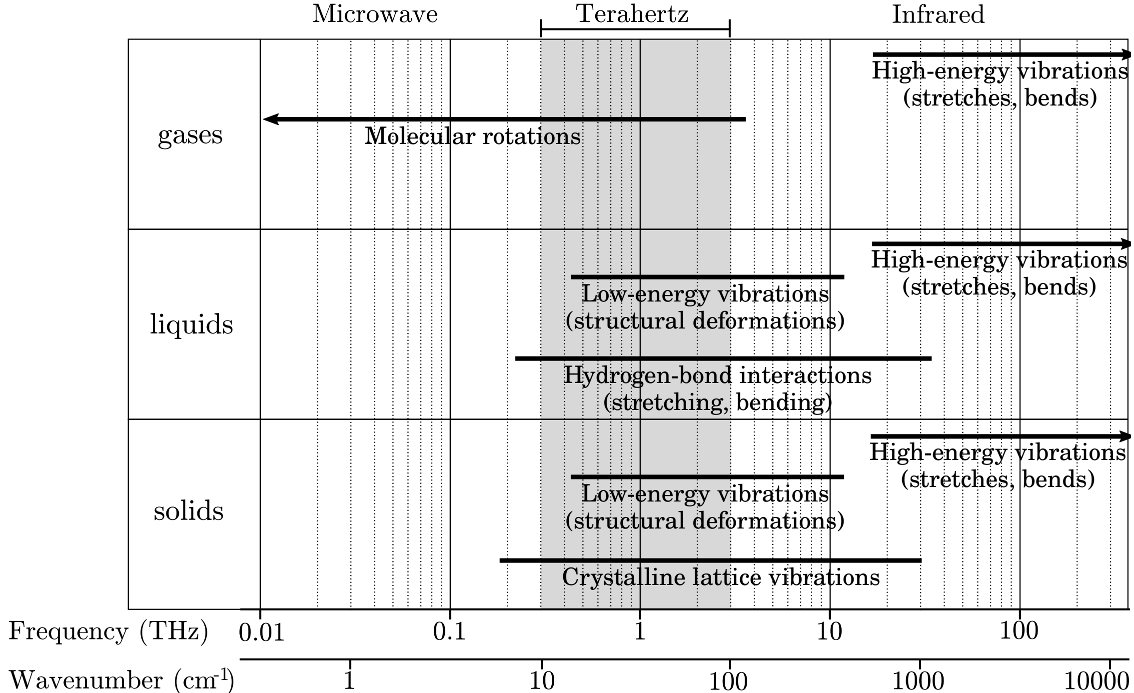

Figure 2.5.: Characteristic frequencies of resonant interaction of THz waves with matter. Adapted from [3].

With increasing frequency, the increasing motion radius leads to higher losses. When the frequency of the applied field is much larger than the inverse of relaxation time ($1/\tau \ll \omega$), the diples cannot follow the field anymore, and no losses due to polarization are induced ($\epsilon_r'' \rightarrow 0$).

Characteristic Frequencies in the THz Band

Figure 2.5 gathers the relevant resonance mechanisms for the different phases of matter that fall into the THz band and its vicinity. In the microwave and THz bands, many gases exhibit distinct spectral absorption fingerprints that are related to transitions between rotational quantum levels of polar molecules [1]. The high specificity of these rotational transitions has made rotational spectroscopy a valuable alternative to the established mid-infrared vibrational and rotational-vibrational spectroscopy, which is based on the high-energy vibrations (bending and stretching of molecules) that are also indicated in Figure 2.5.

In liquids and solids, molecules cannot freely rotate, and such resonances do not exist. However, low-energy vibrational modes associated with large collective motions of molecule systems can show characteristic resonance behavior in the THz range. This has been exploited for a variety of applications, including the detection of illicit drugs [25] and

explosives [26], for the investigation of biomolecules such as DNA [3], and for the probing of solvation dynamics [4]. Furthermore, some fundamental phonon modes in organic and inorganic crystals fall into the THz range [2], [3].

An important note has to be given regarding the specificity of the THz spectra: Since the collision and relaxation rates increase for dense matter, line-widths and quality factors (Qs) are significantly smaller for liquids and solids. Resonances in low-pressure gases show a Q of approximately 10^6, and resonances in gases near atmospheric pressure show a Q of approximately 10^2 [27]. Resonances in liquids and solids, however, show very small Q, leading to almost continuous spectra.

Water as a Contrast Agent

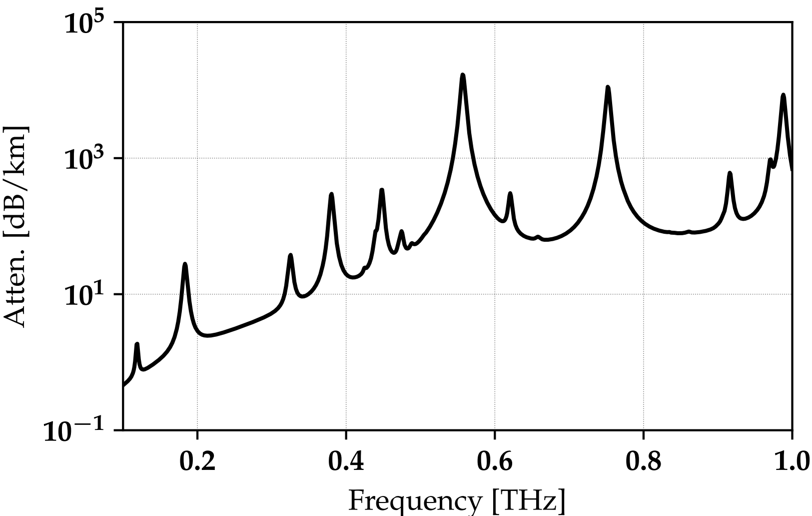

Figure 2.6.: Attenuation of electromagnetic radiation by atmospheric gases. After (ITU-R 2003).

THz waves are very sensitive to water. Water (H_2O) is a polar molecule: The two hydrogen atoms each share an electron with the oxygen atom to form a covalent bond. Since oxygen has a higher electronegativity than hydrogen, the side of the molecule with the oxygen atom is negatively charged. In gases such as water vapor, the dipolar nature of water gives rise to the aforementioned resonant peaks due to rotational transitions. At atmospheric pressure, these resonances lead to broad absorption peaks, which compound the so-called continuum absorption whose physical origins are still debated [28], [29]. As shown in Figure 2.6, THz waves, therefore, attenuate rapidly in the atmosphere (more than $10\,\mathrm{dB\,m^{-1}}$ around 550 GHz). Joined with the free-space path loss and the lack of powerful radiators in the THz band, it is challenging to maintain appropriate signal strength over reasonable path lengths for many terrestrial applications.

In contrast, the lossy character of water in the liquid phase can serve as a valuable contrast mechanism in the THz band. It is not surprising that the first demonstration of THz imaging utilized the strong absorptive contrast between humid and dry features of leaves [30]. Today, the interest in the THz response of water stems primarily from its cardinal importance to biomedical applications. Nearly all biological processes involve water. In biological environments, the hydrogen atoms form hydrogen bonds with other electronegative atoms or with other water molecules. The bulk dielectric relaxation and some distinct intermolecular vibrational energies of hydrogen bond networks fall into the THz band [3]. Such hydrogen bonds exist in practically all biological environments; they thus contribute significantly to the overall dielectric response of relevant biological samples.

The dielectric behavior of water is influenced by two relaxation phenomena (Debye-type), leading to a significant loss in the microwave and low THz frequency band, and by several bending and stretching modes (Lorentz-type) that are resonant above 3 THz [22]. As it is to be shown in Section 2.3.4, we can only access the lower end of the THz spectrum with silicon circuits, where the relaxation dominates the dielectric behavior. A slow relaxation process giving a loss peak at around 20 GHz is related to the cooperate reorientation dynamics of large hydrogen bond structures. A faster relaxation process gives a loss peak at around 1 THz[2].

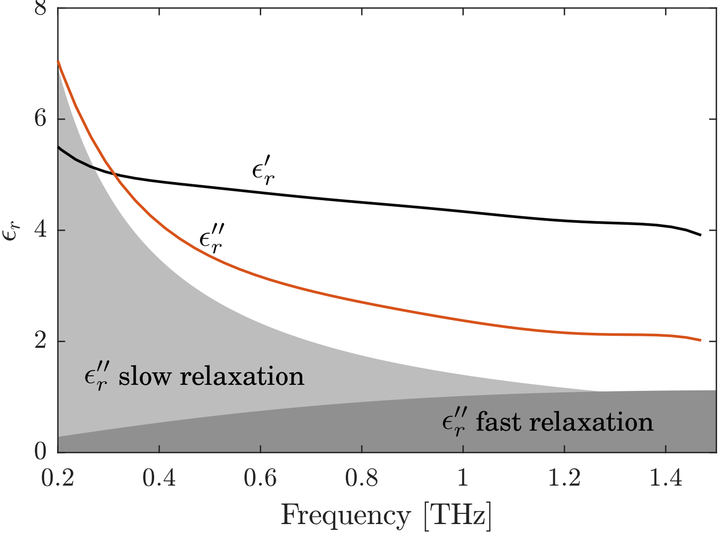

Figure 2.7.: Measured real and imaginary parts of the relative permittivity of liquid water. The imaginary parts resulting from the slow and fast Debye relaxations are also shown. The extracted parameters for the fast and slow Debye term are $\Delta\epsilon_{r,1} = 73.19$, $\tau_1 = 8.33$ ps and $\Delta\epsilon_{r,2} = 2.24$, $\tau_1 = 0.1$ ps. By courtesy of Quentin Cassar, University of Bordeaux, France.

[2] There is still an ongoing debate on the physical origin of the fast relaxation in water. Hypotheses relate the fast relaxation either to rotations of weakly bonded molecules, or to different molecule motions [22]

To demonstrate the dielectric properties of liquid water, its complex relative permittivity was measured with a commercially available THz TDS system (TPS spectra 3000 from TeraView) in a transmission-mode setup between 0.1 THz–1.5 THz. The results are depicted in Figure 2.7. According to the previous remarks, the results were fitted to a dielectric response comprising the superposition of two Debye terms as:

$$\epsilon_r = \epsilon_{r,\infty} + \frac{\Delta\epsilon_{r1}}{1 + j\omega\tau_1} + \frac{\Delta\epsilon_{r2}}{1 + j\omega\tau_2}, \tag{2.32}$$

where $\Delta\epsilon_{1,2}$ denotes the step size in the real part of the permittivity of the relaxation process. The imaginary parts of the fitted Debye terms are also shown. The high-frequency Lorentz terms were omitted because of their low contribution in the measured bandwidth. This model is commonly referred to as the double Debye model. The results underline the aforementioned lossy characteristic of water in the THz range.

2.1.5. Application: Breast Cancer Margin Assessment

In recent years there has been increasing interest in THz techniques for biomedical imaging of human tissues [31]–[33][own1], [own2]. In particular, prior research has shown that malignant tissue exhibits different electromagnetic properties than healthy tissue in the THz band [3]. One of the most promising applications in this field is the use of THz imaging in breast cancer surgeries.With more than 2 million new cases in 2018 [34], breast cancer is the most common cancer type among women by far. Diagnosed women typically undergo surgery to remove the tumor. Due to technological advances in early cancer diagnosis, surgeries removing only the primary tumor while conserving the rest of the breast are increasingly ordinary. This method, however, shows limited precision, and up to 20% of the cases exhibit malignant tissue at the margins of the excised material [35], [36], indicating that the tumor has not been entirely removed. These margins are typically assessed in a postoperative microscopic histopathologic examination, which can take several days. In the case of detection of a positive margin, a second surgery is required, resulting in increased mortality risk and costs. Hence, there is an urgent need for an imaging device providing an accurate and fast assessment of tumor margins in the course of the surgery.

Fitzgerald *et al.* were the first to demonstrate a distinct contrast between healthy and malignant breast tissue in the THz range [37]. Since then, several studies have consistently reported higher refractive indices and absorption coefficients for malignant tissue than for healthy tissue at the lower end of the THz band using THz TDS imaging systems [32], [38], [39][own2]. Figure 2.8 shows exemplary the results presented in [own2]. The results are the mean values of ten fresh tissue samples, and the error bars represent a 95% confidence

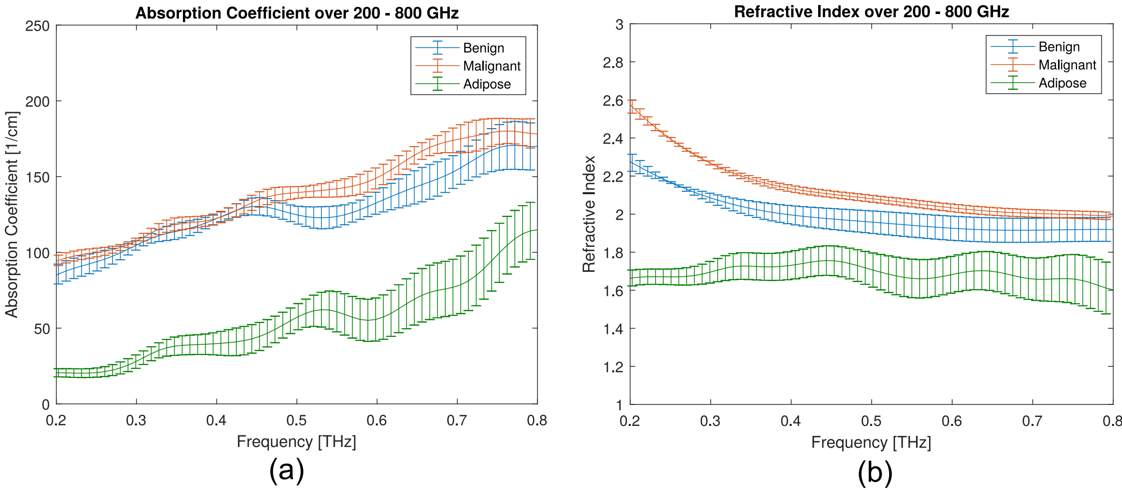

Figure 2.8.: The measured absorption coefficient (a) and refractive index (b) of benign, malignant, and adipose tissue over the frequency range 0.2 THz–0.8 THz. After [own1] © 2019 IEEE.

level. The measurements were obtained with a reflection-mode THz TDS setup. The tissue composition of such samples depends on the patient, but usually includes adipose tissue, benign, and malignant tissue. A strong contrast is visible between adipose and malignant or benign tissue. The differentiation between malignant and benign tissue proves to be more challenging. Malignant tissue clearly depicts a higher refractive index, particularly at low THz frequencies. Below until around 500 GHz, the absorption coefficient is not differentiable, whereas a difference is visible in the 550 GHz range.

The physical origins of the contrast are still under investigation. Human tissue exhibits a complex inhomogeneous cell structure. Since the largest human cells are typically sized some tens of micrometers, it is challenging to link the origins of the observed contrast to microscopic phenomena with the as-yet employed macroscopic imaging techniques. However, the key contrast factor is suspected to be attributed to increased water concentration in the diseased tissue, to which THz waves are particularly sensitive, as explained earlier. Due to the strong correlation of the THz tissue response to the response of water, previous studies have extracted the double Debye model parameters to quantify the dielectric response of different human tissue types at THz frequencies [32][own2]. Note that the material properties show a smooth variation over frequency, and no specific resonances are visible. Therefore, even relative permittivity characterization at a single frequency should offer a useful contrast for tumor identification and margin assessment. This is the key observation justifying the single-frequency operation of the near-field sensors presented in Part III of this thesis.

Figure 2.9 compares a 560 GHz reflection amplitude image with a photograph and the results of a histopathological assessment for the same tissue sample. The THz image was

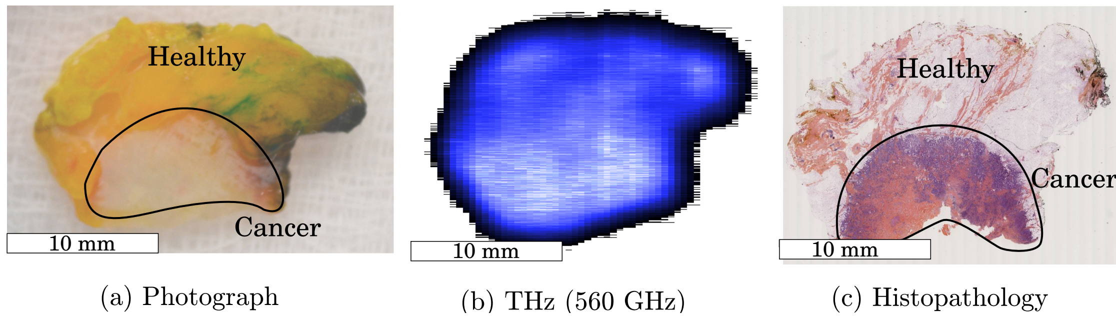

(a) Photograph (b) THz (560 GHz) (c) Histopathology

Figure 2.9.: Image comparison for a tissue sample containing a non-invasive breast carcinoma. Photograph (a), a 560 GHz THz reflection-mode image (b), and histopathology results (c). By courtesy of Quentin Cassar, University of Bordeaux, France.

scanned with a THz TDS setup operating in reflection-mode. The THz image shows a clear contrast between healthy breast tissue and carcinoma. However, it is also visible that the employed far-field imaging technique cannot sufficiently resolve the tumor margins. The exact structure of the tumor is not depicted in the THz image, even for this relatively large tumor. A spatial resolution in the range between 1 µm–10 µm is expected to be necessary to localize tissue margins precisely and to provide insights into the THz properties at the cellular level [own1]. The following section discusses the limitations of spatial resolution in far-field imaging and how these can be overcome with near-field imaging.

2.2. Spatial Resolution in Terahertz Imaging

2.2.1. Limitations of Far-Field Imaging

In far-field imaging systems, propagating electromagnetic waves are used to illuminate an imaging object, whereas the distance between the object and optical elements is significantly larger than the illumination wavelength λ. Ernst Abbe discovered in 1873 that lenses act as diffracting apertures, fundamentally limiting the achievable resolution of far-field imaging systems to around half a wavelength [40]. In the following, the so-called 'angular spectrum representation of optical fields' [41], [42] is used to explain the origin of the diffraction limit.

In imaging applications, we are interested in how spatial information contained in the field distribution in an object plane is transferred to an image plane, as illustrated in Figure 2.10. A monochromatic wave in two-dimensional vacuum is considered here to keep it simple. Now, the complex amplitude of the electrical field $E(x, z)$, describing, for

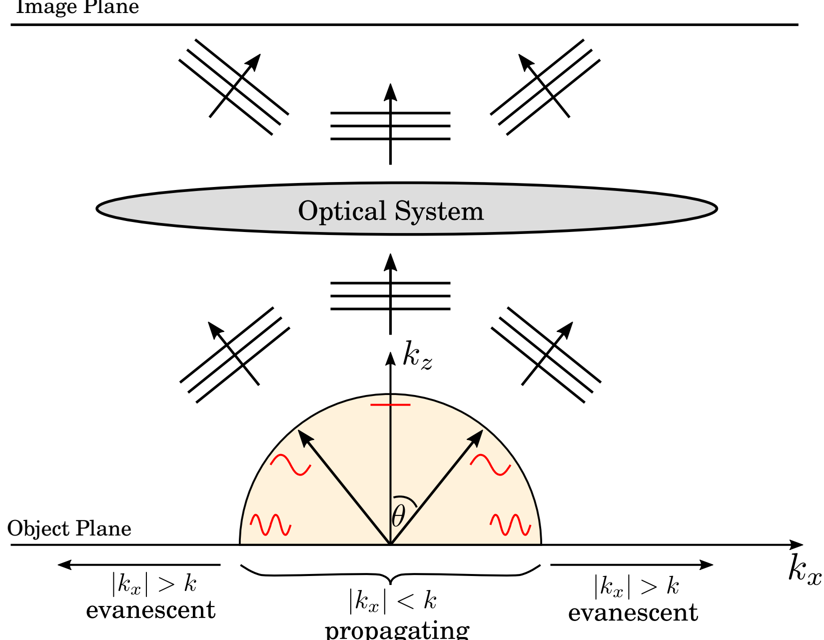

Figure 2.10.: The angular spectrum representation of optical fields in two-dimensional space. The bottom illustrates the waves originating from an object plane in reciprocal space. Transverse spatial frequencies are indicated in red. Transverse wavenumbers (k_x) are restricted to a circular area with radius k. The optical system, depicted in real space, collects only a limited amount of spatial frequencies in the object plane (diffraction). Adapted from [42].

example, a source or a scatterer, is considered to be known in the object plane with $z = 0$. The field is then described as a linear superposition of plane waves. In any plane with $z = const.$, the one-dimensional Fourier transform of $E(x, z)$ with respect to x can be evaluated as:

$$\widehat{E}(k_x, z) = \frac{1}{2\pi} \int_{-\infty}^{\infty} E(x, z) e^{-jk_x x}\, dx, \tag{2.33}$$

where k_x is the angular spatial frequency in the object plane. The complex amplitude $E(x, z)$ of the time-harmonic electrical field with propagation constant $k = \frac{\omega}{c}$ satisfies the Helmholtz equation[3]:

$$\nabla^2 E(x, z) + k^2 E(x, z) = 0. \tag{2.34}$$

To obtain the evolution of the Fourier spectrum with propagation from the object plane towards z-direction, the Fourier transform of the field is inserted into Equation 2.34:

$$\frac{\partial^2 \widehat{E}(k_x, z)}{\partial k_z^2} + k_z^2 \widehat{E}(k_x, z) = 0, \tag{2.35}$$

where the wave vector k_z in propagation direction depends on k_x as can be inferred from

[3]The temporal dependency of the electrical field with $E(x, z, t) = E(x, z)e^{-j\omega t}$ is omitted for simplicity.

the dispersion relation:

$$k_z = \sqrt{k^2 - k_x^2}. \tag{2.36}$$

Assuming that the wave only propagates towards the image plane ($k_z > 0$), the solution to Equation 2.35 is:

$$\widehat{E}(k_x, z) = \widehat{E}(k_x, 0)e^{jk_z z}. \tag{2.37}$$

Applying the inverse Fourier transform to $\widehat{E}(k_x, z)$, a solution to the field for arbitrary z is found:

$$E(x, z) = \int_{-\infty}^{\infty} \widehat{E}(k_x, 0)e^{j(k_x x + k_z z)}\, dk_x. \tag{2.38}$$

Recalling Equation 2.36, two characteristic solutions can be obtained for the spatial frequencies in the object plane. If $|k_x| < k$, k_z is real-valued, producing a propagating plane wave. By contrast, if $|k_x| > k$, k_z is imaginary, producing a wave that decays exponentially in the z-direction. More generally expressed, if the spatial variations of a target located in a certain plane are smaller than the wave vector component in the direction perpendicular to this plane, the resulting wave is not propagating but spatially confined within its vicinity in this direction. An alternative way of interpretation is that the spatial information contained in the object plane is low-pass filtered by wave propagation. Hence, if the field is laterally confined to Δx, the maximum spatial variation for which the spectrum can obtain significant values is $k_x = k \approx \frac{2\pi}{\Delta x}$.

The larger the angle θ between the propagation direction and the z-axis, the larger the propagated spatial oscillation in x-direction. As such, the lateral confinement relates to the angular aperture of the field. This effect is termed diffraction. When propagating through the optical system, the k_x values are furthermore low-pass filtered. The filter cutoff is the maximum angular aperture that the optical system can collect, also called the numerical aperture (NA). Applying the Rayleigh-criterion, the diffraction-limited spatial resolution in the far-field, i.e., at large distances from the object plane, is given as:

$$\Delta x_{min} \approx 0.61 \frac{\lambda}{n \sin\theta}, \tag{2.39}$$

where $n \sin\theta = NA$, and n is the refractive index of the medium between the object and the optical system. A qualitatively similar relation can be derived for the resolution limit imposed by the diffraction-limited spot size of a focused beam.

For air as the propagation medium[4] ($n_{air} \approx 1$) and a hemispherical aperture ($\sin(\theta) = 1$), the maximum resolution for far-field imaging systems is around $\lambda/2$. For example,

[4] While oil-immersion techniques, which are commonly applied in light microscopy, are impractical in the THz frequency band due to strong absorption and sample contamination, solid immersion techniques have been successfully utilized to increase spatial resolution[43]

the spatial resolution of a monochromatic 500 GHz imaging system is around 300 µm at best.

2.2.2. Breaking the Diffraction Limit

The previous discussion highlights that the spatial resolution of far-field imaging systems is determined by the wavelength employed, which is in the millimeter-range at THz frequencies. For applications targeting material characterization, one implication is that the dielectric and conductive properties of a sample are averaged over macroscopic length scales. To characterize the localized electromagnetic properties in microscopic or nanoscopic length scales, one has to access the fields in close vicinity to the object plane – also called the near-field. The methods of near-field probing can be generally categorized into two different groups. One measures evanescent waves emitted due to scattering at sub-wavelength objects [12]. These methods are prevalent for nanoscopic imaging in the THz range, which will be discussed in more detail in Section 2.3.1. The other one employs 'active' probing. Here, the near-field of a probe is brought in close vicinity to a sample, thereby changing the field distribution and the stored energy of the near-field depending on the material properties. Such probes can be realized with sub-wavelength antenna-like devices in the form of electrically small dipoles, open-ended waveguides, or a variety of other geometries [42]. Since a sub-wavelength dipole-type antenna is the basis of the near-field sensor presented later in this work, these devices are briefly discussed in the following.

The fields of an antenna can be separated into three regions: the reactive near-field zone, the radiating near-field zone, and the far-field zone. Both the radiating near-field and the far-field zones encompass the outgoing propagating waves. The fields in the reactive near-field zone are static and not propagating. For a very small electric dipole antenna with diameter $D \ll \lambda$, the reactive near-fields dominate the field pattern, and propagating waves are suppressed [44]. Such a dipole antenna is illustrated in Figure 2.11(a). Note the analogy to the free-space low-pass filtering for small spatial frequencies discussed in the previous section: Since the spatial frequency of the antenna fields is much smaller than the wavelength, no propagating waves are induced. However, the near-field of electrically small antenna probes is an involved function of the antenna geometry and the properties of the surrounding media. It is noted that the term evanescent wave is typically only used for exponentially decaying waves, whereas the near-fields of the small antenna probes decay with the squared distance or faster [42]. Such a probe exhibits almost no radiation losses but rather stores energy in its capacitive reactance. Therefore, the size of the near-field, and hence the spatial resolution, is determined by the characteristic size D of the

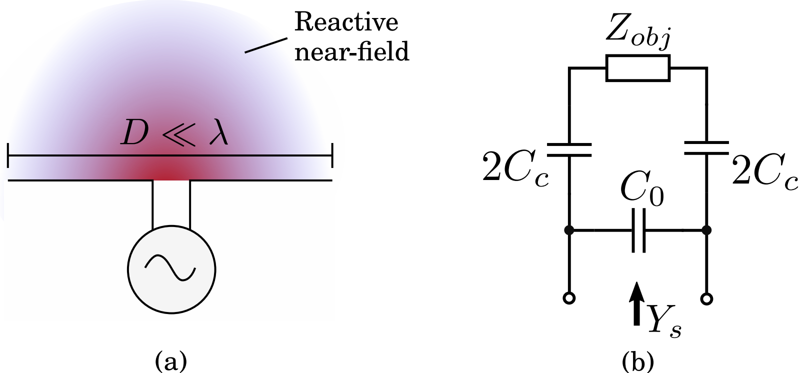

Figure 2.11.: Near-field sensing based on electrically small dipole probes. Illustration of the probe (a), and equivalent circuit of a sensing scenario (b).

probe.

Approaching a sample media with a small antenna probe disturbs the reactive field and induces a change in the input admittance of the probe. The simplified lumped equivalent circuit of a sensing scenario is depicted in Figure 2.11(b), where Z_{obj} is the impedance of the sample, C_0 is the static capacitance of the probe, and C_c is the coupling capacitance of the probe to the sample. The sensing admittance Y_s is given as:

$$Y_s = \left(\frac{1}{j\omega C_c + Z_{obj}}\right)^{-1} + j\omega C_0. \tag{2.40}$$

For a homogeneous bulk sample interacting with the entire volume of the sensing near-field governed by D, the object impedance can be estimated as a capacitor with a geometrical capacitance $\epsilon_0 D$, filled with the permittivity $\epsilon_r = \epsilon_r' - j\epsilon_r''$ of the sample [42]:

$$Z_{obj} \approx \frac{1}{j\omega\epsilon_0\epsilon_r D}. \tag{2.41}$$

With appropriate means of sensing object-induced changes in Y_s, one can achieve sub-wavelength resolution imaging with an imaging contrast based on the complex permittivity. A detailed discussion on this sensing mechanism and on how to integrate such probes in silicon technology follows in Chapters 5, 6, and 7.

2.3. Review of Contemporary THz Technology

This section provides a brief review of contemporary THz technology. To connect with the previous discussion on methods to break the diffraction limit, first, the state of the art in sub-wavelength sensing with THz waves is discussed. This will give the background

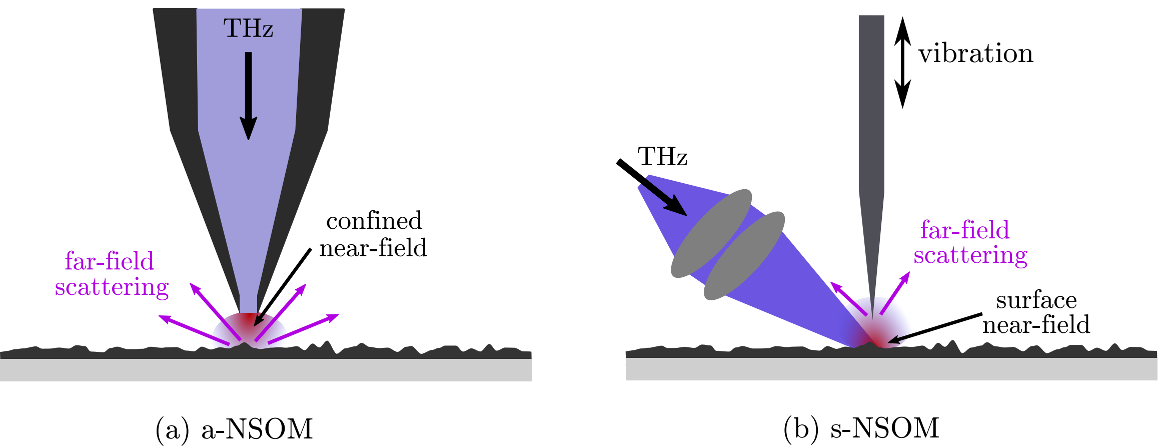

(a) a-NSOM

(b) s-NSOM

Figure 2.12.: Illustration of an exemplary aperture-based THz-near-field scanning optical microscopy (NSOM) system (a-NSOM) (a). A sub-wavelength sized aperture is illuminated with a THz source producing a near-field in the vicinity of the aperture which is scattered by the sample. Illustration of an exemplary scattering-probe-tip-based THz-NSOM system (s-NSOM) (b). A vibrating probe tip is illuminated from the far-field. The near-field information is scattered from the tip and collected with a THz detector and lock-in techniques.

for the near-field imaging part of this work presented in Chapters 5, 6, and 7. Subsequently, a brief review of traditional THz technology and silicon-based THz technology is given to provide a background for the far-field imaging part of this work discussed in Chapters 3, and 4. Parts of the discussion presented in this section have been published in [own7].

2.3.1. Review of THz Near-Field Imaging Methods

The common methods for sub-wavelength resolution (also called super-resolution) imaging in the THz range have been adapted from NSOM in the visible spectrum [45]. NSOM is an umbrella term for methods that exploit the interaction of evanescent waves with a specimen to resolve sub-wavelength sized features in a raster scan. The most common form of NSOM is based on sub-wavelength sized metallic or optically gated apertures (a-NSOM) for field confinement [12]. As depicted in Figure 2.12(a), a remotely illuminated aperture is brought into close vicinity of the specimen leading to object-dependent distortion and scattering of the near-field. In the first demonstration of THz-NSOM in 1998, Hunsche *et al.* achieved a spatial resolution of $\lambda/4$ at 1.3 THz by utilizing far-field illumination of a tapered metal tube with an elliptical aperture and far-field collection of the scattered near-field [46]. However, far-field collection severely limits the signal-to-noise ratio (SNR) of this setup, especially for tiny apertures. Since the near-field signal at the aperture decays exponentially in its direct proximity, large optics are required to collect the scattered waves.

This problem has been addressed by placing detectors in a distance considerably smaller than the aperture size. For example, a spatial resolution of 9 µm was reported in [47], with the setup comprising an 8 µm large aperture and a cooled two-dimensional electron gas as the detector in a gallium arsenide (GaAs)/Aluminum-GaAs heterostructure located 60 nm below the aperture. Moreover, tapered waveguides [48] and corrugated apertures [49] are frequently used to improve the coupling efficiency of the illumination path. However, the aperture cut-off frequency effectively limits the achievable spatial resolution of a-NSOM systems.

THz NSOM methods that exploit scattering probe tips (s-NSOM) have been shown to yield significantly higher resolution down to the nanometer scale [12]. In this technique, tapered metallic tips are illuminated from the far-field, creating a localized near-field in the vicinity of the tip apex, as shown in Figure 2.12(b). The near-field information is transformed into weak propagating fields by scattering in the sample-tip system. The spatial resolution is defined only by the tip geometry, which entails a trade-off between sensitivity and resolution. Furthermore, the weak near-field THz signal is submerged within a strong far-field component of the incident illuminating wave. To extract the weak near-field scatter from this strong background clutter, the probes are mechanically modulated (vibrated), and lock-in techniques are applied. Such methods enable remarkable spatial resolution down to 40 nm by using atomic-force microscopy cantilevers as scattering tips [50]. An alternative method to eliminate the background clutter issue is to collect the near-field in close proximity of the tip using electro-optic crystal plates or photoconductive probe tips. A spatial resolution of 150 nm was reported for a tip with a 30 nm diameter apex illuminated by a monochromatic gas laser source at 2.54 THz [12] and around 5 µm for a broadband system with a photoconductive 1.8 µm wide probe tip [51].

NSOM systems remain highly sophisticated in regard to the required illumination and detection components and the mechanical and optical setup. Even with cooled detectors and high-power THz sources, long integration times are needed to achieve a reasonable SNR. Although a few attempts have been made to reduce the image acquisition time by using multi-pixel [52] or electro-optic crystal detection [53], these systems similarly exhibit a high level of sophistication. The previous remarks clearly illustrate that the high system cost and the low integration level of conventional THz equipment constitutes a bottleneck for the exploration of new applications. Thus, classical NSOM systems are solely applied in laboratory environments and in fundamental science.

2.3.2. Traditional THz Technology

The traditional domain of THz technology is far-field imaging. Far-field imaging modalities can be generally divided into passive and active types. Passive (radiometric) imaging relies on the temperature-dependent intensity contrast of ambient (black-body) THz radiation. Active THz imaging employs THz sources for illumination of objects to increase the SNR. Here, the contrast is governed by the medium-specific attenuated wave propagation and interface interaction detailed above.

The most pervasive applications are found in the areas of radio astronomy and earth observation, where high-sensitivity heterodyne receivers are used to investigate the molecular composition and dynamics of the interstellar medium and Earth's atmosphere [5]. The instrumentation for these applications is based on either local oscillator (LO)-driven Schottky-diode mixers [54]–[56], or on sophisticated detector technology that requires cryogenic cooling. Such detectors, including superconductor-insulator-superconductor devices, hot-electron bolometers, and Josephson junctions, show tremendous sensitivity close to the quantum limit [55], [57]. However, the implications of the cooling requirements on system weight, turn-on time, and cost have impeded the transfer of this technology to other applications.

Today's available THz equipment for terrestrial use can be divided into electronic and photonic solutions. The electronic solutions rely primarily on split-block hollow waveguide assemblies with Schottky diodes and III-V devices or micro-machined bolometer arrays. There are various remarkable advances in this field, including the commercial development of GaAs Schottky-diode-based multiplier sources, delivering up to 35 µW at 1.9 THz [58], and the first demonstration of amplification above 1 THz using an indium phosphite (InP) high-electron-mobility transistor (HEMT) technology [59]. Still, because of non-compatibility with conventional microelectronic packaging, or the necessity of adequate cooling, such THz electronics mostly target performance-driven niches. For example, passive imaging systems based on InP HEMT low-noise preamplification [7], [8] or kinetic inductance bolometer arrays [60], and active radar imaging systems based on Schottky diodes [61], only show potential for imaging applications that can tolerate costly and stationary systems, such as mass transit security and loss prevention. Notably, some electronic THz systems for real-time active transmission imaging are already commercially available for applications such as conveyor belt imaging [62] or the security screening of letters and packages [63].

In the field of photonic THz equipment, THz TDS systems have emerged as a valuable laboratory tool for fundamental THz science and imaging [64], [65]. In THz TDS, a non-

linear crystal, typically low-temperature grown GaAs, is illuminated with an ultra-fast laser pulse from a Ti-Sapphire laser to generate electron-hole pairs. These carriers are accelerated in a static electrical field, leading to a broadband THz pulse. THz TDS can be used for transmission and reflection measurements and allows to extract the material properties in more than a decade of bandwidth, as shown in Section 2.1. Furthermore, continuous-wave (CW) photonic sources based on quantum cascade lasers can now generate up to 1 W of power at 3.4 THz. These sources, however, typically require cooling, and their operation is limited to frequencies above 2 THz [66].

In summary, it can be stated that the aforementioned THz platforms all suffer from distinct drawbacks for mass deployment; namely system cost, achievable integration level, or reliability. Moreover, the currently utilized microelectronic packaging techniques for electronic THz systems cannot easily support the tight tolerance levels required for THz applications and are not scalable to large volumes. Low-cost THz applications, therefore, require single-chip solutions that make complex microelectronic assembly obsolete.

2.3.3. Silicon Technology for THz Systems

Silicon devices have been mostly disregarded as a potential candidate to leverage the practical adoption of THz technology because of their low carrier mobility and long carrier transit times. The typically cited figure-of-merits for transistor speeds are f_T/f_{max}, which respectively describe the maximum frequency at which devices show current gain and the maximum frequency for which devices can amplify power [67]. Since most high-frequency circuits aim to transfer, generate, and amplify power, the f_{max} is usually a more meaningful metric of the device speed.

Complementary metal-oxide semiconductor (CMOS) technology undergoes continuous gate-length scaling, which increases the intrinsic speed of metal-oxide-semiconductor field-effect transistors (MOSFETs) as a by-product. However, the f_{max} of fully-wired devices decreases for the most advanced CMOS nodes (<45 nm) because of the deterioration of gate and via resistances as a consequence of transistor scaling [68]. Moreover, the high mask cost of CMOS wafers in advanced technology nodes necessitates a large volume for CMOS to be economically viable. As of yet, it is unclear if there will be sufficiently large market segments in the THz band to justify the use of CMOS.

An alternative to CMOS is SiGe HBT technology, which requires significantly less lithographic effort for higher f_{max} values. Since integrated SiGe HBTs are vertical devices, improvements in device speed mostly come from the optimization of parasitics and doping profiles rather than from technology scaling alone. Hence, further advances in SiGe HBT

technology are not necessarily linked to increasing mask costs. A 0.13 µm SiGe HBT technology with 500 GHz f_{max} is now commercially available [69], and research activities have demonstrated 700 GHz f_{max} in 0.13 µm SiGe HBT [70]. SiGe HBT technology is just on the verge of enabling circuits showing power gain above 300 GHz [own9][71], [72]. Results obtained from a theoretical analysis of the electrical performance limits of SiGe HBTs indicate that operating frequencies of 1 THz and beyond are within reach in the future [73]. Hybrid technologies that utilize the concurrent integration of high-speed SiGe HBT devices for the THz front-ends and low-cost CMOS for mixed-signal baseband processing thus show great potential to emerge as the primary platform for THz ICs.

However, silicon technology imposes considerable challenges for THz IC integration. First, advances in frequency performance are inherently linked to a reduction in device breakdown voltages. For high-speed 0.13 µm SiGe HBT technology, the open-base collector-emitter breakdown voltage is BV_{ceo} =1.6 V [69], whereas CMOS technology exhibits gate-oxide breakdown voltages of only 1.2 V for the 65 nm node [74] and below for more advanced nodes. Secondly, the technology stack of foundry-level silicon technology presents an increasingly unfavorable environment for antenna and passives implementation in the THz band. Typically, several metal layers are embedded in a thin dielectric stack, commonly denoted as back end of line (BEOL), on top of a lossy silicon substrate. The BEOL fabrication enforces strict design rules on the density of metal structures, which escalate the modeling and design effort of on-chip antennas and passives. The design of on-chip antennas in silicon technology is particularly challenging given potential multi-mode propagation issues (e.g., surface waves) [75], [76], and the difficulties in achieving appropriately high directivity of the antenna system to provide sufficient link budget for practical applications. This motivated the extensive use of back-side radiating on-chip antennas with auxiliary silicon lenses [77], [78].

2.3.4. THz Components in Silicon Technology

Modern nanoscale CMOS and SiGe HBT technologies offer economies of scale, small form-factors, and unprecedented integration capability at the highest industry standards. THz ICs are, therefore, an interesting option for applications that require extremely compact THz microsystems for sensing [15]–[17] or active imaging components at a reasonable price-performance ratio [own3][18]. However, the benefits of economic viability and system size are not the only drivers for research in THz ICs. The design-space, which opens up by device plurality, reconfigurability, and THz-mixed signal cointegration, promises to expand the functional scope of THz imaging systems. Applications such as THz-light field imaging based on CMOS detector focal-plane arrays [79], and broadband passive spectroscopy [80],

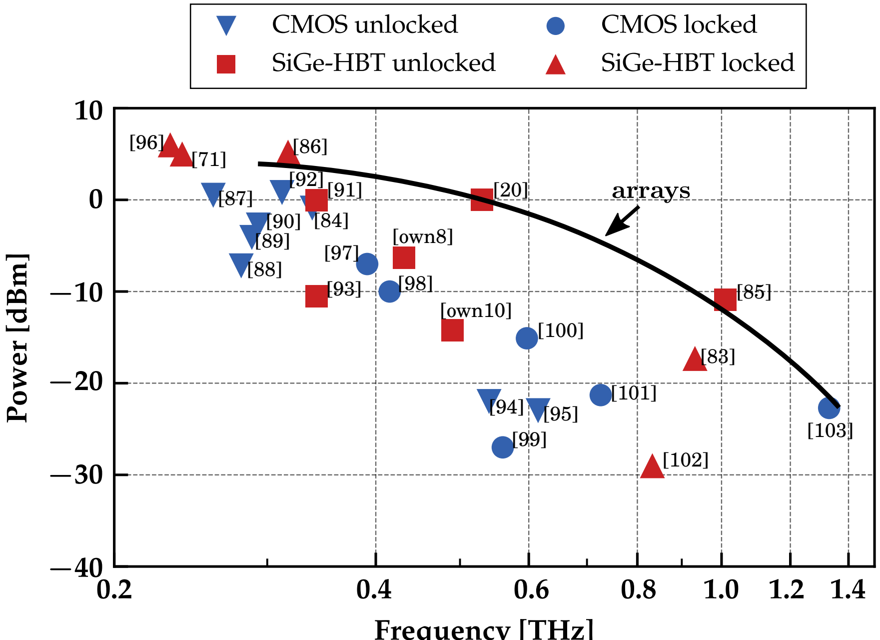

Figure 2.13.: Comparison of state-of-the-art THz sources in CMOS and SiGe HBT technologies. Adapted from [own7].

have been demonstrated based on THz ICs that approach integration-levels comparable to the ones exhibited in conventional consumer electronics. However, most research activities aim at advancing source and detector performance to overcome the speed limitations of silicon devices.

Sources

Since the first demonstration of a CMOS THz source ten years ago [81] which radiated −42 dBm at 410 GHz, tremendous progress has been made towards the provision of suitable power levels for imaging applications with THz ICs. The advances were enabled by both new design methodologies for the proper synthesis of passive embedding networks to optimize the harmonic generation [82], [83][own8], and novel scalable system architectures [20], [84]–[86]. Figure 2.13 depicts a scatter plot of sate-of-the-art CMOS and SiGe HBT radiation sources above 250 GHz. The sources are grouped into unlocked oscillator-based sources [20], [84], [85], [87]–[95][own8], [own10] and into oscillator- or multiplier-chain-based sources that can be locked to an external phase-stable reference signal [71], [83], [86], [96]–[103].

Currently, the upper frequency limit for fundamental circuit operation for the fastest 0.13 µm SiGe HBT technology with f_{max} =500 GHz [69] is just below the mmWave-THz

transition. Radiated power levels up to 8.5 dBm have been demonstrated for power-amplifier-based transmitter front-ends at 240 GHz, with a 3-dB bandwidth of 35 GHz in an experimental 0.13 µm SiGe HBT technology with f_T/f_{max} =350 GHz/550 GHz [96]. Above 300 GHz, amplification is no longer available in practice. Hence, silicon THz sources employ the frequency translation process of strongly driven nonlinear high-speed devices. The nonlinear THz front-end circuit is either directly implemented as a harmonic N-push oscillator or as a frequency multiplier circuit. Both approaches entail a conversion loss, which increases rapidly with the harmonic order and the frequency of the driving signal. Therefore, contrary to the typical 20 dB/decade roll-off for power amplifiers below f_{max} (Johnson Limit) [104], the data-points indicate an around 40 dB/decade power roll-off for single-radiator sources in the THz band.

Notably, the small size of on-chip THz passives and the abundant availability of transistors have motivated the research in single-chip multi-element radiators. Innovative device/electromagnetic codesign architectures that utilize synchronized 2D oscillator arrays broke the power roll-off trend, delivering a power of up to 5.2 dBm at 317 GHz with a 16-element array [86] and −10.9 dBm at 1.01 THz with a 42-element array [85] in 0.13 µm SiGe HBT technology. Furthermore, the baseband processing capabilities of silicon technology have been exploited for the reconfiguration of radiation patterns of multi-element sources to diffuse scene illumination at 530 GHz [20] or phased array functionality at 338 GHz [84] and 400 GHz [97].

Receivers

Similarly to the first silicon-based THz source demonstrations, the first silicon-based THz focal-plane array (FPA) was demonstrated 10 years ago [105]. Since then, the research in silicon THz IC receivers is largely focused on advancing the sensitivity and bandwidth of direct power detectors. Silicon technology features high fabrication yield and the availability of on-chip baseband processing circuits, enabling the integration of detectors into chip-scale FPA with on-chip read-out circuitry. Therefore, silicon detectors offer significantly higher integration capabilities compared to the prevalent room-temperature THz detector technologies like Schottky barrier diodes, InP HEMT low-noise amplifiers, Golay-cells, micro-bolometers and pyroelectric detectors [106]–[109].

Due to the lack of low-noise preamplification in the THz band, silicon power detectors are implemented as antenna-coupled direct detectors. Therefore, the predominantly exploited methods for THz direct detection are either non-quasistatic self-mixing in MOSFET channels [110]–[117] or rectification in the base-emitter junction of a high-speed HBT [76], [118]–[120]. At THz frequencies, both device classes operate close-to or above their cut-off

frequencies defined by the carrier transit time, and their response and operation bandwidth are severely influenced by the efficiency of coupling the THz radiation into the intrinsic device. Since broadband operation is typically desired for practical implementations to allow versatile application scenarios at low cost, classic narrowband microwave matching techniques made way for innovative antenna-device codesign approaches. In particular, antenna systems based on backside-radiating on-chip primary antennas and external hyper-hemispherical silicon lenses have been demonstrated to simultaneously provide pW/$\sqrt{Hz}$-level noise-equivalent power (NEP) across several hundreds of Gigahertz bandwidth [113]–[116], [120].

MOSFET direct power detectors are operated without drain-source bias ('cold') and in moderate inversion for the highest responsivity. The lowest reported NEP is in the range of 12 pW/$\sqrt{\text{Hz}}$–14 pW/$\sqrt{\text{Hz}}$ with a 3-dB radio frequency (RF) operation band of around 650 GHz–1000 GHz in 65 nm CMOS [115]. Please note that although device scaling can result in lower thermal noise of the MOSFET channel, the so far reported detector performance (responsivity, NEP, operation bandwidth) did not considerably improve by migration to nanometric CMOS technology nodes. One of the possible main reasons for that is the very high (kΩ-range) and frequency-dependent impedance of the MOSFET operating in moderate inversion, which makes efficient and broadband coupling to on-chip antennas very challenging. Contrary to that, the impedance levels associated with a base-emitter junction of HBTs at THz frequencies should facilitate considerably broader frequency operation range, although the literature still reports very few implementations of such detectors at THz frequencies. An NEP of 2.7 pW/$\sqrt{\text{Hz}}$ was reported for a dual-polarized detector at 430 GHz for the 0.13 µm SiGe HBT technology node [121], and further base-emitter junction optimization should result in substantial improvements of detector performance. Schottky diodes in CMOS technology were also reported for THz signal rectification at 860 GHz with an NEP of 42 pW/$\sqrt{\text{Hz}}$ [122].

Hetero-/homodyne receivers in silicon technologies above 300 GHz are still very scarce. They rely on a mixer-first architecture with predominantly sub-harmonic operation, yielding relatively poor conversion gain and noise figure [18], [102], [123]. Furthermore, their integration comes with significant complexity. In particular, the design of receiver arrays remains a formidable challenge due to the fundamental issues related to LO power distribution, limited LO drive power, and power consumption [78]. Only a few works have shown low-pixel-count arrays operating at or below the lower boundary of the THz range [124], [125].

Part II.

Far-Field Imaging

Chapter 3

Frequency-Doubler-Based 0.43 THz Source for Active Far-Field Imaging

This part of the thesis addresses active THz far-field imaging with silicon-based components. Active THz imaging systems either operate coherently or incoherently. The coherent approach employs phase-stable locked sources and heterodyne receivers. Coherent active systems provide high sensitivity and concurrent detection of amplitude and phase. Besides the issues of heterodyne receiver implementation mentioned in Section 2.3.4, coherent imaging suffers from unwanted imaging artifacts caused by wave-interference of specular reflections [20]. By contrast, incoherent active imaging only measures the power with direct detectors, which can be conveniently integrated into large-scale FPAs for video-rate imaging [116]. Moreover, sources based on free-running high-frequency oscillators can be exploited for illumination, which naturally exhibit low phase and frequency stability, thereby mitigating the interference effect mentioned above [89].

However, incoherent active imaging systems, especially the ones targeting video-rate imaging with FPAs, require considerable illumination power – usually exceeding the capabilities of current silicon-based THz sources. The work described in this chapter relates to the development of self-sustained doubler-based sources. The chapter presents a source radiating up to $-6.3\,\mathrm{dBm}$ at $430\,\mathrm{GHz}$ implemented in a high-speed $0.13\,\mu\mathrm{m}$ SiGe HBT technology [own8]. The source architecture enables a relatively high DC-to-THz efficiency of $0.14\,\%$ and occupies small chip area. Hence, the source can be conveniently populated into large-scale array modules to overcome the power limitations of a single source in future work. In this context, the presented source lays the foundation for advanced incoherent active imaging concepts, which go beyond the traditional focused illumination concepts

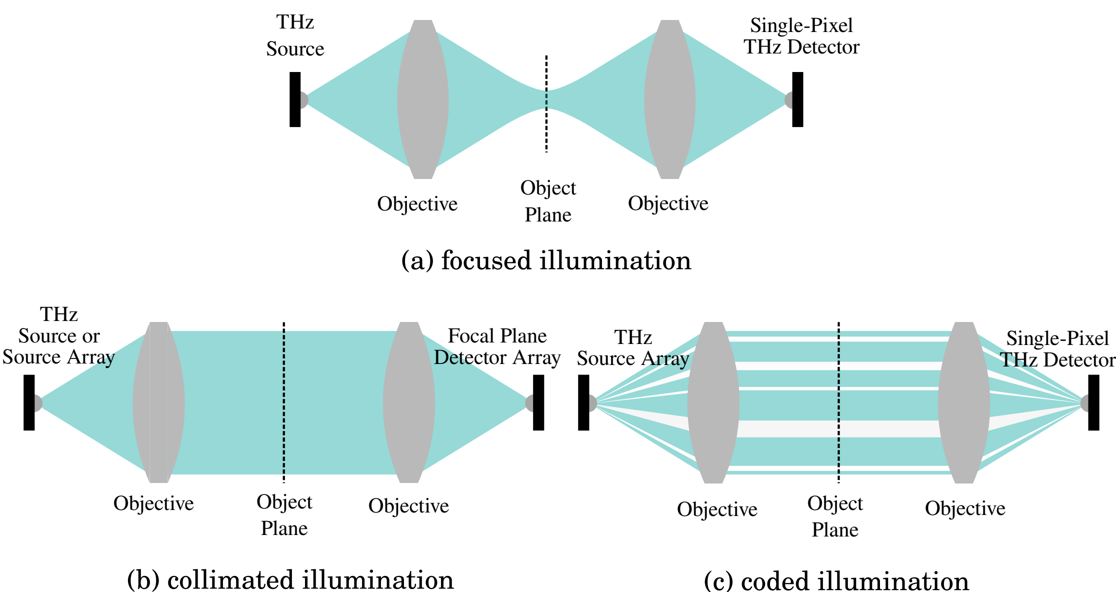

Figure 3.1.: Imaging concepts for active transmission-mode THz imaging. Traditional focused illumination imaging (a), collimated illumination imaging with frames per second (fps) detection (b), and coded illumination imaging (c).

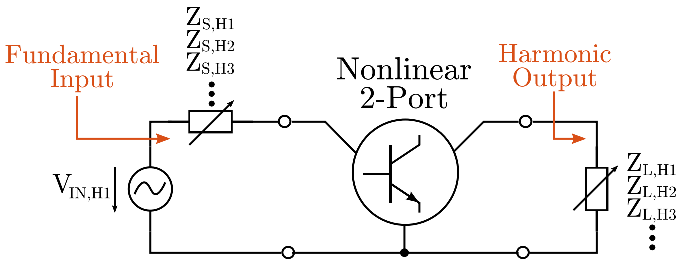

Figure 3.2.: Schematic of a nonlinear two-port used as a harmonic generator. The output power of the desired harmonic depends on the harmonic terminations at the input and at the output.

requiring mechanical translation, as illustrated in Figure 3.1. For example, multi-pixel source modules based on this source can potentially be used in conjunction with FPAs for video-rate collimated-beam imaging [20], or to build single-pixel cameras employing coded illumination for computational imaging [126], [127][own7]. Some of the results and figures presented in this chapter have been originally published in [own8].

3.1. Design Considerations

Power generation close-to or beyond f_{max} relies on the extraction of the harmonic content generated in the nonlinear transconductance, capacitance, and output resistance profile of the device. Figure 3.2 shows the general schematic of a harmonic generator circuit, modeling the transistor as a nonlinear two-port. Given a fixed available drive power at

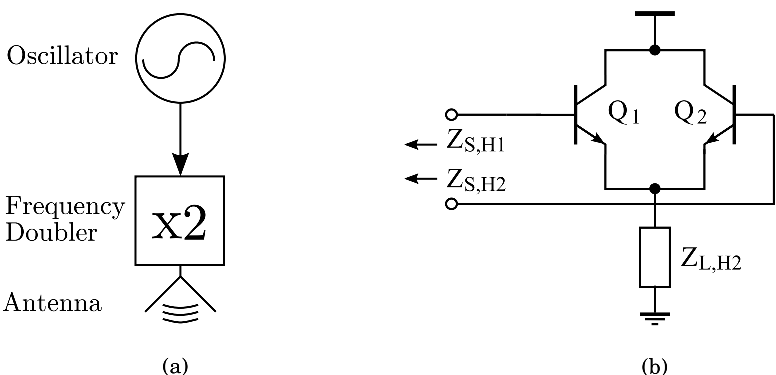

Figure 3.3.: Architecture of the source presented in this work (a). A high-frequency oscillator drives a frequency doubler that connects to an on-chip antenna. The simplified schematic of the doubler in common-collector topology is shown in (b).

the fundamental frequency (H1), two key aspects need to be considered for maximum power extraction at a certain harmonic (Hn). First, the device size and the conduction angle needs to be optimized for maximum harmonic current [128]. Secondly, due to internal mixing of frequency components in the device nonlinearity, the harmonic current at a certain harmonic is an involved function of the voltages at all harmonics [129], [130]. Hence, all relevant harmonic terminations at the two-port need to be optimized individually to maximize the harmonic power transfer to the output. Multi-harmonic load-pull large-signal simulations are usually required to deduce these optimum terminations.

Figure 3.3(a) depicts the circuit architecture of the source presented in this chapter. The source comprises a differential high-frequency oscillator, a balanced frequency doubler, and a single-ended on-chip antenna. Frequency doublers usually employ balanced common-emitter (CE) pairs or balanced common-collector (CC) pairs. The balanced CC circuit architecture depicted in Figure 3.3(b) is used in this work. It was shown in [131] that the CC shows higher maximum output power. More particularly, the second harmonic voltage swing at the emitter terminals can contribute additional second harmonic current through the device transconductances if the phase relations between the common-mode base and emitter voltages are designed appropriately. The balanced CC topology exhibits an AC-ground for the differential fundamental mode at the shared emitter node. Therefore, the key harmonic terminations are the differential input impedance at the fundamental ($Z_{S,H1}$), the common-mode second-harmonic input impedance ($Z_{S,H2}$), and the output impedance at the second harmonic ($Z_{L,H2}$). In order to maximize the fundamental drive voltage, unwanted reflections of the fundamental have to be avoided. Hence, $Z_{S,H1}$ needs to be conjugately matched to the differential input impedance of the CC pair. Due to the strong feedback provided by the base-emitter junction, the optimum selection of $Z_{L,H2}$ and $Z_{S,H2}$

are interdependent. In practice, $Z_{S,H2}$ cannot be easily set independently from $Z_{S,H1}$, as the termination networks share the same passives. It is noted that second harmonic reflectors in the form of short circuit stubs can be implemented without influencing the fundamental matching in a small bandwidth. Such reflectors, however, reduce the output power for the CC topology [131]. Hence, the design of the second harmonic output termination needs to take full consideration of the fundamental matching circuit and the related second harmonic common-mode impedance at the input.

3.2. Implementation

The source is implemented in a 0.13 µm SiGe HBT technology SG13G2 from IHP Microelectronics offering an f_T/f_{max} of 300 GHz/450 GHz and a 12 µm-thick 7-metal aluminum back-end with two thick top-metal layers and MIM-capacitors [69]. Figure 3.4 shows the complete schematic of the source. All inductances are implemented with shielded coplanar-waveguide transmission lines. The oscillator is a differential Colpitts oscillator with a cascode stage. The fundamental oscillation frequency of $f_{H1} \approx 220$ GHz is set by the base transmission line TL_B, the base-emitter junction capacitance of $Q_{1,2}$, and the emitter capacitor C_E. Due to the high loss of integrated varactors, no explicit frequency tuning capabilities are implemented. However, some implicit tunability is given by the bias-dependence of the diffusion capacitances of $Q_{1,2}$. The emitter transmission line TL_E is a quarter-wavelength stub at the oscillation frequency and provides a DC current path to the transistors. The cascode stage serves two purposes. It isolates the oscillator output from the doubler and it increases the output power. The devices are modeled with HICUM models, whereas the passive components are simulated in full-wave EM simulations (Ansys HFSS). The simulated output power of the oscillator is around 5 dBm at 223 GHz.

Based on the simulated oscillator output power, the doubler emitter area is chosen to be $3\times(0.12\times0.96)\mu m^2$. In view of the remarks given in the previous section, the interstage matching network comprising TL_C, TL_1, C_C and TL_2 is designed to concurrently match the fundamental and provide a good solution for the common-mode 2nd-harmonic base termination at the input using load-pull simulations. An optimum second harmonic load for the designed input matching circuit of $Z_{L,H2}=(40+j50)\Omega$ is also deduced from harmonic load-pull simulations. The output termination is realized by transforming the capacitive impedance of an on-chip antenna through the transmission lines TL_4 and TL_6.

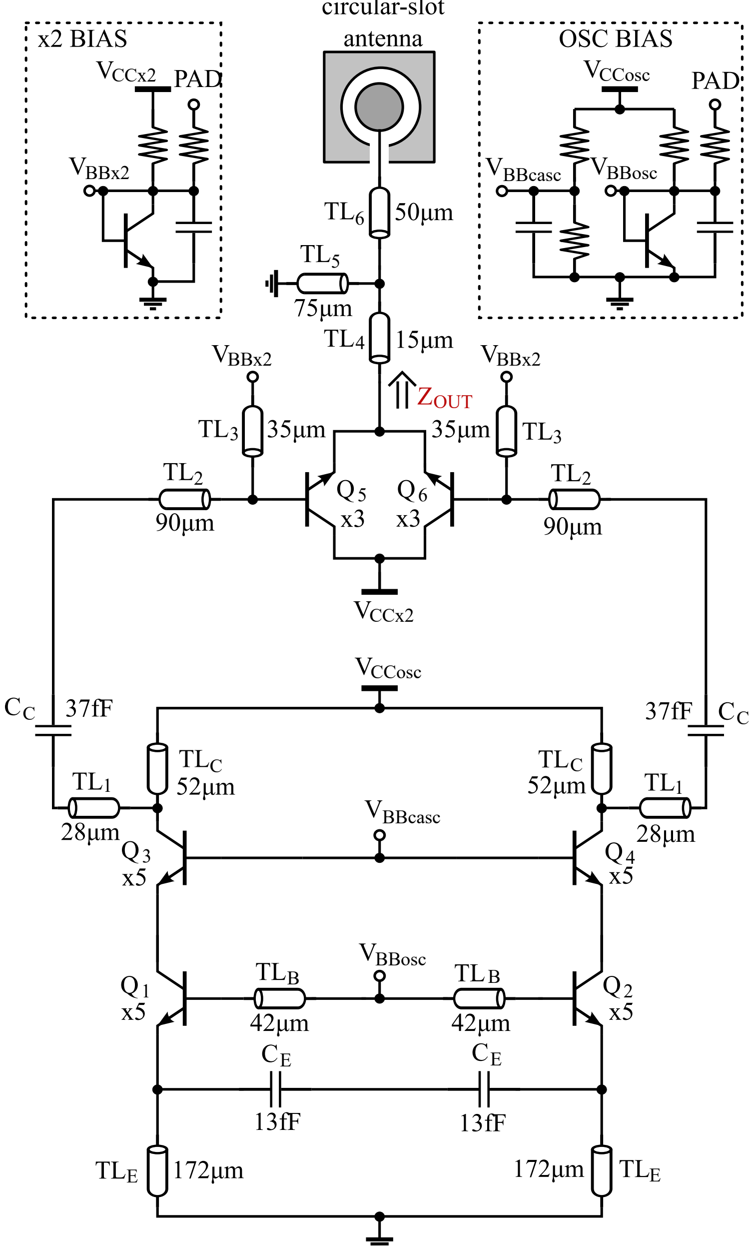

Figure 3.4.: Circuit schematic of the THz source. The unit emitter area is $(0.12{\times}0.96)$ μm^2. The doubler output impedance Z_{OUT} is tuned to optimize the 2nd-harmonic output power. After [own8] © 2017 IEEE.

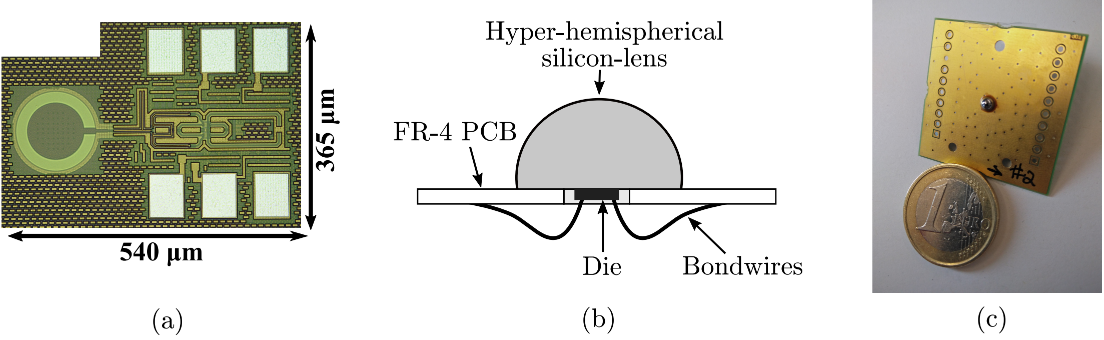

Figure 3.5.: Chip micrograph (a), illustration of the packaging scheme (b), and picture of the assembled source (c). After [own8] © 2017 IEEE.

Figure 3.5(a) shows the chip micrograph. The antenna is a wideband lens-coupled circular-slot antenna and is similar to that presented in [own10][132]. The main radiating slot aperture is created in the common circuit ground plane and supports a linear polarization excited by a circular patch probe located in its center. The power at the fundamental oscillator frequency possibly leaking from the doubler is attenuated by a high antenna input reflection coefficient in this frequency range. The diameters of the circular probe and the ground aperture are 106 µm and 152 µm, respectively. For test purposes, the chip was mounted on the back of a 3-mm diameter hyper-hemispherical lens made of high-resistivity silicon and wire-bonded onto a small FR-4 printed circuit board (PCB). Figure 3.5(b) depicts an illustration of the packaging concept, and Figure 3.5(c) shows a picture of the packaged source. Full-wave simulations of the completely packaged lens-coupled module were performed. The additional implementation loss in the source output power is estimated to be around 20 %. The simulated antenna directivity is 19.5 dBi at the source operating frequency of 430 GHz.

3.3. Experimental Characterization

The setup shown in Figure 3.6(a) was used to measure the frequency and the antenna pattern of the source. Figure 3.6(b) shows the down-converted spectrum of the source in the vicinity of the radiation frequency, and Figure 3.6(c) shows the simulated and measured tuning curve of the source for different oscillator supply voltages and a constant external base voltage. A phase-noise of −89 dBc/Hz at 10 MHz offset was estimated in a measurement with a battery power supply. The measured frequency decreases with increasing supply voltage, which resembles the trend observed in simulations. The source can be tuned between 426 GHz–437 GHz. Figures 3.6(d)(e) show the measured and simulated E-plane and H-plane radiation patterns. The measured directivity is 21.3 dBi, and

the side-lobe level is around -17 dB. The antenna directivity is calculated by integrating the measured values of the 2-D power spectral-density pattern scanned over a sector of the front hemisphere. The back-side radiation was not measured and may lead to some artificially increased antenna directivity.

Absolute free-space power measurements at THz frequencies are very challenging. Power measurement with a harmonic mixer suffers from the poorly calibrated and time-varying mixer conversion gain. The photo-acoustic power meters, such as the Thomas Keating power meter, offer a large aperture and do not require extensive calibration. However, they are not frequency-selective and capture all harmonics potentially radiated by the source. In contrast, power measurements with a calorimeter, such as the Ericson PM4, allow controlling the lower end of the measurement bandwidth by using the cut-off frequency of a waveguide taper inserted between the meter head and the antenna. Here, the power is measured in the far-field and de-embedded from the Friis-transmission equation. This approach naturally exhibits higher uncertainty since the received power levels in the far-field are low, and accurate knowledge of the directivities of the receiving and sending antenna is required. In this work, a combined verification approach is used to mitigate the individual shortcomings of both methods.

For an accurate assessment of the absolute radiated power of the source, the Thomas Keating power meter was used in the measurement setup shown in Figure 3.7(a). Two elliptical mirrors are used to refocus the beam to the meter head at the Brewster's angle. Figure 3.7(b) shows the radiated power measured in this manner and compares it to the simulated on-chip power of the source. The power peaks at -6.6 dBm at a supply voltage around 4.5 V. For higher supply voltages, the oscillator enters the breakdown region, and the power drops rapidly. The measured values are significantly lower than the simulated values at low supply voltages, possibly indicating a lower fundamental drive power. For higher supply voltages, the output power shows a good correlation considering the additional implementation loss of the lens-coupled on-chip antenna.

In order to verify that the power measured with the Thomas Keating power meter is the power at the second harmonic and not at the fundamental, the power was measured with a PM4 calorimeter as shown in Figure 3.7(c). A horn antenna with an estimated directivity of 23 dBi at the operation frequency and a WR2.2 waveguide was used to reject the potential fundamental leakage. Figure 3.7(d) shows the measured power for different distances d between source and the horn antenna and the calculated radiated power derived from Friis-transmission equation for the same source bias point as that applied for the Thomas Keating power meter measurements. The output power follows the expected $1/d^2$ proportionality and is on average -6.3 dBm. The source consumes 165 mW of DC

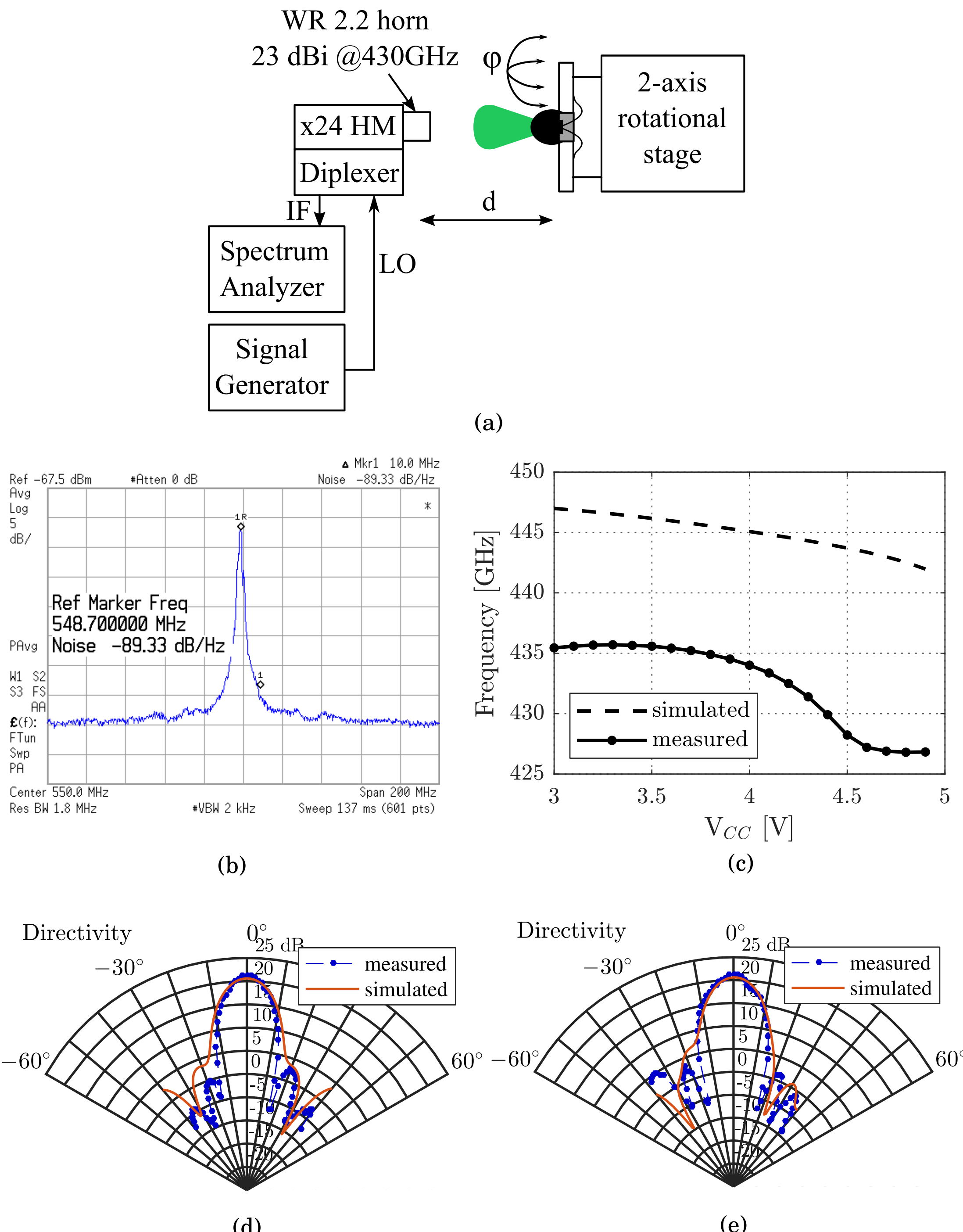

Figure 3.6.: Frequency and antenna pattern characterization of the source. Measurement setup (a), simulated and measured frequency of the source (b), measured E-plane (c) and H-Plane (d) cuts of the co-polar radiation pattern measured at 430 GHz in the transmit mode. After [own8] © 2017 IEEE.

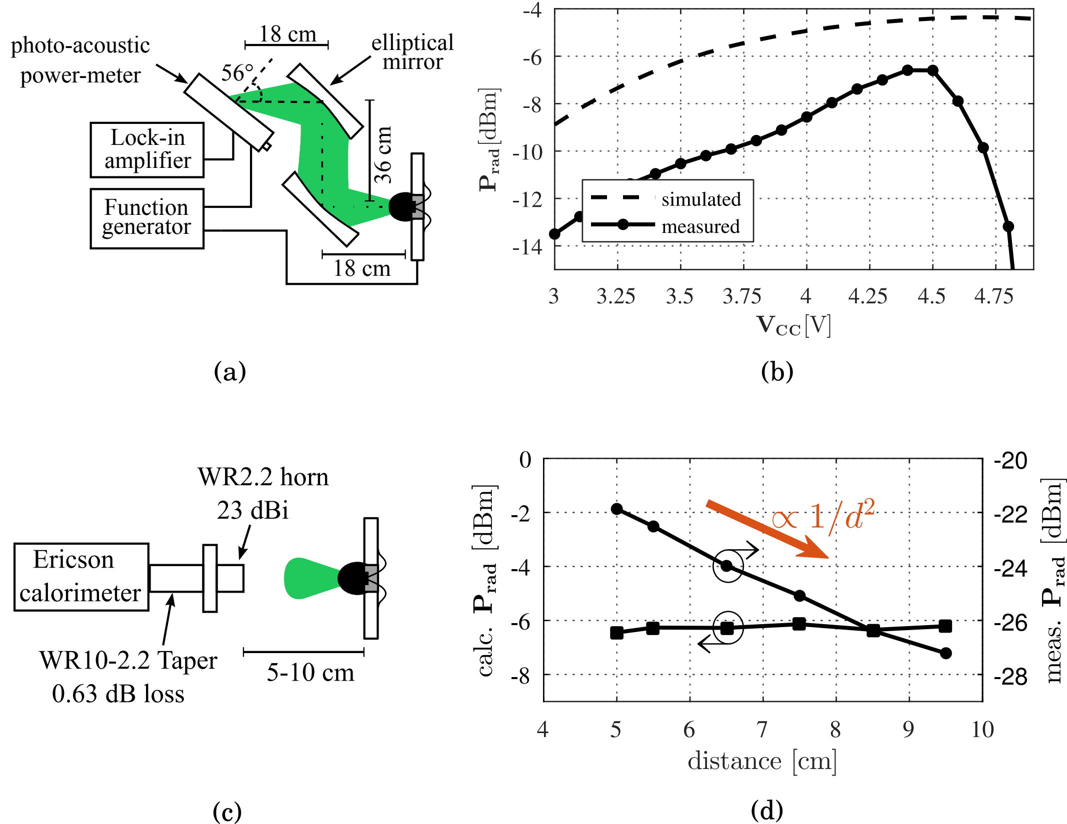

Figure 3.7.: Power measurement. A calorimeter (PM4) is used to measure the 2nd-harmonic power at different distances (a), and measured power for different distances from the source. The radiated power is calculated using Friis-transmission equation with the directivities D_{source} = 21.3 dBi, and D_{horn} = 21.3 dBi, and 0.63 dB insertion loss of the taper. After [own8] © 2017 IEEE.

power, thereby giving a DC-to-THz efficiency of 0.142 %. The fundamental leakage was attempted to be measured in free-space with another antenna-coupled harmonic mixer (OML). The signal levels were found to be below the noise floor of the IF output. From this and the good correlation between the two power measurements, it can be concluded that the fundamental leakage of the source should be very low.

3.4. Summary and Conclusions

A 0.43 THz source implemented in a 0.13 µm SiGe HBT technology has been reported in this chapter. The large-signal optimization of the harmonic terminations of a balanced CC doubler is utilized to optimize the efficiency of the harmonic power extraction close to the f_{max} of the technology. To enable low power and low area consumption, the doubler is driven by a differential Colpitts oscillator. The source radiates up to −6.3 dBm at

0.43 THz and shows a DC-to-THz conversion efficiency of 0.142 %.

The source may find application in large-scale incoherent source arrays for realizing advanced far-field imaging concepts such as video-rate collimated-beam imaging [20], or computational imaging [126], [127][own7]. In particular, it consumes around three times less area and shows four times higher output power as compared to the single source elements employed in the incoherent 0.53 THz source array presented in [20], which represents the current state of the art. However, the increase in output power has to be put into perspective because of the lower operating frequency of the source presented here. The implementation of an array based on this source, however, remains the objective of future work. The following chapter demonstrates the utility of the single-pixel source by using it for THz CT.

Chapter 4

3D Terahertz Imaging Based on Computed Tomography

Since the first demonstration of THz transmission imaging by Hu *et al.* in 1995 [30], most studies on THz imaging were focused on 2D imaging. Because 2D imaging only provides limited information content for thick objects with high volumetric complexity, there has been an increasing effort to extend THz imaging modalities to 3D imaging. 3D visualization of the objects' internal structure may be particularly valuable for applications in industrial quality control, e.g., for the localization of cracks and defects in composite materials, or for the content inspection of packaged goods [133]. Another interesting use case for 3D THz imaging could arise for non-invasive analysis of archaeological findings, e.g., inspection of wrapped mummies [134], sealed pottery [135], or imaging of human bones [136].

Various techniques have been investigated for the acquisition of 3D images at THz frequencies, including time-of-flight measurements in reflection-mode [137], diffraction tomography [138], tomosynthesis [137], imaging with binary lenses [139], and CT with ultra-short THz pulses [140] or CW sources [135]. All these studies, however, have relied on bulky and expensive traditional THz equipment.

THz tomography competes against the highly established X-ray CT, which usually provides far superior image quality in terms of spatial resolution. However, there could be extensive added value in the exploration of THz waves for CT imaging. The absorption in low-density materials is relatively stronger for THz waves because of the higher dielectric

losses. Moreover, hazardous X-ray radiation requires costly security measures. Eventually, the previously detailed advances in silicon-integrated THz components could enable the realization of ultra-low-cost 3D THz CT imaging systems [own3], promising increased exploitation for future industrial applications. The demonstration of such a system is the ultimate aim of the work presented in this chapter.

CT operates in transmission-mode, which sets challenging requirements on the performance of the source and detector components. The resolvable object depth of a THz CT system for a certain material is ultimately limited by the SNR, which is influenced by the source power, the quality of the optical train, and the NEP of the detector. Although the exact performance requirements for the components are application-specific, it is illustrative to construct a hypothetical imaging scenario to strengthen the point. Assuming a moderate acquisition speed with an integration time of τ =1 ms per line projection, the equivalent read-out bandwidth of the detector is 500 Hz ($BW = \frac{1}{2\tau}$). Using a detector with an NEP of 100 pW/$\sqrt{\text{Hz}}$, the minimum detectable power becomes 2.2 nW (P_{min} = NEP$\sqrt{BW}$). For a 4 cm thick plastic object with an attenuation coefficient of $\alpha = 0.5\,\text{cm}^{-1}$ [23], 13.5 % of the power passes through the object. Consequently, for a minimum SNR of 20 dB, the required radiated power of the source is around 1.5 µW. In practice, Fresnel losses of the object and losses of the optical components can tighten these requirements significantly. However, with the advances in THz silicon technology summarized in Section 2.3.4, such performance metrics are now in the feasible range.

The chapter opens by briefly reviewing the fundamentals of CT. After that, a silicon-based THz CT system operating at 430 GHz is described and characterized. Finally, 3D imaging of objects embedded into polystyrene foam is demonstrated. Some of the results and figures presented in this chapter have been originally published in [own7].

4.1. Fundamentals of Computed Tomography

The word tomography is derived from the Greek word *tome* (cut). The imaging procedure aims to reconstruct cross-sectional 2D images of an object (cuts) based on the absorption experienced by an electromagnetic wave due to traveling through the object. This is achieved by acquiring the projection of the object onto a plane for different incident angles of the wave and by subsequent image reconstruction with appropriate algorithms. Figure 4.1 illustrates the principle of CT. CT was initially developed for X-rays. Due to the low permittivity of materials in the X-ray band ($\epsilon_r \approx 1$), Fresnel losses can be mostly neglected. Hence, X-rays can be considered to travel in straight lines through objects.

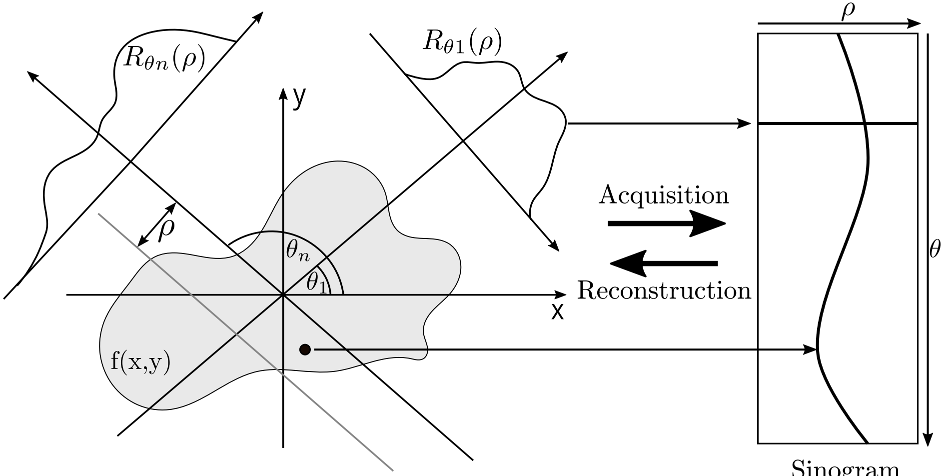

Figure 4.1.: Principle of CT. Absorption projections R_θ are measured for different angles of a half-cycle $\theta \in [0, \pi]$. The measured projects arranged along θ are called sinogram. Reconstruction algorithms are used to synthesize the original object characterized by its absorption function $f(x, y)$ from the sinograms. The process is repeated to allow different heights for 3D reconstruction.

This assumption is carried throughout the following mathematical description of the CT principle, albeit noting that it may lead to inaccurate results for the THz band, where Fresnel losses can contribute significantly to the image contrast. Neglecting reflection and refraction, the intensity of a transmitted wave is determined by the absorption integral along its optical path. According to Equation 2.15, the intensity I is described by the Beer–Lambert Law for inhomogeneous media:

$$I = I_0 e^{-\int_L f(x,y)\,dl}, \tag{4.1}$$

where I_0 denotes the intensity without absorption, L describes the optical path, and $f(x, y)$ is the local absorption function of the object. By rearranging Equation 4.1, the total absorption R, also called projection, can be described as:

$$R(L) = -\log \frac{I}{I_0} = \int_L f(x,y)\,dl. \tag{4.2}$$

Equation 4.2 is the Radon transform of the absorption function $f(x, y)$, which is named after the mathematician Johann Radon who derived that an object can be reconstructed perfectly from a full continuous set of such line integrals [141]. In practice, the intensities I and I_0 are the observables that can be measured with a power detector. Because of the angle-dependency of the projections, the integration lines are more conveniently described in polar coordinates:

$$L_{\theta,s} = \{(x,y) = x\cos\theta + y\sin\theta = \rho\}, \tag{4.3}$$

where θ is the angle between the x-axis and the perpendicular to the integration line, and ρ is the signed orthogonal distance of the line to the origin. One can easily show that the angle-dependent projection of a single point $f(x, y)$ describes a sine function. This is the reason why the illustration that gathers projections is typically called a sinogram. The radon-transformed local absorption function of a cross-section can then be defined as:

$$R(\theta, \rho) = \int_{-\infty}^{\infty} \int_{-\infty}^{+\infty} f(x, y)\delta(\rho - x\cos\theta - y\sin\theta)\, dx\, dy. \tag{4.4}$$

Equation 4.4 is a measured quantity. Since the Radon transform is symmetric ($R(\theta, \rho) = R(\theta + \pi, -\rho)$), it is sufficient to acquire a half-cycle of projection angles, i.e., $\theta \in [0, \pi]$. In typical CT imaging experiments, the sinograms are taken for multiple cross-sections to enable 3D reconstruction of the object.

As of yet, we have just modeled the acquisition process and did not cover the means to reconstruct $f(x, y)$ from the measured quantities. The methods for reconstruction for radon-transformed data can be grouped into two categories. The first category includes direct methods based on the filtered back-projection (FBP). The FBP is given by:

$$f(x, y) = \int_{0}^{\pi} d\theta \left[\int_{-\infty}^{\infty} |\omega|\, \mathcal{F}\left\{R(\theta, \rho)\right\} e^{2\pi j\omega\rho} \right]_{\rho = x\cos\theta + y\sin\theta}, \tag{4.5}$$

where ω is the spatial frequency, and $\mathcal{F}$ is the Fourier transform. In practice, the acquired data is not continuous, and Equation 4.5 is used in a discretized form. Today, the FBP is the standard algorithm for tomographic imaging with X-rays.

The second group includes algebraic methods such as Algebraic Reconstruction Technique (ART) [142], Simultaneous Iterative Reconstruction Technique (SIRT) [143], and Simultaneous Algebraic Reconstruction Technique (SART) [144]. These methods compare the sinograms of computational estimates of the local absorption function with the measured sinograms and correct the estimations iteratively to approach an acceptable solution for the original image [145]. While such methods are much more computationally intensive as compared to FBP, they exhibit several advantages for tomographic imaging in the THz range. First, they offer superior image quality for a smaller set of projections [133]. This is particularly beneficial since long scanning times remain a major problem for THz CT (see Section 4.2). Moreover, the algebraic methods allow the inclusion of *a priori* knowledge of the object, which is commonly given in practical applications in the field of industrial quality control. As such, a combination of ray-tracing and iterative methods could yield significantly enhanced image quality in the presence of Fresnel losses [146]–[148].

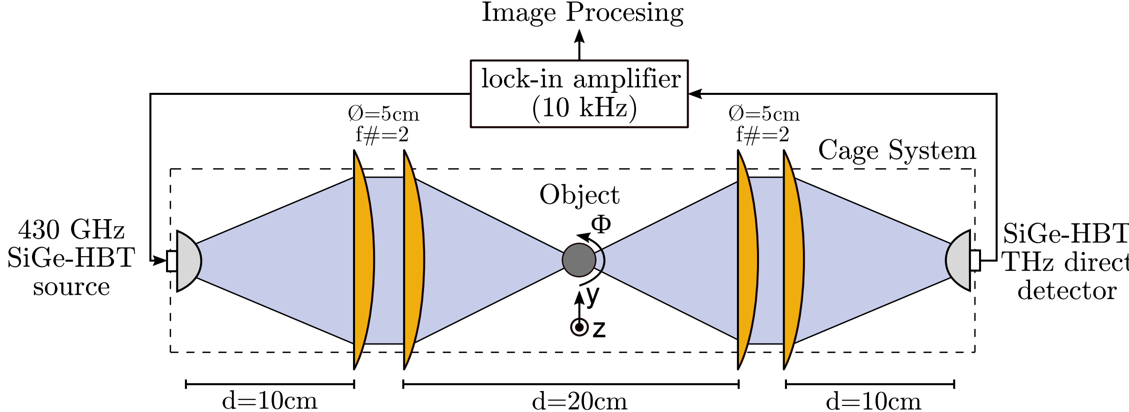

Figure 4.2.: Illustration of the THz CT experiment. The setup consists of a 430 GHz SiGe HBT source, a SiGe HBT detector and an optical train of four $f_{\#}=2$, 50-mm polytetrafluoroethylene (PTFE) lenses. The object is rotated (ϕ) and stepped in the 2D object plane (y,z).

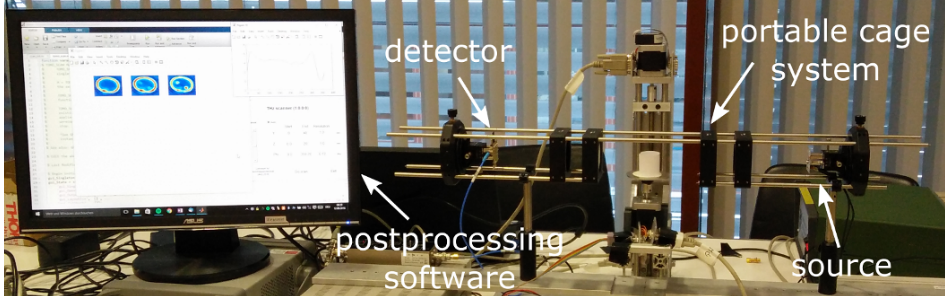

Figure 4.3.: Picture of the THz CT setup. After [own3] © 2017 IEEE.

4.2. THz Computed Tomography with Silicon-Based Components

4.2.1. Experimental Setup

Figure 4.2 depicts the experimental setup of the THz CT system, and Figure 4.3 shows a picture of the system. The object is placed in the focal spot of a $2f$-$2f$ optical train, where f denotes the focal length of the focusing lens. The source beam is focused in the object plane and subsequently refocused to the detector with four 5 cm-diameter PTFE lenses. The lenses exhibit a focal length of 10 cm, and the total size of the optical train is 40 cm. With this arrangement, only a single projection line is acquired at a time. Hence, the object is mounted to a y-z axis stepper motor stage and a piezo rotation stage to enable acquisition of the projections at different heights.

The SiGe HBT source with −6.1 dBm radiated power at 430 GHz presented in Chapter 3 is used as a source. A source antenna gain of approximately 21 dBi is selected by choosing

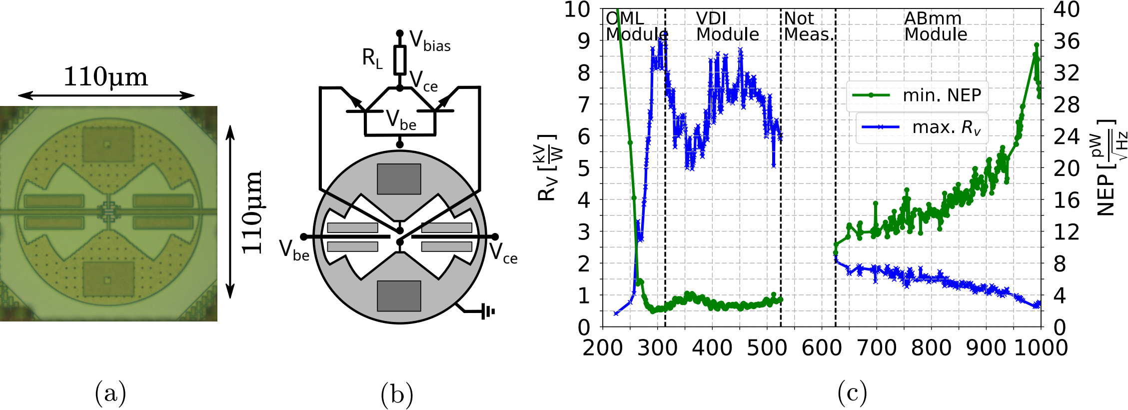

Figure 4.4.: Chip micrograph (a) and the schematic (b) of the antenna-coupled detector. The key characterization results including the NEP voltage responsivity as a function of frequency are depicted in (c). After [149] © 2017 IEEE.

a 4 mm-diameter hyperhemispherical silicon lens to allow the appropriate coupling of the radiation to the optical train. The detector is the broadband antenna-coupled SiGe HBT direct detector presented in [149]. The device was fabricated in an experimental 0.13 µm SiGe HBT technology with a peak f_t/f_{max} of 350 GHz/550 GHz. Figures 4.4(a)(b) show the micrograph and the schematic of the detector. The detector comprises a differentially driven common-base device pair, which provides rectification of the impinging THz wave in its nonlinear base-emitter junction. To supply broadband operation, the impedance profile of the antenna is optimized to represent a broadband complex-conjugated match to the detector. The detector is fixed to a 3-mm diameter hyper-hemispherical silicon lens with epoxy and is assembled to a low-cost FR-4 board. Figure 4.4(c) shows the measured NEP and voltage responsivity R_v (for a 1.83 kΩ external load resistor) as a function of frequency. At the operating frequency of the source of 430 GHz, the NEP and voltage responsivity are $2.8\,\mathrm{pW}/\sqrt{\mathrm{Hz}}$ and $7.5\,\mathrm{kV\,W^{-1}}$, respectively. The reader is referred to [149] for design and measurement details. As it will be detailed in Chapter 5, SiGe HBT detectors suffer from severe low-frequency noise below 100 kHz. To avoid a related deterioration of the dynamic range (DR) of the system, the source is chopped at 120 kHz, and the detector output is read out with an external lock-in amplifier (LIA) with 3 ms integration time. The DR is defined as the ratio between the detected voltage at the LIA output without an object present and the standard deviation of the voltage noise in the absence of the THz beam. The measured DR of this system is 71.2 dB.

The spatial resolution of a focused far-field imaging setup depends on the size of the focus spot, which is influenced by the wavelength and the employed optics. Hence, an appropriate choice of the optical components and their accurate alignment is key to achieve a good imaging resolution. Moreover, the depth of focus of the beam should be chosen based on the lateral extension of the 3D object to ensure uniform sampling of the object.

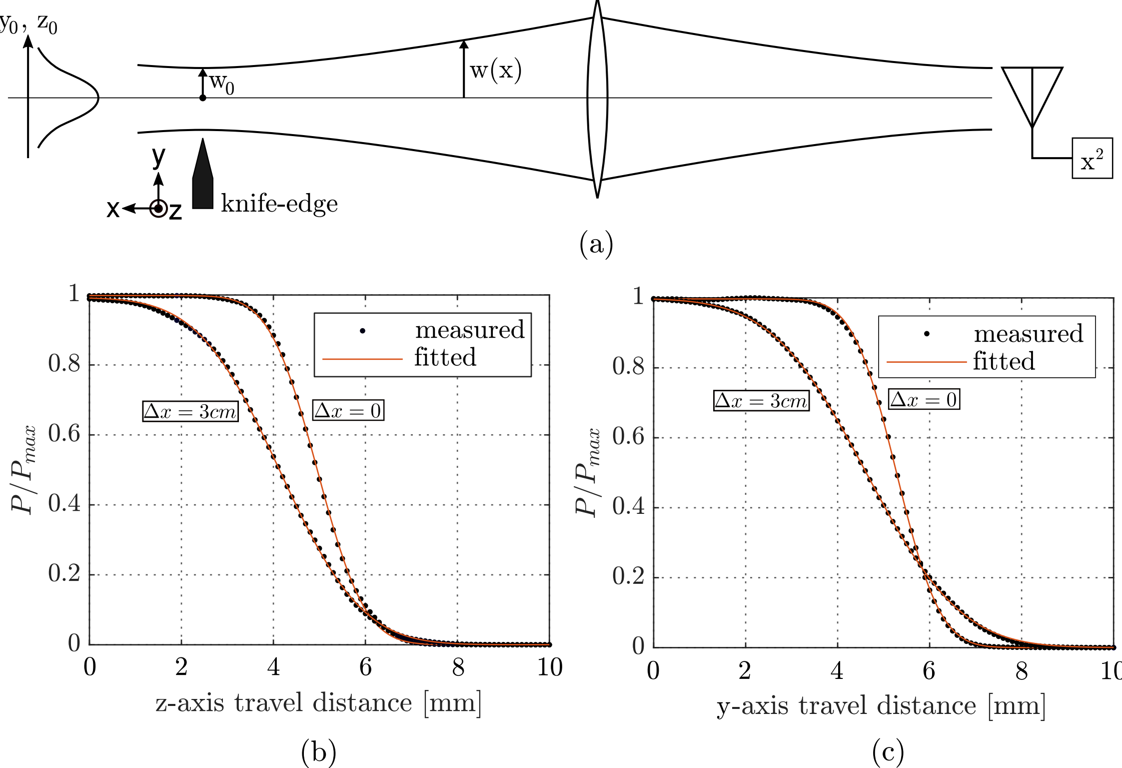

Figure 4.5.: Knife-edge characterization of the beam profile. Illustration of the knife-edge measurement procedure (a). Measured normalized power responses and Gaussian fits in the focus point and 3 cm apart from the focus point for translation in z-direction (b) and y-direction (c). The corresponding axes are shown in Figure 4.2.

The depth of focus of Gaussian beams is commonly described with the Rayleigh length, which is proportional to the square of the beam waist in the focus point [150]. Hence, THz CT setups typically require the spatial resolution to be traded against the depth of focus by employing smaller optics. In the present setup, the optics were designed to accommodate moderately sized objects with a lateral extension of a few centimeters. Based on the measured radiation pattern of the source presented in Figure 3.6, the Gaussian waist radius in the focus point and the Rayleigh length can be calculated to be 1.25 mm and 7 mm at 430 GHz for the PTFE lenses with 10 cm focal length[1], respectively.

To assure a well-behaved Gaussian beam profile along the optical train, the beam propagation was consecutively optimized using element-wise beam profile measurements with the SiGe HBT detector mounted to an industrial robot. All components were subsequently fixed to a cage system to ensure the stability of the optical alignment. The imaging resolution of the setup was quantified using the knife-edge method depicted in Figure 4.5(a). A metal object with a sharp edge was mounted to a high-precision translation stage and

[1]The Gaussian waist radius is here defined as the distance from the optical axis where the intensity of the beam has decreased to $1/e^2$ of its maximum value.

was moved into the beam to block off parts of the radiation. Figures 4.5(b)(c) show the normalized measured power received by the detector for y- and z-axis knife translation in the focus point and 3 cm apart from the focus point. The beam waist radius is then obtained with a Gaussian fit for the transmitted power P as [151]:

$$P = \frac{P_{max}}{2}\left[1 + erf\left(\sqrt{2}\frac{(d-d_0)}{w}\right)\right], \tag{4.6}$$

where P_{max} is the total power of the unblocked beam, $d - d_0$ is the signed knife-edge distance from the point where half of the power is blocked, w is the $1/e^2$ beam radius, and $erf(t)$ is the Gaussian error function defined as follows:

$$erf(t) = \frac{2}{\sqrt{\pi}}e^{-t^2}\,dt. \tag{4.7}$$

The measured Gaussian $1/e^2$ beam radius for the y-axis is 1.49 mm in the focus point and 3.24 mm at 3 cm distance. The respective values for the z-axis are 1.64 mm and 2.81 mm. The measured spot size is slightly larger in comparison to the calculation but shows reasonable agreement in view of uncertainty regarding the exact lens parameters. The beam radius in the spot size for the y-axis translates to a maximum spatial resolution of 1.9 mm according to a 10%-90% edge width criterion.

4.2.2. Imaging Results

A cuboid made of polystyrene with a metal knife blade and a hypodermic needle inside its protective casing was scanned. Polystyrene foam exhibits an absorption coefficient of less than 0.001 cm^{-1} at 1 THz and an almost constant refractive index of $n = 1.02$ in the THz band [152]. The resulting transparency makes it an ideal material for the visualization of embedded objects with THz CT. Figure 4.6(a) shows a picture of the objects, and Figure 4.6(b) shows corresponding results of the volume render after tomographic reconstruction [own7]. A total of 18 projections were acquired in 282 minutes with a 10° angle resolution and a 1 mm step size. The required 2D projection size to capture the whole object was 54 mm×68 mm, leading to a total scanning speed of 11.7 $\mathrm{mm}^3\,\mathrm{s}^{-1}$ when referred to the reconstructed volume. The bottleneck for the scanning time is the mechanical translation in the stepped movement. Due to its better image reconstruction quality for a limited set of projections, a reconstruction algorithm based on SART has been favored over the FBP. Figure 4.6(c) shows the 2D slices for all acquired heights synthesized with the SART algorithm of the ASTRA Tomography Toolbox [153] (360 iterations).

4.2.3. Discussion

The simple, low-cost THz CT setup is capable of visualizing the macroscopic structure of the embedded objects. It is noted that the hypodermic needle inside the plastic casing is, however, not resolved since the needle width (400 µm) is significantly smaller than the spatial resolution of the imaging setup. The results highlight that the image contrast is not solely defined by the absorption of the material but also by Fresnel losses. This leads to an information ambiguity between absorption, refraction, and reflection. The effect is most notably visible at the boundaries of the polystyrene foam in Figure 4.6(c). If the contrast would only rely on the material's absorption, one would expect a subtle but homogeneous signal for the foam. The reconstruction, however, depicts a contour caused by the Fresnel losses for large incident angles of the radiation at the foam boundary. The same reasoning can be given for the fact that the needle casing exhibits a similar image contrast at its boundaries as compared to the fully reflecting metal blade.

4.3. Summary and Conclusions

This chapter demonstrates the feasibility of low-cost THz CT imaging systems, relying only on compact silicon components. Using the 430 GHz source presented in Chapter 3 and a broadband SiGe HBT power detector [149], the 3D structure of an object comprising a knife blade and a packaged hypodermic needle embedded in polystyrene foam was successfully reconstructed. The THz CT system shows a dynamic range of 71.2 dB and an approximate spatial resolution of 1.9 mm. Contrary to this work, prior studies have mostly relied on expensive and bulky pulsed electro-optical components [138], [154], or on high-power Schottky-diode or backward-wave oscillator sources [133], [155]. As such, this study promises increased exploitation of THz CT systems in price-driven applications such as industrial quality control.

However, the required image acquisition time is undoubtedly too long to raise an interest in the practical adoption of this system at the current stage. The total acquisition time for the here presented scan exceeded four hours, whereas practical acquisition times should not exceed a few seconds. The bottleneck for the acquisition time is currently the stepped mechanical translation. In another study, we have shown that the acquisition time can be substantially reduced down to a few minutes with continuous object translation [own3]. Moreover, rapid THz CT volume acquisition within seconds has been readily demonstrated by 1D and 2D collimated beam object illumination with non-silicon high-power sources and concurrent detection with electro-optical crystals [154] or THz cameras [155]. The realization of such approaches with silicon components sets demanding requirements in

terms of source power, but it should be worth to conduct future research in this area in view of the ongoing advances in silicon THz source technology.

An additional arguable weakness of the presented system, but also THz CT systems in general, is the ambiguity regarding the image contrast. Losses due to reflection and refraction lead to severe image distortion, which limits the use of THz CT to objects with low permittivity. Other studies indicate that a combination of ray-tracing and iterative reconstruction methods could significantly mitigate these distortions [146]–[148]. However, an assessment of whether such methods can be reliably applied to THz systems remains the objective of future research.

The results presented in this part of the thesis underline the limitations of the far-field imaging systems in terms of spatial resolution. As detailed in Chapter 2, the diffraction-limited spatial resolution in the millimeter-range may be sufficient for imaging of macroscopic objects, but various applications, in particular biomedical applications, require a spatial resolution in the micrometer-range. The following part of the thesis explores the means to break the diffraction limit for microscopic THz imaging with silicon technology.

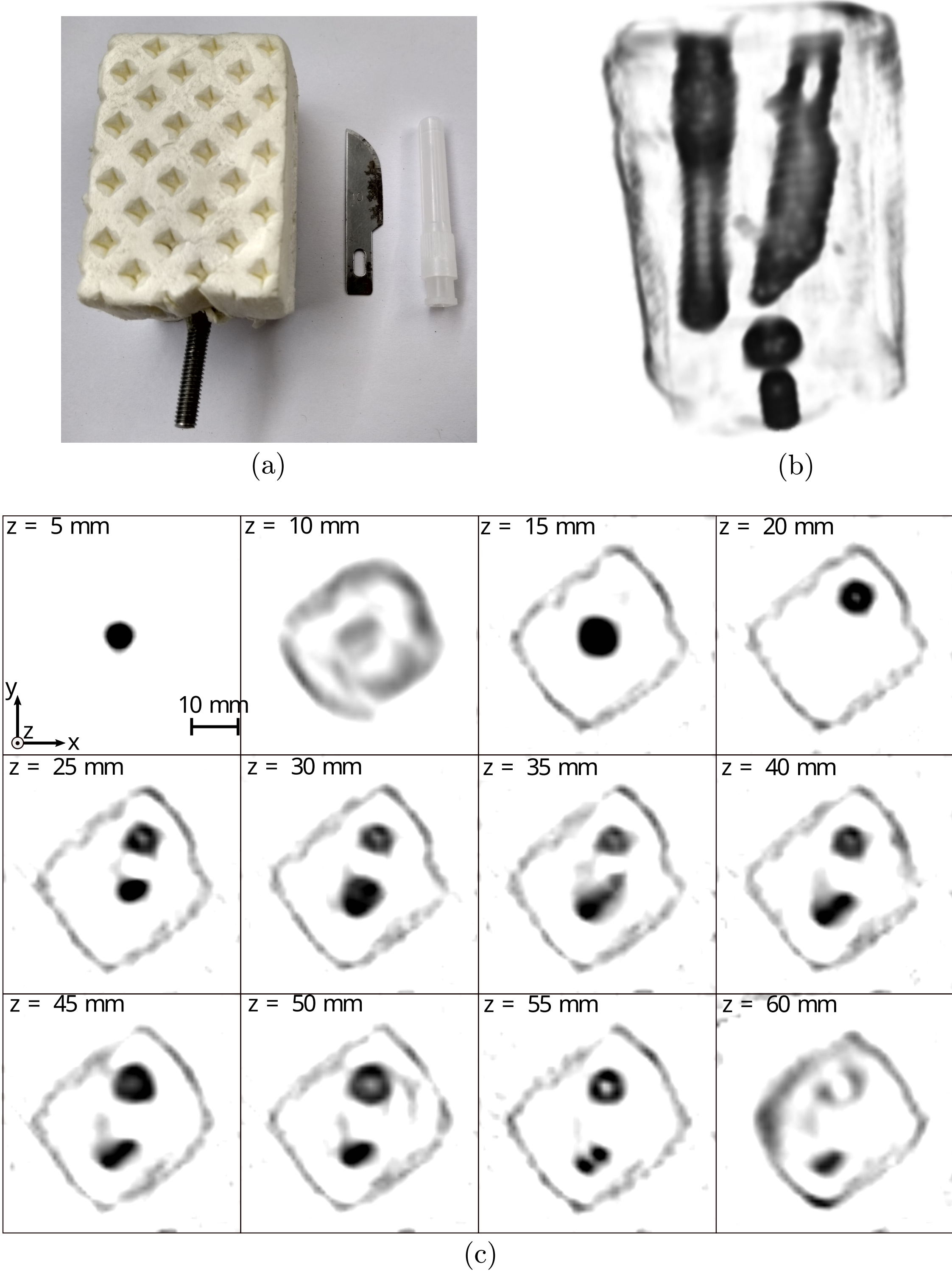

Figure 4.6.: CT-Imaging results for a knife blade and packaged hypodermic needle embedded in polystyrene foam. Picture showing the objects (a), 2D volume render after tomographic reconstruction with SART algorithm [144], [153] (b), and 2D slices in x-y-plane for different heights (z-values) (c). The data was acquired with 1 mm spatial and 10° angular steps. The acquisition time was 282 min. After [own7] © 2019 IEEE.

Part III.

Near-Field Imaging

Chapter 5

THz Near-Field Sensing in Silicon Technology

As elaborated in Section 2.2, THz near-fields interacting with micro- and nanoscale phenomenon show potential for a wide range of applications, most notably in the field of biomedical imaging. So far, these applications remain unexplored because of the low sensitivity, low integration level, and high cost, confining current THz near-field imaging methods, i.e., a-NSOM and s-NSOM, to the laboratory use. However, initial demonstrations of novel THz near-field imaging devices in modern nanoscale silicon technology have successfully cleared some of the bespoke bottlenecks for the practical adoption of THz near-field sensing by substantially increasing the integration level and sensitivity [15], [19][own11], [own12]. More particularly, related advances were enabled by cointegrating a SRR sub-wavelength near-field probe, a THz illumination source, and a THz detector on the same silicon die into a single sensing pixel. These studies were undertaken at our research group at the University of Wuppertal and remain the only demonstrations of single-pixel silicon-integrated THz near-field sensors to date. This chapter reviews this work and, thereby, provides the necessary context for the later chapters of this dissertation. The fundamental sensing principle and the architecture of integrated SRR-based sensors are presented, and prior studies are discussed in view of their performance, limitations, advantages, and drawbacks. In this context, it is noted that some of the results and figures presented here have been originally published in [own11], [own12], and [15], [19].

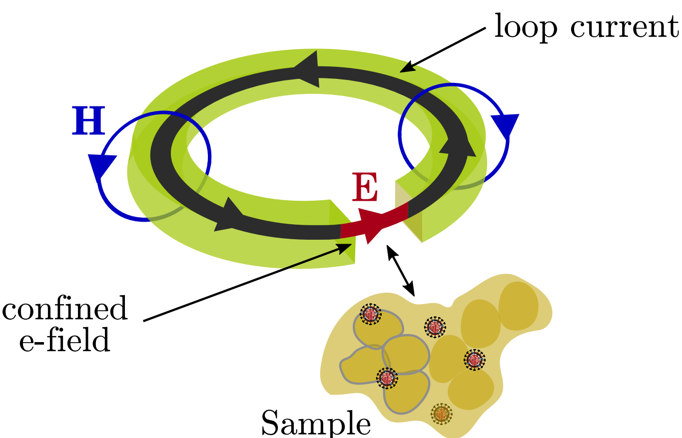

Figure 5.1.: Illustration of a near-field probe based on a SRR. After [own5] © 2018 IEEE.

5.1. Resonator-Based Sensing in Planar Technology

The common methods for electromagnetic material characterization with near-fields fall into one of two categories: non-resonant or resonant methods. The non-resonant methods deduce the material properties from impedance and phase velocity measurements in transmission or reflection setups. Here, the electromagnetic energy is directed towards a sample trough a transmission line, e.g., by microstrip lines, hollow waveguides, or coaxial lines [156]. Since the transmission line bandwidth dictates the total bandwidth, which is typically large, non-resonant methods are well suited for broadband material characterization. By contrast, the resonant methods generally are narrowband. They rely on the measurement of the reflection or transmission behavior of resonant structures that are loaded with a sample. The main advantage of resonant methods is that the rapid changes of the resonator impedance close to the resonance frequency can significantly enhance the accuracy and sensitivity as compared to the non-resonant methods. In view of the implementation challenges associated with building broadband integrated THz systems and the lack of strong spectral features of solids and liquids in the lower THz range (see Section 2.1.5), a resonance method has been favored in the initial studies on integrated THz near-field sensors [own11], [own12][15], [19].

The presented devices rely on resonance-enhanced sensing with SRRs as probes. In essence, a SRR is a simple metal ring with a gap, as depicted in Figure 5.1. The geometry shows an LC-resonance arising from the self-inductance (L) of the metal ring and the capacitance of the split-gap (C). The resonance frequency f_c is described by:

$$f_c = \frac{1}{2\pi\sqrt{LC}}. \tag{5.1}$$

If the SRR is appropriately illuminated at the resonance frequency, charges accumulated in

the ring ends lead to an electric-dipole-type field in the vicinity of the gap. The electric field cyclically exchanges energy with the magnetic fields caused by counteracting ring currents. When the gap spacing is selected to be significantly smaller than the excitation wavelength, the gap acts as a near-field generator with a capacitive and mostly non-radiating response, as detailed in Section 2.2.2. The near-field sensing mechanism based on the split-gap field can be intuitively explained as follows. If the electric field of the resonator is disturbed by a close-by object that increases the effective dielectric permittivity, the capacitance of the split-gap increases, thereby leading to a lower resonance frequency.

5.1.1. Perturbation Theory

A more general formulation of the resonance behavior of a SRR can be given based on the perturbation theory [157]–[159]. Although this theory was first developed for microwave resonant cavities [157], it should be stressed that it can be applied to any electromagnetic resonator, including SRRs [160]. As a consequence of Maxwell's curl equations, the normalized, object-induced change in resonance frequency is given as:

$$\frac{\Delta f}{f_c} = \frac{f_2 - f_c}{f_c} = -\frac{\iiint_V \left(\Delta\epsilon \boldsymbol{E}_2 \cdot \boldsymbol{E}_1^* + \Delta\mu \boldsymbol{H}_2 \cdot \boldsymbol{H}_1^*\right) dV}{\iiint_V \left(\epsilon \boldsymbol{E}_2 \cdot \boldsymbol{E}_1^* + \mu \boldsymbol{H}_2 \cdot \boldsymbol{H}_1^*\right) dV}, \tag{5.2}$$

where V is the perturbed volume, f_2 is the shifted resonance frequency, ϵ and μ are the permittivity and permeability without perturbation, $\Delta\epsilon$ and $\Delta\mu$ are the changes in permittivity and permeability. $\boldsymbol{E}_1$ and $\boldsymbol{H}_1$ represent the fields without perturbation, and $\boldsymbol{E}_2$ and $\boldsymbol{H}_2$ are the fields with perturbation. Although being exact, Equation 5.2 is not very useful since it is typically not possible to find closed-form expressions of the perturbed fields $\boldsymbol{E}_2$ and $\boldsymbol{H}_2$. However, if the perturbation is assumed to be small and the field distribution is assumed to be unchanged, then Equation 5.2 can be approximated as follows:

$$\frac{\Delta f}{f_c} = -\frac{\iiint_V \left(\Delta\epsilon |\boldsymbol{E}_1|^2 + \Delta\mu |\boldsymbol{H}_1|^2\right) dV}{\iiint_V \left(\epsilon |\boldsymbol{E}_1|^2 + \mu |\boldsymbol{H}_1|^2\right) dV}. \tag{5.3}$$

Because of the limited validity of the small perturbation assumption and because of the still required knowledge of the unperturbed fields ($\boldsymbol{E}_1$ and $\boldsymbol{H}_1$) in Equation 5.3, the use of the perturbation theory for analytical extraction of material properties is mostly restricted to special cases and simple geometries; although such extraction has been successfully demonstrated for various scenarios [161], [162]. In Section 6.1 it will be shown that the geometry of the resonator and dielectric in the split-gap vicinity is too complex for an analytical approach to be practical. However, the previously mentioned intuitive explanation of the SRR sensing mechanism finds itself in Equation 5.3. Assuming that there is no perturbation of the permeability ($\Delta\mu = 0$) and noting that in resonance the time average

of the energy stored in the resonator is two times the energy stored in the electric field, Equation 5.3 can be furthermore simplified [159]:

$$\frac{\Delta f}{f_c} \approx -\frac{\iiint_V \Delta\epsilon |\boldsymbol{E}_1|^2 dV}{2\iiint_V \epsilon |\boldsymbol{E}_1|^2 dV}, \tag{5.4}$$

thereby indicating that if the effective permittivity of the volume of the resonance structure increases ($\iiint_V \Delta\epsilon \cdot dV > 0$), the resonance frequency decreases.

5.1.2. Planar SRRs for Imaging

The results from the perturbation theory have important implications on the objective to use SRRs as THz imaging devices. Equation 5.2 highlights that any perturbation of the electric or magnetic field of the SRR leads to a change in resonance frequency. Hence, to operate as an imaging device with well-behaved spatial sampling properties, the field-object interaction should be confined to a localized volume, i.e., the electrical field of the split-gap.

This is a challenging requirement for SRRs that are implemented in a planar technology, and it is the reason why most previous studies on THz sensing with SRRs were limited to bulk material characterization rather than imaging. More particularly, the interaction of near-fields generated by SRR-based metamaterials with objects nearby has been demonstrated for permittivity and thickness sensors in the THz frequency band [163], [164]. Since such sensors rely on transmission minimum measurements, they favor very high resonance frequency shifts per refractive index unit (RIU). Consequently, thin low-permittivity substrates are used as resonator carriers to maximize the electric flux available for interaction with the object above the substrate [165]. Figure 5.2 illustrates the related problem. A planar resonator geometry on an electrically thin substrate carrier exposes reactive near-fields of different types to the sensing surface along its geometry. Asides from the electric field of the split gap, such fields may include the magnetic fields of the ring and other parasitic electric fringing fields. These fields can interact with an imaging sample placed on top, potentially resulting in an adverse sample-position dependent sensor response, ambiguous spatial sampling behavior, and a spatial resolution that is mostly limited to footprint of the whole SRR [19].

In principle, planar technology offers two options to mitigate this problem. One solution is exposing the split-gap field to the edge of the chip instead of the top surface, as shown in Figure 5.3(a). As such, a study using edge sensors on Rogers RT/Duroid laminates successfully demonstrated super-resolution imaging for planar SRR probes at around 6.5 GHz with a lateral resolution of 0.7 mm [166]. Given the present aim of sensor integration into

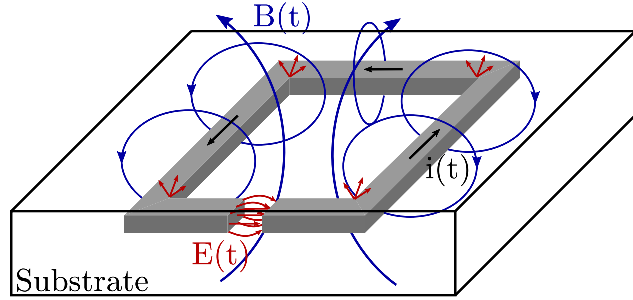

Figure 5.2.: Illustration of the near-fields of a SRR-based surface sensor in a planar technology.

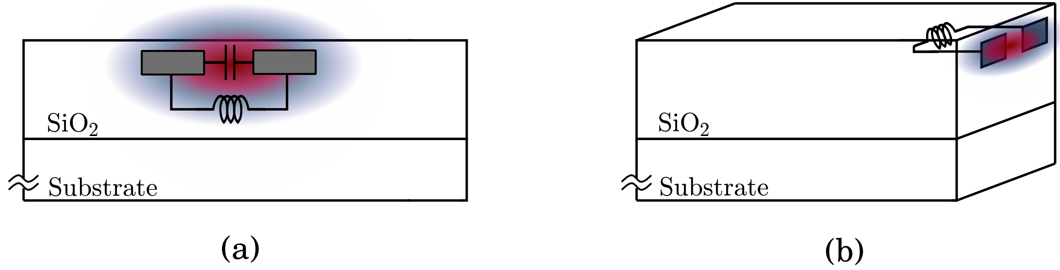

Figure 5.3.: Simplified illustration of the two fundamental sensing topologies for SRR-based near-field sensors in planar technology. The surface sensor exposes a sensing volume to the chip top surface (a) and the edge sensor to the chip edge (b).

silicon technology and achieving spatial resolutions in the μm-range, edge sensors are difficult to apply because the thickness of the dielectric at the chip edge needs to be both accurately controlled and extremely thin. Consequently, costly post-processing of the chip in the form of micro-machining is required.

The other solution is illustrated in Figure 5.3(b). Here a SRR near-field probe that exploits the multi-layer BEOL of a silicon technology is used to build a 3D SRR geometry that limits the surface field exposure to the electric field of the split gap. This implementation was favored for the THz near-field probes shown in [own11], [own12] and [15], [19] because of the ease of fabrication and its potential to scale to 2D arrays. A detailed discussion on related challenges and implementation aspects of the 3D SRR geometry follows in Section 5.3.

5.2. Incoherent Sensing Concept

As outlined in Section 5.1, SRR-based near-field sensors rely on the measurement of the resonant frequency shift induced by objects that are placed in the sensing volume of

the resonator. However, the typically employed methods to detect frequency shifts are not effectively applicable in integrated circuits at THz frequencies but are limited to microwave and mmWave frequencies where the appropriate circuit complexity can be provided by the fastest technology nodes. More particularly, one commonly applied method relies on operating the resonator in transmission-mode and measuring the stopband minimum of the resonator's insertion loss with spectrum analysis [167], [168]. However, unlike as in the lower frequency regions, the transmission minima for THz-SRRs are only poorly defined since high losses of on-chip inductors and transmission lines deteriorate the quality factor of the resonator. Furthermore, spectrum analysis at THz frequencies requires the on-chip integration of a broadband heterodyne two-port system. Such systems typically employ frequency multiplier chains which are not applicable for large-scale array integration since they exhibit excessive power and area consumption [18].

Another method that is more suitable for multi-pixel integration is the direct detection of an oscillation frequency shift induced by the loading of an LC-oscillator tank. Related works have demonstrated low-complexity sensing circuitry and multi-pixel integration based on frequency divider chains in the mm-Wave band [169]–[171]. Unfortunately, neither silicon-based fundamental oscillators nor frequency dividers are yet available at THz frequencies.

In this section, an alternative incoherent sensing concept relying on the measurement of the power transmission modulation through a loaded SRR is discussed. The idea prioritizes implementation simplicity, allowing for a small sensor footprint and scalable circuit architectures while simultaneously providing appropriate sensitivity at THz frequencies.

5.2.1. Concept Description

Contrary to measuring the resonance frequency itself, the frequency shift is translated to the measurement of the temporal power transmission change of a bandstop filter at a fixed frequency. The bandstop characteristic is realized by loading a transmission line (host line) with a SRR. Figure 5.4(a) depicts the block diagram of the related sensor architecture, and Figure 5.4(b) illustrates the operation principle. An on-chip free-running voltage-controlled oscillator (VCO) oscillator illuminates the SRR with a THz wave of frequency f_o, which is typically chosen to be just above the SRR resonant frequency f_c. A broadband THz power detector with a voltage response V_o proportional to the incident power P_i is then used to measure the transmitted power through the bandstop filter. If an imaging object with non-unity relative permittivity is brought into direct vicinity so that it interacts with the electric flux of the SRR, capacitive coupling leads to a reduction in the SRR

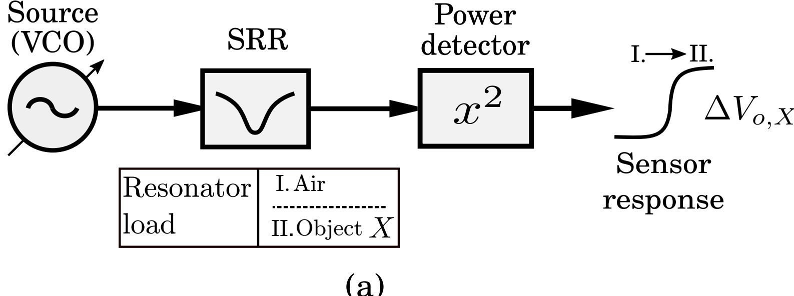

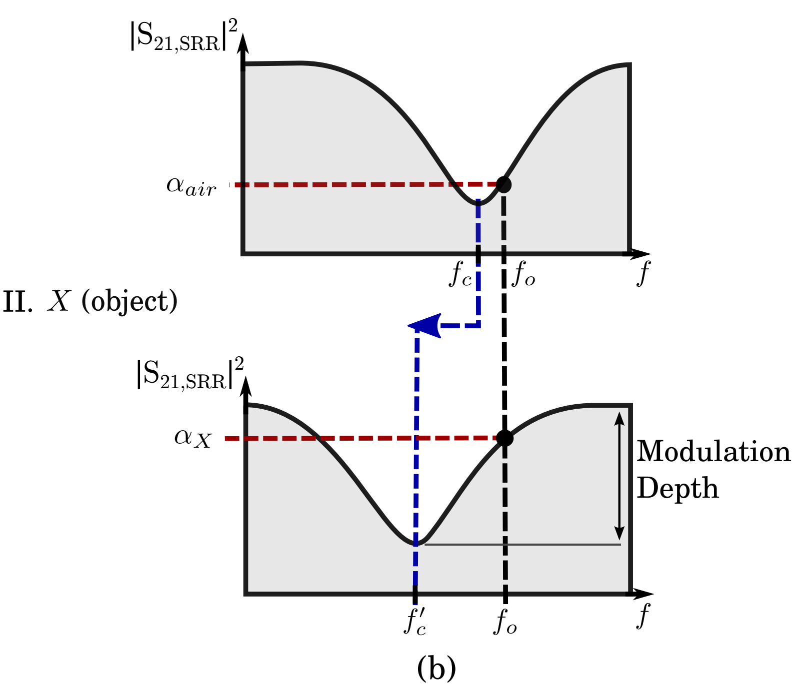

Figure 5.4.: Incoherent near-field sensor. Block diagram (a) and illustration of the sensor operation principle (b). After [own5] © 2018 IEEE.

resonance frequency to f_c'. The loaded SRR thus exhibits a monotonously decreasing resonance frequency for objects with increasing relative permittivity. As a consequence, the SRR transmission coefficient α at frequency f_o is increased. The change in transmitted power compared to a non-loaded reference can be measured at the power detector with a difference measurement.

The resulting difference signal ΔV_o is hereafter termed as the sensor response, which can be expressed as a function of the source, detector, and resonator characteristics. It is assumed that α_X is the SRR power transmission factor ($|S_{21}|^2$) at f_o when object X is placed in the sensing volume of the SRR. The factor α_X, thereby, depends on the complex permittivity of object X. If P_{osc} is the power emitted by the oscillator and R_V is the detector voltage

responsivity, then $\Delta V_{o,X}$ for the object X can be written as:

$$\Delta V_{o,X} = P_{osc}(\alpha_X - \alpha_{noObj})R_V. \tag{5.5}$$

Here, α_{noObj} is the SRR power transmission factor in the absence of any object other than air ($\epsilon_r \approx 1$). Note that since $f_o > f_c$, a reduction in f_c in the presence of an object X would lead to an increased power transmission at f_o.

The described sensing concept translates the sensor response from the frequency domain to the amplitude domain. This entails several considerations regarding the response formation:

- The sensor response does not only depend on the sensitivity in terms of resonance shift per RIU but also on the depth and slope of the bandstop notch. Hence, a high modulation depth needs to be achieved (see Figure 5.4). Along with the source output power, the detector responsivity, and inherent noise contributions, this determines the SNR of the sensor.

- A change in the resonator quality factor, which may be caused by loading the SRR with a lossy medium, causes a change in transmitted power. Consequently, the sensor is prone to response ambiguity between the real and imaginary part of the object's permittivity. Chapter 6 discusses this topic in more detail.

- The dependency on both frequency shift and quality factor implies the necessity of careful electromagnetic design of the SRR to ascertain that the sensor is sensitive for a large range of materials. The sensor response should change gradually with varying permittivity of the objects, reaching saturation for metals ($\epsilon_r \approx \infty$). This is achieved by a well-tailored relationship between resonance shift per RIU and the quality factor of the SRR. A higher quality factor implies a higher sensitivity for a smaller range of measurable permittivity values and vice versa.

5.2.2. Sensor Illumination

Figure 5.5(a) depicts the schematic of a single-ended sensor, showing the SRR-loaded host line at the output of an oscillator. Suppression of the power transmission occurs because the SRR-loaded transmission line shows high impedance at resonance, thereby reflecting the THz wave to the source. To exhibit a transmission zero, the host line and the SRR should be properly aligned with respect to their respective electromagnetic symmetry planes [172]. As it will be detailed in Chapter 6, a transmission line symmetrically loaded

with two SRRs that are oriented orthogonal to the host line axis gives rise to strong single-mode magnetic coupling with aligned magnetic symmetry planes that can be conveniently utilized in planar technology.

Another central aspect of the sensor illumination is the choice and design of the illumination source. The reduced complexity required for the illumination source is a key advantage of the incoherent sensing scheme. As discussed in Chapter 3, compact, high-power on-chip THz sources can be integrated by utilizing free-running fundamental oscillators that operate close to the integration limits in terms of frequency, and harmonic extraction can be used to generate power beyond f_{max}. A few specific requirements for the oscillator design arise in the context of near-field sensing and the incoherent sensing scheme:

1. Similar to the requirement of confinement of the SRR fields detailed in Section 5.1, the oscillator should not be sensitive to objects placed on the top surface of the chip. It is noted that this sensitivity is not only related to the oscillator output power but also to the oscillation frequency since any shift in oscillation frequency is also translated to a change in received power level at the detector.

2. The oscillation frequency should be insensitive to changes in the load impedance so that the power modulation is uniquely caused by the object-induced shift of the SRR resonance frequency.

3. A very high oscillation frequency is required. Although the achievable spatial resolution is not dependent on the frequency but rather on the geometry of the SRR, a high excitation frequency allows using SRRs with a low total footprint, which is crucial for dense multi-pixel sensor integration.

Colpitts triple-push oscillators (TPOs) in CC topology are applied as illumination sources [own11], [own12], [15], [19], which allows harmonic upconversion of the fundamental oscillation frequency, $f_{osc}/3$, with a compact form factor. Figure 5.5(a) shows the simplified schematic of a TPO, and Figure 5.5(b) shows the corresponding phase diagram for output branch currents at the fundamental oscillation frequency and at the third harmonic. The oscillator comprises three individual CC Colpitts oscillators in a star connection with a negative resistance implemented by an emitter capacitance C_e in series feedback. The oscillation frequency is set by the series resonant tank formed by TL_b, the base-emitter junction capacitance, and C_e. To address the first requirements in the aforementioned list, all inductances are implemented with striplines, thereby shielding all electromagnetic fields of the oscillator from the chip top surface. The second and third requirements in the list are fulfilled inherently by the operation principle of the TPO. If the common output

node is loaded sufficiently to suppress fundamental oscillation in the common-mode, a progressive phase shift of 120° is established between the oscillator branches [173]. Hence, the fundamental output current superimposes nondestructively, and the third harmonic current generated in the strongly driven base-emitter junction of the SiGe-HBTs superimposes constructively at the star node. The star node furthermore embodies an AC-ground at the fundamental oscillation frequency, thus preventing any oscillator pulling at the fundamental caused by the strongly varying reflection coefficient of the SRR.

It is noted that the requirement for isolation of the fundamental oscillation with respect to the SRR resonance behavior could be similarly achieved with any N-push topology because all these circuits exhibit an AC-ground at the common node. However, so far, the TPO has been favored because it shows a good compromise between achievable oscillation frequency (above 500 GHz) and available output power level (several tens of µW) for near-field sensing.

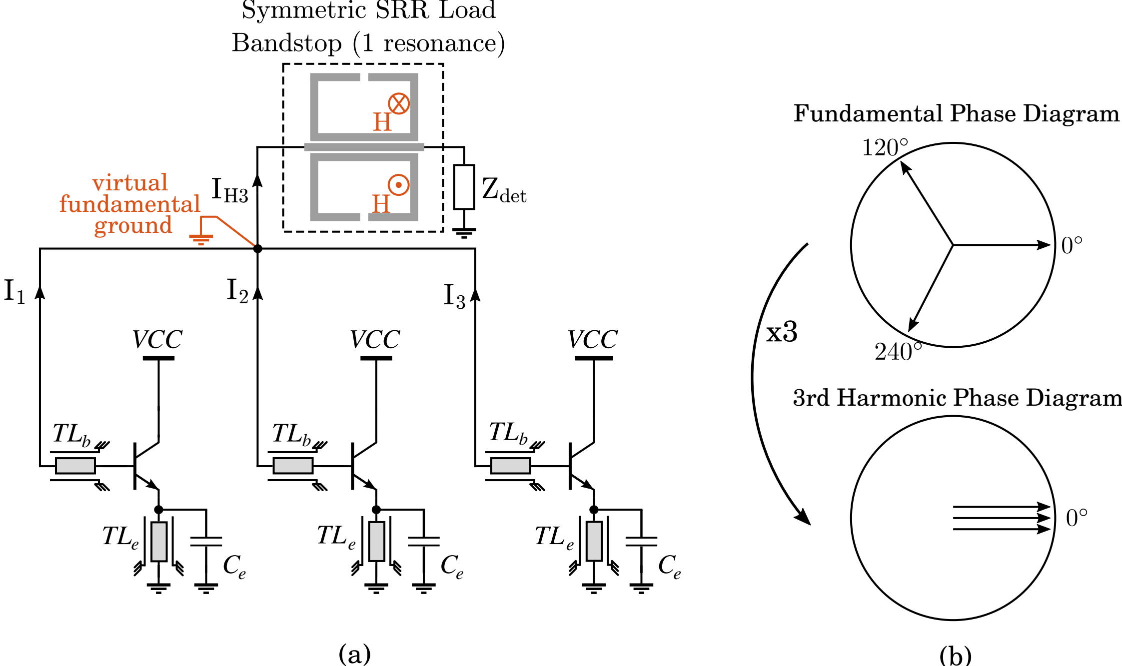

Figure 5.5.: Sensor illumination with Colpitts triple-push oscillators. Simplified sensor schematic (a) and phase relationships for the three oscillator cores at the fundamental oscillation frequency and at the third harmonic (b). Phases superimpose deconstructively and constructively at the fundamental and at the third harmonic, respectively.

5.2.3. Power Detection

The incoherent operating scheme facilitates direct downconversion of the THz wave transmitted through the resonance structure to DC by means of a broadband power detector. For this purpose, the non-linearity of the base-emitter junction of high-speed SiGe-HBT devices has been exploited in all prior studies. SiGe-HBT devices have been favored over MOSFET power detectors as they exhibit significantly lower input impedance, thereby facilitating detector integration without a dedicated tuned frequency-selective structure for matching. Hence, SiGe-HBT detectors provide a more robust near-field sensor design procedure, which relies on the precise frequency alignment of the resonator stopband with the limited tuning range of the oscillator source.

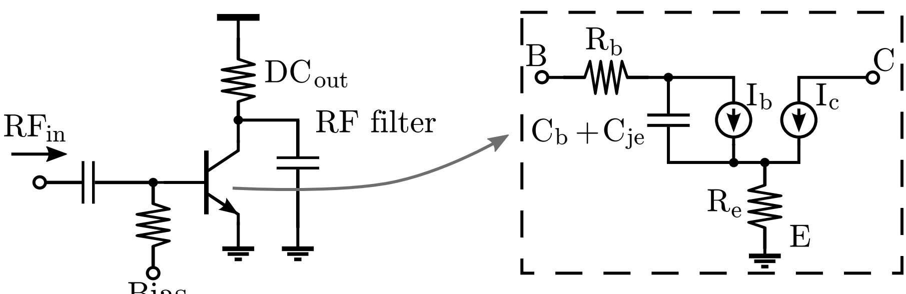

Figure 5.6.: Schematic of a common-emitter SiGe-HBT power detector with equivalent circuit of the transistor.

A SiGe-HBT power detector circuit can be implemented with a single device in common-emitter topology, as shown in Figure 5.6. Contrary to traditional diode-connected rectifiers, the transistor is operated as a 3-terminal device with a disconnected collector and base. This minimizes the parasitic leakage of the THz wave to the substrate through the large collector-substrate capacitance and improves isolation between the RF input and the DC output [19], [120]. To furthermore mitigate the unintended nonlinearities, the RF signals coupling through the base-collector capacitance is suppressed with an RF filter at the collector node, which is designed to provide an AC-ground at the collector.

The nonlinear frequency-dependent response of such a SiGe-HBT detector in forward active region can be analyzed by Volterra series expansion [174]. In the second-order approximation, the output DC-current based on the high-frequency equivalent circuit depicted in Figure 5.6 (C_{bc} is omitted) can be calculated as follows:

$$I_{dc} = \frac{V_{be}^2}{V_t \left[(1 + g_m R_e)^2 + R^2 \omega^2 \left(\frac{g_m}{\omega_t} + C_{je} \right)^2 \right]} \cdot \frac{g_m}{1 + g_m R_e}, \tag{5.6}$$

where $R = R_e + R_b$, R_b is the base resistance, R_e is the emitter resistance, V_{be} is the base-emitter input voltage, g_m is the transconductance, C_{je} is the base-emitter junction capacitance, and ω_t is the small-signal current unity-gain cut-off angular frequency. Notably, V_{be}^2 is proportional to the input power via Ohm's law. Here, the proportionality factor is the frequency-dependent current responsivity R_I of the detector, which drops with 20 dB/dec at high frequencies [175].

Detector Noise

The detector noise contribution in the incoherent sensing scheme is of primary concern for sensitive sensor operation. More particularly, the direct down-conversion of the THz wave to DC requires the detector low-frequency noise to be taken into account. The physical origins of low-frequency noise in contemporary high-speed SiGe-HBT transistors can be diverse, and they are strongly dependent on the bias conditions. On the one hand, the collector current shot noise resulting from discrete majority carrier flow through the base-emitter junction dominates the white (flat) noise spectrum of the intrinsic transistor. On the other hand, the noise of high-speed SiGe-HBT can be seriously penalized at low frequencies due to 1/f noise and generation-recombination (GR) noise caused by defects in the semiconductor layers. Here, the origin of the 1/f-noise are fluctuations in conductivity related to both mobility and number of carriers [176], and the GR noise is due to carrier trapping-detrapping process among energy states [177], [178]. These random nanoscopic effects are particularly pronounced for deeply scaled high-speed devices with low emitter area and perimeter [178]. Hence, low-frequency noise is a serious concern in the incoherent sensing scheme, which favors minimum-size devices for best current responsivity.

Figure 5.7 exemplary shows the measured noise output voltage for a minimum-size detector device in IHP's high-speed 0.13 µm BiCMOS SiGe-HBT technology [179]. A detector bias of V_{be} =0.815 V was selected to yield optimum responsivity, and the device was biased in the forward active region [19]. The previously detailed low-frequency noise is present at frequencies below around 100 kHz, and it can be orders of magnitude higher than the white noise floor of the detector. More particularly, the plateau visible between 1 kHz–10 kHz is untypical for 1/f-noise and thus indicates that GR-noise is the main noise contributor in this frequency range.

Given the described incoherent sensor operation concept, it is therefore desirable to mitigate low-frequency noise contributions by operating with a chopped oscillator signal. Figure 5.8 qualitatively illustrates the power spectral density at the detector output for a CW and a chopped oscillator signal. If the oscillator is periodically turned on and off with a

frequency higher than the low-frequency noise corner frequency, the resultant square-wave signal can subsequently be read out with a higher SNR as compared to the CW operation using lock-in detection.

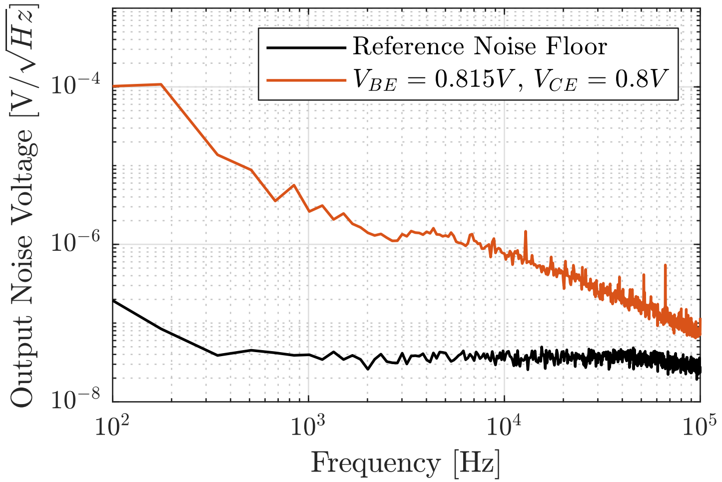

Figure 5.7.: Spectral density of the measured noise output voltage for a minimum-size detector device in IHP's high-speed 0.13 µm BiCMOS SiGe-HBT technoloy [179]. The device is loaded with loaded with a 17 kΩ resistor. After [19].

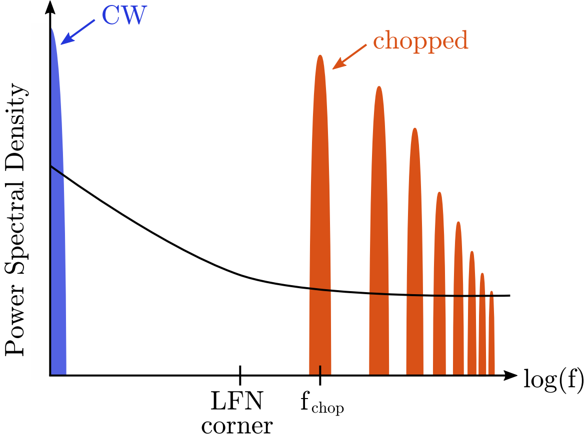

Figure 5.8.: Qualitative illustration of the detector output power spectral density over frequency for a CW and square-wave modulated (chopped) oscillator signal. Chopping leads to a rectangular output signal, which is a superposition of odd harmonics in frequency domain.

5.2.4. Figure-of-Merits

This section discusses the key figures-of-merits of the incoherent sensing scheme and how to interpret them in view of near-field imaging applications.

Sensitivity

The sensor sensitivity is defined as the minimum detectable change in power transmission. For this metric to be meaningful for practical applications, it should be linked to the intended contrast mechanism. As it will be detailed in Section 6, SRR-based near-field sensors respond strongly to both the dielectric permittivity of the object and the spatial displacement of the object. For material characterization, the sensor sensitivity defined as the minimum detectable change in dielectric permittivity is a key parameter. As it will be detailed in Chapter 6, the power transmission through the SRR is sensitive to both the real part ϵ_r' and the imaginary part ϵ_r'' of the relative permittivity, and thus it can also be defined for both.

For small changes in relative permittivity, the relationship between SRR power transmission factor α and ϵ_r can be linearly approximated at the excitation frequency. Thereby, the minimum detectable change in relative permittivity, $\Delta\epsilon_{r,min}$, can be defined as:

$$\Delta\epsilon_{r,min} = \frac{V_{n,int}}{P_{osc} \cdot R_V \frac{\partial\alpha}{\partial\epsilon_r}}, \tag{5.7}$$

where $V_{n,int}$ is the total voltage noise integrated over the sensor read-out bandwidth f_{RBW}. It is important to note that the power transmission sensitivity factor $\frac{\partial\alpha}{\partial\epsilon_r}$ is dependent on the slope of the stopband notch at the excitation frequency and specific resonator frequency shift per RIU for a certain dielectric loading. The sensitivity is thus always required to be put in relation to the excitation and loading conditions. On another note, Equation 5.7 assumes CW illumination and should be modified with an added prefactor in the denominator to account for the different amplitudes of the square-wave Fourier decomposition if the sensor is operated in a chopped operation mode.

Dynamic Range

In accordance with other electronic systems for imaging, a DR can be defined, which describes the fundamental image contrast limit of the sensor. DR is defined as the maximum response $\Delta V_{o,max}$ divided by the total noise at the detector output. Since the maximum α value is obtained for a perfect electrical conductor (PEC) object, the maximum measurable ΔV_o at the sensor is given as:

$$\Delta V_{o,max} = P_{osc} R_V (\alpha_{PEC} - \alpha_{noObj}). \tag{5.8}$$

Therefore, the DR of the sensor is:

$$\begin{aligned} \mathrm{DR}_{[\mathrm{dB}]} &= 20\log_{10}\left(\frac{\Delta V_{o,max}}{\Delta V_{o,min}}\right) \\ &= 20\log_{10}\left(\frac{P_{osc}R_V(\alpha_{PEC}-\alpha_{noObj})}{V_{n,int}}\right). \end{aligned} \tag{5.9}$$

5.3. Single-Pixel THz Near-Field Sensors

The aforementioned SRR-based incoherent sensing concept has been applied to build various types of single-pixel THz near-field imaging devices. The studies include CW and chopped single-ended sensors [19][own12], and a CW differential sensor [15]. Table 5.1 lists the key design aspects, performance metrics, and shows the micrographs of the sensors. All sensors operate around 550 GHz and show lateral resolutions in the range of 10 µm. The sensors presented in [19] and [own12] use the same TPO and SRR, but a chopping technique enabled a significant improvement of the DR from 42 dB to a maximum of 115 dB in a 1 Hz noise integration bandwidth, respectively. In general, the single-ended and differential sensors show similar performance metrics. Since one of the key contributions of this thesis is the demonstration of a multi-pixel sensing SoC based on the single-ended sensor (Chapter 7), this section briefly summarizes important aspects of the related SRR design. The reader is referred to [19] for a more detailed discussion and the characterization of the whole sensor.

5.3.1. Cross-Bridged Double Split-Ring Resonator

As highlighted in Section 5.1.2, to operate as a super-resolution imaging device, the exposed fields of the SRR are required to be highly confined to an electrically small area with high electric flux density. The sensor response needs to be spatially monotonous, and all fields related to the illumination and detection paths and the electromagnetic fields of the resonator outside of the sensing volume need to be enclosed in the substrate to avoid parasitic object interactions.

Hence, a 3D resonator topology exploiting the multilayer BEOL stack of a high-speed SiGe-HBT technology was used to spatially engineer the exposed fields [19][own12]. Figure 5.9 shows the BEOL stack of the 0.13 µm SiGe BiCMOS technology. It exhibits seven aluminum layers, including two thick top metal layers embedded in 15.3 µm thick silicon dioxide on top of a 50 Ω·cm silicon substrate. The chip top surface is furthermore covered

Table 5.1.: State-of-the-art Integrated Single-Pixel THz Near-Field Sensors

Reference	[19]	[own13]	[15][own11]
Micrograph			
Technology	0.13 µm SiGe-HBT	0.13 µm SiGe-HBT	0.13 µm SiGe-HBT
Operation Mode	single-ended, continuous wave	single-ended, chopped	differential, continuous wave
SRR Topology	3-D cross-bridged double SRR	3-D cross-bridged double SRR	3-D SRR
Operating Frequency	534 GHz–562 GHz	532 GHz–562 GHz	533 GHz–555 GHz
Resolution	10 µm–12 µm	10 µm–12 µm	8 µm–10 µm
Dynamic Range	42 dB[1]	115 dB[2]	40 dB[1]
Power Consumption	48 mW	24 mW	112 mW

[1] Estimated from the image in Fig. 19 in [19]. Noise integration bandwidth is unknown.
[2] Referenced to a 1 Hz noise integration bandwidth.
[3] Estimated from the image in Fig. 24a) in [15]. Noise integration bandwidth is unknown.

with a 600 nm thick silicon-nitride passivation. The fundamental idea behind 3D SRR integration is to vertically separate the split-gap from the rest of the resonator and a buried transmission line that couples to the SRR. This can be realized by placing the sensing layer in the topmost metal layer (TM2) and the rest of the resonator and the host line in lower metal layers (M5-TM1).

Figure 5.10 shows the whole coupled SRR structure for near-field imaging at around 550 GHz. The key resonator parameters such as modulation depth, quality factor, spatial resolution, and resonance frequency shift per RIU are complexly dependent on the resonator topology, leading to various implementation challenges. In this regard, a brief discussion of the 3D topology is given as follows.

Resonator Topology

The resonator comprises two parallel SRRs, which are magnetically coupled to a TM1 host line. The two SRRs are 'cross-bridged', meaning that their respective open ring ends are connected in TM2 in the magnetic symmetry plane, thereby forming a shared split-gap without changing the current distribution in the individual rings. This split-gap is realized in the form of two electrically short (15 µm) and closely spaced (3 µm) 4.5 µm-wide parallel strips, which are differentially driven with antiparallel currents by the magnetic excitation to support the generation of an electric-dipole type sensing field. The geometry of the sensing strips defines the spatial resolution of the sensor and is limited in its spatial

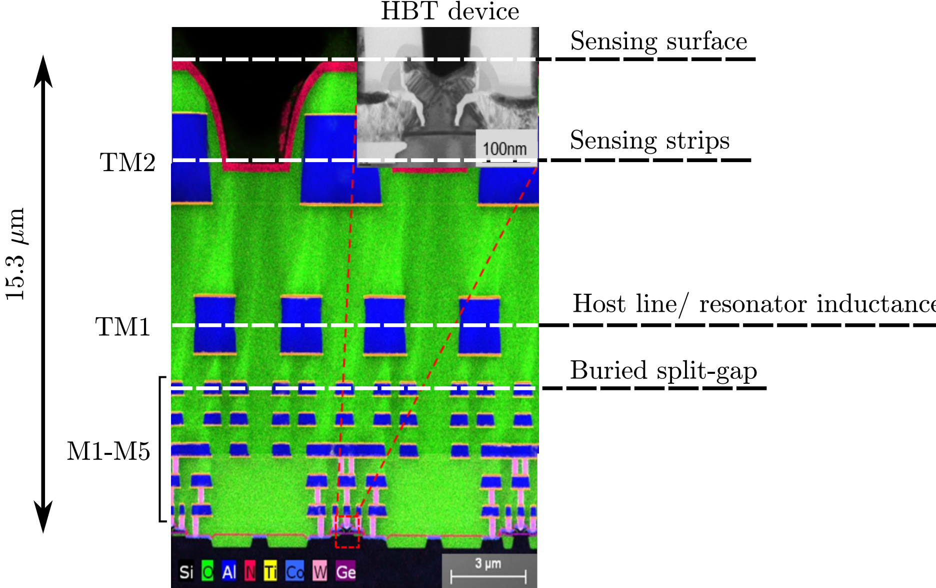

Figure 5.9.: Multi-layer (7-AL) 15.3 µm-thick BEOL-stack of IHP's SG13G2 0.13 µm SiGe-BICMOS technology. The vertical allocations of the SRR elements are indicated. By courtesy of Bernd Heinemann, IHP GmbH, Germany.

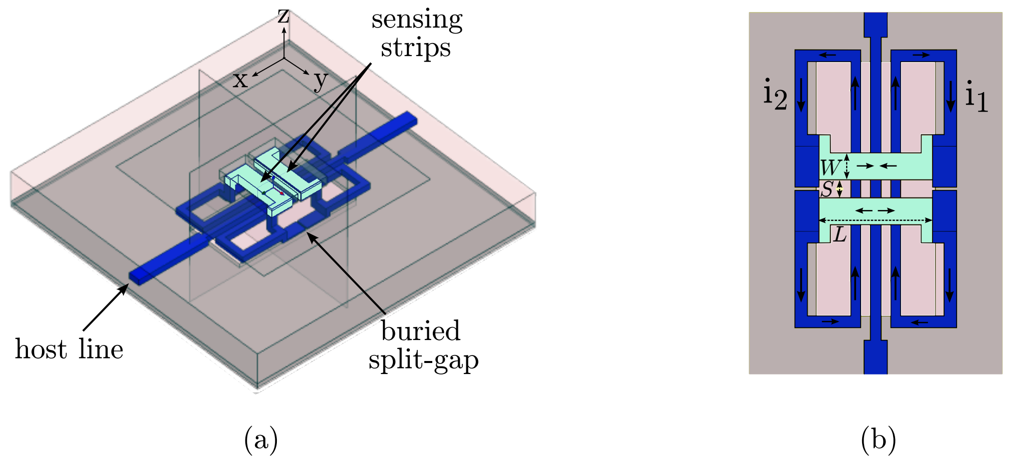

Figure 5.10.: On-chip 3D SRR integrated into a multi-layer BEOL-stack [19]. 3D view (a) and top view (b). The resonator dimensions are: W = 4.5 µm, S = 3 µm, L = 15 µm. After [own5] © 2018 IEEE.

dimensions by the design rules of the technology. It is noted that the sensing strips in TM2 are furthermore covered by a 2 µm thick dielectric layer, which limits the minimum object-to-sensor distance and serves as a protection layer. The rest of the SRR is located in the lower metal layers. In addition to the sensing strips, a deeply buried split-gap (M5) adds to the total capacitance to reduce the footprint of the SRR. The resonator wires comprise two components. First, lines parallel to the host line provide the coupling mechanism through magnetic induction. To increase the coupling strength, the ground shield is patterned underneath these lines. Secondly, TM1 microstrip lines are used to close the ring. Chapter 6 provides a detailed discussion of the means to model this resonator structure.

Simulations of the Electric Field

To analyze the electric field distribution in the sensing volume and the perturbation of these fields when objects are placed in the sensing volume, the 3D SRR was simulated in full-wave electromagnetic simulations (Ansys HFSS). The BEOL-stack was build according to the technology specification, whereas the metal lines were assumed the be made out of aluminum, and the BEOL dielectric was assumed to be made of lossless SiO_2 with a homogeneous relative permittivity of 4.1. As depicted in Figure 5.9, the BEOL top surface of this technology is not chemical-mechanical planarized, thus giving a finite degree of planarization. Most importantly, the specific BEOL topology leads to an air gap located between the sensing strips. Since this is the volume with the highest electric flux density, the BEOL topology has a major influence on the field distribution. Furthermore, its exact topology is difficult to predict for small metal spacings that approach the minimum design rules as it is the case here. In the simulations, the BEOL structure was approximated to be trapezoidal, which yielded the best fit between measurements and simulations [19].

Figure 5.11(a) shows the simulated E-field magnitude on the top sensing surface of the resonator at the nominal resonance frequency of 535 GHz [19], and Figure 5.11(b) shows the total E-fields for the resonator cross-section along the center microstrip host line for various object loads. The objects were modeled as lossless dielectrics and PEC cubes of dimensions 30 µm×30 µm×30 µm and were placed in direct contact with the chip top surface. The amplitudes are calculated for a 1-W reference excitation power. The simulation results in Figure 5.11(a) clearly show the electric-dipole field distribution, with the field in between the strips being predominantly tangential (Ex) to the surface and normal components rising on the top surface (Ez). Moreover, the area of significant field magnitude is limited to the vicinity of the sensing strips, which is the key property to

achieve high spatial resolution. The simulation furthermore highlights the axial symmetry in both vertical and horizontal orientations, which is an essential feature for imaging. As to the field perturbation due to object loading (Figure 5.11(b)), it is visible that the field confinement between the sensing strips and the object surface grows with the sample dielectric permittivity and is highest for the PEC object. This is the underlying effect causing an increased total capacitance in the sensing region.

Simulation of the Sensor Response

Figure 5.12(a) shows the simulated sensor power transmission coefficient. The quality factor of the transmission stopband is five, and the modulation depth is 14.4 dB. Confirming the assertions mentioned in Section 5.2.4, the change rate of resonant shift per RIU is not constant but reduces with increasing dielectric permittivity. Hence, the power transmission to both metallic objects and lossless dielectrics with dielectric permittivity varying from 1 to infinity can be mapped with compression into a monotonic image contrast. This becomes more apparent if the power transmission for the different objects is referenced to the case with no object loading, as shown in Figure 5.12(b). It can be seen that the image contrast is frequency-dependent with a maximum power response of 0.58 appearing for PEC slightly above the resonance frequency at 540 GHz. In view of the remarks in Section 5.2.4, this choice in excitation frequency maximizes the DR but not the sensitivity of the sensor. For the highest sensitivity, the frequency has to be aligned with the steepest slope rate.

5.3.2. On Imaging and Practicability

Although the integrated single-pixel THz near-field sensors offer improvements in DR and system cost as compared to the traditional THz near-field techniques, there remain major challenges for practical applications. The planar integration with the sensing field exposed to the chip top surface restricts the material types to be imaged. In particular, solid objects are required to be exceptionally smooth so that a constant probe-to-object distance can be held without the object crashing into the chip surroundings. This restriction is not present for the NSOM techniques using pointed probes such as scattering tips or tapered apertures, where the probe-to-object distance can be controlled with the methods used in traditional nanoscopy, e.g., laser deflection in contact-mode or force feedback in non-contact-mode [180].

Combined with the requirement for prolonged raster scans, the imaging and material characterization experiments with integrated single-pixel THz near-field sensors have been

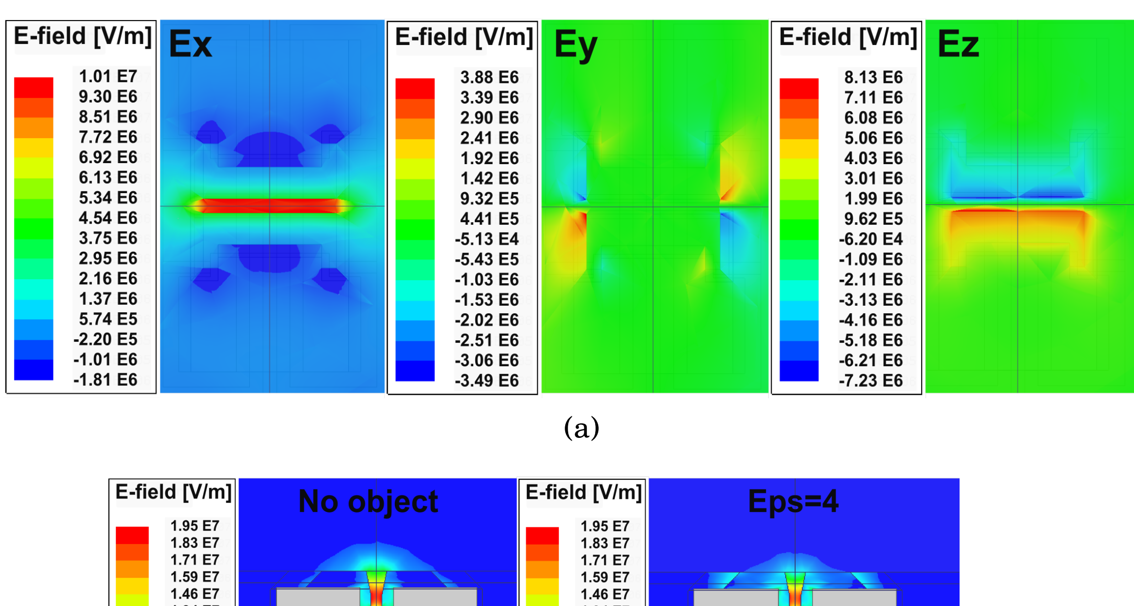

(a)

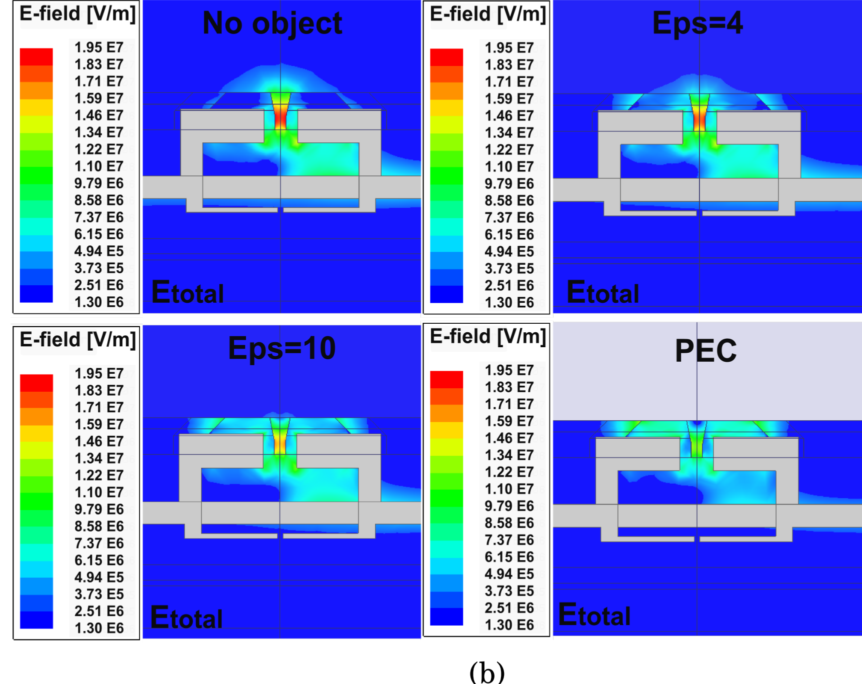

(b)

Figure 5.11.: Simulated E-field maps in the resonator at 535 GHz. (a) E-field components at the sensing surface with no object present and (b) total E-fields for the resonator cross section along the center microstrip host line. The fields are calculated for a 1-W input excitation power. For the coordinate system definition, the reader is referred to Figure 5.10. After [19] © 2017 IEEE.

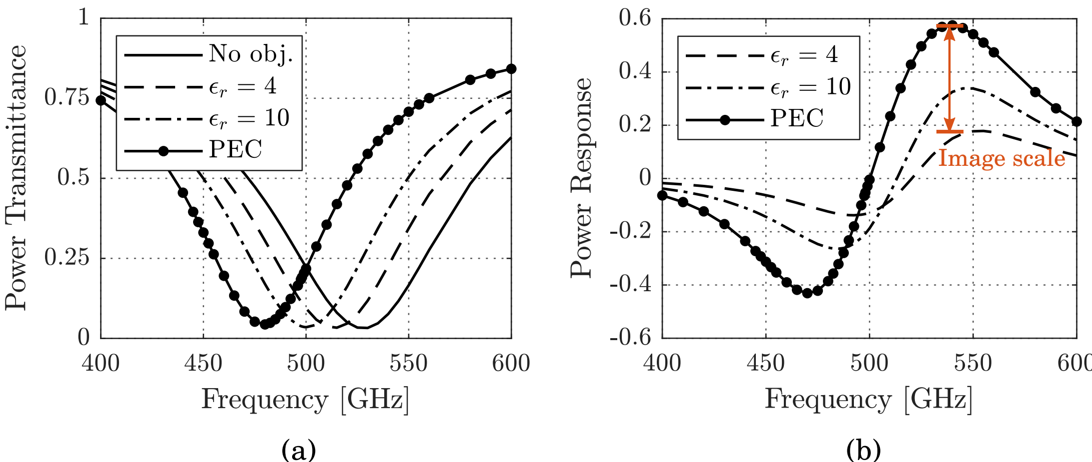

Figure 5.12.: Simulated frequency dependence of the power transmittance of the sensor ($|S_{21}|^2$) (a) and sensor power response ($|S_{21,\mathrm{obj}}|^2 - |S_{21,0}|^2$) with loading of objects with varying dielectric permittivity and for PEC (b). The curves are normalized to the unit input excitation power.

rudimentary in prior studies. They mostly served as a proof-of-concept. In that regard, it was experimentally verified that the sensors exhibit an image contrast that depends on the dielectric permittivity by measuring a varying sensor response for varying material under test (MUT)s [15], [19]. Similarly, another study indicated the potential to use these sensors for aqueous solution analysis and verified that the sensors are responsive to the varying dielectric permittivity of differently concentrated sugar solvents [own13]. With respect to imaging, 2D images of metal cutter blade tips were obtained in around 10 min long raster scans with simple mechanical object fixation and translation using stepper motors [15], [19].

5.4. Summary

The principle of incoherently THz near-field sensing with SRRs is discussed in this chapter. First, the sensing phenomenology is discussed, and an understanding of the design challenges related to building sub-wavelength THz near-field probes in planar silicon technology is provided. The chapter motivates the use of an incoherent sensing concept and includes remarks on its realization and figure-of-merits to quantify its electrical performance. After a brief review of the state of the art in single-pixel near-field sensors, the focus is laid on the SRR design of the single-ended sensor implementations.

Chapter 6

Modeling of Cross-Bridged Double Split-Ring Resonators

This chapter presents a framework for the modeling of cross-bridged double split-ring resonator topology described in Section 5.3.1. First, the focus is laid on modeling the sensing strips and their interaction with objects exhibiting varying material properties and locations. A model describing the whole SRR topology is subsequently introduced, extracted, and validated in full-wave EM simulations for the topology of the 550 GHz SRR reported in [19].

6.1. Modeling of the Sensing Strips

The sensing mechanism of the strips relies on the change in equivalent capacitance induced by objects that disturb the electric field. Such scenarios are commonly described using analytical approaches such as the perturbation theory mentioned in Section 5.1.1 or conformal mapping [181]. However, the BEOL surface in this technology is not planarized (see Figure 5.9), and its factual topology after fabrication is expected to exhibit some uncertainty, especially for small spacings of the sensing strips. The related complex electric field distribution cannot be conveniently expressed analytically.

Therefore, the near-field sensing mechanism is described by means of a physical equivalent circuit model and simulation-based empirical modeling of its effective electric properties. Because of the anti-parallel current flow, the two strips resemble a differentially excited line pair in which the shunt admittance between the lines changes with object loading.

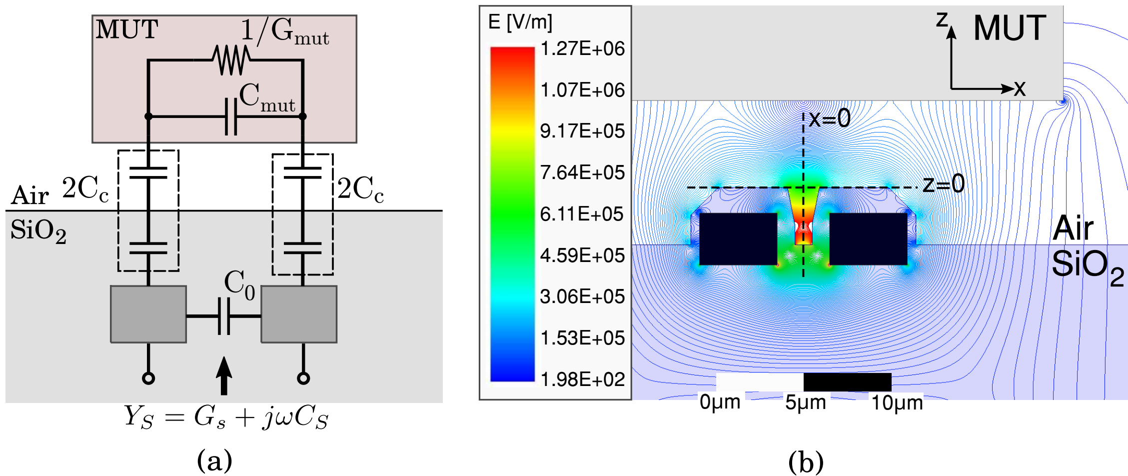

Figure 6.1.: Equivalent circuit model for near-field sensing strips implemented in the top-metal layer of a silicon BEOL (a). 2D simulation setup (Ansys Q3D Solver) for the extraction of the sensing strip parameters C_s' and G_s' at 550 GHz (b). The figure depicts an exemplary result for a centered copper object of dimensions 30 µm×20 µm at 5 µm distance from the chip top surface (y =5 µm). The lines correspond to the lines of constant electric field magnitude for a differential voltage excitation with 1 V magnitude.

The electric field is perpendicular to the line axes, and its direction varies with sinusoidal excitation. Figure 6.1(a) shows the equivalent circuit of the loaded sensing strips. The circuit is similar to the one presented described in Section 2.2.2 and [171]. The capacitance between the sensing strips is divided into a capacitor C_0, which lumps together the direct shunt capacitance between the strips, and a capacitor C_c, representing the coupling capacitance to the MUT through the BEOL and a potentially present air gap between chip and MUT. The MUT itself is modeled by an equivalent circuit for lossy dielectrics comprising the parallel connection of a capacitor C_{mut} and a conductance G_{mut}. While being a complex function of the object geometry and location, C_{mut} and G_{mut} are proportional to the real part $\epsilon'_{r,mut}$ and imaginary part $\epsilon''_{r,mut}$ of the dielectric permittivity, respectively [171].

Based on this model, the input admittance, Y_s, of the loaded sensing strips can be calculated. The imaginary part of Y_s is given by:

$$\mathrm{Im}(Y_s) = \omega C_0 + \frac{\omega C_c G_{mut}^2 + \omega^3 C_c C_{mut} \left(C_c + C_{mut}\right)}{G_{mut}^2 + \omega^2 \left(C_c + C_{mut}\right)^2} \tag{6.1}$$

and the real part is given by:

$$\mathrm{Re}(Y_s) = \frac{C_c^2 G_{mut} \omega^2}{G_{mut}^2 + \omega^2 \left(C_c + C_{mut}\right)^2}. \tag{6.2}$$

The analysis indicates that the model shown in Figure 6.1 can be furthermore transformed into a parallel CG-equivalent circuit with frequency-dependent elements. In the following, the elements of this equivalent circuit are referred to as the sensing capacitance, C_s, and the sensing conductance, G_s. Both C_s and G_s are a function of the complex dielectric permittivity of the MUT described by C_{MUT} and G_{MUT}, which implies that the resonance frequency of the whole SRR is also dependent on the dielectric and conductive losses of the MUT.

Recognizing that the sensing strips resemble an electrically short differential transmission line segment, C_s and G_s can be approximated by simulating the capacitance per unit length C'_S and the conductance per unit length G'_s of the line and subsequent multiplication of these with the physical length of the strips. Figure 6.1(b) depicts the simulation setup in the 2D quasi-static electromagnetic field solver (Ansys Q3D Extractor). With a line spacing of 3 µm and a line width of 4.5 µm, the geometry is chosen to be to equal the strip geometry of the resonator presented in Section 5.3.1 and [19]. Furthermore, the geometry of the dielectric around the sensing strips is approximated to be trapezoidal [19], and the dielectric of the BEOL is assumed to be lossless. A simulative study on the change in C'_s and G'_s with respect to varying material properties and object location is conducted subsequently. The simulation frequency is chosen to be 550 GHz in all simulations, which lies in the middle of the operation region of the SRR.

6.1.1. Response to Varying Material Properties

The influence of a load with varying complex permittivity was simulated by placing a 30 µm×20 µm dielectric block in direct contact with the sensing surface. Figure 6.2(a) shows the simulated capacitance C'_S and Figure 6.2(b) shows the simulated conductance G'_s for different ϵ'_r and loss tangents. For the unloaded case ($\epsilon_r = 1$) and for loading with a PEC object, the simulated C'_s is 77 aF/µm and 128 aF/µm, respectively. The expected behavior of increasing C'_s with increasing ϵ'_r can be observed as well as the dependency of C'_s on the loss tangent, as derived in Equation 6.1. However, the relative change in effective capacitance due to losses in the MUT is only a minor effect as compared to the change related to ϵ'_r.

6.1.2. Response to Spatial Object Displacements

The highly confined electrical fields of the strips clearly entail a high sensitivity to spatial object displacements. The most important related properties are the lateral resolution and the sensor sensitivity as a function of object distance to the sensing surface, which

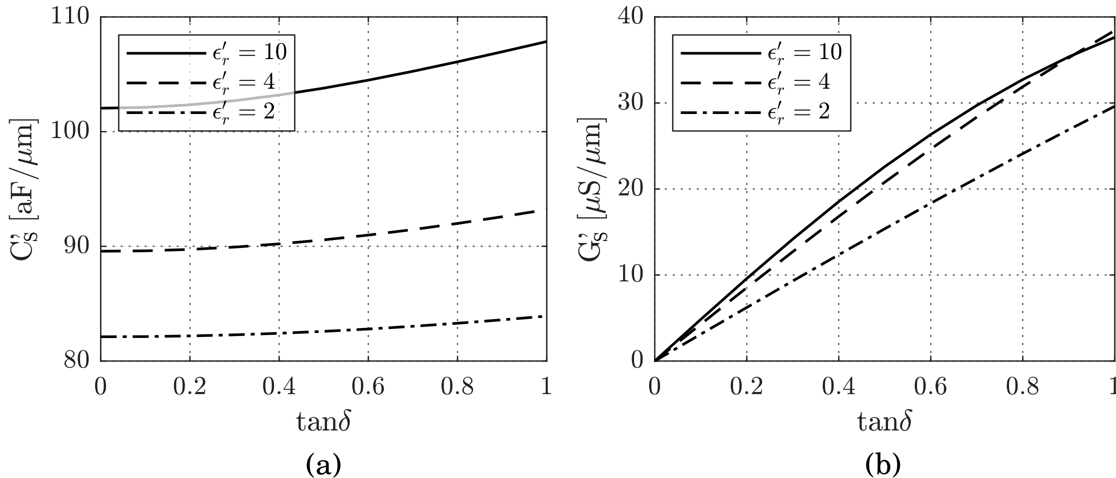

Figure 6.2.: Simulated dependency of the parallel CG-circuit of the sensing strips as a function of the complex permittivity of the object at 550 GHz. Sensing capacitance per unit length (C'_s) (a), and sensing conductance per unit length (G'_s) (b). An object of dimensions 30 µm×20 µm was simulated in direct contact with the sensing surface ($z = 0$).

are primarily dependent on the strip geometry. Although an ample simulative study of these properties requires the full 3D SRR topology to be taken into account because of the non-uniform field distribution of the SRR [19], it is worth pointing out that reducing the simulation problem to 2D lessens the required memory significantly as compared to full-wave 3D simulations.

Figure 6.3 plots the capacitance response as a function of the object distance to the sensing surface for PEC and dielectric objects of dimensions 70 µm×20 µm. The capacitance response is thereby defined as the object-induced change in sensing capacitance C'_s referenced to the capacitance without object loading, $C'_{s,0}$. The observation space was limited to the reactive near-field zone, i.e., to distances d of the object to the sensing surface significantly smaller than the free-space wavelength at 550 GHz. Interestingly, two distinct decay zones can be observed. At distances greater than 5 µm, the decay rate is inversely proportional to $> d^2$, which is in reasonable agreement with the theoretically expected decay behavior of an electric dipole, as described in Section 2.2. In the direct vicinity of the sensing strips (d <5 µm), the capacitive response and, thus, the related electric field magnitude is an involved function of the BEOL and the sensing strip topology. A functional description of the decay behavior could not be inferred by curve fitting here.

Analogously, the lateral resolution was simulated for a PEC as a function of distance from the object to the sensing surface. The object was translated in x- and y-direction. Here, the lateral distance represents the distance from the object center to the origin of the x-axis, as depicted in Figure 6.2. Figure 6.4 shows the sensing capacitance per unit length

C_s' as a function of displacement. The slope of the capacitance response is less abrupt when the distance of the object to the sensing surface increases. This effect originates in the fact that the electric field 'smears out' causing broadening of the surfaces of constant electric field strength. Moreover, the edge response exhibits a plateau which stems from surface regions of low field intensities (see Figure 5.11) caused by the non-planar BEOL geometry. A lateral resolution according to a 10%-90% rising/falling edge criterion can be derived for varying object height and is shown in Figure 6.4(b). In direct contact with the chip surface, the lateral resolution is 10 µm for both metallic and dielectric objects, which is close to the spatial extension of the sensing strips (12 µm). Furthermore, the lateral resolution decays rapidly, e.g., for PEC objects at a distance of 15 µm, it is only 40 µm. It is visible that the decay in lateral resolution for dielectrics is slower as compared to metallic objects. This can be attributed to the different interaction phenomenology between metallic and dielectric objects.

It needs to be emphasized that the here derived lateral resolution can only serve as a qualitative measure for the lateral resolution of the whole SRR when it is operated in the incoherent sensing scheme presented in Section 5.2. The lateral resolution of the entire sensor has to be derived based on the 10%-90% rising/falling edge criterion applied to the power response, which is a complex function of sensing frequency and curvature of the transmission notch [19]. Thus, it is not linearly dependent on the change in SRR capacitance.

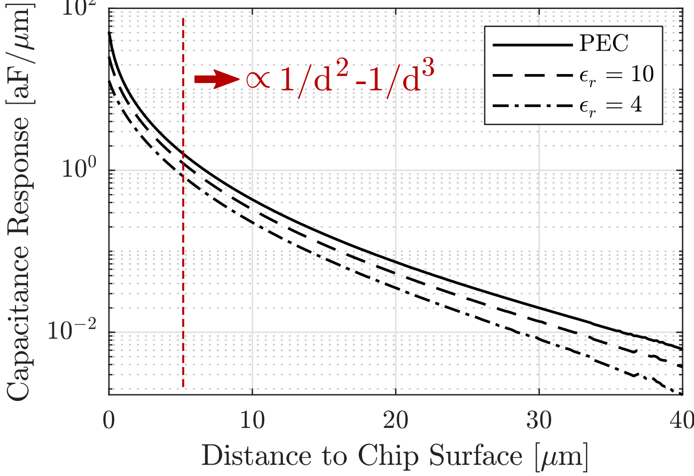

Figure 6.3.: Simulated capacitive response of the sensing strips as a function of object to chip surface distance for different dielectrics and a PEC object. Capacitive response is defined as the object-induced change in sensing capacitance with respect to a unloaded reference ($C_s' - C_{s,0}'$).

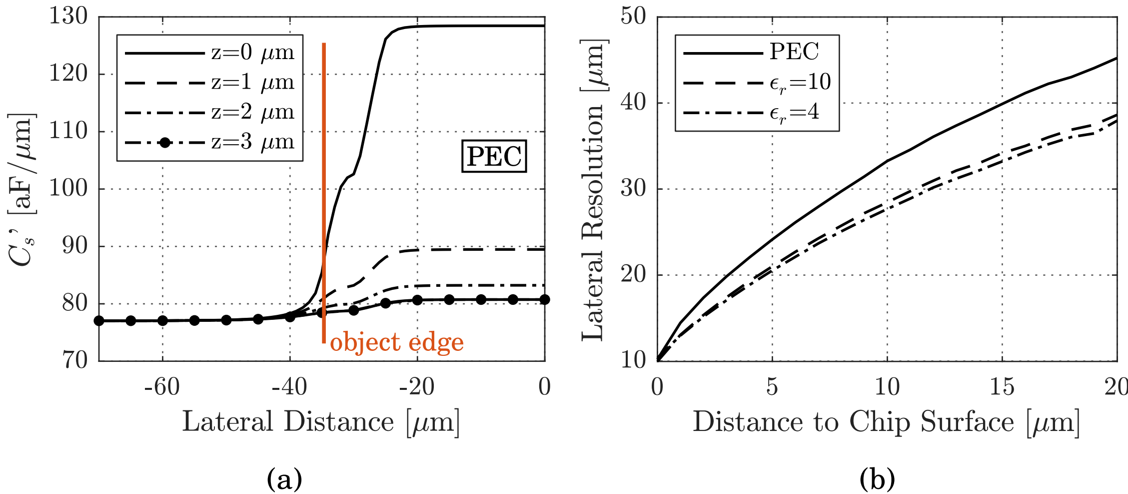

Figure 6.4.: Simulated sensing capacitance C_s' as a function of lateral distance from the symmetry axis ($x = 0$ in Figure 6.1) and the distance of the object from the chip surface for a PEC object (a). Simulated lateral resolution of the capacitive response (10%-90% rising/falling edge criterion) as a function of the object's distance from the chip surface for different dielectrics and a PEC object (b).

6.2. Modeling of the Resonator Topology

Expanding on the results of the previous section, the behavior of the entire 3D SRR topology can be interpreted by means of an equivalent circuit model. Notably, the key resonator dimensions are between $\lambda/20 - \lambda/5$ at the resonance frequency of 550 GHz ($\lambda_{SiO_2} = 272$ µm), which is in the transition region between the valid range for lumped circuit abstraction and the necessity of consideration of distributed effects. For the sake of simplicity, the here presented equivalent circuit model is semi-lumped, which turns out to allow a sufficiently accurate behavioral analysis of the SRR. The schematic of the model shown in Figure 6.5 has been derived in accordance with the models commonly used for metamaterial transmission lines loaded with SRRs [182]–[185]. The element choice and their physical background are discussed in the following:

- **Host line:** The host line is modeled using the nominal-π transmission line representation. C_{tl} represents the shunt admittance. The series impedance is divided into two parts: an uncoupled line section, L_{tl}, modeling the entrance and exit part of the host line and a magnetically coupled line section, L_s, modeling the middle part of the host line. The middle line section exhibits a high magnetic field component due to the ground plane opening.

- **Magnetic coupling:** L_s couples magnetically to the two parallel, equally-sized resonator lines $L_{r1,2}$. In view of the field distortion caused by the cross-bridge con-

necting the two parallel SRRs, a mean mutual inductance, M_1, is derived during parameter extraction. The coupling is thereby assumed to be predominantly magnetic because of the orthogonal orientation of the SRR symmetry plane with respect to the host line axis. Apart from the coupling of the host line to the SRRs, the mutual coupling between the two parallel SRRs is taken into account by introducing the mutual inductance M_2 between the two inductors L_{r1}.

- **Split-ring inductance:** As discussed in Section 5.3.1, the lines closing the SRR rings are led back to the ground-plane to allow a confined, low-loss wave propagation in a microstrip-mode. The inductance of these lines is modeled by inductor L_{r2}, and the line capacitance is absorbed into the split-gap capacitance C_{sg}.

- **Split-ring capacitance:** The buried split-gap is modeled as a series capacitor C_{sg}. Notably, the shunt capacitance of the feed to the split-gap can also be absorbed into C_{sg}. Based on the discussion in Section 6.1, the sensing capacitance can be modeled as the parallel connection of the object-tunable sensing capacitance C_s and sensing conductance G_s.

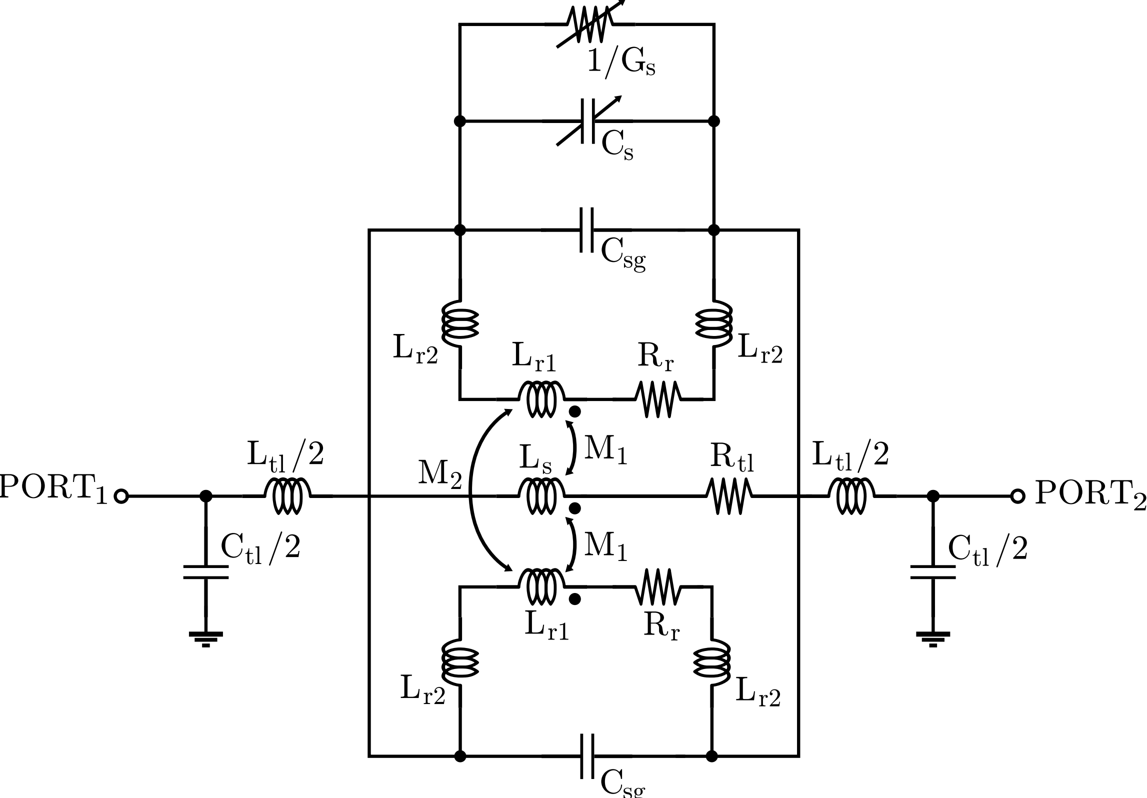

Figure 6.5.: Equivalent circuit model for the cross-bridged double SRR near-field probe topology.

6.2.1. Analysis of the Object-Induced Frequency Shift

The resonance frequency behavior of the SRR can be derived by converting the reciprocal two-port into its π equivalent model, where the impedance of the two shunt branches and of the series branch are expressed by $Z_{p1}(j\omega) = (Y_{11}+Y_{12})^{-1}$, $Z_{p2}(j\omega) = (Y_{22}+Y_{12})^{-1}$, and $Z_s(j\omega) = -Y_{12}^{-1}$, respectively [159]. Since the shunt branches are exclusively capacitive, the transmission zeros of the two-port are defined by the poles of the series reactance, which represents the reflected impedance of the coupled SRR network. To simplify the analysis, the SRR, the host line, and the sensing capacitance are assumed to be lossless by setting $R_r = R_{tl} = 0$ and $G_s = \infty$, which has no influence on the deduction of the resonance frequency. The series impedance of the two-port can then be derived based on Kirchhoff's circuit laws and is found to be:

$$Z_s(j\omega) = j\omega\left(L_s + L_{tl}\right) + \frac{j\omega^3 2C_{srr}M_1^2}{-C_{srr}M_2\omega^2 - \frac{\omega^2}{\omega_0^2} + 1}, \tag{6.3}$$

where $C_{srr} = C_s/2 + C_{sg}$ is the parallel connection of split-gap and sensing capacitance and $\omega_0 = \left[\left(L_s + L_r\right)\left(C_s/2 + C_{sg}\right)\right]^{-1/2}$ is the resonance frequency of a single SRR without cross-coupling. Here, the split-ring inductances L_{r1} and L_{r2} are merged into L_r. Equating the denominator of Equation 6.3 with zero gives the resonance frequency ω_1 of the cross-bridged SRR:

$$\omega_1 = \frac{\omega_0}{\sqrt{1 + M_2/(L_s + L_r))}}. \tag{6.4}$$

Interestingly, the mutual inductive coupling between the two resonators results in a reduction of the resonant frequency. For a negligible mutual coupling between the two resonators ($M_2 = 0$), the SRR resonance frequency ω_1 is equal to ω_0. Moreover, the resonance frequency shift caused by loading the SRR with an object is captured by ω_0, which is a function of C_s.

6.2.2. Parameter Extraction

Parameters for the cross-bridged double SRR topology presented in Section 5.3.1 were extracted. At first, a rough estimate of the component values is derived from individually simulating the equivalent values of the components in the quasi-static field solver Ansys Q3D Extractor at 550 GHz. Thereby, the mutual inductive coupling (M_1, M_2), the self-inductance and capacitance of the host line (L_{tl},L_s,C_{tl}), and of the coupled lines of the

SRR (L_{r1}) are deduced by multi-line 2D simulations. Values for the split-gap capacitance C_{sg} and the partial inductance of the microstrip line L_{r2} are inferred from 3D simulations based on the method of moments. The sensing capacitance C_s and conductance G_s are mapped one-to-one from the simulations conducted in Section 6.1 by multiplying the object-dependent capacitance and conductance per unit length by the 19 µm extension length of the sensing strips. This allows a direct transfer of the simulated 2D strip response caused by spatial displacements and varying materials to the sensor response formation as a whole, building a base for a simplified examination of the SRR behavior.

To account for discontinuity effects between the lumped elements and to accurately model the line-loss in view of parasitic radiation and current crowding effects in the dense 3D geometry, fine-tuning of the equivalent circuit parameters is conducted based on the whole 3D SRR geometry. Thus, a final set of parameters listed in Table 6.1 is inferred by the fitting of the SRR scattering parameters derived from the equivalent model to the results of full-wave EM simulations. Pursuing a similar simulation setup as compared to the one described in Section 5.3.1, the 3D resonator topology was loaded with a 30 µm×30 µm×15 µm cube placed in direct contact with the sensing surface. Initially, the mutual inductance accounting for the resonator cross-coupling is derived by comparing the resonance frequency of the 3D half-circuit with a single SRR (ω_0 in Equation 6.4) with the resonance frequency for the whole cross-bridged double SRR topology (ω_1 in Equation 6.4). While not being negligible, the influence of the cross-coupling is minor, shifting the resonance frequency only from 527 GHz to 519 GHz. Subsequently, tuning of the total SRR inductance and capacitance ratio is conducted by matching the object-induced frequency shift of the model to simulation results. Finally, the line losses and the mutual inductance M_1 are inferred by matching the resonator quality factor and modulation the depth.

6.3. Model Validation

To validate the proposed model, a comparison with full-wave electromagnetic simulations (Ansys HFSS) regarding the power transmittance ($|S_{21}|^2$) through the SRR is conducted. Since the notch slopes and the baseline power transmittance are very sensitive to the resonator load defined by the source and load impedance, the model port impedances are reconciled with the simulated wave impedance of the host line ($Z = 96\,\Omega$). A collection of curves for i) lossless objects with varying dielectric permittivity and PEC and ii) objects with a fixed ϵ_r' of 4 and varying loss tangents is depicted in Figure 6.6 and Figure 6.7. A good quantitative agreement can be observed for the whole curve set. Most notably,

Table 6.1.: Extracted parameters of the equivalent circuit for the SRR shown in Figure 5.10.

Parameter	Value
L_{TL}	7.7 pH
L_s	22.4 pH
L_{r1}	22.4 pH
L_{r2}	9.1 pH
C_{TL}	2.1 fF
C_{sg}	1.5 fF
C_s	object-dependent – 1.46 fF-2.44 fF[1]
G_s	object-dependent
R_s	2.4 Ω
R_{tl}	5.4 Ω
M_1	13.05 pH
M_2	1.3 pH

[1] The stated capacitance range spans from the lowest perceivable capacitance occurring in the unloaded case ($\epsilon_r = 1$) to the highest one occurring for PEC objects.

the region of interest for incoherent sensor operation, i.e., the steep rising slope of the transmission notch, is accurately modeled.

The comparison furthermore verifies the validity of the presented modeling approach for the sensing strips loaded with lossy objects presented in Section 6.1. An increasing loss tangent leads to a slight reduction in resonant frequency, which is more pronounced for high loss tangents ($\tan\delta > 0.4$). This is in line with the simulated dependency of the sensing capacitance on the object losses, as shown in Figure 6.2.

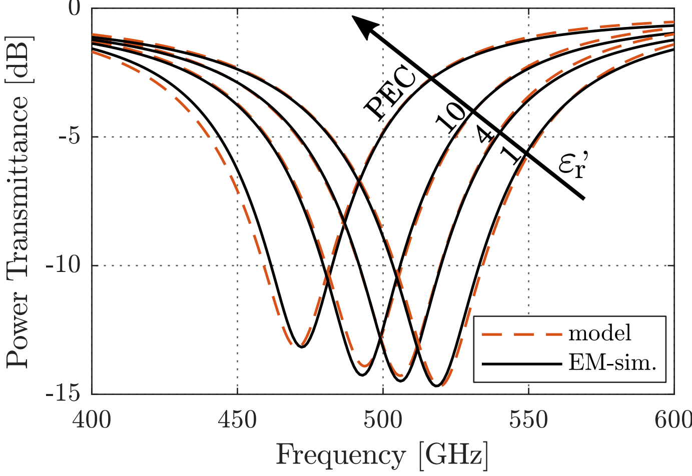

Figure 6.6.: Comparison of the power transmittance ($|S_{21}|^2_{dB}$) between the equivalent circuit model and electromagnetic simulations for different lossless dielectrics and a PEC object.

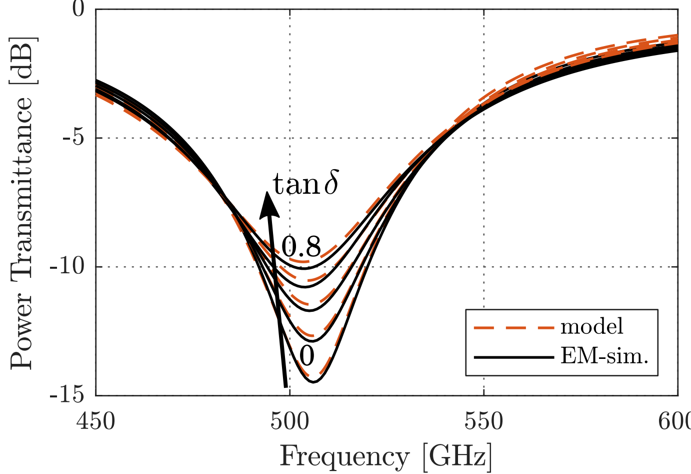

Figure 6.7.: Comparison of the power transmittance ($|S_{21}|^2_{dB}$) between the equivalent circuit model and electromagnetic simulations for a dielectric with an ϵ_r' of 4 and varying loss tangents.

6.4. Discussion

The herein developed framework for modeling and understanding of the SRR behavior provides valuable insight into the interpretation of the sensor response in view of the object-induced transmission modulation scheme described in Section 5.2.

6.4.1. Sensor Response Ambiguity

Most importantly, the sensor voltage response ΔV_o (see Equation 5.5) is ambiguous to the material properties and spatial displacement of the target object:

$$\Delta V_o = f(e_r, x, y, z), \tag{6.5}$$

where x,y, and z describe the object location in the 3D volume. As such, the measurement of the object-induced transmission modulation prohibits direct evaluation of the quantitative material data. For example, in imaging experiments where either the surface topology of an object or the absolute distance of the object to the sensor is unknown, the imaging contrast cannot be uniquely attributed to the relative permittivity of the object. To make it worse, the high spatial confinement of the resonator near-fields leads to a significantly higher sensor sensitivity to spatial object displacements as compared to material variations, which can only be accounted for by very accurate distance control in the nanometer-range.

On another note, the sensor response ambiguity to the real and imaginary part of the relative permittivity turns out to be frequency-dependent. To illustrate this, Figure 6.8 shows the simulated power transmittance sensitivity $\delta|S_{21}|^2/\delta\epsilon_r$ to both for a lossy object with $\epsilon_{r,0} = 4 - j2.4$ and a lossless object with $\epsilon_{r,0} = 4$. The sensitivity to the imaginary part shows a positive peak close at the resonance frequency due to modulation of the notch depth. With increasing frequency, it crosses zero before showing a negative peak at the higher end of the bandstop slope. The sensitivity to the real part peaks at the frequency exhibiting the highest power transmission gradient. A suitable allocation of the excitation frequency can thus be chosen to isolate the responses caused by the real or the imaginary part of the object, e.g., by selecting a frequency at the zero-crossings of the respective sensitivity curves. In practice, however, it is challenging to supply the required excitation bandwidth for optimization of both the sensitivity to the real part and to the imaginary part for a wide range of materials due to the tuning range limitations of integrated THz-VCOs.

6.4.2. Considerations for Practical Applications

The sensor exhibits a sensitivity reduction to the real part with increasing losses, which can be attributed to a decrease in modulation depth and quality factor, leading to a lower power transmission gradient (see Figure 6.7). For the simulated lossy object, the peak sensitivity to the real part drops below the sensitivity to the imaginary part. As such, an appropriate allocation of the excitation frequency has to be assessed based on the desired application-specific imaging contrast mechanism. For example, for the imaging of semiconductor doping concentrations, the dominant contrast can be expected to stem from changes in the material's bulk conductivity. Placing the excitation frequency at the resonance frequency should thus be preferred in this case. Other target applications for the sensor such as the discrimination of benign and malignant tissue, as described in Section 2.1.5, are expected to exhibit a mixed contrast that is dependent on both imaginary and real part of the relative permittivity.

To illustrate this, full-wave EM simulations of the power transmittance for different tissue types in direct contract with the sensing surface are shown in Figure 6.9. The real and imaginary parts of the dielectric permittivity for cancerous, fatty, and fibrous tissue at around 500 GHz were extracted from the THz TDS measurements published in [39]. The power transmittance features a high contrast of up to 3 dB between fatty and fibrous or cancerous tissue. A distinction between cancerous and fibrous tissue, however, can be expected to be challenging with a maximum difference in power transmittance of 0.5 dB. Although the difference in complex permittivity for these tissue types is only

subtle, cancerous tissue exhibits a higher real part and more losses, thereby leading to a synergistic increase in power transmission. Notably, this can not be formulated as a general statement for all material constellations since objects may also exhibit counter-acting dependency. In these cases, measurement of the rising slope gradient by detuning the oscillator excitation frequency could potentially be used to solve the related response ambiguity.

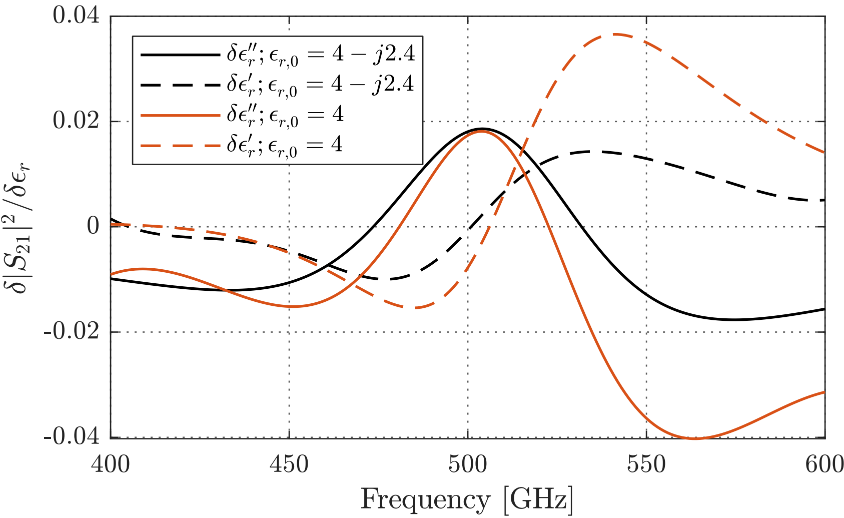

Figure 6.8.: Simulated power transmittance sensitivity $\delta|S_{21}|^2/\delta\epsilon_r$ to the real and imaginary part of the relative permittivity for a lossy object with $\epsilon_{r,0} = 4 - j2.4$ and a lossless object with $\epsilon_{r,0} = 4$. The resonance frequency is around 505 GHz for both objects.

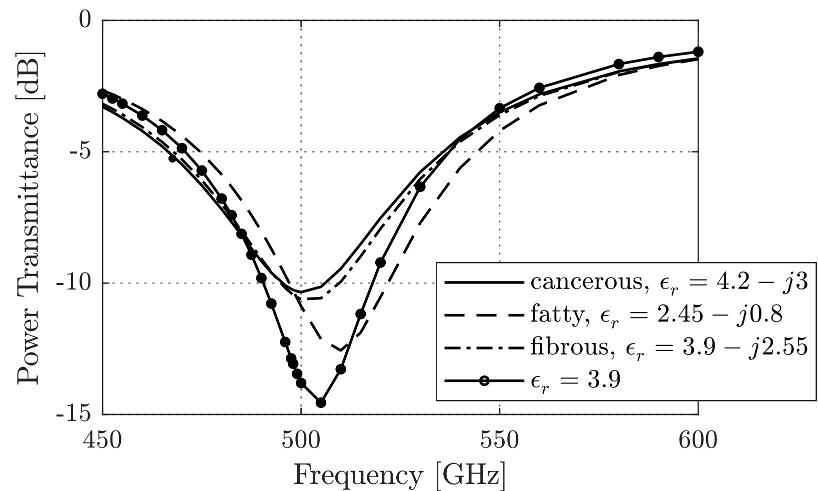

Figure 6.9.: Simulated frequency dependence of the power transmittance of the sensor ($|S_{21}|^2$) for different breast tissue types. Complex permittivity values for the tissues are extracted from [39].

Chapter 7

A THz Near-Field Sensor System-on-a-Chip in SiGe-HBT Technology

The framework for understanding, analyzing, and modeling integrated SRR-based THz near-field sensors presented in Chapter 5 and Chapter 6 referred to the first research on single-pixel prototypes [15], [19] [own11], [own13]. In Chapter 5, it is shown that such sensors promise improvements compared to THz-NSOM regarding sensitivity and integration levels. In that regard, the achieved lateral resolution of 10 µm combined with an SNR around 40 dB enabled the acquisition of 2D THz near-field images with low-cost hardware. However, single-pixel sensors require raster scanning for image acquisition, which hampers their use in practical applications. For example, interoperative *ex vivo* imaging for cancer margin detection has to deal with soft tissue samples which are accompanied by blood and other fluids. In this context, raster scanning is simply impossible because the sample will stick to the sensor and cause inhomogeneous image acquisition. One could potentially circumvent such problems by integrating large-scale sensor arrays to eliminate the need for mechanical translation. Ultimately, a 2D array implementation would solve the scanning issue, but remains objective of future work due to as yet unstated challenges for ultra-dense SRR packaging, which will be discussed in Section 7.1.

The ultimate aim of the study presented in this chapter is to investigate whether a 1D chip-scale near-field array can be integrated with high pixel density to reduce the required mechanical translation for 2D image acquisition to one axis, thereby enhancing

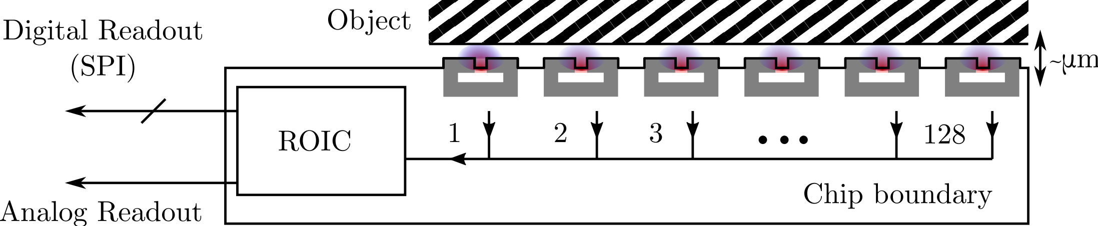

Figure 7.1.: Illustration of the 1D near-field sensor SoC. 128 near-field pixels are arranged in a line and cointegrated with a readout integrated circuit (ROIC). The chip supports both analog and a digital read-out mode. After [own5] © 2018 IEEE.

the practicability of THz near-field sensing. Furthermore, it is investigated if such sensors can be advanced towards SoC-level integration, being comparable with ubiquitous imaging hardware such as optical CMOS image sensors and capacitive fingerprint sensors. For the whole study presented in this chapter, a commercial high-speed 0.13 µm SiGe-BiCMOS technology with an f_t/f_{max} of 300/450 GHz from IHP Microelectronics is used as a design platform. The contributions of this chapter mostly accord with the contributions published in [own4], [own14], [own5], and [own1]. They can be summarized as follows:

- A 128-pixel near-field sensing SoC for real-time (up to 28 fps) imaging at 550 GHz with around 10 µm lateral resolution is demonstrated. An illustration of the near-field sensor SoC, indicating the compact cointegration of THz front-end and a mixed-signal ROIC, is depicted in Figure 7.1. The SoC is packaged into a 3-layer FR-4 PCB module comprising FPGA-based control and external supply regulation. Since the module includes all sensing functionality, including illumination, sensing, detection, and post-processing, it can be operated as a stand-alone imaging device – powered and interfaced only by a conventional Universal Serial Bus (USB) port.

- To facilitate chip-scale sensor integration, a scalable THz front-end for multi-pixel near-field arrays is introduced (Section 7.1). The front-end reuses the 550 GHz SRR and the TPO presented in [19]. It makes use of a parallel sensor excitation scheme and utilizes 4-way equal-power splitter networks to enable dense SRR placement along a line. In regard, the design of integrated Wilkinson power splitters in the THz range along with the associated parasitic cross-coupling effects in between pixels is discussed.

- A rolling shutter array read-out architecture for incoherent near-field sensor operation employing SiGe-HBT power detectors is proposed (Section 7.2). It encompasses digitally controlled analog signal conditioning and an on-chip lock-in amplifier for phase-sensitive detection outside of the detector low-frequency noise in real-time.

The SoC furthermore supports on-chip analog-to-digital (A/D) conversion for a digital-only read-out via a Serial Peripheral Interface (SPI).

- Imaging experiments are conducted to demonstrate the utility of the SoC (Section 7.5). Imaging of planar solids is demonstrated by using a fine AFM-calibration nickel grid as an imaging object to evaluate the 2D imaging performance. Furthermore, biometric human fingerprint reading is demonstrated as a use case for profilometric imaging. Lastly, imaging of a 5 µm thick excised breast tissue sample is shown.

7.1. A Scalable Front-End for THz Near-Field Sensors

It is asserted in Section 5.2 that the object-induced transmission modulation scheme is suitable for large-scale sensor array integration due to its implementation simplicity. While this is true since the non-coherent sensor operation enables low power and low energy consumption, multiple challenges still remain. These become clear when the design objectives for a multi-pixel architecture are defined: A multi-pixel near-field imager should allow for a dense imaging object coverage without dead zones between the sensing elements, while simultaneously providing sufficient sensor sensitivity in view of potential pixel cross-coupling effects.

As depicted in the micrographs gathered in Table 5.1, the single-pixel sensors presented in prior studies [15], [19] [own11], [own13] exhibit a severe size mismatch between the sub-wavelength sized SRR and the illumination source. In general, on-chip harmonic THz oscillators whose operating frequency is set close to the practical limit of device operation (around $f_{max}/3$) require low-loss inductances implemented as wavelength-scale transmission lines. Similar to the sensing strips of the SRR, these lines are typically allocated in the thick top-metal layers of the BEOL to increase the surface area for current conduction and thereby increase the quality factor of the inductance. Given that the SRR dimensions are of sub-wavelength size, the illumination source dominates the total sensor footprint. Therefore, integration of many of such pixels would lead to massively spatially undersampled imaging arrays with low sensor fill factors[1]. For example, the fill factors for the sensors in [15], and [own13] are limited to around 5 % for 1D arrays and 0.5 % for 2D arrays.

[1]In analogy to CMOS image sensors the fill factor is here defined as the ratio of the image sensor's sensitive area to it's total area.

7.1.1. A 1D Multi-Pixel Architecture

The proposed solution to increase the sensor fill factor is to have multiple SRRs sharing a common oscillator. In this work, a parallel illumination architecture uses a power splitter network to distribute the oscillator power to a line of SRRs spatially. Figure 7.2 illustrates the arrangement. The sensors are grouped into subarrays of four SRR-detector units and are connected in parallel to a corresponding source element by means of a 4-way equal-power splitter. The SRRs in each group are arranged in a line with 50 µm pitch between the elements, which is selected as a compromise between fill factor and pixel cross-coupling through the near-field, as to be detailed in Section 7.1.3.

The described arrangement facilitates 2D imaging for translational scans orthogonal to the sensing line. To further double the 1D pixel density for such imaging experiments, two sensor rows are vertically mirrored and offset by half the sensor pitch, resulting in a staggered arrangement. The two opposing sensing rows are separated by 110 µm. This gives an array architecture that is scalable in one dimension with a fill factor of 48 % and a 1D pixel density of 1016 dpi.

However, as a result of the discrete 1D pixel pitch of 25 µm, images remain slightly undersampled with respect to the intrinsic pixel resolution, which is around 10 µm for the SRR utilized in the present design [19]. As a consequence, the maximum unambiguously resolvable image features are limited to dimensions of 50 µm by the Nyquist-Shannon sampling theorem. Nevertheless, the array could also be used in a 2D raster-scanned imaging setup to allow the acquisition of 2D images with the intrinsic SRR-limited lateral resolution.

7.1.2. Design of a Shielded Wilkinson Power Splitter Network

The power splitter network has a determining influence on the overall performance of the multi-pixel architecture. Given that the sensor's DR and SNR are proportional to the excitation power (Equation 5.8), maintaining a low insertion loss of the network is crucial. Another key property is the isolation between output ports. As a consequence of the parallelization, the SRRs of a subarray are coupled through the shared power splitters. Since the SRRs innately exhibit a strongly object-dependent input impedance when being operated in resonance, there is a necessity to isolate the output ports so that reflected signals do not propagate through other SRRs in the subarray, thereby leading to pixel cross-coupling. These requirements preclude non-isolating power combiner/splitter types commonly used in mm-Wave ICs such as transformer-based series and parallel combiners

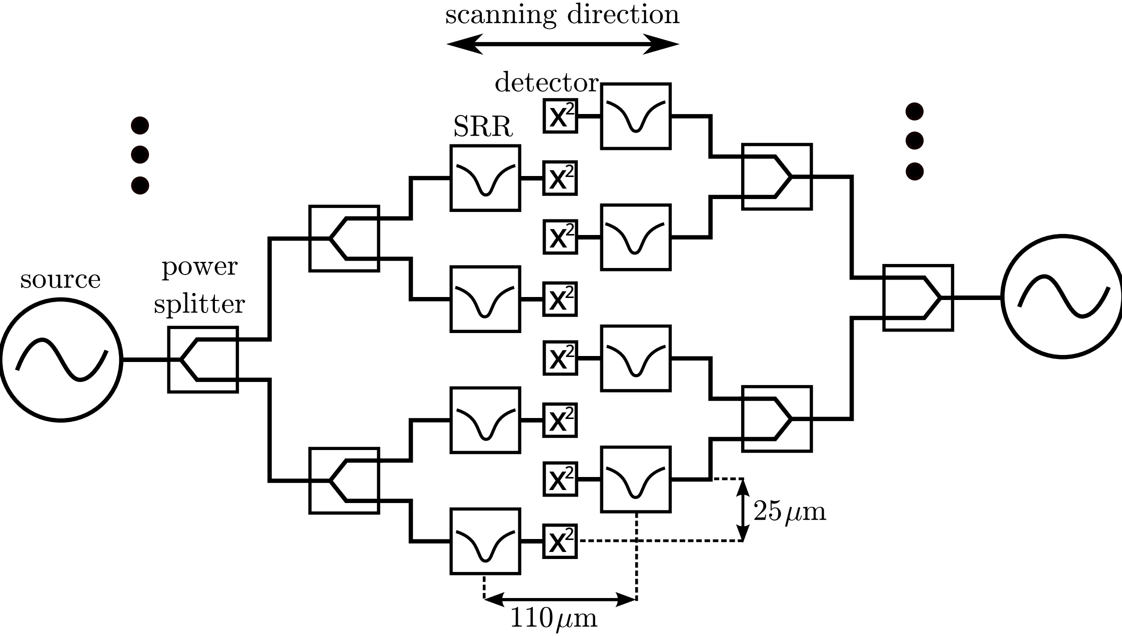

Figure 7.2.: Parallel power splitter based sensor illumination scheme. Two rows are vertically mirrored and offset by half the single-row sensor pitch of 50 µm to double the fill factor.

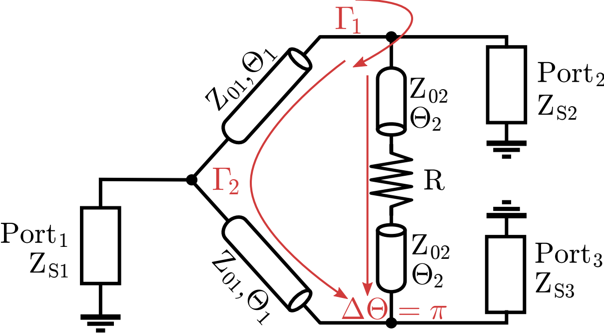

Figure 7.3.: Schematic of the modified Wilkinson power splitter [189].

[186] and zero-degree combiners [187] and favor the use of a Wilkinson power divider, which exhibits isolation of the output ports for matched input ports [188].

However, in order to be compatible with integration at THz frequencies and with the intend of spatial power distribution, the classic design from Wilkinson needs to be extended with additional transmission line segments. Figure 7.3 shows the schematic of the modified Wilkinson power splitter [189]. In the classic Wilkinson divider implementation, the electrical length Θ_2 is zero. When the other circuit parameters are selected as $Z_{01} = \sqrt{2}Z_{S1}$, $\Theta_{01} = \pi/2$, and $R = 2Z_{S1}$, the isolation is provided by destructive interference: If a signal is reflected at Port_2, the wave traveling along the resistor branch and the wave reflected from the source are out of phase and of equal amplitude at Port_3. Thereby, the isolation resistor R should behave ideally as a lumped element without introducing a phase shift.

However, since resistors are typically implemented as resistive sheets in the front end of line, large via stacks are required to access the resistor, inevitably leading to a significant phase shift at THz frequencies. In addition, the two splitter branches are very close to each other if Θ_2 is zero. Therefore, proximity effects can severely reduce the isolation and complicate the design process. To avoid these problems, the Wilkinson power splitter can be modified by adding transmission lines in series to the isolation resistors, as depicted in Figure 7.3. Thereby, the parasitic phase shift of the via stack and the distributed effects of the resistor sheet can be absorbed into the line, and the branches can be spatially separated. It is noted that isolation between Port_2 and Port_3 can still be generally provided with the modified structure if the splitter is designed accordingly [189]. Most importantly, the difference between electrical lengths of the two branches for the reflected waves should be half a wavelength ($\Delta\Theta = 2\Theta_1 - 2\Theta_2 = \pi$).

An additional design requirement for near-field sensors is that the insertion loss of the power splitter should not be sensitive to objects placed on top of it. In the same way as the illumination source, the power splitter fields are thus required to be confined within the BEOL to avoid potential disturbances of the insertion loss caused by object-induced changes in the characteristic impedance of the transmission lines. Hence, the lines have to be implemented as striplines with a ground plane in the topmost aluminum layer, limiting the maximum characteristic impedance to around $50\,\Omega$ in the present BEOL stack. It is noted that the related limited design space for the line impedances also prohibits the use of the classic N-way Wilkinson designs because the characteristic impedances of the lines have to scale with $\sqrt{N}$ [159].

The design of the 550 GHz power splitter network is conducted by inferring initial parameters by hand calculations based on the design equations listed in [189] and subsequent electromagnetic optimization. Figure 7.4 shows a 3D view of the simulation model of the 4-pixel subarray, including the 4-way equal-power splitter network. The power splitter is implemented in a ladder structure with three 2-way modified Wilkinson splitters and is matched to the $50\,\Omega$ output impedance of the illumination source. The physical line lengths of the arm segments and spacers are selected to simultaneously provide isolation and sufficient spatial separation for the SRR placement; they are $90\,\mu\text{m}$ and $14\,\mu\text{m}$, respectively. The lines are implemented as $50\,\Omega$ striplines with the signal conductor placed in the second layer from the top. The resistor R is a $40\,\Omega$ poly-silicon resistor. Figure 7.4 furthermore shows 25 fF metal-insulator-metal (MIM) capacitors between the SRRs and the detectors. The capacitors are self-resonant at 550 GHz and provide DC-isolation between the illumination source and the power detectors to facilitate a chopped operation mode.

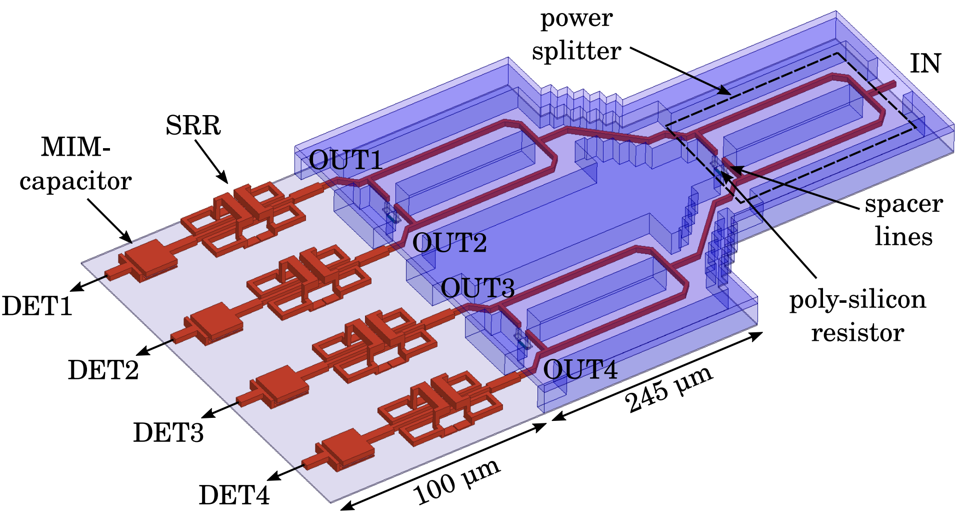

Figure 7.4.: Simplified EM-model of the 4-pixel sensor subarray including 4-way power splitter, four sensors, and series MIM capacitors. Simulation ports are indicated as IN (power divider input), OUT1-4 (power divider outputs), and DET1-4 (power detector inputs). After [own5] © 2018 IEEE.

Using full-wave simulations (Ansys HFSS), the splitter network characteristics are analyzed. Figure 7.5 provides the S-parameters of the 4-way splitter network. The parasitically added insertion loss of a single 2-way power splitter is 0.9 dB at 540 GHz, leading to a total insertion loss of 7.8 dB in between the input port (IN) and each of the output ports (OUT1-4). For matched port conditions, the isolation of all output ports is larger than 30 dB in the operation bandwidth. Figure 7.6 shows the simulated power response of a single SRR, including the power divider network and the series MIM capacitor for various object loading conditions. Conducting a similar simulation method as in Chapter 5, 30 µm×30 µm×20 µm sized dielectric and metallic (PEC) blocks are placed in direct contact with the chip top surface. It is visible that the sensor response is well preserved in the presence of the capacitor. For the entire subarray circuit, the maximum power response for a metal object occurs at 535 GHz and is 7.2 % of the power available from the oscillator.

7.1.3. Impact of Parasitic Cross-Coupling Effects

As mentioned before, parasitic coupling mechanisms between pixels have to be taken into account. Because of the specific row arrangement, two different coupling phenomena need to be considered: i.) Direct coupling through the power splitter network, and ii.) coupling through the reactive and radiative near field. Both phenomena are discussed in the following.

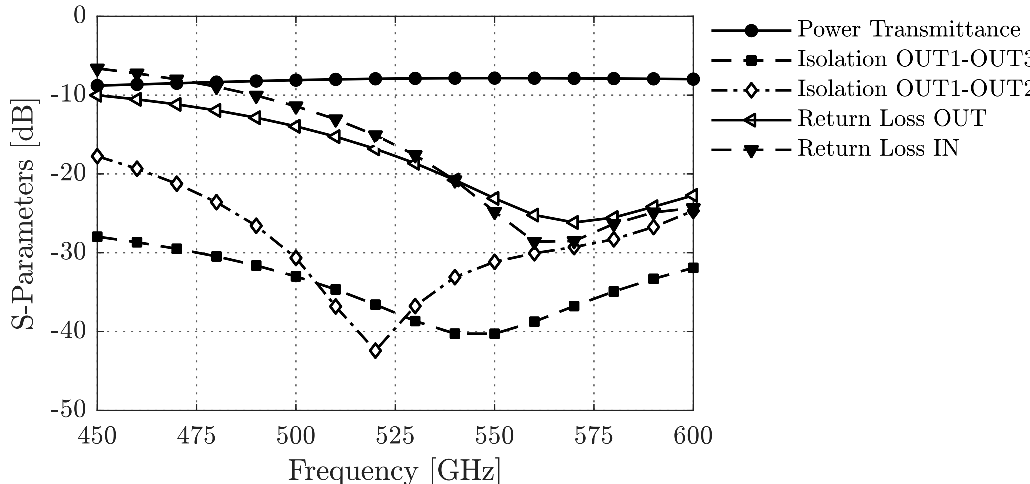

Figure 7.5.: Simulation results of the complete 4-way divider. The isolation is shown only for two representative output ports.

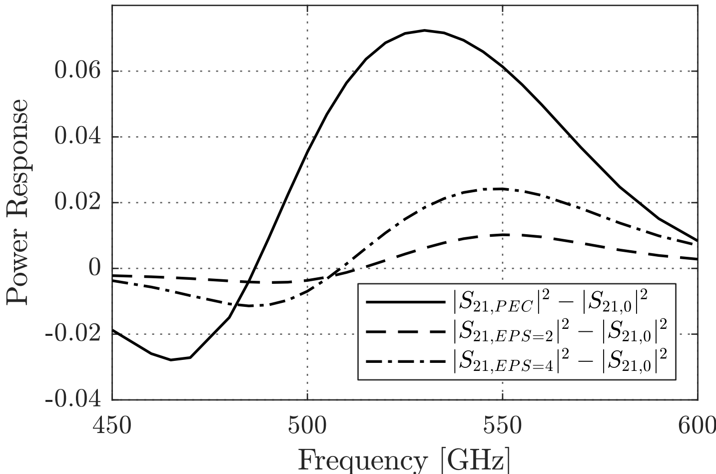

Figure 7.6.: Simulated power response for objects with $\epsilon_r = 2$, 4, and PEC at a single SRR with a 25 fF series MIM capacitor including feed network.

Coupling Through the Power Splitter Network

The overall splitter network operates with unmatched boundary conditions on all ports, and these vary dynamically with different object loading conditions. The resulting reflections and impedance imbalances at the internal divider nodes lead to a finite variation of the power division ratios. Although the good isolation between the detector ports provided by the power splitter strongly mitigates this effect (Figure 7.5), isolation is still finite, and the described effect is not negligible. It is noted that since the sensor response is derived from absolute power difference measurements, the parasitic cross-coupling translates to ambiguity and desensitization in the sensor response. In other words, if the sensor response of an observed pixel changes with the objects present on the neighboring pixels, the

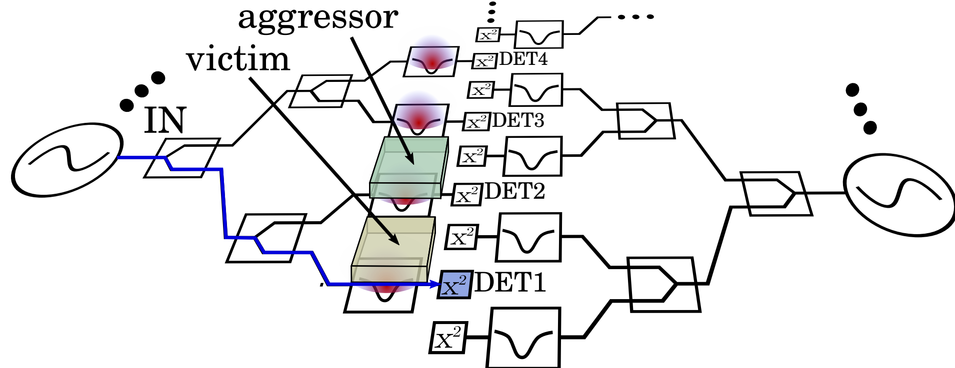

Figure 7.7.: Parallel power divider based sensor illumination scheme. Two rows are vertically mirrored and offset by half the single-row sensor pitch to double the fill factor. The arrangement requires pixel cross-coupling to be taken into account.

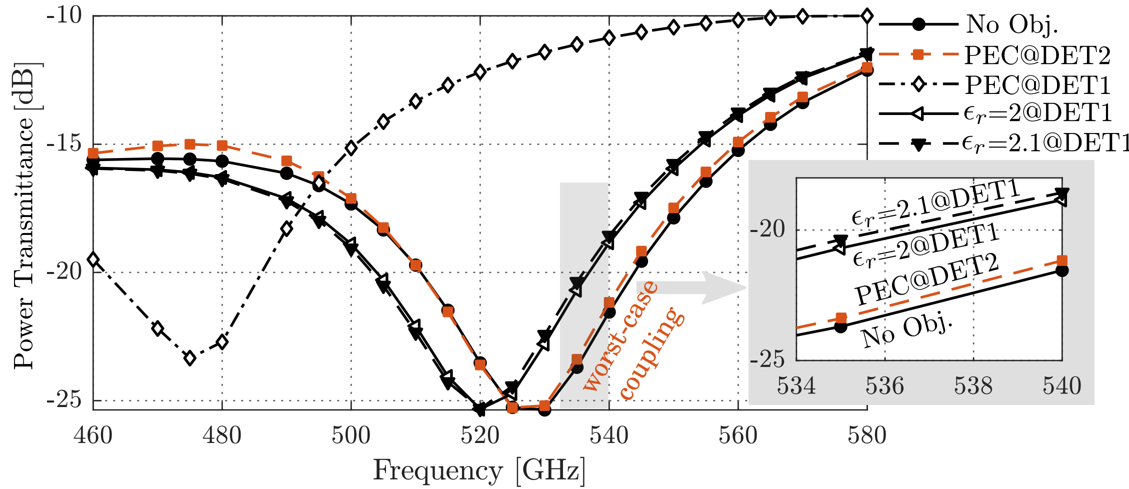

Figure 7.8.: Simulated power transmission (IN-to-DETx) for one selected detection path (DET1) in a 4-way power sensor arrangement as a function of frequency for different object loading conditions while influenced by a closest-proximity pixel (DET2).

object present on the observed pixel cannot be accurately identified.

This desensitization was also investigated with electromagnetic simulations (Ansys HFSS). Figure 7.7 illustrates the simulation test case. In order to emulate a realistic coupling scenario, the power transmission through one selected detection path (DET1), which is referred to as the victim pixel, is simulated for different object loading conditions (No Object, PEC, $\epsilon_r = 2, 2.1, 4$) while being influenced by an aggressor pixel (DET2) with varying object material properties (PEC, $\epsilon_r = 4$). Figure 7.8 gathers the relevant simulation results. The worst-case coupling scenario occurs for a metal aggressor on the neighbor pixel and no object on the victim pixel. In this case, the resonant curve of the victim pixel is shifted down in frequency. For frequencies from 540 GHz–560 GHz, this shift corresponds

to a relative power change at the detector input between −21 dB and −14 dB when referred to the maximum power response for a metal object. This, in turn, relates to a relative permittivity uncertainty of around 0.1 for an object with $\epsilon_r = 2$, for example. It is noted that when the aggressor object is placed in the other branch (DET3, DET4) the response is found to be complementary in terms of the frequency shift variation of the resonant curve.

As such, the coupling through the power splitter network is expected to be a limiting factor for the sensitivity of the system, which is also verified in the experimental characterization in Section 7.4. However, the practical limitations that the cross-coupling imposes on the system are complex and can vary from application to application. For example, the derived relative permittivity uncertainty of 0.1 is only valid for the investigated worst-case where a low permittivity object needs to be sensed in the presence of metal features in the object. However, in the targeted applications such as the differentiation of tissue types, the object under test is more homogeneous (Figure 6.9). Since the uncertainties scale with the material-dependent sensor response, the cross-coupling is expected to be less significant in such applications.

Coupling Through the Reactive and Radiative Near Field

The dense SRR arrangement additionally introduces cross-coupling between the adjacent pixels due to the radiative and reactive near-field zones of the SRRs. Figure 7.9 shows the simulated coupling between two sensors that are separated by 50 µm (center-to-center) and not connected through the power divider network. The coupling is taken as the parasitic power received at one detector output while driven by another resonator input port. Similar to the previous analysis, the most critical configuration occurs if the aggressor sensor is covered with metal while the victim has no object above it. For this configuration, the coupling level change was simulated to be below −46 dB at the detector input for the entire sensor frequency operation range and is thus considered to have minor influence when compared with the coupling introduced by the power division network. The coupling, however, increases rapidly when the SRR pitch is reduced.

7.2. Design and Implementation of the SoC

Having expounded on a suitable THz front-end architecture for large-scale integration of 1D near-field arrays, this section presents an entire SoC design based on this architecture.

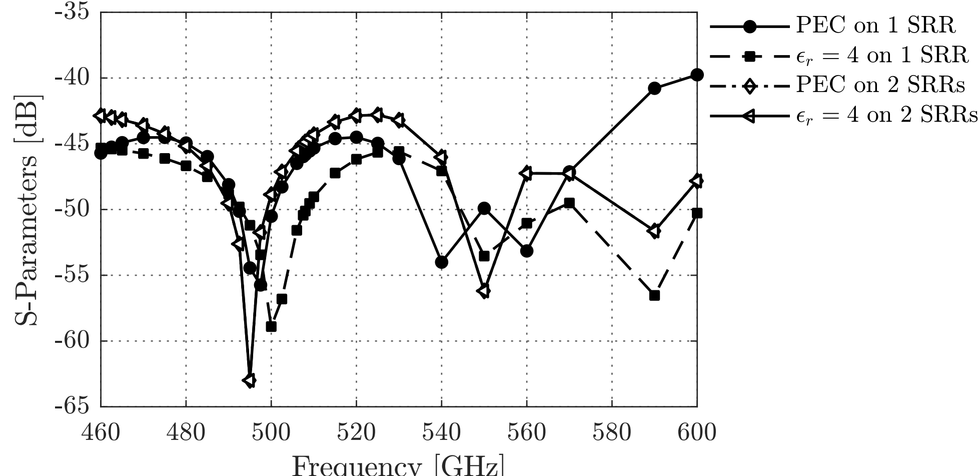

Figure 7.9.: Simulated coupling between two pixels with 50 µm pitch that are not connected through the power divider network. The coupling is taken as the parasitic power received at one detector output (DETx) while driven by another resonator input port (OUTy) and includes complete feed layout as shown in Figure 7.4.

So far, most studies on integrated THz systems do not go beyond prototype implementations by the standards of modern integrated systems. As such, they typically implement only the THz functionality and have to rely on additional external equipment and electronics for post-processing. Although some studies on the large-scale integration of THz detectors and THz sources with digital pixel selection logic have indicated directions towards more integrated THz systems [20], [116], being components for far-field imaging, they innately require secondary hardware in form of external optics and a radiation or detection counterpart to be practical. Interestingly, such practical limitations to integration are not present for THz near-field imaging. Here, all functionality, including illumination, sensing, detection, and post-processing can be integrated on a single die, thereby allowing to get rid of every secondary hardware – enabling to build a stand-alone THz imaging device.

7.2.1. System-on-a-Chip Architecture

Figure 7.10 shows the chip micrograph of the SoC. The total die size is 1.75 mm×6.10 mm. The sensor array comprises a total of 128 pixels. The sensing strip length is 3.2 mm, which represents the object's size limit for 1D scans. However, the architecture presented here is scalable and thereby applicable to larger arrays and die sizes. Two options for chip-to-package interconnects are supplied. The chip can be connected either via wire bonding or via thermocompression bond bumps and through-silicon vias (TSVs), which

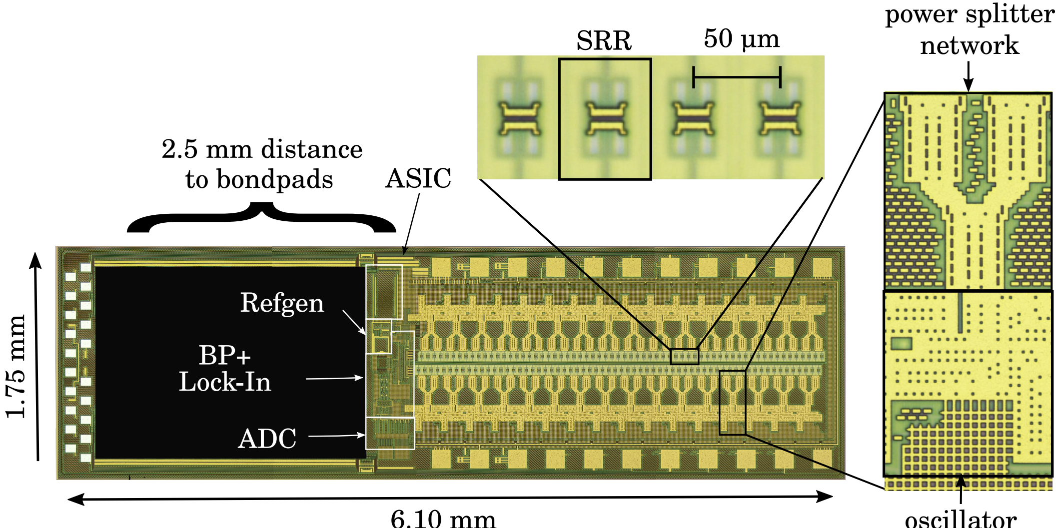

Figure 7.10.: SoC chip micrograph (6.10 × 1.75 mm^2). The total sensing area is 3.2 mm long. The blacked-out region contains circuits that are not related to the near-field array. After [own5] © 2018 IEEE.

will be detailed in Section 7.3.1. To prevent physical damage of the bondwires in the wire bonding option, some separation of the sensing area to the bond pads is required. Hence, a 2.5 mm long spacer is introduced. The spacer area contains circuits that are not related to the SoC and thus has been blacked-out in the micrograph.

Figure 7.11 shows the block diagram of the chip. An overview of the SoC's functionality and the architectural choices is given as follows:

- **Illumination/ Sensing/ Detection:** The array consists of two 64-pixel rows of SRRs and SiGe-HBT power detectors. Each row is divided into 16 subarrays of four pixels that are driven concurrently from an individual chopped 0.56 THz TPO (Section 7.2.2) using the power splitter network presented in Section 7.1.1.

- **Rolling Shutter Operation:** The array is operated in a rolling shutter mode. Only a single TPO and a single detector are powered on at a time, and the sensing array is scanned sequentially. This architectural choice is motivated by the low efficiency of on-chip THz sources, as detailed in Chapter 3. More particularly, a concurrent illumination of a large-scale array would increase power consumption significantly [20], which is especially harmful in view of potential temperature-sensitive imaging objects placed in close proximity to the chip. By contrast, the rolling shutter mode allows a scalable circuit architecture with low power consumption.

- **Analog Signal Conditioning:** The sequential operation furthermore enables implementation of a global read-out chain. Hence, all pixels share an active p-channel MOSFET (pMOS) load. Since the realized SiGe-HBT detector circuit requires a

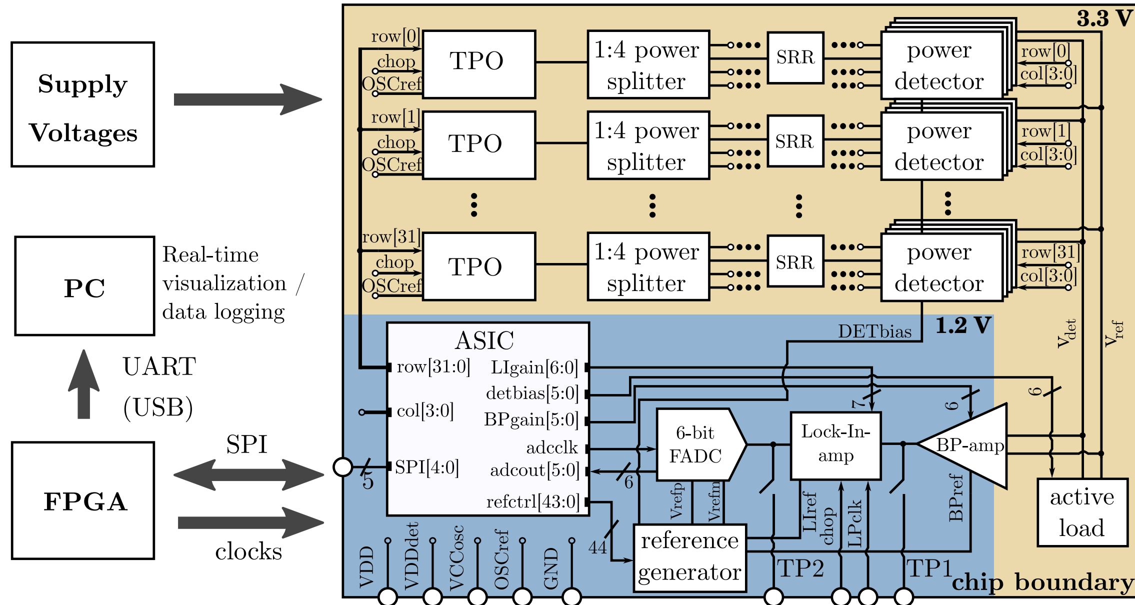

Figure 7.11.: Block diagram of the implemented SoC with the externally required components. The chip comprises a total of 128 near-field pixels and an on-chip lock-in amplifier read-out. An application-specific integrated circuit (ASIC) controls pixel selection (row, col) analog-to-digital converter (ADC) clocking (adcclk) and gain and reference settings of the read-out (LIgain, detbias, BPgain, refctrl).

high supply voltage in the range of 3.3 V (Section 7.2.3), a variable gain band-pass amplifier is used to condition the analog signal for low-voltage 1.2 V mixed-signal post-processing (Section 7.2.4).

- **Lock-In Amplification:** As detailed in Section 5.2.3, low-frequency noise of the SiGe-HBT power detector can severely limit the achievable sensor sensitivity for CW operation. In addition, the noise 1/f-noise contribution of the shared active pMOS load exaggerates the problem. Therefore, the THz wave for sensor illumination is chopped by periodically powering down the active TPO. Subsequent on-chip demodulation of the down-converted rectangular signal is facilitated by a LIA (Section 7.2.4).

- **Analog-to-Digital Conversion:** The chip can be operated either by monitoring the analog outputs of the band-pass amplifier or the lock-in amplifier (TP1 and TP2 in Figure 7.11) or in a fully digital mode. Therefore, the lock-in amplifier output is digitized with a 6-bit flash ADC (Section 7.2.5).

- **Digital Interfacing/ SoC Reference Control:** To be robust to process variations and be compatible with a wide range of imaging scenarios, the SoC is equipped with means of adjusting the gain and the bias voltages of the read-out chain digitally.

In addition, a band-gap reference generator is used to provide process, voltage, and temperature (PVT) stable voltages to the chip. A cointegrated ASIC provides all digital functionality including the control of the reference voltages, the control of the rolling shutter pixel select logic, the procvessing of the ADC signals, and the external communication based on an SPI interface. The ASIC was synthesized directly from Verilog-Code using the standard cell library provided by the foundry.

The following sections provide more detailed descriptions of the individual circuit blocks.

7.2.2. Triple-Push Illumination Source

The on-chip oscillators are based on the strip-line shielded common-collector TPO topology that is described in Section 5.2. Figure 7.12 shows the circuit schematic. The RF design of the TPO is similar to the one shown in [19]. The fundamental oscillation frequency is set by the 6.5 fF large MIM-capacitor C_E, the base-emitter junction capacitance of the $5\times0.13\,\mu m\times0.96\,\mu m$ large core devices (T_1-T_3) and the stripline TL_B, which has a simulated equivalent inductance 37 pH. The dependence of the oscillation frequency on the base-emitter junction capacitance allows for frequency tuning by changing the base bias voltage. Due to the strong reverse transmission behavior of the common-collector Colpitts topology, the collector reactance has a high impact on the third harmonic power matching at the base terminal [20][own10]. Therefore, a 12 pH collector inductance (TL_C) is used to tune out the imaginary part of the base input impedance at the third harmonic and optimize the third harmonic power. In accordance with [19], the TPO layout was simulated with a 3D full-wave EM solver (Ansys HFSS). Circuit simulations based on a HICUM device model predict an output power of 50 µW and an oscillation frequency around 0.53 THz.

The TPO biasing circuit supports electronic chopping. The base bias is provided with a quarter-wavelength stub (TL_{bias}), which is shorted with a self-resonant capacitor at the third harmonic (C_{bias}). A current-mirror biasing scheme is applied for external reference current control (OSC_{REF}), source chopping, and oscillator addressing. To allow rolling shutter operation, a single oscillator is selected with the row enable signal (row), provided by thin-gate-oxide 1.2 V CMOS logic from the ASIC. The row signal is additionally and-gated with an externally supplied chopping signal (chop). The resulting signal is used to periodically turn on/off the selected TPO by switching the common DC base bias between a low-ohmic connection to OSC_{REF} and ground through analog switches $M_{1,2}$. The pull-up and pull-down time constants were selected to allow chopping at frequencies higher than the low-frequency noise corner of the detector read-out ($\approx$100 kHz).

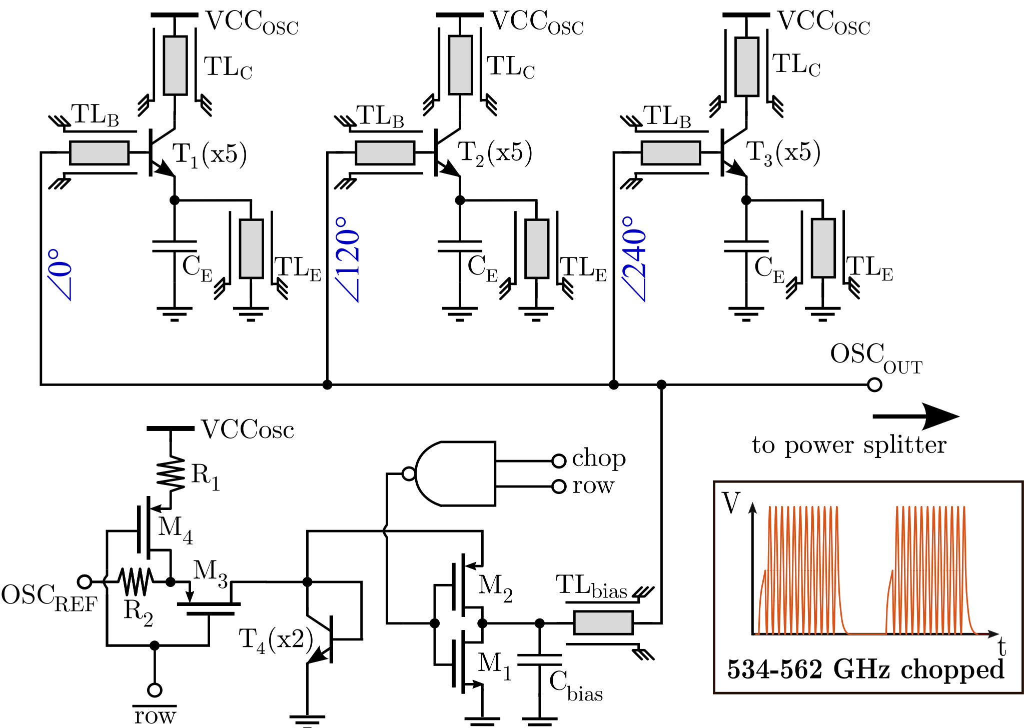

Figure 7.12.: Circuit schematic of the triple-push oscillator including base pull-down logic for oscillator selection and source chopping. The emitter area of the SiGe-HBT devices is $A_E = 0.12{\times}0.96\ \mu m^2\ ({\times}1)$.

7.2.3. Power Detection Circuits

Figure 7.13 illustrates the circuit hierarchy of the analog front-end. After the SRRs, the THz wave is coupled capacitively ($C_c = 25\,fF$) to SiGe-HBT power detectors with $0.12\,\mu m{\times}0.96\,\mu m$ emitter area (T_6). As described in Section 5.2.3, the base-emitter junction non-linearity of the high-speed transistors is exploited for broadband THz rectification beyond the device f_{max} [120].

To avoid mitigation of the detector sensitivity due to common-mode noise, the detector circuit exhibits a pseudo-differential architecture. Two SiGe-HBT devices, T_5 and T_6, are biased at the same current through the globally shared current mirror formed by M_5, M_6, and M_7. The THz wave is coupled directly to the base of T_6, and T_5 serves as a reference device. The quiescent detector current can be digitally controlled with 5-bit accuracy through an integrated current-steering digital-to-analog converter (DAC) (not shown) to cover the bias voltages in which the SiGe-HBT devices are most sensitive to THz waves [19], i.e., the DAC supplies the currents for active device operation at base bias voltages V_{BE} between 0.8 V–0.86 V. Contrary to the implementation in [19], where the detector base is inherently biased by the oscillator base node, the DC isolation provided by C_c necessitates a distinct detector bias circuit. For this purpose, a resistive biasing

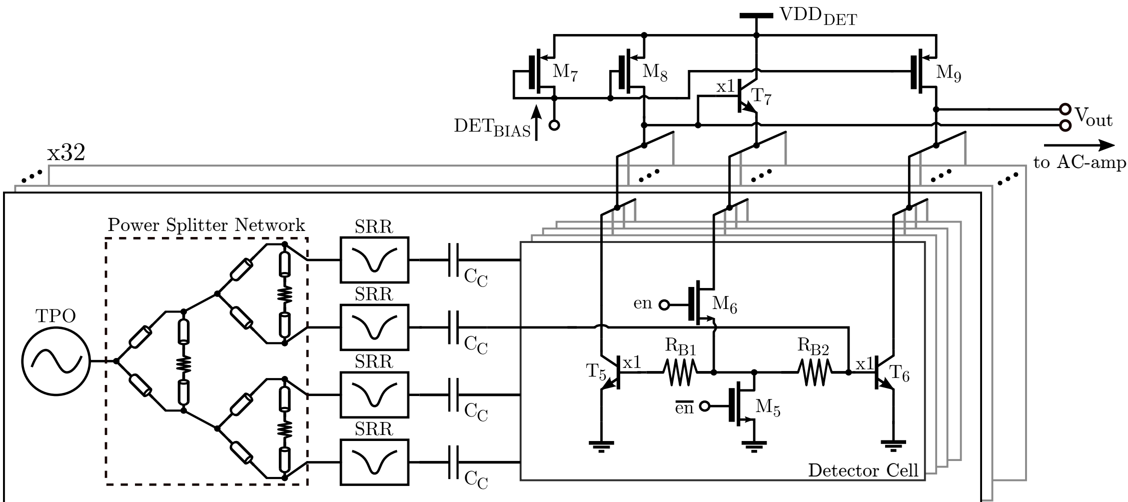

Figure 7.13.: Circuit architecture of the THz front-end and analog read-out circuitry. The unit emitter area of the SiGe-HBT devices is $A_E(x1) = 0.12 \times 0.96\ \mu m^2$. After [own5] © 2018 IEEE.

scheme with the base resistors R_{B1} and R_{B2} was selected. The resistors thereby serve as high-ohmic blockers for the THz signal and prevent leakage of the THz power to T_5. It is noted that resistive biasing was favored over biasing with a THz choke because there is practically no chip area available for transmission line implementation in the vicinity of the SRRs. However, resistive biasing contributes significant thermal noise at the detector output. More particularly, since the detector device T_6 is biased in the active region, the noise current of R_{B1} and R_{B2} is amplified by the device's current gain. Hence, the resistor size has to be selected as a compromise between noise performance and RF-blocking characteristics. For the present design, a resistor size of $600\,\Omega$ was selected, resulting in an 8.4 dB reduction in noise performance.

The detector base current is applied through a beta-helper current mirror reference branch. Whereas the mirror device (T_5) is implemented at the pixel level, and the beta-helper transistor (T_7) is shared among all pixels. Detector selection can thus be performed with small-size thick-gate-oxide analog switches ($M_{5,6}$) that are controlled by the ASIC after voltage level conversion from 1.2 V to 3.3 V logic levels. As described in Section 7.2.1, only a single detector in the array is selected at a time, while all the other detectors are off. Thereby, only one detector drives the shared active pMOS load formed by M_6 and M_7. The load devices are designed to be large enough so that their noise contribution is negligible ($W_{6,7}/L_{6,7}$=200 µm/10 µm).

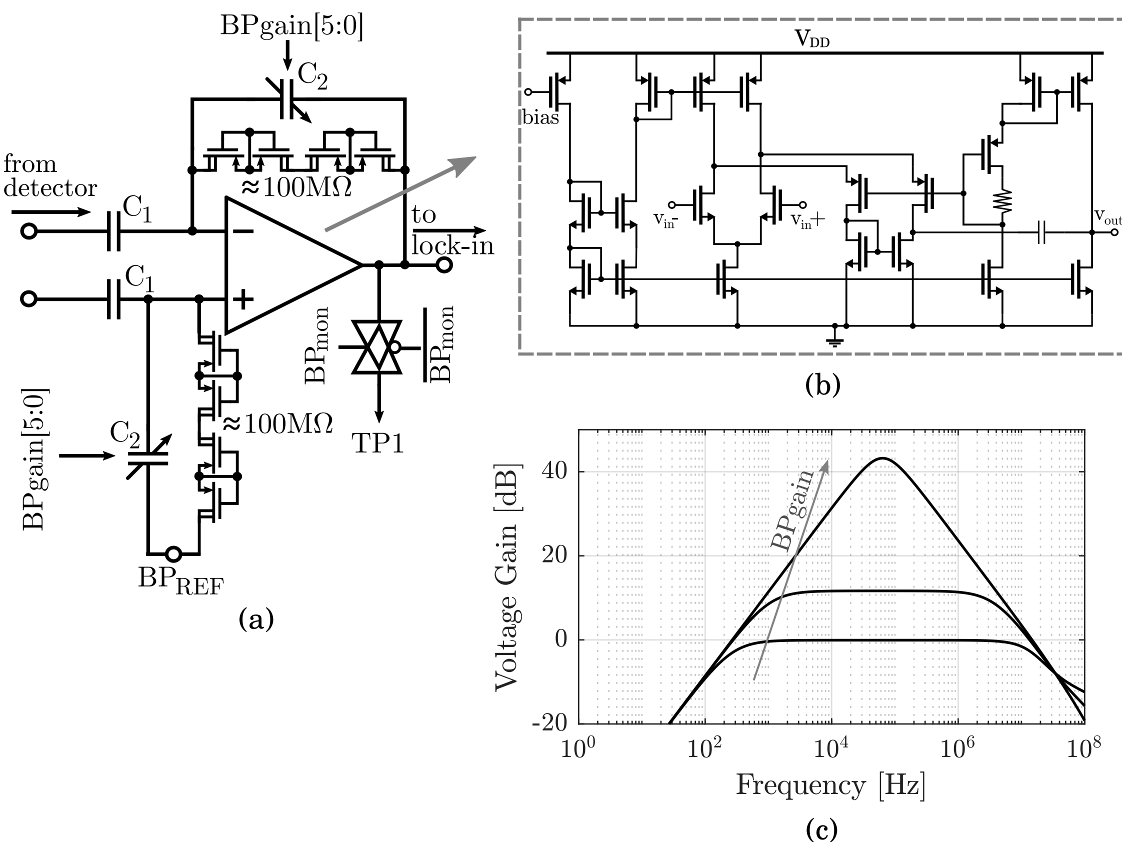

Figure 7.14.: Schematic of the AC-coupled band-pass amplifier with digital gain control (a), schematic of the low-voltage op-amp used in the band-pass amplifier (b), and simulated voltage gain versus frequency for maximum, medium, and minimum gain setting (c).

7.2.4. Analog Signal Processing

AC-Coupled Band-Pass Amplifier

The detector output requires buffering and DC-level conversion to be subsequently processed with either the 1.2 V read-out chain or with external measurement equipment. For this task, a band-pass amplifier with DC offset rejection is implemented [190]. The amplifier is based on an operational amplifier (op-amp) in a feedback configuration. Figure 7.14 shows the schematic. The core amplifier is a noise-optimized CMOS two-stage op-amp with n-channel differential inputs and a Miller compensated class-A output stage. Contrary to using the typically employed current-mirror loaded differential input stages, current-source loads, and subsequent differential to single-ended conversion with a folded cascode current mirror is used to increase the common-mode input range [191]. Owing to the thereby achieved large input common-mode range of 0.38 V–0.96 V, the op-amp can serve as the core amplifier in multiple other circuits of the SoC. The op-amp furthermore shows an open-loop gain of 62 dB, 58° phase margin, a gain-bandwidth product of 15 MHz, and a

noise spectral density of around $100\,\mathrm{nV}\,\sqrt{\mathrm{Hz}}^{-1}$ in the chopping frequency range around 100 kHz. Therefore, the noise contribution of the amplifier is minor, and the total noise of the read-out chain remains dominated by the detector noise.

The band-pass amplifier exhibits a low-frequency high-pass corner defined by parallel RC-feedback. The feedback comprises MOS-bipolar pseudo-resistors to achieve feedback resistance values of around 100 MΩ with small area consumption and digitally-controllable MIM-capacitor banks to control the gain by adjusting the ratio C_1/C_2. The midband center frequency (≈70 kHz) is aligned to cover the targeted chopping frequency range, and the midband gain can be set in a range between 0 dB–42 dB. This enables robust signal conditioning for different oscillator and detector bias points. The band-pass output is also multiplexed to a pad, which is used as a test point (TP1) for array characterization in an analog read-out mode (see Section 7.4.3).

Lock-in Amplification

The LIA schematic is presented in Figure 7.15. First, a passive switched capacitor (SC) mixer down-converts the electronically chopped output of the band-pass filter to DC by multiplying it with the same chopping signal deriving the base-bias of the TPO. The resulting pseudo-differential signal is then filtered with a third-order SC low-pass filter, whose cut-off frequency is carefully selected to allow for a real-time video-rate read-out while minimizing the total integrated noise at the output. A read-out rate of 28 fps for 128 pixels allows for a maximum integration time of around 280 µs per pixel. Assuming that the RC filter requires a settling time of 4τ (where τ is the filter time constant) to reach a steady-state, this results in a filter cut-off frequency of around 2.27 kHz. This is adjusted with an external sampling clock LP_{clk} of 1.5 MHz, which can be further tuned to optimize the frame rate and the SNR. The filtered signal is buffered through an instrumentation amplifier based on the same op-amp as shown in Figure 7.14, whose gain can be adjusted in the range of 0 dB–30.8 dB via a digitally programmable resistor bank.

7.2.5. Digital Interfacing and ASIC

The output of the instrumentation amplifier is thereafter sampled with a 6-bit flash ADC. The flash architecture was chosen to support fast sampling for the potential use of successive approximation algorithms and runtime adjustments of the DR to accommodate oscillator and detector PVT variations and different sensor response values due to different materials. The measured effective number of bits (ENOB) for the ADC is 5.85, and

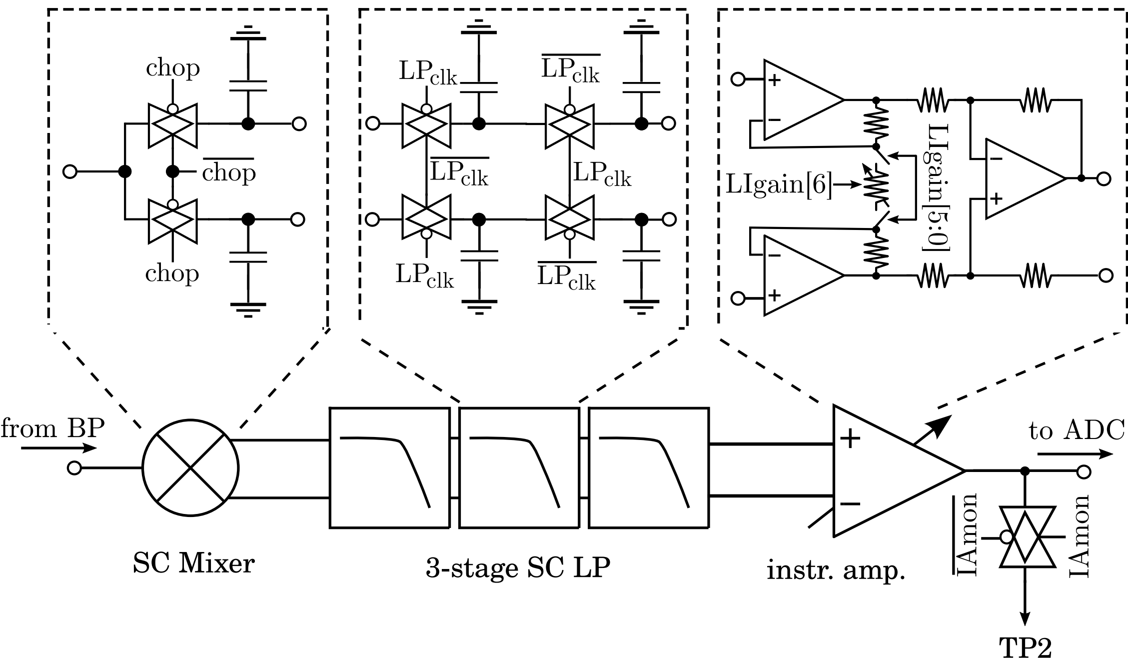

Figure 7.15.: LIA schematic. The LIA comprises a switched-capacitor mixer, a 3-stage SC low-pass filter and a variable-gain instrumentation amplifier. After [own5] © 2018 IEEE.

the ADC reference voltage is programmable to a minimum voltage range of 300 mV (min. LSB ≈ 4.7 mV).

Figure 7.16 shows the block diagram of the ASIC. A finite state machine sequences the processing of the flash ADC data and the writing of the on-chip control registers for the read-out gain, the voltage references, and the detector bias. The ASIC furthermore includes an SPI slave for communication with an external controller. To economize on the number of I/O-pads, the ADC sampling clock is directly derived with a divide-by-10 clock divider from the clock of the SPI bus. The flash ADC clock furthermore triggers the increment of a row/column counter to sequence the rolling-shutter operation with a subsequent encoding of the binary counter data into a one-hot code. To enable zooming into a sub-array or monitoring of only a single pixel, the counting range can be adjusted with row and column limiting registers. The rolling shutter control scans through the defined pixel range and continuously streams out the ADC values taken at the end of the pixel observation periods through the SPI interface. As such, only a single ADC value is captured for every pixel.

However, the array can be programmed to dwell on a single pixel for multiple ADC samples by setting the limiting registers so that only a single-pixel is selected. As such, external software averaging or accumulate-and-dump filtering can be used to increase the digital DR. It is noted that the limiting registers can be reprogrammed on-the-fly so that fast

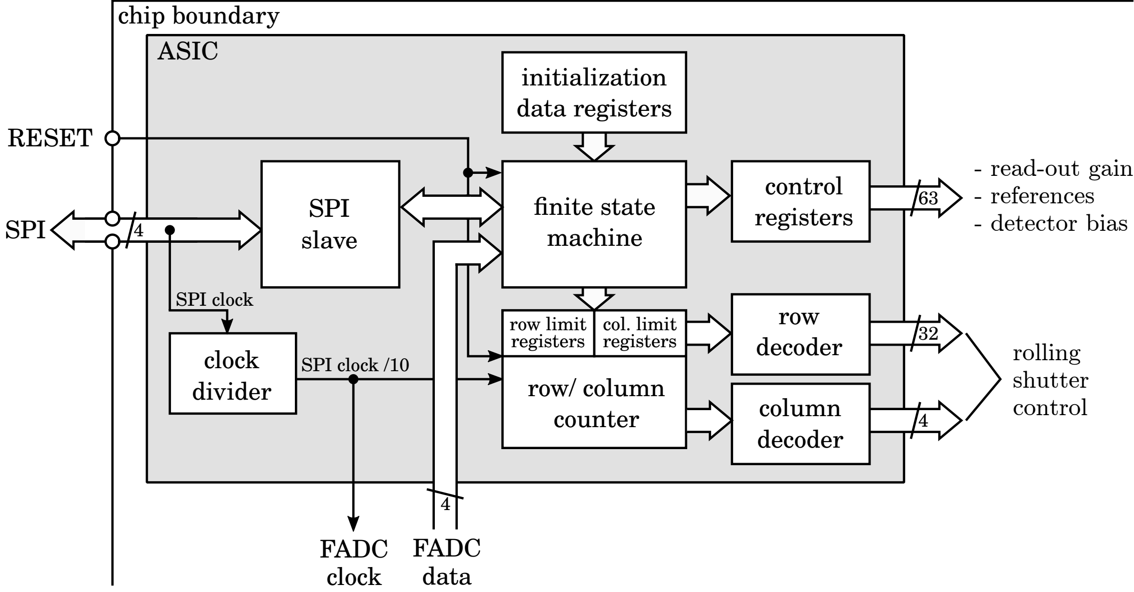

Figure 7.16.: Block diagram of the ASIC.

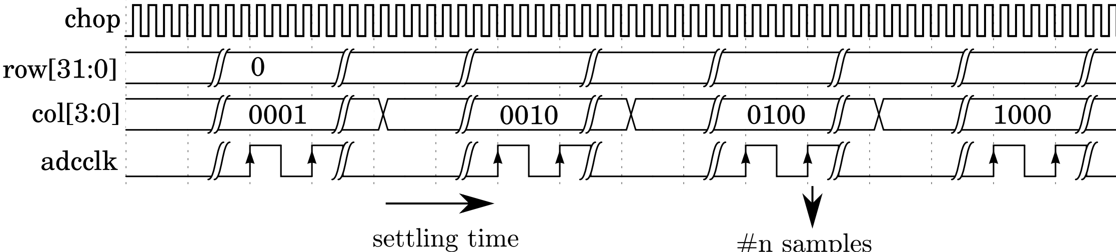

Figure 7.17.: Simplified timing diagram of the rolling shutter mode taking multiple samples per pixel.

rolling shutter operation is still facilitated in this operation mode. Figure 7.17 shows the related timing diagram. As to be detailed in Section 7.4.3, after each pixel switch, a settling time for the DC of the read-out chain must be awaited before the ADC samples can be considered valid.

7.2.6. SoC Reference Generation

To allow accurate long-term measurements, the temperature stability of the read-out chain is of critical importance. Therefore, the SoC features a variable biasing scheme that can either use dedicated external low-noise voltage/current references for highly demanding applications or an on-chip reference generator enabling a compact sensor module design and fast digital reconfiguration. The supply voltages for the THz front-end in the 3.3 V-domain, i.e., the oscillator and detector voltages, are supplied exclusively externally because of the high current requirements. The critical read-out voltages in the 1.2 V-domain

with absolute voltage dependence and low current drive requirements such as the ADC and lock-in amplifier reference voltages can be either derived directly from a band-gap voltage reference and digitally controllable DC-amplifiers or they can be supplied externally. The on-chip band-gap circuit is a BiCMOS ultra-low-voltage reference [192], [193] with 3-bit trimmable sink resistors to compensate for PVT variations of the voltage and temperature curvature, showing a simulated nominal output voltage of 600 mV and a temperature coefficient of 13.66 ppm/°C between 0 °C–100 °C.

7.3. Sensor Module

7.3.1. Packaging

Since the sensor should support the imaging of wet and soft samples in direct-contact measurements, proper sensor encapsulation and packaging are of critical importance for practical use scenarios of the SoC. The first level of sensor protection is facilitated by the 2 µm thick passivation layer, which is part of the BEOL-stack of the technology. The SoC features the two packaging options. The first option, depicted in Figure 7.18(a), utilizes TSVs to connect the die to a PCB carrier via thermocompression bond bumps through its backside. Ultimately, this is the preferred option as it leads to a flat scanning surface, thereby facilitating imaging of objects with dimensions exceeding the size of the die itself. Although the chip mask-set provides the means of enabling this option, TSVs with patterned backside metallization have been unavailable for the manufacturing process in this work. It is, however, planned to implement TSVs in future fabrication cycles.

Since the potential lack of TSV integration was already presumed during the design, the SoC was equipped with a second packaging option based on regular wire-bonding, as shown in Figure 7.18(b). As noted in Section 7.2.1, a 2.5 mm safety distance from the sensors to the bondpads is introduced, which increases the allowed object size for flat solids given the uneven scanning surface resulting from the bondwires. To furthermore mitigate the risk of collisions between bondwires and the scanned object and to avoid current conduction between bondwires in wet environments, the bondwires and the PCB area surrounding the chip are encapsulated with the preselected epoxy resin so that only the sensing surface is left exposed.

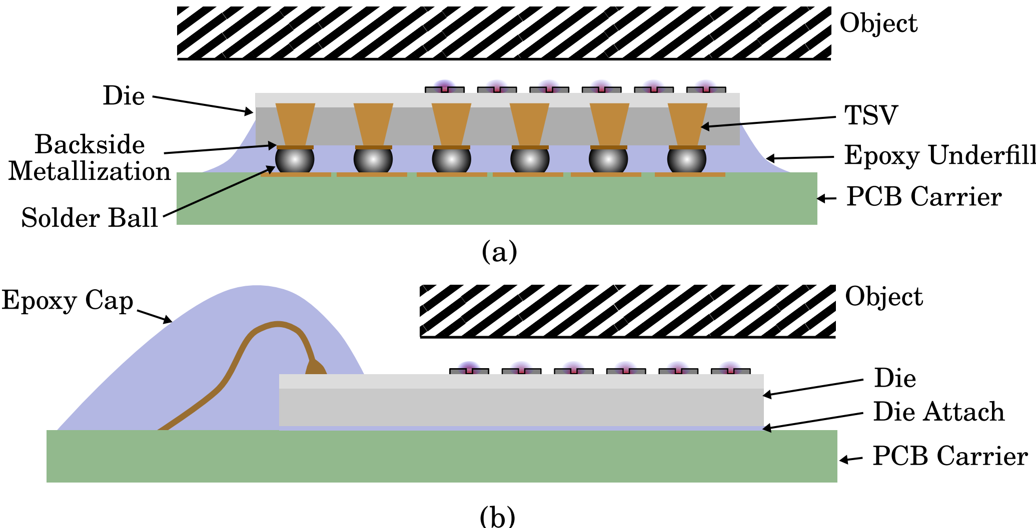

Figure 7.18.: Illustration of the two packaging options. SoC assembly with the die connected to a PCB carrier through the chip backside using TSVs (a) and standard wire-bonding and bondwire encapsulation (b).

7.3.2. Module and Electronic Periphery

The sensor module is assembled in a three-layer FR-4 PCB stack with the top PCB carrying the SoC and the lower two PCBs carrying discrete electronic periphery. Figure 7.19 depicts the near-field sensor module and a close-up of the encapsulated SoC. The dimensions of the module are 6 cm×5 cm×3 cm. The total power consumption of the SoC is between 37 mW–104 mW, which is dominated by the oscillator power consumption, which is 30.4 mW for $V_{CCosc} = 1.6$ V and 97.4 mW for $V_{CCosc} = 2.2$ V. The detector circuitry including the 3.3 V logic consumes 1.6 mW, and the 1.2 V mixed-signal read-out circuitry consumes 4.8 mW. All supply voltages are derived from the 5-V power supply of a USB connection using linear voltage regulators, resulting in a total power consumption of 0.6 W for the complete imaging module.

The SoC is interfaced with a Xilinx Spartan 6 field-programmable gate array (FPGA) via an SPI bus that is clocked at 10 MHz. The chopping and low-pass clocks are directly provided by the FPGA. The chip continuously streams out the ADC values to the FPGA via SPI, which passes the output to a computer via USB after averaging and offset-correction. Hence, the module can be controlled and powered with a single USB-port from the computer level with software-packages based on MATLAB or Python.

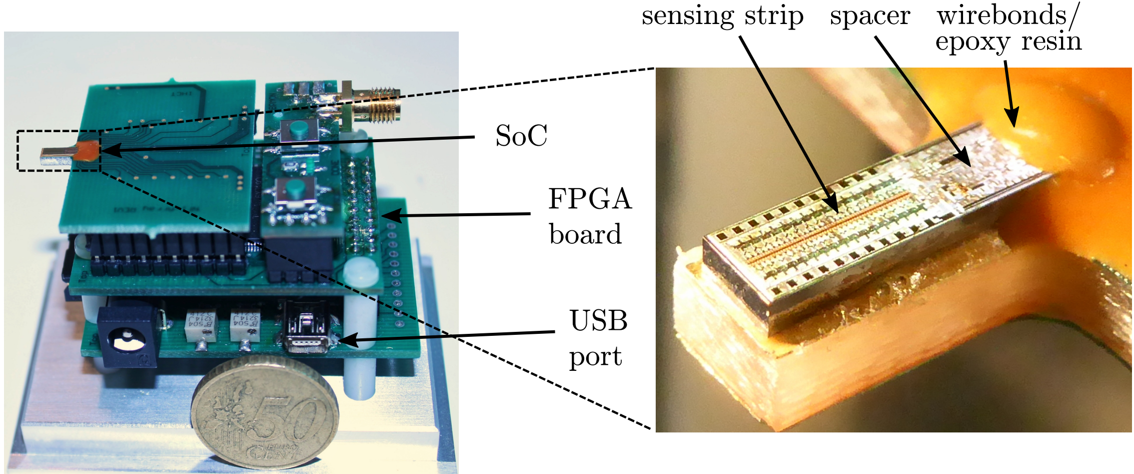

Figure 7.19.: Picture of the packaged imaging module with a 50 cent euro coin for size comparison. The chip is wire-bonded and encapsulated with epoxy resin. After [own5] © 2018 IEEE.

7.4. Experimental Characterization

This section details the experimental characterization of the SoC. The parameters characterizing the sensor operation can be separated into two groups. The first group is related to the spatial distribution of the electrical near-fields in the sensing volume and includes parameters such as the lateral resolution and the response decay rate. The second group is related to the electronic performance of the mixed-signal read-out circuitry of the SoC and encompasses the DR, the sensitivity, and reliability considerations such as pixel variations and pixel cross-coupling. However, an integral characterization of the inherent sensor characteristics is problematic because of the employed incoherent sensing scheme and the limitations of the available THz on-wafer measurement equipment. For example, the SRR excitation frequency and the SRR stopband characteristics cannot be measured directly when embedded in the SoC. In order to nevertheless allow for proper deembedding of the sensor characteristics, the output power and frequency tuning range of the oscillator were first measured with a breakout circuit in free-space. Another problem is the lack of reference materials and objects with well-defined complex permittivity at the measurement frequency around 550 GHz and proper microscale geometry for the characterization of the sensor sensitivity and the lateral resolution. In view of these limitations, some of the parameters derived in this section remain estimations based on the currently available measurement capabilities.

The measurements conducted with the SoC were performed primarily with the measurement setup depicted in Figure 7.20. An object was positioned above the sensing surface with a 3D translation stage at a wafer probe station to measure the spatial and static

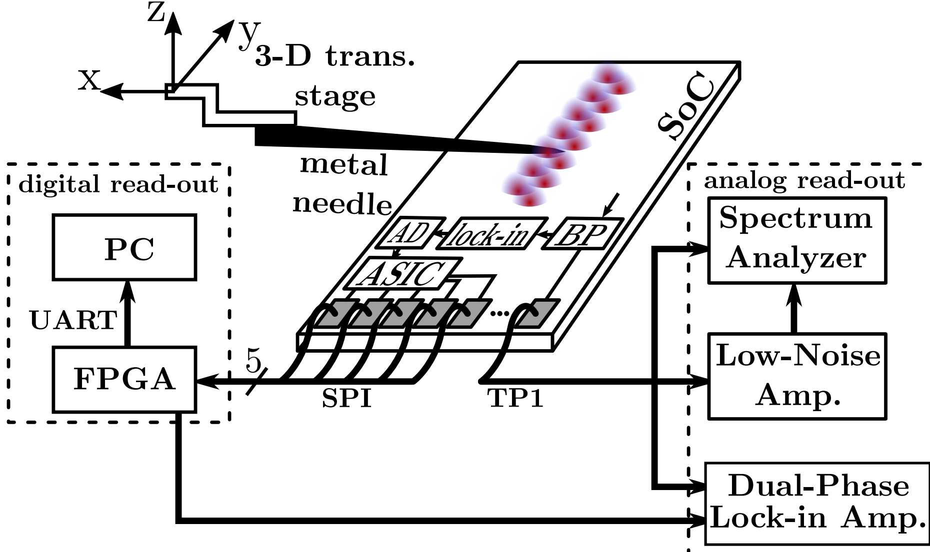

Figure 7.20.: Characterization setup of the SoC. A metal needle is positioned above the sensing surface for characterization of the sensor response. After [own5] © 2018 IEEE.

sensor response for both the analog read-out measured at TP1 and the digital read-out using the on-chip LIA and ADC. The measurement of the spatial resolution is inferred from [19], where a single-pixel version of the sensor is similarly characterized on a wafer probe station with the object mounted to a 3D translation stage. A more detailed description of the experimental methods used to measure the different parameters is given in the corresponding sections.

7.4.1. Oscillator Breakout Measurements

Because of the aforementioned problems of measuring the oscillator characteristics of the SoC, a break-out circuit of the TPO was fabricated to facilitate free-space characterization. For this purpose, a wideband lens-coupled on-chip circular slot antenna [132],[own10] was designed to operate in the same impedance system to preserve the inherent oscillator characteristics. The backside of the chip was glued to a 3-mm hyper-hemispherical silicon lens. The additional implementation loss of the antenna system due to finite antenna efficiency and multiple reflections at the lens aperture [194] was estimated to be around 20 %–30 % for the antenna operating in the transmit mode based on full-wave EM simulations (Ansys HFSS).

Figure 7.21(a-d) shows the measurement setups respectively for the free-space frequency and power measurements, the breakout micrograph, and the measured results. The frequency tuning range of the oscillator was measured with a spectrum analyzer and an

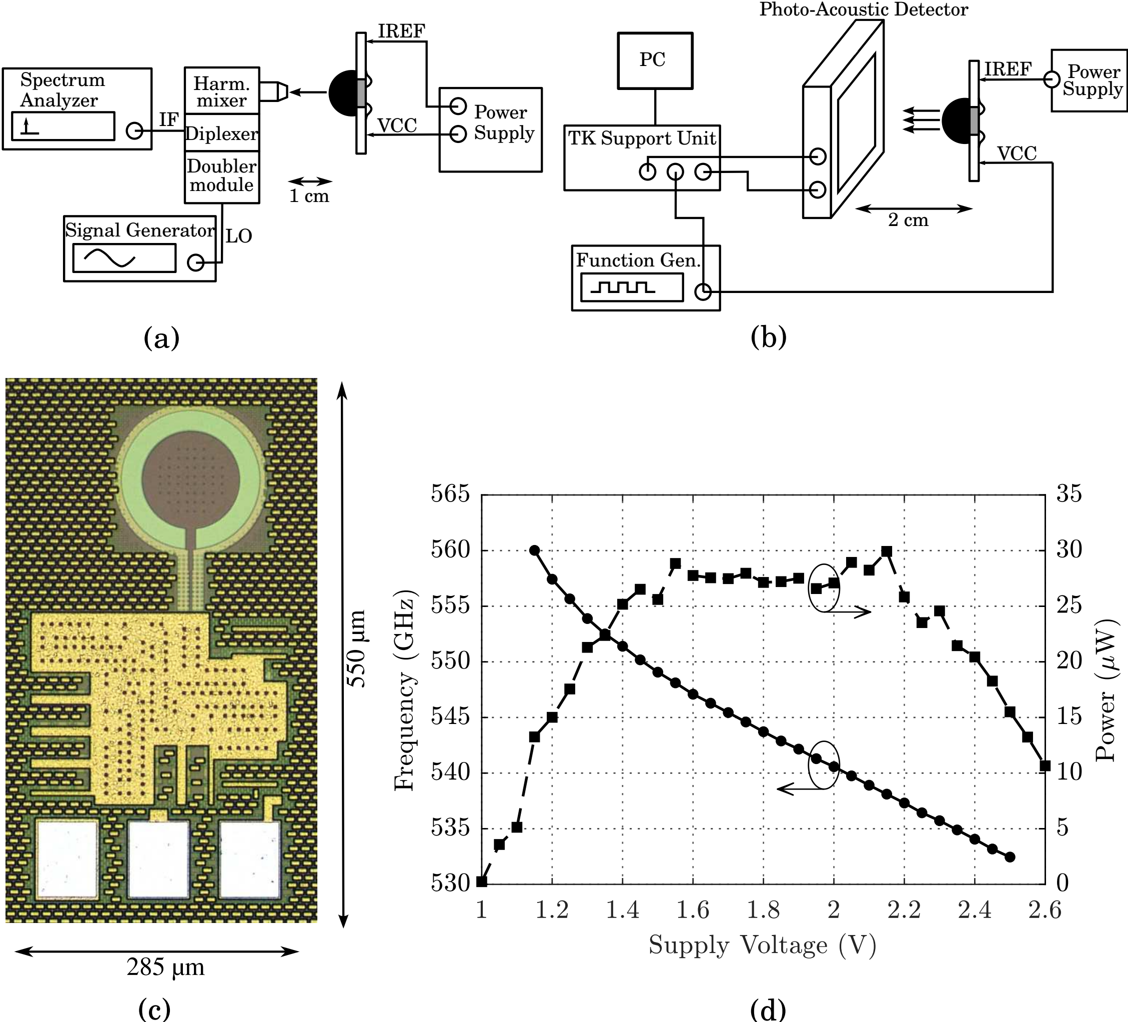

Figure 7.21.: TPO breakout measurements are gathered, including frequency measurement setup (a), power measurement setup (b), breakout micrograph (c), and measured frequency and power of the TPO as a function of supply voltage (d). After [19] © 2017 IEEE.

antenna-coupled 18th-harmonic mixer from Radiometer Physics, whereas the free-space output power was characterized with a Thomas Keating photoacoustic absolute power meter. The oscillator was chopped electronically at 35 Hz to avoid the influence of thermal emission on the measured power. For oscillator supply voltages between 1 V–2.6 V, the measured frequency tuning range is 534 GHz–562.5 GHz, and the radiated power stays within 5.1 µW–28.2 µW. Considering the mentioned antenna implementation loss, the maximum power of the on-chip TPO can be estimated to be around 35.25 µW.

When comparing the TPO tuning range with the rising slope of the SRR stopband (previously shown in Figure 5.12), it is visible that both are well aligned. It is noted that the base bias circuit of the TPOs in the SoC is different from the one employed in the break-

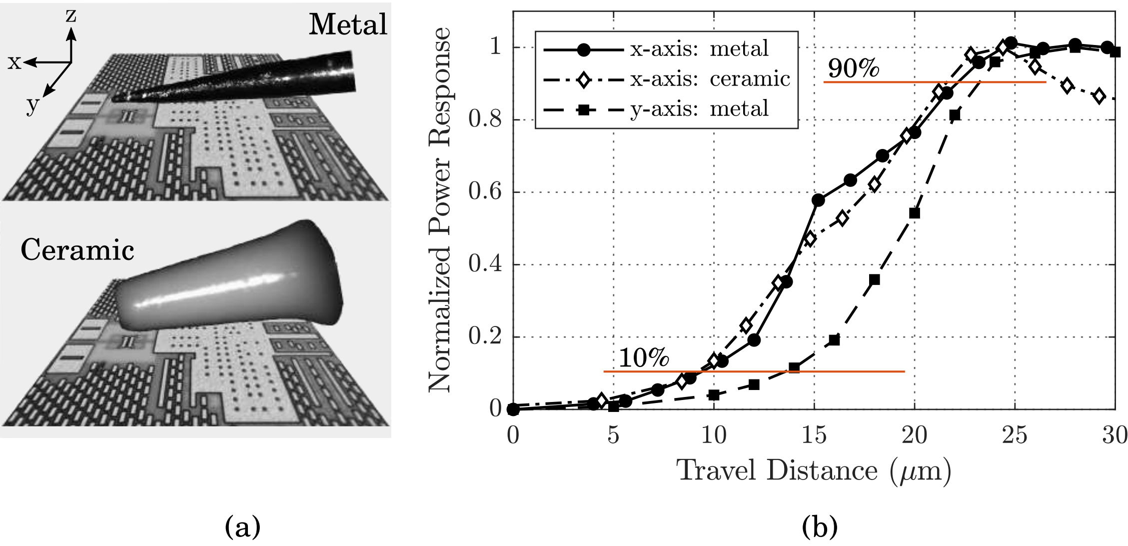

Figure 7.22.: Measured lateral resolution of the sensor for a metallic object (tip) for two different operation frequencies along x-axis (a) and y-axis (b). After [19] © 2017 IEEE.

out. In view of the resulting distinct supply-dependent device capacitances, the curves shown in Figure 7.21 cannot be mapped one-to-one to the TPO of the SoC. However, the measurement is expected to provide a reasonable estimation since all measured bias conditions can also be covered by the TPO of the SoC by appropriate adjustment of the external base-bias voltage OSC_{REF} (Section 7.2.2).

7.4.2. Measurement of the Lateral Resolution

An accurate determination of the lateral resolution according to the 10 %–90 % rising/falling edge criterion [195] requires objects that exhibit very sharp edges. As elaborated in Section 6.1.2, the perturbation of the sensor near-fields is considerable if an object is placed several micrometers apart from the sensing surface. Therefore, the edges should also be at least 5 µm–6 µm high so that the sensor can develop the full response. In view of the difficulties of fabricating such samples, the lateral resolution was estimated with acute metallic and ceramic objects, i.e., a 30 µm wide metallic tip and a 55 µm wide ceramic capillary made of Alumina Zirconia (Al_2O_3+ZrO_2) with dielectric permittivities of Alumina and Zirconia of around 10 and 22, respectively.

Figure 7.22(a) illustrates a perspective sketch of the objects placed above the single-pixel sensor. To minimize the edge rounding effects caused by the oval shape of the objects, they were positioned to be parallel to the chip surface and translated along their length (x-axis) [19]. This scanning direction allows more accurate measurement of the edge response since the edge roundness orthogonal to this direction is more distinct as compared to the

edge roundness parallel to it. However, only a single edge response can be measured in this way because the sensor stays completely covered by the object when it passed its edge. It is furthermore noted that round object edges lead to an underestimation of the resolution.

Figure 7.22(b) shows the measured normalized edge responses at 545.4 GHz [19]. For the metallic tip, the 10 %–90 % distances along x-axis and y-axis are estimated to be 11 µm–12 µm and 10 µm–11 µm, respectively. For the ceramic capillary, the edge response was only measured along x-axis. The measured 10 %–90 % distance is with 12 µm–13 µm slightly worse as compared to the metallic object, which is to be expected from simulations [19]. However, the difference is within the positioning inaccuracy of the measurement setup, which is around 1 µm–2 µm. The measurements generally show reasonable agreement with the 2D simulations from Section 6.1.2 (x-direction only) and the full-wave electromagnetic (EM) simulations presented in [19]. It is noted that for both measurements along the x-axis the plateau of the edge response seen in simulations is reproduced (see Figure 6.4). Such a plateau is not visible for the y-axis scan. All slopes, however, remain monotonic, thereby leading to a unique spatial response, which is a critical feature for imaging.

7.4.3. Analog Read-Out

Time-Domain Measurements

Figure 7.23 shows measured time-domain voltages at the band-pass output (TP1). The first plot depicts a 5 ms long time series with the array operated in rolling shutter mode. Since the dwell time per pixel was set to 1.2 ms for this measurement, the time series includes four pixel switches. The plot clearly depicts the presence of unwanted voltage spikes initiated by the pixel switch events. The spike direction and amplitude depend on between which pixels the transition happens and is repeatable for the same switching event. Therefore, it is presumed that the spikes arise from process-induced variations of the DC transconductance of the power detectors, which in combination with high-ohmic active pMOS loads lead to varying DC voltage levels at the band-pass inputs. Due to the AC-coupling, the charges on the band-pass input capacitors require rebalancing. This is a slow process because of the high feedback resistance. For some switching events, the voltage spikes are so pronounced that the op-amp rails, leaving the common-mode input range. Hence, a minimum settling time of 250 ms is introduced, which limits the maximum frame rate for the read-out of the 128-pixel array to 31.25 fps. To illustrate the behavior of the band-pass output voltage when the monitored sensor is loaded with an object, the

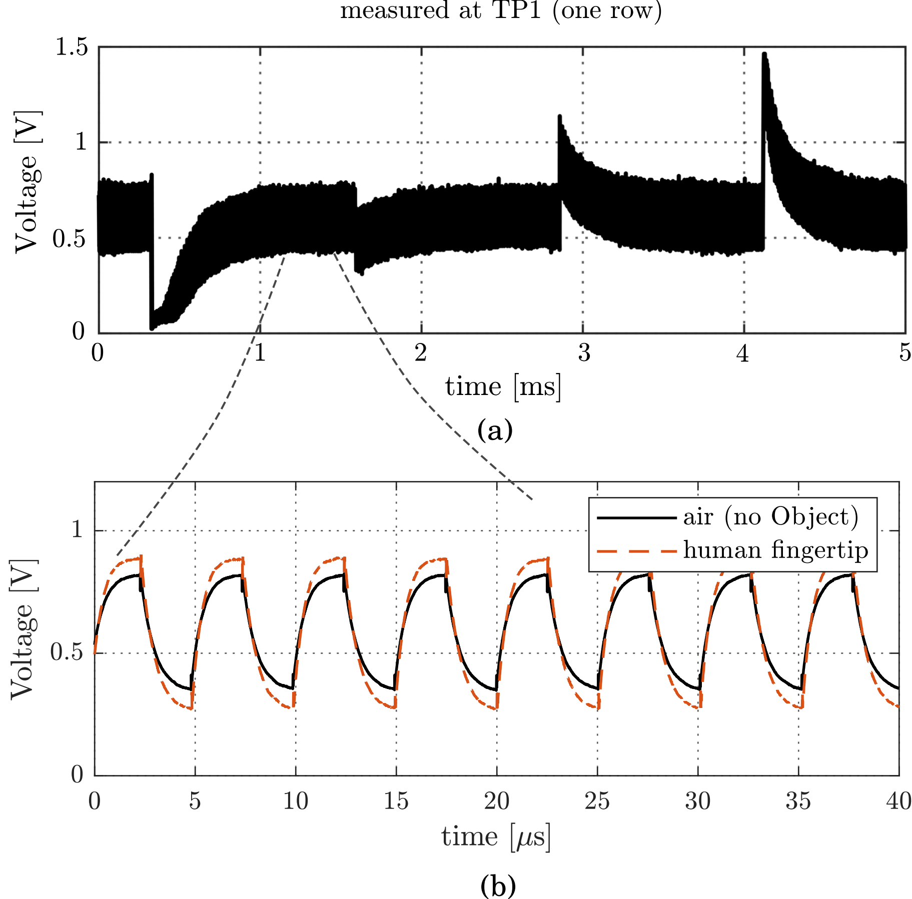

Figure 7.23.: Transient voltages measured at the band-pass output (TP1). A 5 ms time-frame including four pixel switches (a) and a 40 ms time frame for an unloaded sensor (air) and a sensor loaded with a human fingertip (b). (V_{BE} = 816 mV, G_{BP} = 0 dB, f_{chop} = 200 kHz).

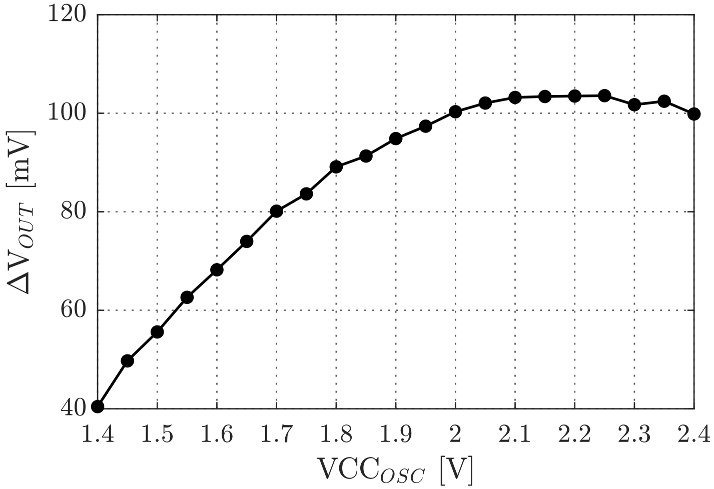

Figure 7.24.: Measured voltage response of a single pixel for full coverage with a metal needle as a function of oscillator supply voltage, VCC_{OSC}. (V_{BE} = 816 mV, G_{BP} = 0 dB, f_{chop} = 100 kHz). After [own5] © 2018 IEEE.

measured voltage for a 40 µs time series for a single pixel being unloaded (air) and loaded with a human fingertip is shown Figure 7.23(b). Even without object coverage, a significant AC offset is present, which underlines the necessity of defining the voltage response as a difference between loaded and unloaded conditions (Equation 5.5).

Measurement of the Voltage Response

Figure 7.24 shows the maximum voltage response of a single sensor as a function of the oscillator supply voltage. A detector base bias voltage of 0.816 V, a band-pass gain of G_{BP} = 0 dB, and a chopping frequency f_{chop} = 100 kHz was chosen as the nominal operation setting after experimentally optimizing the voltage response with respect to the voltage headroom of the read-out circuitry. The measurements were performed by subtracting the RMS voltage of the first chopper harmonic at TP1 with full metal-needle coverage in direct contact from the measured value with no object present. The highest sensor response of around 103 mV is achieved between VCC_{osc} = 2 V–2.2 V. The trend shows good correlation to the single-pixel results exhibiting the same TPO and SRR combination [19].

Noise Measurements

The measured and simulated noise-voltage spectral density for different detector base bias voltages is given in Figure 7.25. The noise roll-off caused by the limited bandwidth of the detector read-out accurately follows the trend predicted by simulation, whereas

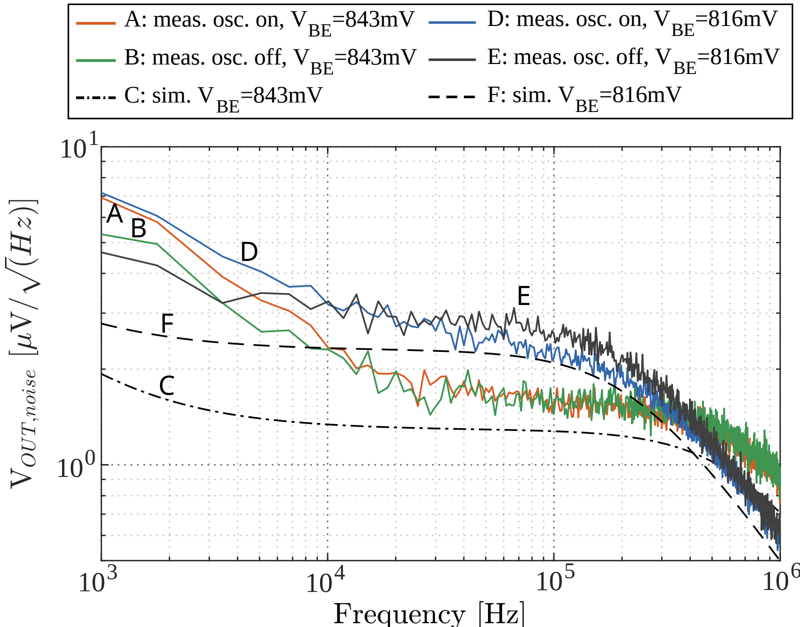

Figure 7.25.: Measured and simulated noise voltage at the band-pass output (TP1) (G_{BP} = 0 dB) for different detector base bias voltages (V_{BE}). After [own5] © 2018 IEEE.

the measured noise floor is around 2.2 dB higher compared with simulations. The curve pairs A,B and D,E compare the measured noise floor when the oscillator is continuously running or is turned off. The differences between the curves are found to be not significant and verify that no broadband noise is downconverted by the square-law detector.

Dynamic Range Measurements

The DR of the analog read-out was characterized with an external 5210 Dual Phase Analog LIA set to a 1 ms integration time with 12 dB/Octave filter slope, which corresponds to an equivalent noise bandwidth (ENBW) of 125 Hz and a frame-rate of 1.17 fps for the array considering settling to 99 % of the final value of each pixel. The oscillator was operated at VCC_{OSC} = 2.2 V and with the aforementioned nominal operation setting. The LIA reference was directly derived from the chopper signal of the FPGA. Figure 7.27 shows a 180 s long time series that was recorded at TP1. The output amplitude exhibits a compelling low-frequency background drift with a long-term noise voltage of 322 μV_{rms}. Since the TPO and detector operate well beyond f_{max}, the total power transfer is strongly vulnerable to temperature variations.

However, because of the applied source modulation, the low-frequency background drift is not dominated by the detector 1/f-noise, and thus, still significantly mitigated as com-

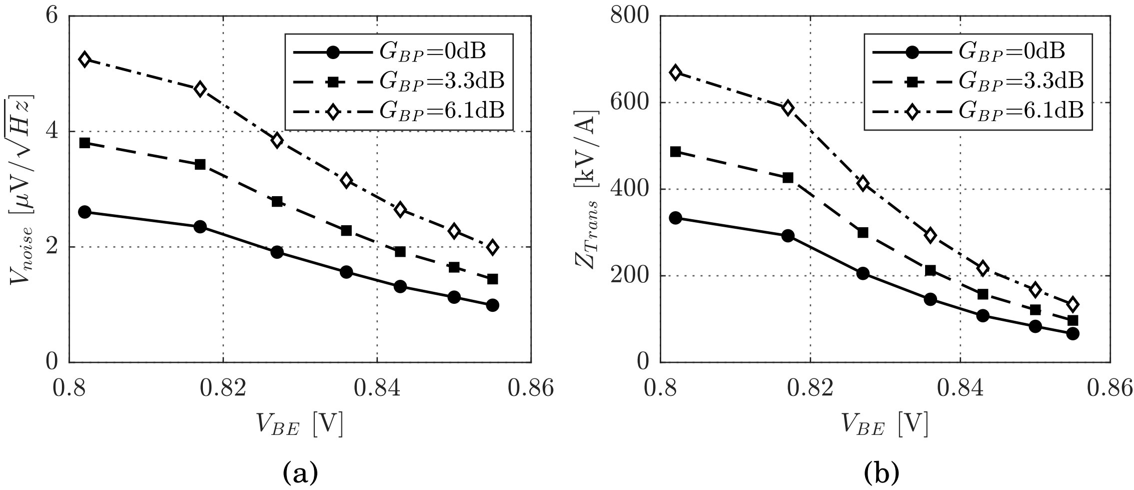

Figure 7.26.: Simulated spot noise at 100 kHz at the band-pass output (V_{noise}) (a) and transimpedance Z_{Trans} from the detector to the band-pass output (b) for different power detector base bias voltages (V_{BE}) and band-pass gain settings (G_{BP}). After [own5] © 2018 IEEE.

pared to the DC-operated single-pixel sensors [19][15]. A median filter with 1 Hz cut-off frequency was applied to the measured data and subtracted from the raw data to remove the background drift, as shown in Figure 7.27. The noise voltage in the filtered signal is 66 µV_{rms}. With the measured voltage response of $\Delta V_{o,max}$ = 103.5 mV (Figure 7.24) this results in DR_a = 63.8 dB for the analog read-out. For comparison, the DR for the nominal operation setting can be estimated based on simulations of the analog read-out circuitry and the oscillator measurements detailed in Section 7.4.1. Figure 7.26 shows the simulated spot noise at 100 kHz at the band-pass output and the transimpedance, Z_{Trans}, from the detector to the band-pass amplifier output for various THz detector bias currents and band-pass gain settings. Taking into account the Fourier decomposition, which introduces a factor of $\frac{\sqrt{2}}{\pi}$ for the first harmonic of the chopped signal, the DR can be calculated according to Equation 5.8 as:

$$\mathrm{DR[dB]} = 20\log_{10}\frac{\frac{\sqrt{2}}{\pi}P_{osc}(\alpha_{PEC}-\alpha_{noObj})R_I\cdot Z_{Trans}}{V_{n,int}}, \qquad (7.1)$$

where R_I is the current responsivity of the THz detector. Based on the measured oscillator output power (35 µW), the simulated transmission factors of α_{PEC} = 0.087 and α_{noObj} = 0.016 (Figure 7.6), and the detector current responsivity (0.48 A/W [19]), the maximum DR can be estimated to be $DR_{sim,1Hz}$ = 96.3 dB when referred to a 1 Hz noise bandwidth. Considering the ENBW of 125 Hz of the external LIA, the expected DR inferred from simulations is $DR_{sim,125Hz}$ = 75.3 dB, indicating that the signal exhibits additional noise components close to the carrier, such as low-frequency amplitude noise introduced by the TPO or the detector, which are not considered in the DR calcula-

tion.

Sensitivity Estimation

A measurement of the sensitivity of the sensor requires reference materials whose complex dielectric permittivity is accurately known within the permille range. Since such materials are currently not available, the sensor sensitivity is estimated based on the measured RMS voltage noise, the stopband properties, and read-out simulations. For small changes in relative permittivity, the relationship between SRR power transmission factor α and ϵ_r can be assumed to be approximately linear. Thereby, the minimum detectable change in relative permittivity, $\Delta\epsilon_{r,min}$, can be estimated as follows:

$$\Delta\epsilon_{r,min} = \frac{V_{n,int}}{\frac{\sqrt{2}}{\pi}P_{osc} \cdot R_I \cdot Z_{Trans}\frac{\partial\alpha}{\partial\epsilon_r}}, \tag{7.2}$$

where $\frac{\partial\alpha}{\partial\epsilon_r}$ is the power transmission factor gradient for a certain SRR excitation frequency and object permittivity. For example, for an object with $\epsilon_r = 4$ and an excitation frequency of 540 GHz, the simulated $\frac{\partial\alpha}{\partial\epsilon_r}$ is 0.0105, and $\Delta\epsilon_{r,min}$ can be estimated to be 0.003 for the measured DR of 63.8 dB and 0.015 when the background drift is not removed.

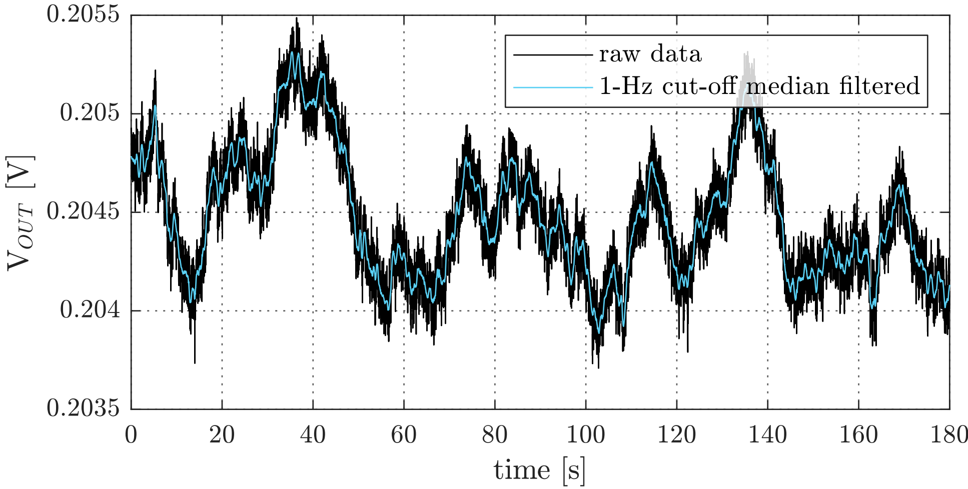

Figure 7.27.: Measured 180 s long time series at TP1. The long-term and short-term noise voltage is 322 μV_{rms} and 66 μV_{rms} for 1 ms lock-in integration time, respectively. For short-term noise, the raw data was filtered with a median filter with a 1 Hz cutoff frequency. ($V_{CCosc} = 2.2$ V, $V_{BE} = 816$ mV, $G_{BP} = 0$ dB, $f_{chop} = 100$ kHz). After [own5] © 2018 IEEE.

7.4.4. Measurement of the Response Decay-Rate

The measured decay-rate of the sensor voltage response as a function of the sample distance is shown in Figure 7.28 for a metallic tip. The sample-to-object distance was changed with a z-axis stepper motor. Because of the limited accuracy of the measurement setup, four measurement series were recorded and averaged. The shown response is normalized to the maximum response when the tip is in direct contact with the passivation. The measured results show good agreement with the simulated and measured decay-rate for small distances (< 5 µm) that were previously shown in [19]. For distances larger than 5 µm, the voltage response decays with around $-1\,\mathrm{dB}\,\mu\mathrm{m}^{-1}$. The SNR at 20 µm distance for the metal object was measured to be around 20 dB in a 51 Hz read-out bandwidth. Compared with the DC-operated sensor in [19], the DR increase by using chopping techniques enables a considerable extension of the sensing range.

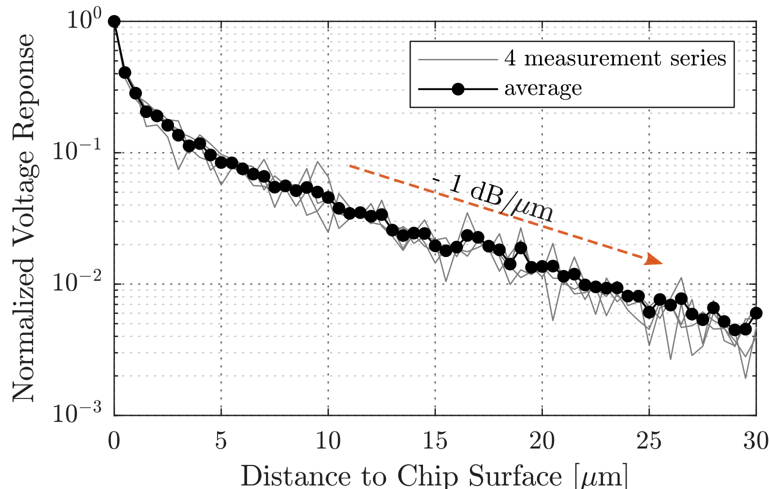

Figure 7.28.: Measured normalized voltage response decay-rate for a metallic tip as a function of sensor-to-object distance averaged (black) over four measurement series (grey). The red line indicated a decay rate of around -1 dB/µm for distances > 5µm. (V_{CCosc} = 2.2 V, V_{BE} = 816 mV, G_{BP} = 0 dB, f_{chop} = 100 kHz).

7.4.5. Measurement of Pixel Cross-Coupling

As discussed in Section 7.1.3, cross-coupling caused by the 4-way power division network leads to an uncertainty of the measured values that scales with the material-dependent response values and can be of concern if absolute permittivity values are of interest rather than image contrast. Cross-coupling was characterized for the worst-case scenario. Thereby, the change in transmitted power through a single SRR caused by placing a metal

needle on top of another pixel in the same subarray was measured, similarly to the simulations provided in Section 7.1.3. The measurement was repeated for all victim/aggressor combinations in the 4-pixel subarray. The coupling was found to be between $-12\,\mathrm{dB}$ and $-16\,\mathrm{dB}$ with respect to the maximum power response of the sensor at the detector input and is thus 2 dB–5 dB higher compared with the simulation results, which hints to a frequency misalignment of the power divider network and the SRR. According to Equation 7.2, the absolute uncertainty in relative permittivity can be calculated by replacing $V_{n,int}$ with the measured parasitic voltage response. For the worst-case, the uncertainty can be estimated to be around 0.33 for $\mathrm{VCC_{OSC}} = 2.2\,\mathrm{V}$ and $\frac{\partial \alpha}{\partial \epsilon_r} = 0.01$ for an object with $\epsilon_r = 1$.

7.4.6. Impact of Process Variations

Another source of uncertainty of the absolute read-out values stems from process variation. Figure 7.29 plots a histogram for the normalized voltage response for all 128 pixels of a single die. The pixels were subsequently selected and monitored. The sensors show a normalized mean response of 76 % of the maximum response. There are a few outliers that show low voltage response. Trials on several samples revealed that the position of these outliers on the chip is random and not correlated to a specific circuit pattern or global process gradient. In particular, high variance in the sensor excitation power between different sub-arrays can be excluded as a potential cause, because a low response is observed for a few but not for all of the pixels in the sub-array. Hence, these variations are expected to primarily originate from process variations in the sensitive THz power detector devices. Note that a pixel-dependent correction factor can compensate variations in the detector responsivity or TPO output power. A suitable calibration procedure to derive this factor, however, requires reference measurements with accurately defined material properties for every pixel and thus remains objective of future studies. Moreover, the SoC supports individual pixel biasing, and it can thus be calibrated to yield a similar absolute sensor response for all pixels.

7.4.7. Digital Read-Out

For the characterization of the digital read-out mode, a chopping frequency of 197.2 kHz and an SC sampling clock $\mathrm{LP_{clk}}$ of 1.5 MHz (filter cutoff 2.27 kHz) were used. The instrumentation amplifier voltage gain was set to 0 dB, and the ADC reference voltages were experimentally adjusted to cover the signal swing at the LIA output while minimizing extra voltage margins to provide an optimum resolution. The corresponding lower and upper

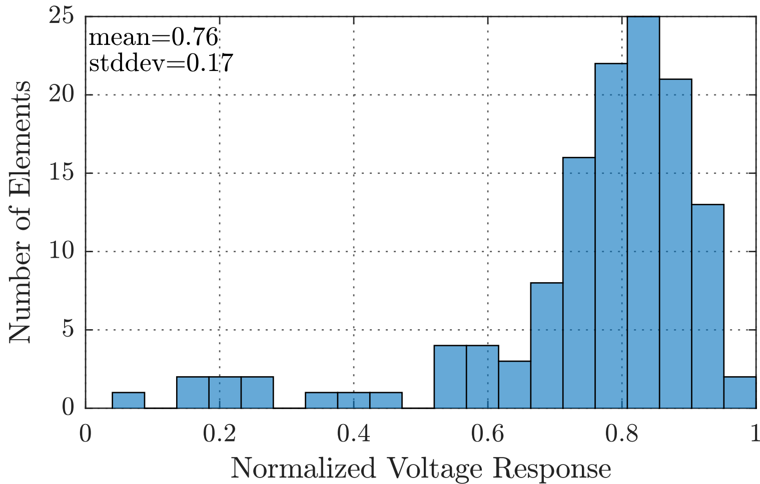

Figure 7.29.: Measured normalized voltage response variations for full coverage with a metal needle for for all 128 pixels of a single die. After [own5] © 2018 IEEE.

reference voltages were 0.409 V and 0.954 V, respectively, indicating an ADC resolution of around 9.8 mV.

Repeated measurements were made for the object response to characterize the statistical noise. Because of the aforementioned voltage spikes at the pixel switching events, a waiting period of 280 µs was programmed between each measurement, allowing the LIA output to reach its steady state. After each wait time, multiple samples were recorded with the ADC in a burst mode at 1 MHz, which were then averaged in an external FPGA. A standard deviation was calculated from a large number (>50,000) of such averaged samples, which was considered equivalent to the noise for DR calculations. Expected frame rates were also calculated by dividing the measurement rate by the number of pixels in the array.

Figure 7.30 shows the measured DR and the frame rate as a function of the averaging factor. The measured DR exhibits reasonable agreement with the expected 3 dB/octave noise reduction due to oversampling and is $\mathrm{DR}_{\mathrm{d,28fps}} = 38.5\,\mathrm{dB}$ for a frame rate of 28 fps with 4 averaged samples. The high dynamic current drawn by the chopped oscillators introduces ground-bounce and chopping transients at the ADC input, which deteriorate the DR for small numbers of averaged samples because of aliasing.

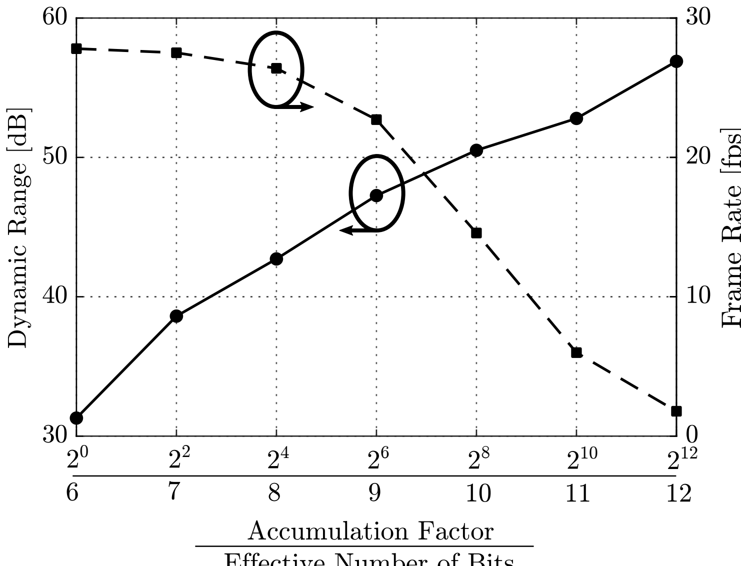

Figure 7.30.: Measured dynamic range and frame rate of the digital read-out for different accumulation factors of the external average-and-dump filter. The resulting ENOB at the filter output is also indicated. ($V_{CCosc} = 2.2\,V$, $V_{BE} = 816\,mV$, $f_{chop} = 197.2\,kHz$).

7.5. Imaging Experiments

7.5.1. Imaging of a Human Fingerprint

Context

As discussed earlier, the sensor response is a function of the material-dependent electrical field disturbance in the sensing volume of the resonator. For imaging objects with homogeneous dielectric permittivity, the sensor can be used for µm-scale profilometry by mapping the decay of the electrical field strength and the resulting sensor response to the sensor-to-object distance. Whilst absolute distance measurements require thorough calibration as well as accurate reference measurements of the object's dielectric permittivity, relative measurements are sufficient for applications that aim to distinguish characteristic topology features. The imaging of ridges and valleys of human fingerprints is one such example.

Biometric fingerprint scanning is today widely adopted. Apart from its traditional application fields in forensic sciences and homeland security, fingerprint scanners are now the de facto standard access barrier for smartphones. There exists a variety of image acquisition methods, from which the most widely adopted are optical, ultrasonic, and capacitive sensing. The optical sensors rely on the illumination of a transparent prism and measurement of the reflection pattern with the finger placed on top of the prism. This

method is expensive and easy to spoof, but one can achieve high image resolution and large acquisition areas. The ultrasonic sensors measure acoustic pulse echoes at the tissue boundaries and have recently been applied in solid-state electronics [196]. These sensors enable imaging of the sub-surface dermal fingerprint and are thus particularly spoof resistant and reliable, even in wet environments. Their fabrication, however, relies on expensive wafer-bonded two-chip assemblies comprising a high-voltage LDMOS driver chip and a MEMS chip to implement piezoelectric micromachined ultrasonic transducers. The contemporary low-cost imaging technique is based on capacitive sensing. Here, electrode arrays sensing the change in electrode capacitance induced by a finger are implemented as single-chip solutions in conventional CMOS technology [197]. Despite their exceptional price-performance ratio, capacitive sensors suffer from low SNR, require the finger to be very close to the electrodes ($< 100\,\mu m$), and they perform poorly when the finger is wet or exceptionally dry. In this study, a proof-of-concept is demonstrated, showing that THz near-field imaging can function as an alternative to the aforementioned imaging methods for biometric fingerprint acquisition. With the small sensing range of the near-field SoC, it's high sensitivity to water and other contaminants, and it's low fabrication cost it shares most of the advantages and disadvantages of capacitive sensors.

Experiment

Figure 7.31 shows an optical image of an ink-and-paper fingerprint, as well as a THz near-field image of the same finger. For the acquisition of this image, the near-field array was translated in a continuous 1D movement along the direction orthogonal to the sensing stripe. The finger was in direct contact with the chip surface without the support of any high-precision mechanical setup – a similar scanning procedure as compared with conventional optical or capacitive swipe sensors. The on-chip digital read-out was utilized for data logging and was operated with a speed of 15 fps. A total image size of 842×128 pixels with a pixel pitch of $25\,\mu m$ in y-direction and $14.25\,\mu m$ in x-direction was acquired in a scanning time of about 30 s. Because of the staggered pixel arrangement, offset correction of $110\,\mu m$ was applied in post-processing. The measurements were repeated multiple times with no damage to the sensing surface. However, after each scan, particle leftovers had to be removed with isopropanol.

Discussion

The results demonstrate that the characteristic ridges and valleys, sized between $100\,\mu m$–$500\,\mu m$, can be easily resolved by the near-field SoC. Similarly, the ridge bifurcation points

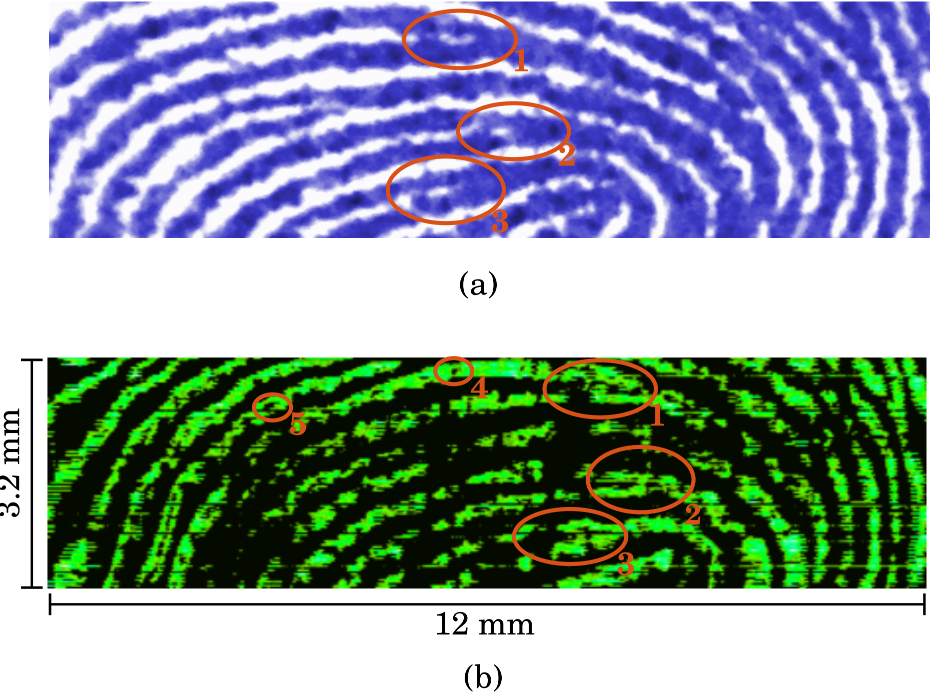

Figure 7.31.: Optical image of an ink-and-paper fingerprint (a) and scanned THz near-field image (b). Data was acquired with continuous 1D translation. The ridge bifurcation points (1-3) and some sweat pores (4-5) are marked. Image size = 842×128, $T_{scan} \approx 30\,s$. After [own5] © 2018 IEEE.

can be identified. The image further suggests that the ridge sweat pores, which are not visible in the ink-and-paper image, can also be resolved. Thus, the sensor resolves all levels of specific ridge details [197]. The image is substantially oversampled, and the image acquisition time can be reduced to 5 s without losing information.

The results indicate a competitive image quality to other techniques [196]. Most particularly, the fixed image resolution in y-direction of 1016 dpi, defined by the SRR spacing, exceeds the resolution of most state-of-the-art fingerprint sensors [197] and the minimum resolution required for FBI certification by a factor of two [198]. However, a study comparing the presented THz near-field technique with the conventional methods should be conducted in the future to assess the sensor performance for this application quantitatively. Future studies may also aim to identify if additional information related to person-dependent dielectric properties of the finger skin at THz frequencies can serve as an additional tool for identification. Finally, it is noted that the SoC design did not explicitly target this application and that there may be several means of improving the applicability of THz near-field imaging for biometric fingerprint imaging as compared to the present implementation. For example, the lateral resolution could be reduced to increase the sensing range, hence facilitating additional sensor protection such as a protective silicate layer. The main disadvantage compared to state-of-the-art sensors, however, remains the

1D sensor implementation requiring a swipe movement. Future 2D array integration is thus instrumental in having any realistic chance of biometric THz near-field fingerprint imaging to be applied in practice.

7.5.2. Imaging of a Nickel Grid

Experiment

A first THz near-field microscopy experiment with accurately controlled 1D sensor translation was conducted on a fine metal grid to demonstrate the feasibility of imaging of planar solids and to verify the spatial resolution inferred by the single-pixel measurements detailed in Section 7.4.2. Contrary to the uncomplicated methodology for fingerprint acquisition, imaging of solid samples necessitates accurate height control and a stable mechanical setup to prevent deterioration of the image SNR due to mechanical vibrations and to avoid damaging of the SoC passivation. For this purpose, a commercially available scanning tunneling microscope (STM) setup (Semilab Navigator 220) was modified to accommodate the sensor. Figure 7.32 gathers pictures of the imaging setup. A stepper motor translation stage for the z-axis is mounted together with an optical microscope and a tilt-adjustable high-precision x,y piezo table on a rigid granite boulder to minimize relative vibrations. At the time of this experiment, the sensor module design detailed in Section 7.3 was in its early development stages. Therefore, an external FPGA and external power supplies were used. The sensor was mounted to the x,y-table, and the grid was glued to a rubber holder, which was fixed at the z-axis stage. The imaging object was a nickel transmission electron microscopy (TEM) support grid with 50 µm bar width and a 250 µm pitch between bars (VecoSpecimen Grid 0100-NI). The grid z-position was aligned to yield the maximum sensor response. Hence it is expected that the grid was in close to direct contact to the sensor surface ($< 5\,\mu m$). The exact distance of the grid to the sensor could, however, not be quantified because of the limitations of the measurement setup.

Figure 7.33 shows the image of the grid acquired with a 1 µm step size, an accumulation factor of 1024, and a frame rate of 6 fps. The image size is 1500×128 pixels and was captured in a scanning time of 6 min 45 s. It is noted that the 1 µm step size leads to substantial oversampling. Considering a 25 µm step size and an optimized electrical/ mechanical timing, the scanning time for the same area could potentially be reduced to around 22 s, and even less is lower accumulation factors are used. In the same way as compared to the fingerprint measurement, offset correction of 110 µm was applied in post-processing.

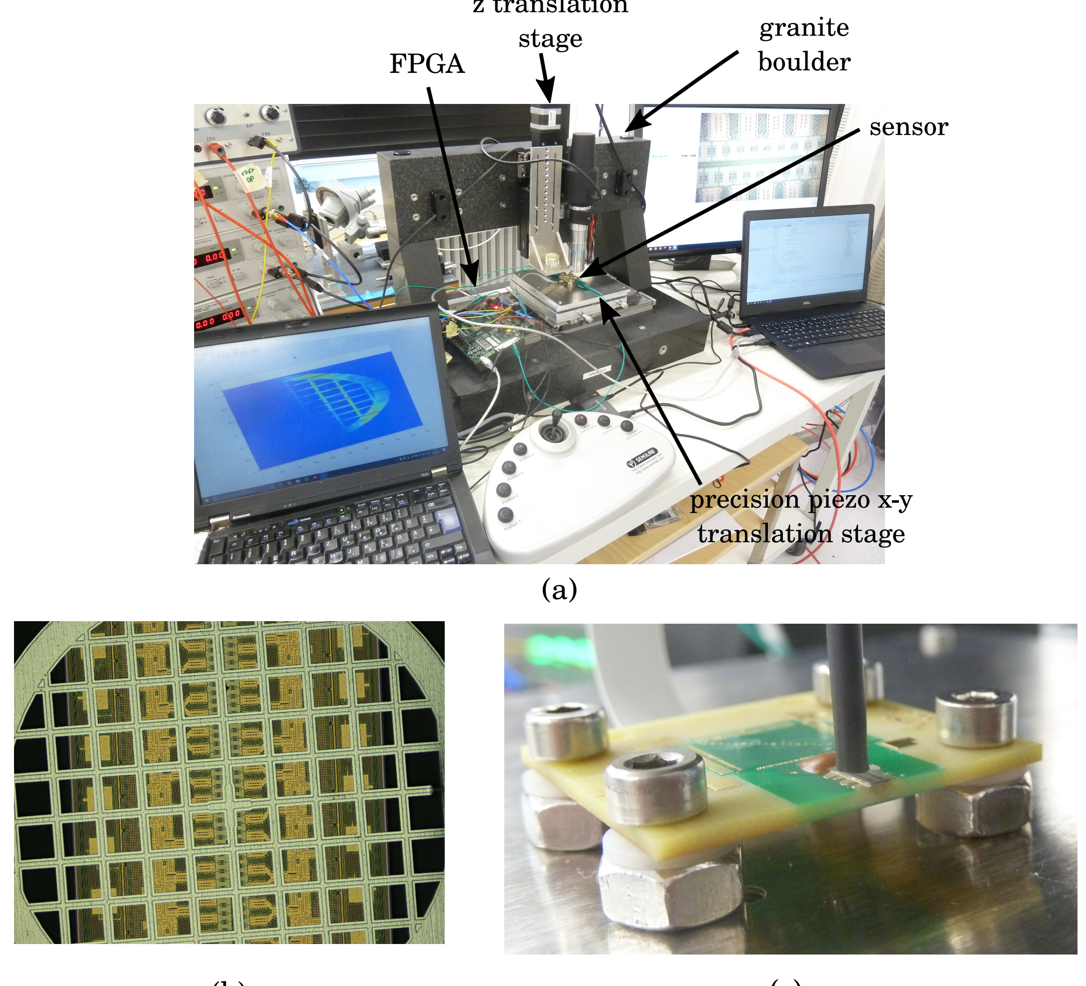

Figure 7.32.: Pictures of the imaging setup (a),(b), and micrograph of the grid and the chip to visualize the size relations (c). The sensor is mounted to a piezo controlled x-y translation stage and the nickel mesh is glued to a rubber holder and mounted to a z-translation stage on a granite boulder.

Discussion

The microscopic structure of the grid is visible in the image. Except for offset correction, no post-processing or response calibration was applied to the sensor. Hence, the image depicts a vertical line pattern related to the varying response of the individual pixels. Some of the pixels show no response at all, which is to be expected in the presence of the low-response pixels identified in Section 7.4.6. A varying contrast strength can be observed for different regions of the grid, thereby indicating that the grid was not perfectly planar but slightly bend. Figure 7.33(b) plots the ADC count of four adjacent pixels for translation along a single bar-edge, which is highlighted in Figure 7.33(a). The bar edges are resolved with 14 µm–18 µm according to a 10 %–90 % rising-to-falling edge criterion. This is slightly higher than the lateral resolution of 10 µm–12 µm measured with the metal

needle (Section 7.4.2). The difference can potentially be attributed to a softer bar-edge profile of the grid.

7.5.3. Imaging of Breast Tissue

Context

THz near-field imaging shows potential for *ex vivo* histopathology, as detailed in Section 2.1.5. In particular, previous studies identified the dielectric permittivity at THz frequencies as a promising contrast mechanism for the differentiation between benign and malignant tissue but, so far, the conventional spectroscopic far-field THz imaging techniques lack the required resolution for accurate margin identification. To make an initial assessment of the applicability of the developed SoC for such applications, an imaging experiment was conducted on a human breast tissue sample. The experimental method was compliant with the fundamental ethical principles stipulated in the Helsinki Declaration and its later revisions [199].

Experiment

First, the tissue sample was excised from a patient in a breast-conserving surgery. Then, the fresh tissue was paraffinized, cut into 5 µm-thick slices, deposited on a glass specimen slide, and deparaffinized. The slide was subsequently mounted to the z-axis translation stage of the aforementioned modified STM setup. Figure 7.34 shows a picture of the experimental setup. With the imaging object and the sensor being a planar solid, the setup required further means of relative planarization between both. Hence, the z-axis was equipped with a manual tilt adjustment stage and an objective holder at the x,y-table to enable sample planarization through optical focus alignment from the bottom.

Figure 7.35 gathers an optical microscopic image, a height map acquired with a Veeco Dektak 150 Surface Profiler, and scanned 0.55 THz near-field images [own1]. A key difference to typical microscopic sensing methods relying on raster scanning with small apertures or tips is that the present sensor exhibits a large solid and planar surface, making measurements with constant object-to-sample-distance impossible. Therefore, the THz images were scanned at three constant heights: in direct contact and at distances of 1 and 2 µm, as respectively shown in Figure 7.35(c)-(e). To deduce the direct-contact height, the sensor was approached with the sample until no further change in sensor response could be observed. The absolute distance was then deduced from the relative distance to

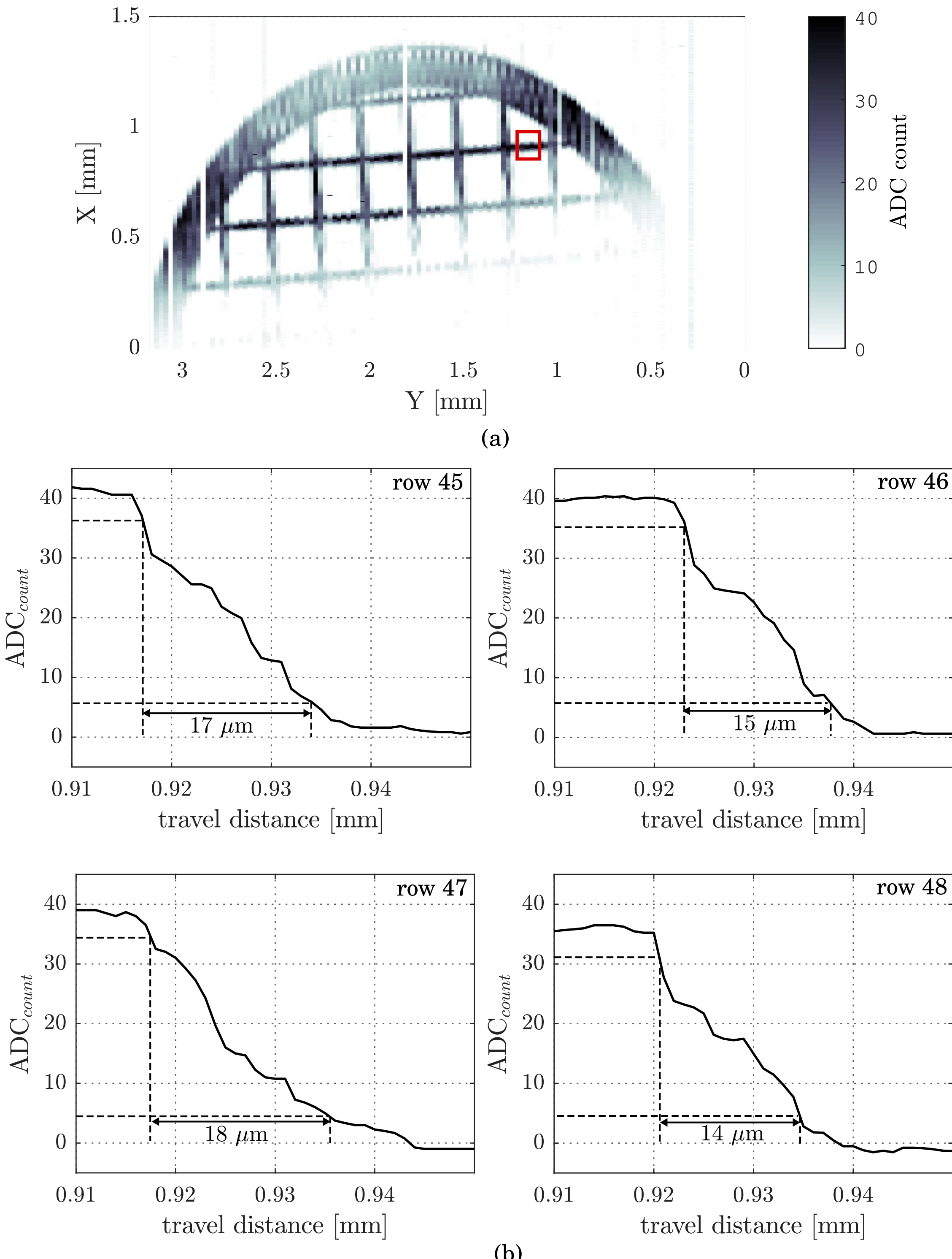

Figure 7.33.: Scanned 2D image of a nickel mesh (a), and ADC output for translation along a single bar edge for four adjacent pixels (b). The mesh exhibits a bar width and pitch of 50 µm and 250 µm, respectively. Image size = 128×1500, Step-size = 1 µm, T_{scan} = 6 min 45 s. The section for the bar edge measurement is highlighted in (a). Lateral resolution based on 10 %–90 % rising-to-falling edge criterion is also indicated. After [own5] © 2018 IEEE.

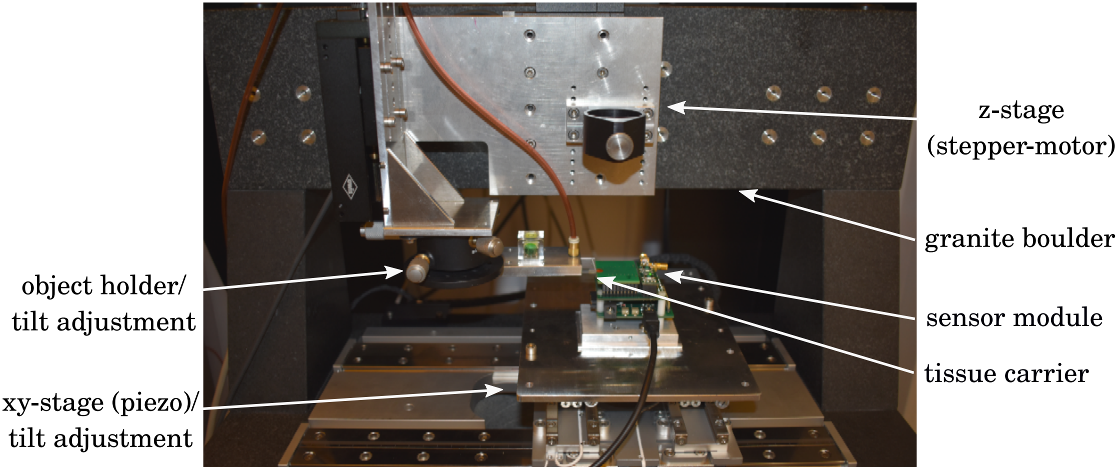

Figure 7.34.: Picture of the measurement setup for the tissue scan.

the direct-contact height. The scan time for the 3.1 mm×3.2 mm large imaging area was 11 min at a 22 µm horizontal step size, giving 142×128 pixels. The image was stepped only in x-direction, with a step and dwell time of 2 s and 2.5 s, respectively. The dwell time was chosen as a compromise between a sufficiently large settling time and an averaging factor of 3840. The images were post-processed with the software Gwyddion [200]. The image tilt was leveled by mean plane subtraction, and the row pattern resulting from sensor sensitivity variations of the individual pixels was aligned with a median of differences algorithm.

Discussion

In comparison with the THz far-field images of excised tissue shown in Section 2.1.5, the near-field images clearly exhibit sufficiently high contrast and resolution to facilitate microscopic feature extraction. The best image quality is achieved in direct contact with the sample ($\Delta z = 0$), giving a DR of the image of 38.7 dB. At one micrometer distance, the DR drops to 35.5 dB, which is about 7 dB more than expected from the measurement of the response decay on the first micrometer (Figure 7.28). A potential reason for this discrepancy could be a slight tilt misalignment between the sensor and the glass specimen slide leading to a finite distance and reduced response in the direct-contact scan. At a two micrometer distance, the DR of 27.6 dB roughly aligns with the expected decay.

It is clearly visible that the near-field images mostly resemble the height profile depicted in Figure 7.35. This is expected in view of the pronounced height variation of the tissue sample. To isolate the image contrast resulting from electromagnetic material properties of such samples, calibration methods that account for the distance have to be investigated in future work. For example, the function of the response decay-rate could be used to subtract

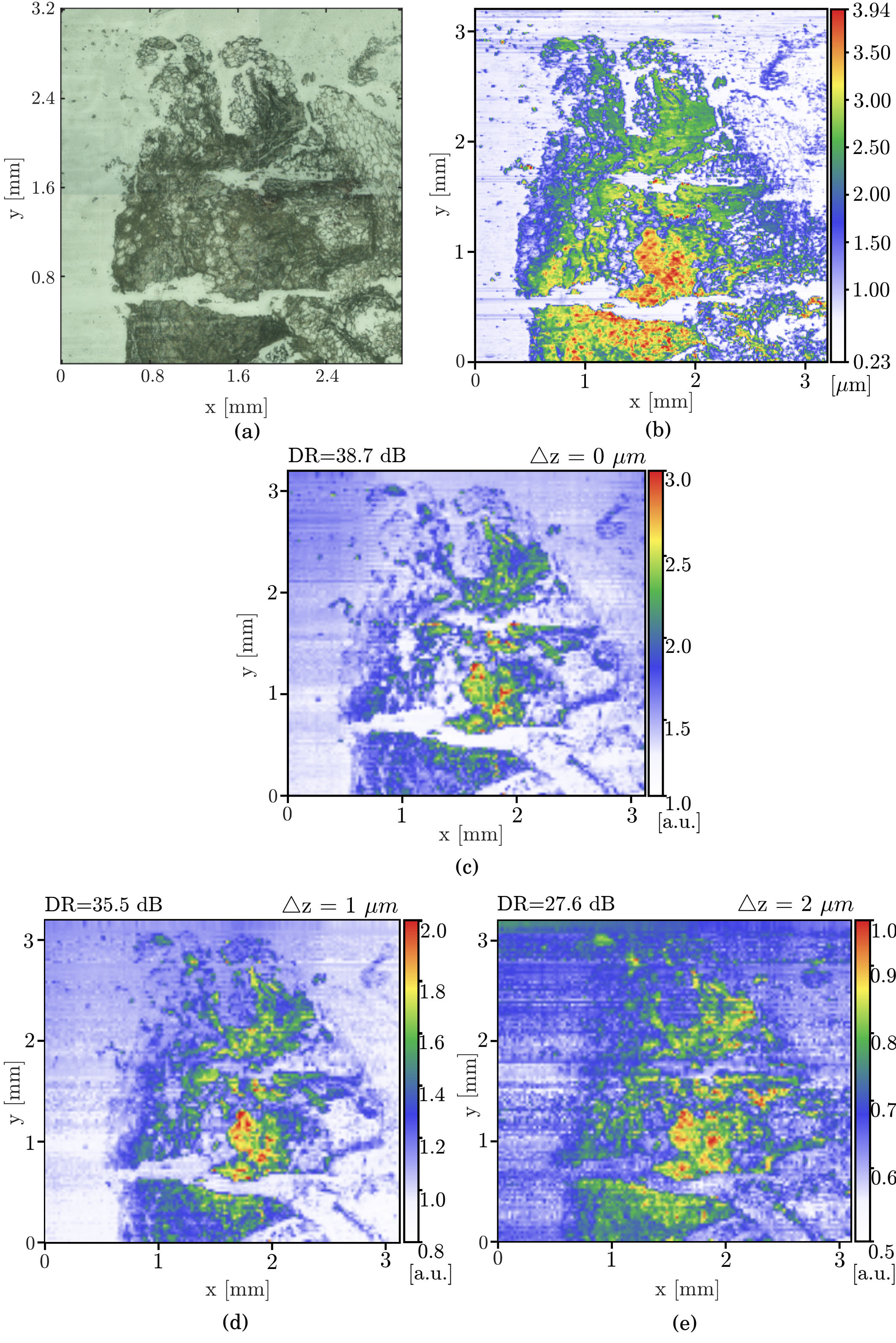

Figure 7.35.: Imaging of breast tissue. Micrograph (a), height profile (b), and THz near-field images at different distances (Δz) from the sample (c)–(e). The dynamic range of the images is indicated. It represents the ratio between maximum signal amplifude and the rms background noise in the bottom-left 15×15 pixel image section.

out the height dependency. It is noted that the decay rates have to be measured with more accuracy and for more material types to enable this calibration approach. Moreover, in view of the non-continuous response decay at small distances (Figure 7.28), measurement of the absolute object-to-sample-distance is required for calibration, which was not possible with the employed experimental setup. On another note, no histopathological results could be obtained for the tissue sample so that an evaluation of the sensor's capability to differentiate between healthy was not possible.

In summary, the ability to operate many near-field sensors concurrently in a SoC implementation provides, for the first time, the required simultaneous imaging speed and resolution to support intraoperative applications. However, whether or not THz near-field imagers can be established as a medical tool with good sensitivity and specificity for tumor margin identification during cancer surgeries requires future investigations. The presented imaging SoC can, however, be used for the conduction of such statistically significant studies, and thereby assess the medical relevance of THz contrast mechanisms for bioimaging applications in general. Unlike as compared to spectroscopy, where double Debye model parameters are often used for classification, the SoC measures at a single frequency. Therefore, other classifiers and variables need to be found in the future. The question of whether an absolute or a contrast-based measurement brings more insight needs to be answered as well. This requires further studies for pathology assessment in an operating room.

7.6. Summary and Conclusion

The study presented in this chapter set out to determine whether THz near-field sensing can be accelerated toward practical applications by the integration of sensor arrays in silicon technology. For this purpose, a 128-pixel SoC for THz near-field imaging at 550 GHz was fully integrated in 0.13 µm SiGe BiCMOS technology and assembled into a stand-alone sensor module. All THz functions, such as sensor illumination, near-field sensing, and power detection, are concurrently integrated with a large-scale read-out scheme, an integrated lock-in amplifier, and digital signal processing.

The chip exploits the interaction of the highly-confined E-fields of 3D SRRs with an imaging object. It achieves a lateral resolution around 10 µm with an imaging contrast based on the dielectric permittivity in the THz range. The worst-case estimated uncertainty for the real part of the relative permittivity is 0.33. A 1D array architecture is proposed that makes use of THz power distribution networks to account for the size mismatch of THz on-chip oscillators and super-resolution sensing elements. Thereby, a high 1D fill factor

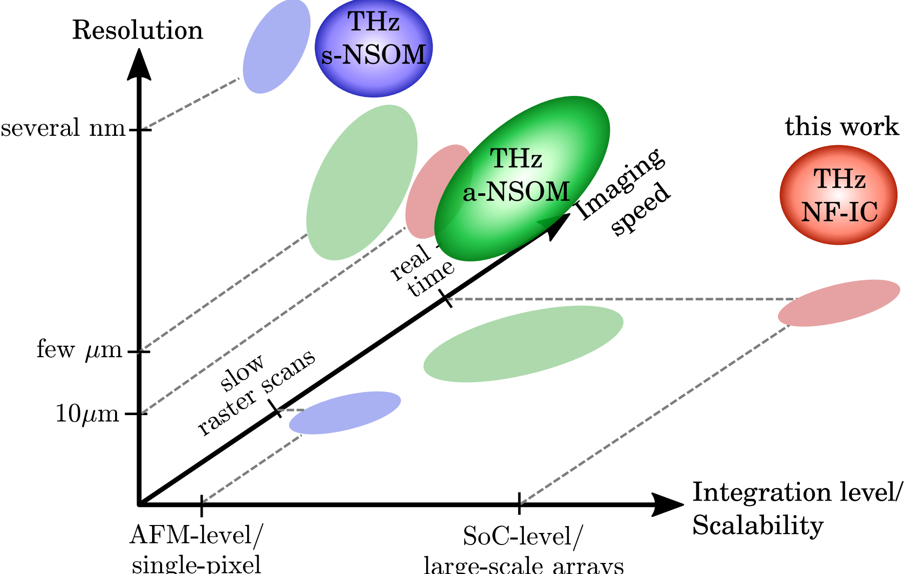

Figure 7.36.: Illustrative comparison between the presented THz near-field sensor IC and contemporary THz near-field technology.

of 48 % with a 1D pixel density of 1016 dpi is achieved. The chip shows a dynamic range of $DR_{d,28fps} = 38.5$ dB at a frame rate of 28 fps in a digital read-out mode and a dynamic range of $DR_a = 63.8$ dB in an analog read-out mode for external lock-in detection with a 1 ms time-constant.

Table 7.1 compares the presented sensor with different terahertz and microwave near-field imaging methods and devices, and Figure 7.36 shows a qualitative comparision with conventional THz NSOM methods. The presented sensor overcomes various bottlenecks of traditional THz near-field imaging technology. In particular, the on-chip cointegration of all sensor functions mitigates the sensitivity problems of THz NSOM methods resulting from remote illumination and detection. By further employing multi-pixel integration on a chip-scale, real-time imaging with unprecedented SNR is presented, enabling microscopic THz image acquisition within seconds. At the same time, the presented sensor exhibits shortcomings such as a solid, planar sensing surface, narrowband operation, and a design-rule-limited spatial resolution around 10 µm. As such, the presented device is not generally set to challenge THz NSOM in its laboratory use. Rather, new THz microscopy applications fundamentally requiring integrated microsystems and high-speed imaging are targeted. In this context, successful demonstrations of microscopic imaging of human tissue and biometrical fingerprint acquisition are shown in this chapter. However, this work only assesses a portion of the potential application scope for the sensor. Other potential applications can be found, for example, in microfluidics, where the sensor may be used to simultaneously measure filling levels and the state and dynamics of liquid mixtures. Or it may be employed for the quality control of semiconductor fabrication, e.g., for the

measurement of doping gradients.

Table 7.1.: State-of-the-art terahertz and microwave near-field imaging systems

Reference	**Method**	**Technology**	**Frequency [THz]**	**Spatial Resolution [µm]**	**SNR [dB]**	**Notes on Integration**	**Number of Pixels**
[166]	SRRs	laminate	0.006–0.012	700	–	external VNA	1–8
[171]	on-chip LC-tanks	65 nm CMOS	0.06/0.12	≈25–35[a]	–	integrated sensors	128/192
[201]	near-field scanning microwave microscopy	AFM tip	1-20	<0.1	–	external VNA	1
[50]	s-NSOM	gas laser + AFM-tip, bolometer	2.54	0.04	–	remote components	1
[47]	a-NSOM	gas laser, GaAs/AlGaAs heterostructure	1.40/2.52	9	–	aperture/detector cointegration	1
[202]	a-NSOM	Ti:Sapphire laser, GaAs/LT-GaAs on Al_2O_3	0.2–2.5	7	≈10[b]	aperture/detector cointegration	1
[53]	electro-optical crystal	Ti:Sapphire laser, $LiNbO_3$ crystal, CCD camera	0.2–2.5	14[c]	52	remote components	131072
[19]	on-chip SRRs	0.13 µm SiGe-BiCMOS	0.543–0.562	10–12	42	integrated sensor	1
This Work	on-chip SRRs	0.13 µm SiGe-BiCMOS	0.543–0.562	10–12	63[d]/37[e]	SoC integration	128

[a] Estimated from Fig. 14 in [171].
[b] Estimated from Fig. 6 in [202] for an aperture size of 5 µm.
[c] Extracted at 0.7 THz.
[d] For the analog read-out for an external lock-in integration time constatnt of 1 ms.
[e] For the digital read-out with a frame-rate of 28 fps.

Part IV.

Conclusion

Chapter 8

Thesis Summary

8.1. Summary and Conclusions

This thesis described the development of highly-integrated systems in silicon technology for novel imaging concepts with terahertz (THz) waves. So far, the progress towards practical adoption of THz technology is inhibited by the size and cost limitations of traditional electronic and photonic THz equipment. Despite its low device speeds, silicon technology offers the means to increase the societal impact of THz technology significantly. The advantages of silicon technology are twofold. First, integrated THz circuits can be manufactured at low cost and packaged into compact systems whose integration-level is comparable to the ones we are used to from conventional consumer electronics. Secondly, the mixed-signal capabilities and the yield offered by silicon technology enable the integration of chip-scale THz systems with enhanced functionality. The work described in this thesis exploits both advantages to demonstrate low-cost microscopic and volumetric THz imaging with compact silicon components for the first time.

Although the strong sensitivity of THz waves to water promises to enable a variety of applications in life sciences, THz imaging techniques either lacked the spatial resolution or the appropriate integration level to be applied in practice. In particular, the thesis motivated the use of THz imaging for the assessment of tumor margins in breast cancer treatment, which requires a spatial resolution on the scale of micrometers and image acquisition within a few minutes. In this context, the central aim of this research was to develop a silicon-based sensor system for real-time imaging of the microscopic material properties in the THz frequency band.

To achieve this aim, a fully integrated 128-pixel System-on-a-Chip (SoC) for real-time super-resolution near-field imaging at around 550 GHz in a 0.13 µm SiGe BiCMOS technology was developed in this thesis. Following previous research on integrated single-pixel sensors [15], [19][own11], [own13], the chip exploits the capacitive interaction between on-chip split-ring-resonators (SRRs) and the imaging object. Three-dimensional cross-bridge double SRRs showing a spatial resolution of around 10 µm were used [19]. To increase the understanding of the sensor response formation, a lumped equivalent circuit model of the complex 3D sensor structure was developed and analyzed within the scope of this work. It was shown that appropriate allocation of the SRR excitation frequency is key to control the sensor sensitivity regarding the real-part and imaginary-part of the permittivity. Two key contributions enabled the chip-scale integration of near-field sensors. First, a parallel sensor excitation scheme based on 4-way power division networks was proposed for the one-dimensional scaling of SRR near-field sensors with high fill factor. Secondly, a rolling-shutter sensor read-out architecture utilizing on-chip lock-in detection was developed. To allow a compact implementation and real-time operation, the here developed SoC offers the full set of functionality, including THz near-field sensing, analog signal conditioning, analog-to-digital conversion, and a digital communication interface. The finally presented imaging module operates as a stand-alone device. It can be powered and controlled only by a conventional USB port, not requiring any additional THz instrumentation for imaging. These contributions significantly enhance the practicability of THz near-field imaging. More particularly, they enabled the demonstration of image acquisition of objects with dimensions of several mm^2 within a few minutes. High-resolution THz imaging of excised human breast tissue and human fingerprints was shown, which constitutes the first demonstration of microscopic THz imaging with integrated multi-pixel near-field sensors.

Furthermore, the thesis explored a low-cost all-silicon volumetric THz imaging system operating at 430 GHz. The system is based on the principle of computed tomography and acquires 3D absorption data of an object in a focused transmission-mode setup. In contrast to previous demonstrations of THz CT systems relying on costly and bulky traditional THz equipment, both transmitter and receiver were implemented in a 0.13 µm SiGe HBT technology and packaged into very compact modules. Imaging results of a polystyrene foam cube with a concealed knife blade and a packaged hypodermic needle were presented, demonstrating the feasibility of the implemented imaging system to be used for applications in non-destructive industrial quality control. The key enabler for the THz CT system is a high-power 430 GHz radiation source, whose development was also presented in this thesis. A record in radiated power for silicon-integrated sources above 350 GHz of -6.3 dBm was achieved by utilizing optimized harmonic extraction for a circuit

architecture comprising a high-frequency oscillator and a doubler coupled to an on-chip antenna.

8.2. Future Directions

Microscopic Imaging This thesis established the novel research area of fast microscopic THz imaging with integrated circuits. It is hoped that the potential significance of this area for applications in life sciences encourages future research to address the shortcomings and limitations of this study. More particularly, the scope of this thesis was limited to sensor development and initial demonstrations of the imaging functionality. Therefore, more research is required to assess the applicability of integrated THz near-field sensors for biomedical applications such as cancer diagnostics. It is noted that this research needs to be interdisciplinary, involving medical scientists, physicists and electrical engineers. Such a collaborative approach is pursued in the second phase of the ongoing research project *Near-Sense: A silicon-based terahertz near-field imaging array for ex vivo life-science applications*, which was funded by the German Research Foundation within the Priority Program SPP 1857 *Electromagnetic Sensors for Life Sciences (ESSENCE)*. The herein presented sensor array allows *ESSENCE* to statistically investigate the medical relevance of THz near-field sensing for marker-free breast cancer margin identification on a large set of samples. The premise for such studies is that the image contrast uniquely depends on the electromagnetic material properties, and not the object's distance to the sensor. Therefore, we propose a method in which freshly extracted tissue samples are pressed directly onto the sensor surface to planarize the sample and to remove blood and other fluids from the imaged regions. The potential of this method can be already assessed with the current 1D sensor array implementation, but eventually requires 2D sensor arrays and a flip-chip sensor packaging concept where all interconnects are accessible on the chip back-side to be practical. Notably, applications may also desire absolute determination of the complex permittivity in non-contact measurements, which will require further research on calibration methods for resolving the ambiguity between object distance and material properties.

From the design perspective, the large-scale integration of 2D near-field sensor arrays remains challenging. In particular, the 1D pixel geometry of the presented THz front-end is not scalable to 2D geometries without introducing significant spatial under-sampling due to the size of the employed oscillators and power distribution networks. Hence, new design methodologies and different sensing concepts are required to facilitate 2D sensor integration and single-shot imaging. Moreover, the read-out architecture presented in this thesis operates in a rolling-shutter mode, which limits the individual pixel observation

time. The research into new read-out architectures for continuous pixel observation in a global shutter mode could significantly increase the signal-to-noise ratio and the imaging speed.

Volumetric Imaging The advances in THz CT presented in this thesis are not yet sufficient for the widespread adoption of this imaging method. Future research will have to address the prohibitively long scanning times ranging from several minutes to a few hours, to accelerate the progress towards real-world applications. As such, it is essential to remove the bottleneck of 3D mechanical translation by realizing methods for 2D imaging without raster-scanning such as collimated-beam imaging or compressed sensing with silicon components. However, for such methods to be applicable, future research in high-power silicon-integrated THz sources is required. To advance silicon THz source technology towards sufficient performance remains a highly sought-after achievement – not only for the herein presented THz CT system but for THz science as a whole. Future research may push the collaborative progress in high-speed silicon technology development and THz design technique. In particular, a continued effort in exploiting the abundance of devices available in silicon technology will be required to counteract the speed limitations of single devices. Here, the large-scale implementation of THz sub-circuits that use the codesign of electromagnetic structures and active circuitry for power combining [84]–[86], [88], [93], and the design of large-scale source modules with individually reconfigurable source units [20] range among the most promising research directions.

Bibliography

Own Publications

[own1] U. R. Pfeiffer, P. Hillger, R. Jain, *et al.*, “Ex Vivo Breast Tumor Identification: Advances Toward a Silicon-Based Terahertz Near-Field Imaging Sensor,” *IEEE Microw. Mag.*, vol. 20, no. 9, pp. 32–46, Sep. 2019.

[own2] Q. Cassar, A. Al-Ibadi, L. Mavarani, *et al.*, “Pilot study of freshly excised breast tissue response in the 300–600 GHz range,” *Biomed. Opt. Express*, vol. 9, no. 7, pp. 2930–2942, Jun. 2018.

[own3] P. Hillger, A. Schlüter, R. Jain, S. Malz, J. Grzyb, and U. Pfeiffer, “Low-cost 0.5 THz computed tomography based on silicon components,” in *42nd Int. Conf. on Infrared, Millimeter, and Terahertz Waves*, Cancun, Mexico, Aug. 2017, pp. 1–2.

[own4] P. Hillger, R. Jain, J. Grzyb, *et al.*, “A 128-pixel 0.56THz sensing array for real-time near-field imaging in 0.13 μm SiGe BiCMOS,” in *IEEE Int. Solid-State Circuits Conf.*, San Francisco, CA, USA, Feb. 2018, pp. 418–420.

[own5] P. Hillger, R. Jain, J. Grzyb, *et al.*, “A 128-Pixel System-on-a-Chip for Real-Time Super-Resolution Terahertz Near-Field Imaging,” *IEEE J. Solid-State Circuits*, vol. 53, no. 12, pp. 3599–3612, Dec. 2018.

[own6] P. Hillger, R. Jain, J. Grzyb, *et al.*, “A solid-state 0.56 THz near-field array for µM-scale surface imaging,” in *43rd International Conference on Infrared, Millimeter, and Terahertz Waves (IRMMW-THz)*, Nagoya, Japan, Sep. 2018, pp. 1–2.

[own7] P. Hillger, J. Grzyb, R. Jain, and U. R. Pfeiffer, “Terahertz Imaging and Sensing Applications With Silicon-Based Technologies,” *IEEE Trans. THz Sci. Technol.*, vol. 9, no. 1, pp. 1–19, Jan. 2019.

[own8] P. Hillger, J. Grzyb, S. Malz, B. Heinemann, and U. Pfeiffer, “A lens-integrated 430 GHz SiGe HBT source with up to -6.3 dBm radiated power,” in *IEEE Radio Frequency Integrated Circuits Symp.*, Honolulu, HI, USA, Jun. 2017, pp. 160–163.

[own9] S. Malz, P. Hillger, B. Heinemann, and U. R. Pfeiffer, “A 275 GHz amplifier in 0.13 µm SiGe,” in *11th European Microwave Integrated Circuits Conf.*, London, UK, 2016, pp. 185–188.

[own10] P. Hillger, J. Grzyb, R. Lachner, and U. Pfeiffer, “An antenna-coupled 0.49 THz SiGe HBT source for active illumination in terahertz imaging applications,” in *10th European Microwave Integrated Circuits Conf.*, Paris, France, Sep. 2015, pp. 180–183.

[own11] P. Hillger, J. Grzyb, and U. Pfeiffer, “A fully-integrated terahertz near-field sensor for super-resolution imaging in SiGe BiCMOS,” in *2016 41st International Conference on Infrared, Millimeter, and Terahertz waves (IRMMW-THz)*, Sep. 2016, pp. 1–2.

[own12] L. Mavarani, P. Hillger, T. Bücher, *et al.*, “NearSense–Advances Towards a Silicon-Based Terahertz Near-Field Imaging Sensor for Ex Vivo Breast Tumour Identification,” *Frequenz*, vol. 72, no. 3-4, pp. 93–99, 2018.

[own13] L. Mavarani, P. Hillger, J. Grzyb, *et al.*, "A novel approach of aqueous solution analysis using a fully-integrated terahertz near-field sensor," in *2017 42nd International Conference on Infrared, Millimeter, and Terahertz Waves (IRMMW-THz)*, Aug. 2017, pp. 1–2.

[own14] P. Hillger, R. Jain, J. Grzyb, *et al.*, "A solid-state 0.56 thz near-field array for µm-scale surface imaging," in *2018 43rd International Conference on Infrared, Millimeter, and Terahertz Waves (IRMMW-THz)*, Sep. 2018, pp. 1–2.

Cited References

[1] D. M. Mittleman, R. H. Jacobsen, R. Neelamani, R. G. Baraniuk, and M. C. Nuss, "Gas sensing using terahertz time-domain spectroscopy," *Applied Physics B: Lasers and Optics*, vol. 67, no. 3, pp. 379–390, 1998.

[2] M. Schall, M. Walther, and P. U. Jepsen, "Fundamental and second-order phonon processes in CdTe and ZnTe," *Physical Review B*, vol. 64, no. 9, p. 094 301, 2001.

[3] J.-H. Son, *Terahertz biomedical science and technology.* CRC Press, 2014.

[4] D. M. Leitner, M. Gruebele, and M. Havenith, "Solvation dynamics of biomolecules: modeling and terahertz experiments," *HFSP journal*, vol. 2, no. 6, pp. 314–323, 2008.

[5] C. Kulesa, "Terahertz spectroscopy for astronomy: From comets to cosmology," *IEEE Trans. THz Sci. Technol.*, vol. 1, no. 1, pp. 232–240, Sep. 2011.

[6] P. Siegel, "Terahertz technology," *IEEE Trans. Microw. Theory Techn.*, vol. 50, no. 3, pp. 910–928, Mar. 2002.

[7] E. N. Grossman, K. Leong, X. Mei, and W. Deal, "Low-frequency noise and passive imaging with 670 GHz HEMT low-noise amplifiers," *IEEE Trans. THz Sci. Technol.*, vol. 4, no. 6, pp. 749–752, Nov. 2014.

[8] J. J. Lynch, H. P. Moyer, J. H. Schaffner, Y. Royter, M. Sokolich, B. Hughes, Y. J. Yoon, and J. N. Schulman, "Passive millimeter-wave imaging module with preamplified zero-bias detection," *IEEE Trans. Microw. Theory Techn.*, vol. 56, no. 7, pp. 1592–1600, Jul. 2008.

[9] C. Fattinger and D. Grischkowsky, "Point source terahertz optics," *Applied Physics Letters*, vol. 53, no. 16, pp. 1480–1482, 1988.

[10] M. Van Exter, C. Fattinger, and D. Grischkowsky, "Terahertz time-domain spectroscopy of water vapor," *Optics letters*, vol. 14, no. 20, pp. 1128–1130, 1989.

[11] P. H. Bolivar, M. Brucherseifer, M. Nagel, H. Kurz, A. Bosserhoff, and R. Büttner, "Label-free probing of genes by time-domain terahertz sensing," *Physics in Medicine & Biology*, vol. 47, no. 21, p. 3815, 2002.

[12] A. J. L. Adam, "Review of near-field terahertz measurement methods and their applications," *J. Infrared, Millimeter, and Terahertz Waves*, vol. 32, no. 8, p. 976, Jul. 2011.

[13] H.-T. Chen, R. Kersting, and G. C. Cho, "Terahertz imaging with nanometer resolution," *Applied Physics Letters*, vol. 83, no. 15, pp. 3009–3011, Oct. 2003.

[14] C. Liewald, S. Mastel, J. Hesler, A. J. Huber, R. Hillenbrand, and F. Keilmann, "All-electronic terahertz nanoscopy," *Optica*, vol. 5, no. 2, pp. 159–163, 2018.

[15] J. Grzyb, B. Heinemann, and U. R. Pfeiffer, "A 0.55 THz near-field sensor with a μm-range lateral resolution fully integrated in 130 nm SiGe BiCMOS," *IEEE J. Solid-State Circuits*, vol. 51, no. 12, pp. 3063–3077, Dec. 2016.

[16] D. Wang, K. Schmalz, M. H. Eissa, *et al.*, "Integrated 240-GHz dielectric sensor with dc readout circuit in a 130-nm SiGe BiCMOS technology," *IEEE Trans. Microw. Theory Techn.*, vol. 66, no. 9, pp. 4232–4241, Sep. 2018.

[17] C. Wang, B. Perkins, Z. Wang, and R. Han, "Molecular detection for unconcentrated gas with ppm sensitivity using 220-to-320-GHz dual-frequency-comb spectrometer in CMOS," *IEEE Trans. Biomed. Circuits Syst.*, vol. 12, no. 3, pp. 709–721, Jun. 2018.

[18] K. Statnikov, J. Grzyb, B. Heinemann, and U. R. Pfeiffer, "160-GHz to 1-THz multi-color active imaging with a lens-coupled SiGe HBT chip-set," *IEEE Trans. THz Sci. Technol.*, vol. 63, no. 2, pp. 520–532, Feb. 2015.

[19] J. Grzyb, B. Heinemann, and U. R. Pfeiffer, "Solid-state terahertz superresolution imaging device in 130-nm SiGe BiCMOS technology," *IEEE Trans. Microw. Theory Techn.*, vol. 65, no. 11, pp. 4357–4372, Nov. 2017.

[20] U. R. Pfeiffer, Y. Zhao, J. Grzyb, R. Al Hadi, N. Sarmah, W. Förster, H. Rücker, and B. Heinemann, "A 0.53 THz reconfigurable source module with up to 1 mW radiated power for diffuse illumination in terahertz imaging applications," *IEEE J. Solid-State Circuits*, vol. 49, no. 12, pp. 2938–2950, Dec. 2014.

[21] R. de L. Kronig, "On the Theory of Dispersion of X-Rays," *J. Opt. Soc. Am.*, vol. 12, no. 6, pp. 547–557, Jun. 1926.

[22] I. Popov, P. B. Ishai, A. Khamzin, and Y. Feldman, "The mechanism of the dielectric relaxation in water," *Physical Chemistry Chemical Physics*, vol. 18, no. 20, pp. 13 941–13 953, 2016.

[23] Y.-S. Lee, *Principles of terahertz science and technology.* Springer Science & Business Media, 2009, vol. 170.

[24] D. Saeedkia, *Handbook of terahertz technology for imaging, sensing and communications.* Elsevier, 2013.

[25] K. Kawase, Y. Ogawa, Y. Watanabe, and H. Inoue, "Non-destructive terahertz imaging of illicit drugs using spectral fingerprints," *Opt. Express*, vol. 11, no. 20, pp. 2549–2554, Oct. 2003.

[26] Y. Chen, H. Liu, Y. Deng, *et al.*, "Spectroscopic characterization of explosives in the far-infrared region," in *Terahertz for Military and Security Applications II*, International Society for Optics and Photonics, vol. 5411, 2004, pp. 1–8.

[27] D. Mittleman, *Sensing with terahertz radiation.* Springer, 2013, vol. 85.

[28] Q. Ma and R. Tipping, "Water vapor continuum in the millimeter spectral region," *The Journal of chemical physics*, vol. 93, no. 9, pp. 6127–6139, 1990.

[29] P. W. Rosenkranz, "Water vapor microwave continuum absorption: A comparison of measurements and models," *Radio Science*, vol. 33, no. 4, pp. 919–928, 1998.

[30] B. B. Hu and M. C. Nuss, "Imaging with terahertz waves," *Opt. Lett.*, vol. 20, no. 16, pp. 1716–1718, Aug. 1995.

[31] V. P. Wallace, A. J. Fitzgerald, E. Pickwell, R. J. Pye, P. F. Taday, N. Flanagan, and T. Ha, "Terahertz pulsed spectroscopy of human basal cell carcinoma," *Applied spectroscopy*, vol. 60, no. 10, pp. 1127–1133, 2006.

[32] A. J. Fitzgerald, E. Pickwell-MacPherson, and V. P. Wallace, "Use of finite difference time domain simulations and Debye theory for modelling the terahertz reflection response of normal and tumour breast tissue," *PLoS One*, vol. 9, no. 7, e99291, 2014.

[33] C.-M. Chiu, H.-W. Chen, Y.-R. Huang, Y.-J. Hwang, W.-J. Lee, H.-Y. Huang, and C.-K. Sun, "All-terahertz fiber-scanning near-field microscopy," *Opt. Lett.*, vol. 34, no. 7, pp. 1084–1086, Apr. 2009.

[34] F. Bray, J. Ferlay, I. Soerjomataram, R. L. Siegel, L. A. Torre, and A. Jemal, "Global cancer statistics 2018: Globocan estimates of incidence and mortality worldwide for 36 cancers in 185 countries," *CA: a cancer journal for clinicians*, vol. 68, no. 6, pp. 394–424, 2018.

[35] J. Landercasper, E. Whitacre, A. C. Degnim, and M. Al-Hamadani, “Reasons for re-excision after lumpectomy for breast cancer: insight from the American Society of Breast Surgeons Mastery SM database,” *Annals of surgical oncology*, vol. 21, no. 10, pp. 3185–3191, 2014.

[36] R. Jeevan, D. Cromwell, M. Trivella, *et al.*, “Reoperation rates after breast conserving surgery for breast cancer among women in england: Retrospective study of hospital episode statistics,” *Bmj*, vol. 345, e4505, 2012.

[37] A. J. Fitzgerald, V. P. Wallace, M. Jimenez-Linan, L. Bobrow, R. J. Pye, A. D. Purushotham, and D. D. Arnone, “Terahertz pulsed imaging of human breast tumors,” *Radiology*, vol. 239, no. 2, pp. 533–540, 2006.

[38] P. C. Ashworth, E. Pickwell-MacPherson, E. Provenzano, S. E. Pinder, A. D. Purushotham, M. Pepper, and V. P. Wallace, “Terahertz pulsed spectroscopy of freshly excised human breast cancer,” *Optics express*, vol. 17, no. 15, pp. 12 444–12 454, 2009.

[39] B. C. Q. Truong, H. D. Tuan, A. J. Fitzgerald, V. P. Wallace, and H. T. Nguyen, “A Dielectric Model of Human Breast Tissue in Terahertz Regime,” *IEEE Trans. Biomed. Eng.*, vol. 62, no. 2, pp. 699–707, Feb. 2015.

[40] E. Abbe, “Beiträge zur Theorie des Mikroskops und der mikroskopischen Wahrnehmung,” *Archiv für mikroskopische Anatomie*, vol. 9, no. 1, pp. 413–418, Dec. 1873.

[41] L. Novotny and B. Hecht, *Principles of nano-optics*. Cambridge university press, 2012.

[42] S. V. Kalinin and A. Gruverman, *Scanning probe microscopy: electrical and electromechanical phenomena at the nanoscale*. Springer Science & Business Media, 2007, vol. 1.

[43] N. V. Chernomyrdin, A. O. Schadko, S. P. Lebedev, *et al.*, “Solid immersion terahertz imaging with sub-wavelength resolution,” *Applied Physics Letters*, vol. 110, no. 22, p. 221 109, 2017.

[44] C. A. Balanis, *Antenna theory: analysis and design*. John wiley & sons, 2016.

[45] E. Betzig and J. K. Trautman, “Near-Field Optics: Microscopy, Spectroscopy, and Surface Modification Beyond the Diffraction Limit,” *Science*, vol. 257, no. 5067, pp. 189–195, 1992.

[46] S. Hunsche, M. Koch, I. Brener, and M. Nuss, “Thz near-field imaging,” *Optics Communications*, vol. 150, no. 1, pp. 22–26, 1998.

[47] Y. Kawano and K. Ishibashi, “An on-chip near-field terahertz probe and detector,” *Nature Photonics*, vol. 2, no. 10, p. 618, 2008.

[48] H. Zhan, R. Mendis, and D. M. Mittleman, “Superfocusing terahertz waves below $\lambda/250$ using plasmonic parallel-plate waveguides,” *Opt. Express*, vol. 18, no. 9, pp. 9643–9650, Apr. 2010.

[49] K. Ishihara, T. Ikari, H. Minamide, J.-i. Shikata, K. Ohashi, H. Yokoyama, and H. Ito, “Terahertz Near-Field Imaging Using Enhanced Transmission through a Single Subwavelength Aperture,” *Japanese Journal of Applied Physics*, vol. 44, no. No. 29, pp. L929–L931, Jul. 2005.

[50] A. J. Huber, F. Keilmann, J. Wittborn, J. Aizpurua, and R. Hillenbrand, “Terahertz near-field nanoscopy of mobile carriers in single semiconductor nanodevices,” *Nano Letters*, vol. 8, no. 11, pp. 3766–3770, Nov. 2008.

[51] M. Wächter, M. Nagel, and H. Kurz, “Tapered photoconductive terahertz field probe tip with subwavelength spatial resolution,” *Applied Physics Letters*, vol. 95, no. 4, p. 041 112, 2009.

[52] J. Szelc and H. Rutt, “Near-Field THz imaging and spectroscopy using a multiple subwavelength aperture modulator,” *IEEE Trans. THz Sci. Technol.*, vol. 3, no. 2, pp. 165–171, Mar. 2013.

[53] F. Blanchard, A. Doi, T. Tanaka, H. Hirori, H. Tanaka, Y. Kadoya, and K. Tanaka, "Real-time terahertz near-field microscope," *Optics Express*, vol. 19, no. 9, pp. 8277–8284, Apr. 2011.

[54] I. Mehdi, J. V. Siles, C. Lee, and E. Schlecht, "THz Diode Technology: Status, Prospects, and Applications," *Proceedings of the IEEE*, vol. 105, no. 6, pp. 990–1007, Jun. 2017.

[55] H. Hübers, "Terahertz heterodyne receivers," *IEEE J. Sel. Topics Quantum Electron.*, vol. 14, no. 2, pp. 378–391, Mar. 2008.

[56] A. Maestrini, B. Thomas, H. Wang, *et al.*, "Schottky diode-based terahertz frequency multipliers and mixers," *Comptes Rendus Physique*, vol. 11, no. 7-8, pp. 480–495, Oct. 2010.

[57] A. L. Betz and R. T. Boreiko, "Far-infrared heterodyne spectrometer for SOFIA," Colorado Univ.; Center for Astrophysics and Space Astronomy; Boulder, CO United States, Tech. Rep. NASA Grant NAG 2-1062, Jan. 1998.

[58] T. W. Crowe, J. L. Hesler, S. A. Retzloff, and D. S. Kurtz, "Higher power multipliers for terahertz sources," in *41st Int. Conf. on Infrared, Millimeter, and THz waves (IRMMW-THz)*, Copenhagen, Denmark, Sep. 2016.

[59] X. Mei, W. Yoshida, M. Lange, *et al.*, "First demonstration of amplification at 1 THz using 25-nm InP high electron mobility transistor process," *IEEE Electron Device Lett.*, vol. 36, no. 4, pp. 327–329, Apr. 2015.

[60] A. Timofeev, J. Luomahaara, L. Grönberg, *et al.*, "Optical and electrical characterization of a large kinetic inductance bolometer focal plane array," *IEEE Trans. THz Sci. Technol.*, vol. 7, no. 2, pp. 218–224, Mar. 2017.

[61] K. B. Cooper, R. J. Dengler, N. Llombart, B. Thomas, G. Chattopadhyay, and P. H. Siegel, "THz imaging radar for standoff personnel screening," *IEEE Trans. THz Sci. Technol.*, vol. 1, no. 1, pp. 169–182, Sep. 2011.

[62] S.-P. Han, H. Ko, N. Kim, *et al.*, "Real-time continuous-wave terahertz line scanner based on a compact 1×240 InGaAs Schottky barrier diode array detector," *Opt. Express*, vol. 22, no. 23, pp. 28 977–28 983, Nov. 2014.

[63] R. Al Hadi, H. Sherry, J. Grzyb, *et al.*, "A broadband 0.6 to 1 THz CMOS imaging detector with an integrated lens," in *2011 IEEE MTT-S International Microwave Symposium*, IEEE, Jun. 2011, pp. 1–4.

[64] N. Palka, M. Szala, and E. Czerwinska, "Characterization of prospective explosive materials using terahertz time-domain spectroscopy," *Appl. Opt.*, vol. 55, no. 17, pp. 4575–4583, Jun. 2016.

[65] T. Bowman, M. El-Shenawee, and L. K. Campbell, "Terahertz transmission vs reflection imaging and model-based characterization for excised breast carcinomas," *Biomed. Opt. Express*, vol. 7, no. 9, pp. 3756–3783, Sep. 2016.

[66] L. Li, L. Chen, J. Zhu, J. Freeman, P. Dean, A. Valavanis, A. G. Davies, and E. H. Linfield, "Terahertz quantum cascade lasers with >1 W output powers," *Electronics Letters*, vol. 50, no. 4, pp. 309–311, Feb. 2014.

[67] S. Mason, "Power Gain in Feedback Amplifier," *Transactions of the IRE Professional Group on Circuit Theory*, vol. CT-1, no. 2, pp. 20–25, Jun. 1954.

[68] S. P. Voinigescu, A. Tomkins, E. Dacquay, P. Chevalier, J. Hasch, A. Chantre, and B. Sautreuil, "A study of SiGe HBT signal sources in the 220–330-GHz range," *IEEE J. Solid-State Circuits*, vol. 48, no. 9, pp. 2011–2021, Sep. 2013.

[69] B. Heinemann, R. Barth, D. Bolze, *et al.*, "SiGe HBT technology with f_T/f_{max} of 300GHz/ 500GHz and 2.0 ps CML gate delay," in *IEEE Int. Electron Devices Meeting*, San Francisco, CA, USA, Dec. 2010, pp. 30.5.1–30.5.4.

[70] B. Heinemann, H. Rucker, R. Barth, *et al.*, "SiGe HBT with f_T/f_{max} of 505 GHz /720 GHz," in *IEEE Int. Electron Devices Meeting*, San Francisco, CA, USA, 2016, pp. 3.1.1–3.1.4.

[71] J. Grzyb, K. Statnikov, N. Sarmah, B. Heinemann, and U. R. Pfeiffer, "A 210–270-GHz circularly polarized FMCW radar with a single-lens-coupled SiGe HBT chip," *IEEE Trans. THz Sci. Technol.*, vol. 6, no. 6, pp. 771–783, Nov. 2016.

[72] M. H. Eissa, A. Malignaggi, R. Wang, M. Elkhouly, K. Schmalz, A. C. Ulusoy, and D. Kissinger, "Wideband 240-GHz transmitter and receiver in BiCMOS technology with 25-Gbit/s data rate," *IEEE J. Solid-State Circuits*, vol. 53, no. 9, pp. 2532–2542, Sep. 2018.

[73] M. Schröter, T. Rosenbaum, P. Chevalier, B. Heinemann, S. P. Voinigescu, E. Preisler, J. Bock, and A. Mukherjee, "SiGe HBT technology: Future trends and TCAD-based roadmap," *Proc. IEEE*, vol. 105, no. 6, pp. 1068–1086, Jun. 2017.

[74] I. Post, M. Akbar, G. Curello, *et al.*, "A 65nm CMOS SOC technology featuring strained silicon transistors for RF applications," in *IEEE Int. Electron Devices Meeting*, San Francisco, CA, USA, 2006, pp. 1–3.

[75] C. A. Balanis, *Advanced engineering electromagnetics*. John Wiley & Sons, 2012, p. 1018.

[76] K. Sengupta, D. Seo, L. Yang, and A. Hajimiri, "Silicon integrated 280 GHz imaging chipset with 4×4 SiGe receiver array and CMOS source," *IEEE Trans. THz Sci. Technol.*, vol. 5, no. 3, pp. 427–437, May 2015.

[77] D. Filipovic, S. Gearhart, and G. Rebeiz, "Double-slot antennas on extended hemispherical and elliptical silicon dielectric lenses," *IEEE Trans. THz Sci. Technol.*, vol. 41, no. 10, pp. 1738–1749, Oct. 1993.

[78] J. Grzyb and U. Pfeiffer, "THz direct detector and heterodyne receiver arrays in silicon nanoscale technologies," *J. Infrared, Millimeter, and Terahertz Waves*, vol. 36, no. 10, pp. 998–1032, Oct. 2015.

[79] R. Jain, J. Grzyb, and U. R. Pfeiffer, "Terahertz Light-Field Imaging," *IEEE Trans. THz Sci. Technol.*, vol. 6, no. 5, pp. 649–657, Sep. 2016.

[80] X. Wu and K. Sengupta, "On-chip THz spectroscope exploiting electromagnetic scattering with multi-port antenna," *IEEE J. Solid-State Circuits*, vol. 51, no. 12, pp. 3049–3062, Dec. 2016.

[81] E. Seok, C. Cao, D. Shim, D. J. Arenas, D. B. Tanner, C. Hung, and K. O. Kenneth, "A 410GHz CMOS push-push oscillator with an on-chip patch antenna," in *IEEE Int. Solid-State Circuits Conf.*, San Francisco, CA, USA, Feb. 2008, pp. 472–629.

[82] O. Momeni and E. Afshari, "High power terahertz and milimeter-wave oscillator design: A systematic approach," *IEEE J. Solid-State Circuits*, vol. 46, no. 3, pp. 583–597, Mar. 2011.

[83] H. Aghasi, A. Cathelin, and E. Afshari, "A 0.92-THz SiGe power radiator based on a nonlinear theory for harmonic generation," *IEEE J. Solid-State Circuits*, vol. 52, no. 2, pp. 406–422, Feb. 2017.

[84] Y. Tousi and E. Afshari, "A high-power and scalable 2-D phased array for terahertz CMOS integrated systems," *IEEE J. Solid-State Circuits*, vol. 50, no. 2, pp. 597–609, Feb. 2015.

[85] Z. Hu, M. Kaynak, and R. Han, "High-power radiation at 1 THz in silicon: A fully scalable array using a multi-functional radiating mesh structure," *IEEE J. Solid-State Circuits*, vol. 53, no. 5, pp. 1313–1327, May 2018.

[86] R. Han, C. Jiang, A. Mostajeran, M. Emadi, H. Aghasi, H. Sherry, A. Cathelin, and E. Afshari, "A SiGe terahertz heterodyne imaging transmitter with 3.3 mW radiated power and fully-integrated phase-locked loop," *IEEE J. Solid-State Circuits*, vol. 50, no. 12, pp. 2935–2947, Sep. 2015.

[87] R. Han and E. Afshari, “A CMOS high-power broadband 260-GHz radiator array for spectroscopy,” *IEEE J. Solid-State Circuits*, vol. 48, no. 12, pp. 3090–3104, Dec. 2013.

[88] K. Sengupta and A. Hajimiri, “A 0.28 THz power-generation and beam-steering array in CMOS based on distributed active radiators,” *IEEE J. Solid-State Circuits*, vol. 47, no. 12, pp. 3013–3031, Dec. 2012.

[89] J. Grzyb, Y. Zhao, and U. R. Pfeiffer, “A 288-GHz lens-integrated balanced triple-push source in a 65-nm CMOS technology,” *IEEE J. Solid-State Circuits*, vol. 48, no. 7, pp. 1751–1761, Jul. 2013.

[90] S. Jameson and E. Socher, “High efficiency 293 GHz radiating source in 65 nm CMOS,” *IEEE Microw. Wireless Compon. Lett.*, vol. 24, no. 7, pp. 463–465, Jul. 2014.

[91] J. Al-Eryani, H. Knapp, J. Kammerer, K. Aufinger, H. Li, and L. Maurer, “Fully integrated single-chip 305–375-GHz transceiver with on-chip antennas in SiGe BiCMOS,” *IEEE Trans. THz Sci. Technol.*, vol. 8, no. 3, pp. 329–339, May 2018.

[92] L. Wu, S. Liao, and Q. Xue, “A 312-GHz CMOS injection-locked radiator with chip-and-package distributed antenna,” *IEEE J. Solid-State Circuits*, vol. 52, no. 11, pp. 2920–2933, Nov. 2017.

[93] H. Jalili and O. Momeni, “A 0.34-THz varactor-less scalable standing wave radiator array with 5.9% tuning range in 130nm BiCMOS,” in *IEEE Radio Frequency Integrated Circuits Symp.*, San Francisco, CA, USA, May 2016, pp. 182–185.

[94] K. Guo, A. Standaert, and P. Reynaert, “A 525–556-GHz radiating source with a dielectric lens antenna in 28-nm CMOS,” *IEEE Trans. THz Sci. Technol.*, vol. 8, no. 3, pp. 340–349, May 2018.

[95] B. Khamaisi, S. Jameson, and E. Socher, “0.61THz radiating source with on-chip antenna on 65nm CMOS,” in *11th European Microwave Integrated Circuits Conf.*, London, UK, Oct. 2016, pp. 389–392.

[96] P. Rodriguez-Vazquez, J. Grzyb, N. Sarmah, B. Heinemann, and U. R. Pfeiffer, “A 65 Gbps QPSK one meter wireless link operating at a 225–255 GHz tunable carrier in a SiGe HBT technology,” in *IEEE Radio and Wireless Symp.*, Anaheim, CA, USA, 2018, pp. 146–149.

[97] Y. Yang, O. D. Gurbuz, and G. M. Rebeiz, “An eight-element 370–410-GHz phased-array transmitter in 45-nm CMOS SOI with peak EIRP of 8–8.5 dBm,” *IEEE Trans. THz Sci. Technol.*, vol. 64, no. 12, pp. 4241–4249, Dec. 2016.

[98] F. Golcuk, O. D. Gurbuz, and G. M. Rebeiz, “A 0.39–0.44 THz 2×4 amplifier-quadrupler array with peak EIRP of 3–4 dBm,” *IEEE Trans. Microw. Theory Techn.*, vol. 61, no. 12, pp. 4483–4491, Dec. 2013.

[99] Y. Zhao, Z.-Z. Chen, Y. Du, *et al.*, “A 0.56 THz phase-locked frequency synthesizer in 65 nm CMOS technology,” *IEEE J. Solid-State Circuits*, vol. 51, no. 12, pp. 3005–3019, Dec. 2016.

[100] B. Khamaisi, S. Jameson, and E. Socher, “A 0.58–0.61THz single on-chip antenna transceiver based on active X30 LO chain on 65nm CMOS,” in *11th European Microwave Integrated Circuits Conf.*, London, UK, Oct. 2016, pp. 97–100.

[101] Z. Ahmad and K. O. Kenneth, “0.65-0.73THz quintupler with an on-chip antenna in 65-nm CMOS,” in *Symp. on VLSI Circuits*, Kyoto, Japan, Jun. 2015, pp. C310–C311.

[102] E. Öjefors, J. Grzyb, Y. Zhao, B. Heinemann, B. Tillack, and U. R. Pfeiffer, “A 820GHz SiGe chipset for terahertz active imaging applications,” in *IEEE Int. Solid-State Circuits Conf.*, San Francisco, CA, USA, Feb. 2011, pp. 224–226.

[103] Z. Ahmad, M. Lee, and K. K. O, “20.5 1.4THz, -13dBm-EIRP frequency multiplier chain using symmetric- and asymmetric-CV varactors in 65nm CMOS,” in *IEEE Int. Solid-State Circuits Conf.*, San Francisco, CA, USA, Jan. 2016, pp. 350–351.

[104] E. Johnson, “Physical limitations on frequency and power parameters of transistors,” in *1958 IRE International Convention Record*, vol. 13, New York, NY, USA, Mar. 1965, pp. 27–34.

[105] U. R. Pfeiffer and E. Ojefors, “A 600-GHz CMOS focal-plane array for terahertz imaging applications,” in *European Solid-State Circuits Conference*, Edinburgh, UK, Sep. 2008, pp. 110–113.

[106] F. F. Sizov, V. P. Reva, A. G. Golenkov, and V. V. Zabudsky, “Uncooled Detectors Challenges for THz/sub-THz Arrays Imaging,” *Journal of Infrared, Millimeter, and Terahertz Waves*, vol. 32, no. 10, pp. 1192–1206, Oct. 2011.

[107] J. L. Hesler and T. W. Crowe, “NEP and responsivity of THz zero-bias Schottky diode detectors,” in *Joint 32nd Int. Conf. on Infrared and Millimeter Waves and the 15th Int. Conf. on Terahertz Electronics*, Sep. 2007, pp. 844–845.

[108] V. Radisic, K. M. K. H. Leong, X. Mei, S. Sarkozy, W. Yoshida, and W. R. Deal, “Power Amplification at 0.65 THz Using InP HEMTs,” *IEEE Trans. Microw. Theory Techn.*, vol. 60, no. 3, pp. 724–729, Mar. 2012.

[109] C. Middleton, G. Zummo, A. Weeks, A. Pergande, L. Mirth, and G. Boreman, “Passive millimeter-wave focal plane array,” in *Joint 29th Int. Conf. on Infrared and Millimeter Waves and 12th Int. Conf. on Terahertz Electronics*, Sep. 2004, pp. 745–746.

[110] G. Karolyi, D. Gergelyi, and P. Foldesy, “Sub-THz sensor array with embedded signal processing in 90 nm CMOS technology,” *IEEE Sensors J.*, vol. 14, no. 8, pp. 2432–2441, Aug. 2014.

[111] S. Boppel, A. Lisauskas, M. Mundt, *et al.*, “CMOS integrated antenna-coupled field-effect transistors for the detection of radiation from 0.2 to 4.3 THz,” *IEEE Trans. Microw. Theory Techn.*, vol. 60, no. 12, pp. 3834–3843, Dec. 2012.

[112] A. Boukhayma, A. Dupret, J.-P. Rostaing, and C. Enz, “A low-noise CMOS THz imager based on bource modulation and an in-pixel high-Q passive switched-capacitor N-path filter.,” *Sensors (Basel, Switzerland)*, vol. 16(3): 325, Mar. 2016.

[113] H. Sherry, R. A. Hadi, J. Grzyb, E. Öjefors, A. Cathelin, A. Kaiser, and U. R. Pfeiffer, “Lens-integrated THz imaging arrays in 65nm CMOS technologies,” in *IEEE Radio Frequency Integrated Circuits Symp.*, Baltimore, MD, USA, Jun. 2011, pp. 1–4.

[114] R. Jain, H. Rucker, and U. R. Pfeiffer, “Zero gate-bias terahertz detection with an asymmetric NMOS transistor,” in *41st Int. Conf. on Infrared, Millimeter, and Terahertz waves*, Sep. 2016, pp. 1–2.

[115] U. R. Pfeiffer, J. Grzyb, H. Sherry, A. Cathelin, and A. Kaiser, “Toward low-NEP room-temperature THz MOSFET direct detectors in CMOS technology,” in *38th Int. Conf. on Infrared, Millimeter, and Terahertz Waves*, Mainz, Germany, Sep. 2013, pp. 1–2.

[116] R. Al Hadi, H. Sherry, J. Grzyb, *et al.*, “A 1 k-pixel video camera for 0.7–1.1 terahertz imaging applications in 65-nm CMOS,” *IEEE J. Solid-State Circuits*, vol. 47, no. 12, pp. 2999–3012, Dec. 2012.

[117] Z.-y. Liu, L.-y. Liu, J. Yang, and N.-j. Wu, “A CMOS fully integrated 860-GHz terahertz sensor,” *IEEE Trans. THz Sci. Technol.*, vol. 7, no. 4, pp. 455–465, Jul. 2017.

[118] D. Yoon, J. Kim, J. Yun, M. Kaynak, B. Tillack, and J.-S. Rieh, “300-GHz direct and heterodyne active imagers based on 0.13-μm SiGe HBT technology,” *IEEE Trans. THz Sci. Technol.*, vol. 7, no. 5, pp. 536–545, Sep. 2017.

[119] M. Uzunkol, O. D. Gurbuz, F. Golcuk, and G. M. Rebeiz, “A 0.32 THz SiGe 4$\times$4 imaging array using high-efficiency on-chip antennas,” *IEEE J. Solid-State Circuits*, vol. 48, no. 9, pp. 2056–2066, Sep. 2013.

[120] R. Al Hadi, J. Grzyb, B. Heinemann, and U. R. Pfeiffer, “A terahertz detector array in a SiGe HBT technology,” *IEEE J. Solid-State Circuits*, vol. 48, no. 9, pp. 2002–2010, Sep. 2013.

[121] M. Andree, J. Grzyb, R. Jain, B. Heinemann, and U. R. Pfeiffer, "A Broadband Dual-Polarized Terahertz Direct Detector in a 0.13-µm SiGe HBT Technology," in *2019 IEEE MTT-S International Microwave Symposium (IMS)*, Jun. 2019, pp. 500–503.

[122] R. Han, Y. Zhang, Y. Kim, D. Y. Kim, H. Shichijo, E. Afshari, and K. K. O, "Active terahertz imaging using schottky diodes in CMOS: Array and 860-GHz pixel," *IEEE J. Solid-State Circuits*, vol. 48, no. 10, pp. 2296–2308, Oct. 2013.

[123] E. Öjefors and U. R. Pfeiffer, "A 650 GHz SiGe receiver front-end for terahertz imaging arrays," in *IEEE Int. Solid-State Circuits Conf.*, San Francisco, CA, USA, Feb. 2010, pp. 430–431.

[124] C. Jiang, A. Mostajeran, R. Han, M. Emadi, H. Sherry, A. Cathelin, and E. Afshari, "A fully integrated 320 ghz coherent imaging transceiver in 130 nm sige bicmos," *IEEE J. Solid-State Circuits*, vol. 51, no. 11, pp. 2596–2609, Nov. 2016.

[125] Z. Hu, C. Wang, and R. Han, "A 32-unit 240-ghz heterodyne receiver array in 65-nm cmos with array-wide phase locking," *IEEE J. Solid-State Circuits*, vol. 54, no. 5, pp. 1216–1227, May 2019.

[126] C. M. Watts, D. Shrekenhamer, J. Montoya, *et al.*, "Terahertz compressive imaging with metamaterial spatial light modulators," *Nature Photonics*, vol. 8, no. 8, p. 605, Jun. 2014.

[127] S. Augustin, J. Hieronymus, P. Jung, and H.-W. Hübers, "Compressed sensing in a fully non-mechanical 350 GHz imaging setting," *J. Infrared, Millimeter, and Terahertz Waves*, vol. 36, no. 5, pp. 496–512, May 2015.

[128] S. Voinigescu, *High-frequency integrated circuits*. Cambridge University Press, 2013.

[129] H. Aghasi, A. Cathelin, and E. Afshari, "A 0.92-THz SiGe Power Radiator Based on a Nonlinear Theory for Harmonic Generation," *IEEE J. Solid-State Circuits*, vol. 52, no. 2, pp. 406–422, Feb. 2017.

[130] Verspecht and D. E. Root, "Polyharmonic distortion modeling," *IEEE Microw. Mag.*, vol. 7, no. 3, pp. 44–57, Jun. 2006.

[131] S. Shopov, A. Balteanu, J. Hasch, P. Chevalier, A. Cathelin, and S. P. Voinigescu, "A 234-261-GHz 55-nm SiGe BiCMOS signal source with 5.4-7.2 dBm output power, 1.3% DC-to-RF efficiency, and 1-GHz divided-down output," *IEEE J. Solid-State Circuits*, vol. 51, no. 9, pp. 2054–2065, 2016.

[132] K. Statnikov, E. Öjefors, J. Grzyb, P. Chevalier, and U. R. Pfeiffer, "A 0.32 THz FMCW radar system based on low-cost lens-integrated SiGe HBT front-ends," in *2013 Proceedings of the ESSCIRC (ESSCIRC)*, Sep. 2013, pp. 81–84.

[133] J. P. Guillet, B. Recur, L. Frederique, B. Bousquet, L. Canioni, I. Manek-Hönninger, P. Desbarats, and P. Mounaix, "Review of terahertz tomography techniques," *Journal of Infrared, Millimeter, and Terahertz Waves*, vol. 35, no. 4, pp. 382–411, 2014.

[134] L. Öhrström, A. Bitzer, M. Walther, and F. J. Rühli, "Technical note: Terahertz imaging of ancient mummies and bone," *American J. of Physical Anthropology*, vol. 142, no. 3, pp. 497–500, Apr. 2010.

[135] J.-P. Caumes, A. Younus, S. Salort, B. Chassagne, B. Recur, A. Ziéglé, A. Dautant, and E. Abraham, "Terahertz tomographic imaging of XVIIIth dynasty egyptian sealed pottery," *Appl. Opt.*, vol. 50, no. 20, pp. 3604–3608, Jul. 2011.

[136] M. Bessou, B. Chassagne, J.-P. Caumes, C. Pradère, P. Maire, M. Tondusson, and E. Abraham, "Three-dimensional terahertz computed tomography of human bones," *Appl. Opt.*, vol. 51, no. 28, pp. 6738–6744, Oct. 2012.

[137] J. Takayanagi, H. Jinno, S. Ichino, *et al.*, "High-resolution time-of-flight terahertz tomography using a femtosecond fiber laser," *Optics Express*, vol. 17, no. 9, p. 7533, Apr. 2009.

[138] B. Ferguson, S. Wang, D. Gray, D. Abbot, and X.-C. Zhang, "T-ray computed tomography," *Opt. Lett.*, vol. 27, no. 15, pp. 1312–1314, Aug. 2002.

[139] S. Wang and X.-C. Zhang, "Tomographic imaging with a terahertz binary lens," *Applied Physics Letters*, vol. 82, no. 12, pp. 1821–1823, Mar. 2003.

[140] A. Brahm, M. Kunz, S. Riehemann, G. Notni, and A. Tünnermann, "Volumetric spectral analysis of materials using terahertz-tomography techniques," *Applied Physics B*, vol. 100, no. 1, pp. 151–158, Jul. 2010.

[141] J. Radon, "1.1 über die Bestimmung von Funktionen durch ihre Integralwerte längs gewisser Mannigfaltigkeiten," *Classic papers in modern diagnostic radiology*, vol. 5, p. 21, 2005.

[142] R. Gordon, R. Bender, and G. T. Herman, "Algebraic reconstruction techniques (ART) for three-dimensional electron microscopy and X-ray photography," *Journal of theoretical Biology*, vol. 29, no. 3, pp. 471–481, 1970.

[143] P. Gilbert, "Iterative methods for the three-dimensional reconstruction of an object from projections," *Journal of theoretical biology*, vol. 36, no. 1, pp. 105–117, 1972.

[144] A. H. Andersen and A. C. Kak, "Simultaneous algebraic reconstruction technique (SART): a superior implementation of the ART algorithm," *Ultrasonic imaging*, vol. 6, no. 1, pp. 81–94, 1984.

[145] L. L. Geyer, U. J. Schoepf, F. G. Meinel, *et al.*, "State of the art: iterative CT reconstruction techniques," *Radiology*, vol. 276, no. 2, pp. 339–357, 2015.

[146] R. J. Lytle and K. A. Dines, "Iterative Ray Tracing between Boreholes for Underground Image Reconstruction," *IEEE Transactions on Geoscience and Remote Sensing*, vol. GE-18, no. 3, pp. 234–240, Jul. 1980.

[147] S. Cha and C. Vest, "Tomographic reconstruction of strongly refracting fields and its application to interferometric measurement of boundary layers," *Applied Optics*, vol. 20, no. 16, pp. 2787–2794, 1981.

[148] J. Tepe, T. Schuster, and B. Littau, "A modified algebraic reconstruction technique taking refraction into account with an application in terahertz tomography," *Inverse Problems in Science and Engineering*, vol. 25, no. 10, pp. 1448–1473, 2017.

[149] M. Andree, J. Grzyb, R. Jain, B. Heinemann, and U. R. Pfeiffer, "A Broadband Antenna-Coupled Terahertz Direct Detector in a 0.13-µm SiGe HBT Technology," in *14th European Microwave Integrated Circuits Conference (EuMIC)*, Sep. 2019, to be published.

[150] J. Braat and P. Török, *Imaging Optics*. Cambridge University Press, 2019.

[151] M. González-Cardel, P. Arguijo, and R. Díaz-Uribe, "Gaussian beam radius measurement with a knife-edge: a polynomial approximation to the inverse error function," *Applied Optics*, vol. 52, no. 16, p. 3849, Jun. 2013.

[152] X.-C. Zhang and J. Xu, *Introduction to THz wave photonics*. Springer, 2010, vol. 29.

[153] W. van Aarle, W. J. Palenstijn, J. De Beenhouwer, T. Altantzis, S. Bals, K. J. Batenburg, and J. Sijbers, "The ASTRA Toolbox: A platform for advanced algorithm development in electron tomography," *Ultramicroscopy*, vol. 157, pp. 35–47, Oct. 2015.

[154] M. Jewariya, E. Abraham, T. Kitaguchi, Y. Ohgi, M.-a. Minami, T. Araki, and T. Yasui, "Fast three-dimensional terahertz computed tomography using real-time line projection of intense terahertz pulse," *Optics Express*, vol. 21, no. 2, p. 2423, Jan. 2013.

[155] G. C. Trichopoulos and K. Sertel, "Broadband terahertz computed tomography using a 5k-pixel real-time THz camera," *J. Infrared, Millimeter, and Terahertz Waves*, vol. 36, pp. 675–686, Feb. 2015.

[156] L.-F. Chen, C. Ong, C. Neo, V. Varadan, and V. K. Varadan, *Microwave electronics: measurement and materials characterization*. John Wiley & Sons, 2004.

[157] R. A. Waldron, "Perturbation theory of resonant cavities," *Proceedings of the IEE - Part C: Monographs*, vol. 107, no. 12, pp. 272–274, Sep. 1960.

[158] M. Schueler, C. Mandel, M. Puentes, and R. Jakoby, "Metamaterial Inspired Microwave Sensors," *IEEE Microw. Mag.*, vol. 13, no. 2, pp. 57–68, Mar. 2012.

[159] D. Pozar, *Microwave Engineering, 4th Edition*. Wiley, 2011.

[160] O. Klein, S. Donovan, M. Dressel, and G. Grüner, "Microwave cavity perturbation technique: Part I: Principles," *International Journal of Infrared and Millimeter Waves*, vol. 14, no. 12, pp. 2423–2457, Dec. 1993.

[161] C. Gao, T. Wei, F. Duewer, Y. Lu, and X.-D. Xiang, "High spatial resolution quantitative microwave impedance microscopy by a scanning tip microwave near-field microscope," *Applied Physics Letters*, vol. 71, no. 13, pp. 1872–1874, 1997.

[162] C. Gao and X.-D. Xiang, "Quantitative microwave near-field microscopy of dielectric properties," *Review of Scientific Instruments*, vol. 69, no. 11, pp. 3846–3851, 1998.

[163] B. Reinhard, K. M. Schmitt, V. Wollrab, J. Neu, R. Beigang, and M. Rahm, "Metamaterial near-field sensor for deep-subwavelength thickness measurements and sensitive refractometry in the terahertz frequency range," *Applied Physics Letters*, vol. 100, no. 22, p. 221 101, May 2012.

[164] J. F. O'Hara, R. Singh, I. Brener, E. Smirnova, J. Han, A. J. Taylor, and W. Zhang, "Thin-film sensing with planar terahertz metamaterials: sensitivity and limitations," *Opt. Express*, vol. 16, no. 3, pp. 1786–1795, Feb. 2008.

[165] S.-Y. Chiam, R. Singh, W. Zhang, and A. A. Bettiol, "Controlling metamaterial resonances via dielectric and aspect ratio effects," *Applied Physics Letters*, vol. 97, no. 19, p. 191 906, 2010.

[166] S. Mukherjee, X. Shi, L. Udpa, S. Udpa, Y. Deng, and P. Chahal, "Design of a Split-Ring Resonator Sensor for Near-Field Microwave Imaging," *IEEE Sensors J.*, vol. 18, no. 17, pp. 7066–7076, Sep. 2018.

[167] M. A. H. Ansari, A. K. Jha, and M. J. Akhtar, "Design and application of the CSRR-based planar sensor for noninvasive measurement of complex permittivity," *IEEE Sensors J.*, vol. 15, no. 12, pp. 7181–7189, Dec. 2015.

[168] C. Lee and C. Yang, "Thickness and Permittivity Measurement in Multi-Layered Dielectric Structures Using Complementary Split-Ring Resonators," *IEEE Sensors Journal*, vol. 14, no. 3, pp. 695–700, Mar. 2014.

[169] H. Wang, Y. Chen, A. Hassibi, A. Scherer, and A. Hajimiri, "A frequency-shift CMOS magnetic biosensor array with single-bead sensitivity and no external magnet," in *2009 IEEE International Solid-State Circuits Conference - Digest of Technical Papers*, Feb. 2009, 438–439, 439a.

[170] H. Wang, C. Weng, and A. Hajimiri, "Phase noise and fundamental sensitivity of oscillator-based reactance sensors," *IEEE Trans. Microw. Theory Techn.*, vol. 61, no. 5, pp. 2215–2229, May 2013.

[171] T. Mitsunaka, D. Sato, N. Ashida, A. Saito, K. Iizuka, T. Suzuki, Y. Ogawa, and M. Fujishima, "CMOS biosensor IC focusing on dielectric relaxations of biological water with 120 and 60 GHz oscillator arrays," *IEEE J. Solid-State Circuits*, vol. 51, no. 11, pp. 2534–2544, Nov. 2016.

[172] J. Naqui, *Symmetry properties in transmission lines loaded with electrically small resonators: circuit modeling and applications*. Springer, 2015.

[173] Y. L. Tang and H. Wang, "Triple-push oscillator approach: Theory and experiments," *IEEE J. Solid-State Circuits*, vol. 36, no. 10, pp. 1472–1479, Oct. 2001.

[174] J. W. May and G. M. Rebeiz, "Design and Characterization of W-Band SiGe RFICs for Passive Millimeter-Wave Imaging," *IEEE Trans. Microw. Theory Techn.*, vol. 58, no. 5, pp. 1420–1430, May 2010.

[175] R. Al Hadi, "Terahertz Integrated Circuits in Silicon Technologies," PhD thesis, Universität Wuppertal, Fakultät für Elektrotechnik, Informationstechnik und ..., 2018.

[176] G. Niu, "Noise in SiGe HBT RF technology: Physics, modeling, and circuit implications," *Proceedings of the IEEE*, vol. 93, no. 9, pp. 1583–1597, 2005.

[177] M. Bouhouche, S. Latreche, and C. Gontrand, "Low Frequency Noise in SiGe Bipolar Transistor: Effect of Extrinsic base Implantation Traps," *International Journal of Computer Applications*, vol. 975, p. 8887, 2011.

[178] C. Mukherjee, T. Jacquet, A. Chakravorty, T. Zimmer, J. Böck, K. Aufinger, and C. Maneux, "Low-frequency noise in advanced sige: C hbts—part i: Analysis," *IEEE Transactions on Electron Devices*, vol. 63, no. 9, pp. 3649–3656, 2016.

[179] H. Rucker, B. Heinemann, and A. Fox, "Half-Terahertz SiGe BiCMOS technology," in *2012 IEEE 12th Topical Meeting on Silicon Monolithic Integrated Circuits in RF Systems*, Jan. 2012, pp. 133–136.

[180] H.-G. von Ribbeck, "THz Near-Field Microscopy and Spectroscopy," PhD thesis, Technische Universität Dresden, Dresden, 2015.

[181] S. G. McMeekin, A. Z. Khokhar, B. Lahiri, M. Richard, and N. P. Johnson, "Analysis of resonant responses of split ring resonators using conformal mapping techniques," in *Metamaterials II*, International Society for Optics and Photonics, vol. 6581, 2007, p. 65810V.

[182] L. Su, J. Naqui, J. Mata-Contreras, and F. Martín, "Modeling Metamaterial Transmission Lines Loaded With Pairs of Coupled Split-Ring Resonators," *IEEE Antennas Wireless Propag. Lett.*, vol. 14, pp. 68–71, 2015.

[183] L. Su, J. Naqui, J. Mata, and F. Martín, "Recent advances in modeling metamaterial transmission lines based on pairs of split ring resonators (SRRs): Coupling between the SRRs forming the pair," in *2014 8th International Congress on Advanced Electromagnetic Materials in Microwaves and Optics*, Aug. 2014, pp. 382–384.

[184] P. Vélez, L. Su, K. Grenier, J. Mata-Contreras, D. Dubuc, and F. Martín, "Microwave Microfluidic Sensor Based on a Microstrip Splitter/Combiner Configuration and Split Ring Resonators (SRRs) for Dielectric Characterization of Liquids," *IEEE Sensors J.*, vol. 17, no. 20, pp. 6589–6598, Oct. 2017.

[185] F. Aznar, J. Bonache, and F. Martín, "Improved circuit model for left-handed lines loaded with split ring resonators," *Applied Physics Letters*, vol. 92, no. 4, p. 043 512, 2008.

[186] A. D. Pye and M. M. Hella, "Analysis and Optimization of Transformer-Based Series Power Combining for Reconfigurable Power Amplifiers," *IEEE Trans. Circuits Syst. I*, vol. 58, no. 1, pp. 37–50, Jan. 2011.

[187] N. Sarmah, K. Aufinger, R. Lachner, and U. R. Pfeiffer, "A 200–225 GHz SiGe Power Amplifier with peak Psatof 9.6 dBm using wideband power combination," in *ESSCIRC Conference 2016: 42nd European Solid-State Circuits Conference*, Sep. 2016, pp. 193–196.

[188] E. J. Wilkinson, "An N-Way Hybrid Power Divider," *IRE Transactions on Microwave Theory and Techniques*, vol. 8, no. 1, pp. 116–118, Jan. 1960.

[189] S. Horst, R. Bairavasubramanian, M. M. Tentzeris, and J. Papapolymerou, "Modified wilkinson power dividers for millimeter-wave integrated circuits," *IEEE Trans. Microw. Theory Techn.*, vol. 55, no. 11, pp. 2439–2445, Nov. 2007.

[190] R. R. Harrison and C. Charles, "A low-power low-noise CMOS amplifier for neural recording applications," *IEEE J. Solid-State Circuits*, vol. 38, no. 6, pp. 958–965, Jun. 2003.

[191] P. E. Allen and D. R. Holberg, *CMOS analog circuit design*. Elsevier, 2011.

[192] H. Banba, H. Shiga, A. Umezawa, T. Miyaba, T. Tanzawa, S. Atsumi, and K. Sakui, "A CMOS bandgap reference circuit with sub-1-V operation," *IEEE J. Solid-State Circuits*, vol. 34, no. 5, pp. 670–674, May 1999.

[193] P. Malcovati, F. Maloberti, C. Fiocchi, and M. Pruzzi, "Curvature-compensated BiCMOS bandgap with 1-V supply voltage," *IEEE J. Solid-State Circuits*, vol. 36, no. 7, pp. 1076–1081, Jul. 2001.

[194] M. J. M. van der Vorst, P. J. I. de Maagt, A. Neto, A. L. Reynolds, R. M. Heeres, W. Luinge, and M. H. A. J. Herben, "Effect of internal reflections on the radiation properties and input impedance of integrated lens antennas-comparison between theory and measurements," *IEEE Trans. Microw. Theory Techn.*, vol. 49, no. 6, pp. 1118–1125, Jun. 2001.

[195] S. W. Smith, *The Scientist and Engineer's Guide to Digital Signal Processing.* San Diego, CA, USA: California Technical Publishing, 1997.

[196] H. Tang, Y. Lu, X. Jiang, E. J. Ng, J. M. Tsai, D. A. Horsley, and B. E. Boser, "3-D Ultrasonic Fingerprint Sensor-on-a-Chip," *IEEE J. Solid-State Circuits*, vol. 51, no. 11, pp. 2522–2533, Nov. 2016.

[197] H. AlShehri, M. Hussain, H. AboAlSamh, and M. AlZuair, "A Large-Scale Study of Fingerprint Matching Systems for Sensor Interoperability Problem," *Sensors*, vol. 18, no. 4, 2018.

[198] D. Maltoni, D. Maio, A. K. Jain, and S. Prabhakar, *Handbook of fingerprint recognition.* Springer Science & Business Media, 2009.

[199] W. M. Association *et al.*, "World Medical Association Declaration of Helsinki. Ethical principles for medical research involving human subjects.," *Bulletin of the World Health Organization*, vol. 79, no. 4, p. 373, 2001.

[200] D. Nečas and P. Klapetek, "Gwyddion: An open-source software for SPM data analysis," *Central European Journal of Physics*, vol. 10, pp. 181–188, 1 2012.

[201] H. P. Huber, I. Humer, M. Hochleitner, *et al.*, "Calibrated nanoscale dopant profiling using a scanning microwave microscope," *Journal of Applied Physics*, vol. 111, no. 1, p. 014 301, 2012.

[202] O. Mitrofanov, M. Lee, J. W. P. Hsu, *et al.*, "Collection-mode near-field imaging with 0.5-THz pulses," *IEEE J. Sel. Topics Quantum Electron.*, vol. 7, no. 4, pp. 600–607, Jul. 2001.